

https://dspace.org/

Seismological and mineralogical studies of the world's deepest gold-bearing horizon, the Carbon Leader Reef, West Wits Line goldfields (South Africa): implications for its poor seismic reflective character

Nkosi, Nomqhele Zamaswazi

2016

http://hdl.handle.net/10539/21713

Nkosi, Nomqhele Zamaswazi (2016) Seismological and mineralogical studies of the world's deepest gold-bearing horizon, the Carbon Leader Reef, West Wits Line goldfields (South Africa): implications for its poor seismic reflective character, University of Witwatersrand, Johannesburg, <http://wiredspace.wits.ac.za/handle/10539/21713>

Downloaded from a DSpace repository. https://dspace.org/

Seismological and mineralogical studies of the world's deepest gold-bearing horizon, the Carbon Leader Reef, West Wits Line goldfields (South Africa): Implications for its poor seismic reflective character

By

Nomqhele Zamaswazi Nkosi

A dissertation submitted to the
Faculty of Science, University of the Witwatersrand
in fulfilment of the requirements for the degree of

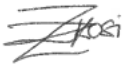
Master of Science

School of Geosciences
2016



Declaration

I declare that this dissertation is my own, unaided work. It is being submitted for the Degree of Master of Science at the University of the Witwatersrand, Johannesburg. It has not been submitted before for any degree or examination in any other University.

Nomqhele Zamaswazi Nkosi: 

__**04th**__ day of __**November**__ 2016, at __**the University of the Witwatersrand, Johannesburg**__.

Abstract

The measurements of physical rock properties, seismic velocities in particular, associated with ore deposits and their host rocks are crucial in interpreting seismic data collected at the surface for mineral exploration purposes. The understanding of the seismic velocities and densities of rock units can help to improve the understanding of seismic reflections and thus lead to accurate interpretations of the subsurface geology and structures. This study aims to determine the basic acoustic properties and to better understand the nature of the seismic reflectivity of the world's deepest gold-bearing reef, the Carbon Leader Reef (CLR). This was done by measuring the physical properties (ultrasonic velocities and bulk densities) as well as conducting mineralogical analyses on drill-core samples.

Ultrasonic measurements of P- and S-wave velocities were determined at ambient and elevated stresses, up to 65 MPa. The results show that the quartzite samples overlying and underlying the CLR exhibit similar velocities (~ 5028 m/s-5480 m/s and ~ 4777 m/s-5211 m/s, respectively) and bulk densities (~ 2.68 g/cm^3 and 2.66 g/cm^3). This is due to similar mineralogy and chemical compositions observed within the units. However, the CLR has slightly higher velocity (~ 5070 m/s-5468 m/s) and bulk density (~ 2.78 g/cm^3) than the surrounding quartzite units probably due to higher pyrite content in the reef, which increases the velocity. The hangingwall Green Bar shale exhibits higher velocity (5124 m/s-5914 m/s) and density values (~ 2.89 g/cm^3-3.15 g/cm^3) compared to all the quartzite units (including the CLR), as a result of its finer grain size and higher iron and magnesium content. In the data set it is found that seismic velocities are influence by silica, iron and pyrite content as well as the grain size of the samples, i.e., seismic velocities increase with (1) decreasing silica content, (2) increasing iron and pyrite content and (3) decreasing grain size. Reflection coefficients calculated using the seismic velocities and densities at the boundaries between the CLR and its hangingwall and footwall units range between ~0.02 and 0.05, which is below the suggested minimum of 0.06 required to produce a strong reflection between two lithological units. This suggests that reflection seismic methods might not be able to directly image the CLR as a prominent reflector, as observed from the seismic data.

The influence of micro-cracks is observed in the unconfined uniaxial compressive stress tests where two regimes can be identified: (1) From 0 - 25 MPa the P-wave velocities increase with progressive loading, but at different rates in shale and quartzite rocks owing to the presence of micro-cracks and (2) above stresses of ~20 - 25 MPa, the velocity stress relationship becomes constant, possibly indicating total closure of micro-cracks.

The second part of the study integrates 3D reflection seismic data, seismic attributes and information from borehole logs and underground mapping to better image and model important fault systems that might have a direct effect on mining in the West Wits Line goldfields. 3D seismic data have delineated first-, second- and third-order scale faults that crosscut key gold-bearing horizons by tens to hundreds of metres. Applying the modified seismic attribute has improved the imaging of the CLR by sharpening the seismic traces. Conventional interpretation of the seismic data shows that faults with throws greater than 25 m can be clearly seen. Faults with throws less than 25 m were identified through volumetric (edge enhancement and ant-tracking seismic attributes) and horizon-based (dip, dip-azimuth and edge detection seismic attributes) seismic attribute analysis. These attributes provided more accurate mapping of the depths, dip and strikes of the key seismic horizon (Roodepoort shale), yielding a better understanding of the relationship between fault activity, methane migration and relative chronology of tectonic events in the goldfield. The strato-structural model derived for the West Wits Line gold mines can be used to guide future mine planning and designs to (1) reduce the risks posed by mining activities and (2) improve the resource evaluation of the gold-bearing reefs in the West Wits Line goldfields.

Dedicated to my parents,

Lennox and Gcina

Acknowledgements

I would like to express my sincere gratitude to my principal supervisor, Doctor Musa Manzi, and co-supervisor Professor Gillian Drennan for their scientific expertise, patience and guidance throughout my MSc career. I am particularly grateful to Musa who saw the potential in me and encouraged me to pursue an MSc degree and for always having time for my questions in his very busy schedule and for the words of encouragement when things seemed bleak, I thank you. I am very honoured to have worked with Musa and Gill who possess vast knowledge and skills in the 3D reflection seismic technique and exploration geology, respectively.

The support and enthusiasm provided by the AngloGold Ashanti Ltd representatives (Carletonville), Rob Burnett, Simone Hartman and Felicia Shumba has been invaluable and for providing geological and geophysical data used in this project. I would also like to thank Sibanye Gold Ltd for swiftly jumping on board with this project and supplying very vital borehole core that were crucial in meeting the aims of the study. This project would not have been successful if not for the good working relationship between the academic staff at the University of the Witwatersrand and personnel from the respective mining companies. I would like to acknowledge the financial support from Thuthuka Funding (NRF), CIMERA (Centre of Excellence for Integrated Mineral and Energy Resource Analysis), CGG and Shell South Africa. I would also like to acknowledge IHS Kingdom for providing the Kingdom Suite® interpretation software and Schlumberger for providing the Petrel® interpretation software used in this study.

Thanks also goes out to the technicians from the various laboratories who helped me with sample preparation and conducting the various analyses; Caiphus Majola, Musa Cebekhulu, Marvin Padayachee and Andrew Carpede. To Musa C. and Andrew for being with me during the long hours when the ultrasonic equipment malfunctioned and to Dr. Halil Yilmaz for lending a hand during difficult time but most importantly for his knowledge on rock strength. I would also like to thank Stephanie Enslin for her comments and suggestions that greatly improved the quality of this dissertation.

Of course, I would like to thank my friends Sikhonzile ‘Skhokhopops’ Shabane and Buhle ‘Bubu’ Mazibuko (the Dreamteam), Percy Dlamini, Nelisa Mbonane and Thulani Malambule for providing much needed breaks during my most stressful times, and for always encouraging and motivating me to endure the hardships of my project and finish my degree. Very special thanks to my siblings, Ntuthuko, Mbongeni and his lovely wife Tiisetso, Noku, Sithu and Pumla , for their love, understanding and support throughout my career.

Lastly, I would like to thank my mom and dad for all their love, support, encouragement and patience throughout my MSc career. For the daily phone calls (yes daily) and constant motivation and your never give up spirit I am truly grateful. I owe everything I have and am to you. Thank you.

Contents

Declaration i

Abstract ii

Dedication iv

Acknowledgements v

List of Figures viii

List of Tables xii

List of Equations xiii

1. Introduction 1

1.1 Aims and objectives of the study 4

1.2 Study area and mining background 5

1.3 Chapter descriptions 6

2 Geological and structural setting 8

2.1 Kaapvaal Craton 8

2.2 Witwatersrand Basin 8

2.3 Regional geology of the Carbon Leader Reef 12

2.4 Structural setting 13

3 Physical rock properties 15

3.1 Seismic waves 15

3.2 Body waves 15

3.3 Seismic wave propagation in rocks 18

3.4 Effects of bulk density on seismic wave velocities 19

3.5 Effects of porosity and stress on seismic velocities 19

3.6 Effects of mineral composition on seismic velocities 20

4 The 3D seismic reflection method 22

4.1 Background 22

4.2 Seismic survey design and acquisition 22

4.3 Seismic data processing 27

4.4 Seismic data Interpretation 28

4.4.1 Seismic sections 29

4.4.2 Autotracking and manual picking 29

4.4.3 Seismic interpretation of structures 31
4.4.3.1 Folds 31
4.4.3.2 Faults 33
4.4.3.3 Effect of faults and dykes on mining activities 34
4.4.4 Seismic attributes 35
4.4.4.1 Volumetric seismic attributes 35
4.4.4.2 Horizon based seismic attributes 38
5 Methodology 43
5.1 Core-logging and sampling 43
5.2 X-ray Fluorescence (XRF) 45
5.3 X-ray Diffraction (XRD) 46
5.3.1 Sodium polytungstate (SPT) mineral separation 47
5.4 Polished thin sections and ore blocks (petrography) 48
5.5 Physical property measurements 48
5.5.1 Density 48
5.5.2 Seismic velocities 49
5.5.3 Applied stress 50
5.6 Interpretation of 3D seismic reflection data 51
6 Scientific contributions 52
6.1 Authorship statement 52
6.2 Summary of papers 54
7 Manuscript 1 59
8 Manuscript 2 98
9 Manuscript 3 145
10 Discussion 168
11 Conclusions 176
11.1 Recommendations 177
12 References 178
Appendices 187

List of Figures

Figure 1.1 A simplified geological map of the Witwatersrand Basin showing the location of the West Wits Line goldfield (Carletonville goldfield) as well as the locations of major faults (after Grové and Harris 2010). 4

Figure 1.2 The map showing the Witwatersrand Basin and the various gold mines across the West Wits Line goldfield. The north-east trending first-order scale Bank Fault and West Rand Fault are shown. The Bank Fault cuts through the south-east margin of the Driefontein gold mine. The map also shows the locations of the 9 surface and underground boreholes used to derive samples for this study (after Dankert and Hein 2010). 6

Figure 2.1 Stratigraphy of the Witwatersrand Basin highlighting the location of the strong reflectors throughout the basin. The local stratigraphy at the base of the Central Rand Group and at the top of the West Rand Group along the West Wits Line goldfield is illustrated on the far right, as observed from borehole intersections (after Guy *et al.* 2010). 9

Figure 3.1 Body waves and their propagation directions. (a) Particle motion of P-waves is parallel to the direction of wave propagation. (b) Particle motion of S-waves is perpendicular to the direction of wave propagation (after Veeken 2007). 16

Figure 3.2 Hypothetical example of the arrival of P- and S-waves at a seismic station. The P-waves are the first waves to arrive and the next sets of waves are the S-waves which have a larger amplitude than the P-waves (after Mussett and Khan 2000). 17

Figure 3.3 Nafe-Drake curve is a plot of compressional wave velocity (Vp) versus density for silicate rocks and sulphide ores. From the diagram it can be seen that quartzites usually have seismic velocities in the range of ~5 - 5.5 km/s and densities of ~2.5 g/cm^3 - 2.7 g/cm^3 (after Salisbury and Snyder 2007). 21

Figure 4.1 Schematic diagram of source-receiver geometry and the signal recorded by receivers. The diagram shows the reflection wave paths over a horizontal interface across which there is an acoustic impedance contrast, where $v2\rho2 > v1\rho1$ or $v2\rho2 < v1\rho1$ (after Salisbury and Snyder 2007). The two-way travel time increases with depth and $v1\rho1$ and $v2\rho2$ are the velocity and density for medium 1 and medium 2, respectively. 23

Figure 4.2 Seismic section (amplitude display) across the Mponeng gold mine showing the imaging of the reflective interface between the dolomites of the Transvaal Supergroup and the ultra-mafic to mafic lavas of the Klipriviersberg Group, which coincides with the Black Reef (BLR) horizon; the reflective interface of the Klipriviersberg lavas and the quartzites of the Central Rand Group, which coincides with the Ventersdorp Contact Reef (VCR) horizon; and the reflective boundary of the quartzites of the Central Rand Group and the chloritoid-rich shales of the West Rand Group, which coincides with the Roodepoort shale (RS) horizon. 25

Figure 4.3 Fresnel zone (Kearey and Brooks 1991). The Fresnel zone is the area on a reflector where the energy of the incident ray is returned within a half-wavelength of the central ray. For seismic data with high signal-to-noise ratio the vertical resolution is defined by $\lambda 8$ and by $\lambda 4$ for data with low signal-to-noise where λ is the dominant wavelength of the data. Therefore, the wavelength is essentially the measure of the seismic resolution. 26

Figure 4.4 Conventional amplitude display seismic sections showing the correlation of the Roodepoort shale (RS) picks on the vertical sections represented by the (a) inline section and (b) crossline section and on the horizontal section represented by (c) the depth slice. The solid yellow lines represent areas where the confidence in picking was high due to the strong and continuous reflection of the horizon. The dashed yellow lines that are highlighted by the black circles in (c) show areas of structural complexity and low confidence in picking. Line A-A' and B-B'' show the location of inline and crossline sections, respectively. F: Fault. 30

Figure 4.5 Depth structure map of the Roodepoort shale derived from manual picking. The map shows faults of various orientations that crosscut the horizon. 31

Figure 4.6 Schematic diagrams of basic fold structures. (a) Symmetrical anticline; (b) symmetrical syncline; (c) monocline. The anticline and syncline are characterized by two limbs orientated concave downward or concave upward, respectively. The monocline has only one limb (after Davis and Reynolds 1996). 32

Figure 4.7 Showing examples of folds identified in the seismic data. The depth slice in (a) shows the extent of the first-order scale Bank Fault and the termination of horizons against the fault at 5000 m depth. The yellow circles highlight anticlines and line A-A' shows the location of the crossline in B. The crossline in (b) shows a vertical view of the roll-over anticlines against the Bank Fault. 33

Figure 4.8 Amplitude display seismic section showing various types of faults across the survey areas. These faults crosscut the Roodepoort shale (RS) horizon at the top of the West Rand Group as well

as the Ventersdorp Contact Reef (VCR) at the base of the Ventersdorp Supergroup. The seismic section also shows near vertical features (dykes) associated with highly attenuated seismic amplitudes. 34

Figure 4.9 Depth slices at 5000 m showing (a) the amplitude display and (b) edge enhancement display. 36

Figure 4.10 Resultant (a) depth slice at 5000 m and (b) antrack crossline (xline) extracted from the antrack volume. The depth slice shows the improved imaging of the Roodepoort shale and enhancement of fractures associated with the Bank Fault. The crossline shows the improved imaging of the Black Reef (BLR), Ventersdorp Contact Reef (VCR) and the Rooderpoort shale (RS) horizons. The crossline also shows the improved mapping of faults to shallow depths (VCR and BLR levels). . 38

Figure 4.11 Roodepoort shale surface obtained from (a) conventional picking and (b) smoothed Roodepoort shale surface. The application of the smoothing operators has reduced the noise and spikes in the data. 39

Figure 4.12 Schematic representation of how the dip and azimuth are calculated in seismic data. ... 39
Figure 4.13 Seismic attributes computed for the Roodepoort shale horizon. (a) Dip attribute display, showing the clear mapping of the Pretorius Fault (PF) and the Fault (F4) and Fault 5 (F5) (colour bar given in degrees). (b) Dip-azimuth display, showing the extent of the PF, Fault 7 (F7) and Fault 4 (F4) (colour bar is given in degrees). The dip-azimuth map also shows the extent of some NE-trending faults on the western margin of the map. 40

Figure 4.14 Roodepoort shale edge detection attribute map. The white arrows show faults which were clearly mapped by the dip and dip-azimuth maps in figure 14.11a and b and the red arrows show newly enhanced faults, which were not mapped by the dip-amplitude and dip-azimuth displays. 41

Figure 5.1 The map showing the location of the boreholes used for the physical property measurements and used to constrain the interpretation of the seismic data. The 9 boreholes are located within the Anglo Gold Ashanti Ltd and the Sibanye Gold Ltd mining boarders, but most importantly within the seismic volume. The map also shows the optimum mapping of the Pretorius Fault and dykes by underground geological mapping method. 43

Figure 5.2 3D visualization of the migrated seismic volume covering Anglo Gold Ashanti and Sibanye Gold mines along the West Wits Line Goldfields, showing strong seismic reflectors and location of

boreholes (BH-A to BH-H). VCR: Ventersdorp Contact Reef, TWR: Top of the West Rand, RS: Roodepoort shale, CLR: Carbon Leader Reef. 44

Figure 5.3 Apparatus used in conducting the XRF analysis. (a) Pestle and mortar used to the grind sample, (b) Polyvinylalcohol is used to thicken the texture of the sample, (c) Mould is used as a holding dish after the sample has been consolidated, (d) Sample holder is used to keep the sample confined and make sure that it is evenly flattened at the top when the pellet is made, (c) Pellet press machine used to compress the sample and (d) Axios PANanalytical machine which performs the analysis for both the major and minor elements. 46

Figure 5.4 Ultrasonic velocity measurement apparatus at ambient (a and b) and elevated stresses (c and d). (a) Larger transducer (diameter=32 mm, 0.5 MHz) set used to measure seismic velocities for large samples (b) smaller transducer (diameter=16 mm, 0.5 MHz) set used to measure seismic velocities for smaller samples. (c) The uniaxial compressional loading is produced by hydraulic pistons that are driven by a computer controlled load holding pump. The induced load is monitored on a stress measuring gauge (insert in c). (d) The image shows the placement of the sample between the transducers positioned on pistons within the chamber. 50

List of Tables

Table 2.1 Stratigraphy of the Witwatersrand Supergroup across the West Wits Line goldfield (summarized from Armstrong *et al.* 1991; Robb and Meyer 1995; Zhao *et al*. 2006). 11

Table 3.1 Summary of the P-wave velocities ($\boldsymbol{Vp, in\ km/s}$) of common Earth materials (after Kearey *et al.* 2002). 18

Table 4.1 Summary of the processing parameters for the 2003 Kloof-South Deep and 1994 Leeudoorn 3D seismic data sets and merging with the 1995 Western Ultra-Deep Levels (WUDLs) seismic data (Manzi *et al.* 2012b) 27

List of Equations

Equation 1 P-wave velocity……..…...16

Equation 2 S-wave velocity……..…...16

Equation 3 Propagation velocity of P- and S-waves……..…17

Equation 4 Poisson's ratio……...17

Equation 5 Acoustic Impedance…….……..…...23

Equation 6 Reflection coefficient……..…….…….…24

Equation 7 Tuning thickness……..…….……26

Equation 8 Complex seismic trace……..……..….35

Equation 9 Dip-amplitude……..……..….40

Equation 10 Dip-azimuth……..……...…40

Equation 11 Density measurement.....48

Equation 12 Ultrasonic P-wave velocity ……..…...49

Equation 13 Ultrasonic S-wave velocity ……..……49

1 Introduction

The gold-bearing conglomerate units (reefs) of South Africa are hosted in one of the greatest metallogenic provinces in the world, the Archaean Witwatersrand Basin (Fig. 1.1). The Witwatersrand Basin has produced over 95% of the gold ever mined in South Africa and has contributed significantly to the economic growth of the country. There are several challenges, however, that face the gold mining companies. With the remaining shallow resources being mined out, the majority of the economic gold resources are now at depths between 3 km and 5 km. At such depths, it is difficult to understand the subsurface geology and structural framework using conventional exploration tools such as surface and underground geological mapping, drilling, gravity, magnetic and 2D reflection seismic methods. The deep mining, high stress levels and structural complexity of the mining areas at these depths make it difficult to derive appropriate ore body and structural models, thus compromising mine production and safety.

In the late 1980s, the Witwatersrand Basin gold mines acquired several 3D reflection seismic surveys across their mines to map gold-bearing horizons, faults, dykes and folds for mine planning, and to mitigate risks associated with mining activities. The application of the 3D reflection seismic technique provided high-resolution mapping of depths, dip and strike of the economic horizons compared to conventional exploration methods, in particular the 2D reflection seismic method (Gibson *et al.* 2000; Pretorius *et al.* 2003; Malehmir *et al.* 2012; Manzi *et al.* 2012a; Manzi *et al.* 2013; Malehmir *et al.* 2014; Manzi *et al.* 2014). The interpretation of the 3D reflection seismic data were integrated with borehole information to better constrain depth positions of the gold-bearing reefs, thus providing the mines with more reliable geological and structural models (Manzi *et al.* 2012a; Malehmir *et al.* 2013; Manzi *et al.* 2013). However, the 3D reflection seismic data have failed to delineate the Carbon Leader Reef (CLR), the deepest and one of the richest gold-bearing conglomerate reefs in the Witwatersrand Basin, due to the insignificant acoustic impedance contrast between it and its host rocks (quartzite units).

Although numerous 3D reflection seismic surveys have been conducted over the Witwatersrand Basin goldfields to map gold-bearing horizons, direct measurements of physical rock properties (e.g., seismic velocities, bulk density and porosity) of the CLR and its hangingwall and footwall rocks have not been done to better investigate the scientific reasons for the poor seismic mapping of the CLR and to provide guidelines for future seismic surveys in the basin. It is, therefore, important to understand the physical rock properties of ore-bearing horizons and their host rocks to better interpret seismic data acquired for mineral exploration. Laboratory measurements of physical rock parameters can also enhance understanding of mineralized zones, their host rocks and surrounding lithological units.

To date, thousands of borehole geophysical surveys (sonic and density logs) have been conducted worldwide in major metallogenic regions to provide information about the acoustic impedances of mineralized zones, their host rocks and main lithological units (e.g., Salisbury *et al.* 2000; Malehmir and Bellefluer 2009; Malehmir *et al.* 2012, 2013, 2014). In particular, measurements of seismic velocities, especially at great depths (~2 km - 3 km) under high stress conditions (~65 MPa - 70 MPa), are crucial for proper interpretation of reflection seismic data, and therefore, for understanding the seismic reflective nature of the lithological boundaries.

In this study, deep (>3 km) exploration boreholes were used to investigate the poor seismic reflective nature of the CLR. These deep boreholes were drilled in areas covered by the 3D seismic data through the entire Witwatersrand Supergroup. There have been no or few down-hole geophysical loggings or direct elastic wave velocity measurements carried out on these drill-cores, but other physical properties such as magnetic susceptibility measurements were made to further constrain magmatic processes in this basin (Hart et al. 2011).

These drill-cores also provide the opportunity to study the role of anisotropy and macro-and micro-fracture effects on the seismic velocities of the rocks. Such information could benefit future exploration seismic surveys of the CLR horizon, or other economic horizons hosted in similar geological environments within the basin or worldwide, by providing improved knowledge about the physical properties of the rocks. Furthermore, deriving the impedance contrasts and reflection coefficients (RC) using the seismic velocities and densities of the hangingwall and footwall of the CLR could be used for future seismic surveys to resolve the controversy regarding the poor seismic reflectivity associated with the CLR.

Integration of laboratory-measured seismic velocities with seismic reflection methods has played a key role in understanding deeply buried seismic reflectors in mineral exploration worldwide (e.g., Salisbury *et al.* 2000; Malehmir and Bellefluer 2009; Dehghannejad *et al.* 2010, 2012; Bellefluer *et al.* 2012; Kukkonen *et al.* 2012; Malehmir *et al.* 2012, 2013, 2014; Urosevic *et al.* 2012; White *et al.* 2012; Wood *et al.* 2012). Laboratory measurements of P- and S-wave velocities are commonly made in earth materials to permit empirical correlations or to test theoretical expressions relating the velocities to some parameter of interest. These relations can then be used to infer *in situ* velocity measurements for the desired parameter such as the effective stress, porosity (Wyllie *et al.* 1958; Han *et al.* 1986) and static strength (Blake and Gilbert 1997). Using relationships established from laboratory measurements on samples, velocity information gathered from *in situ* well log measurements, velocity analysis, impedance inversion, or amplitude-versus-offset (AVO) analysis of seismic imaging data, can be interpreted for the subsurface rock properties.

The possibility as to whether the potential reflectors can be imaged seismically is dependent on a number of factors. These include the contrast in acoustic impedance (a product of velocity and bulk density) between the horizon and its host rocks, the geometry and structural complexity of rock horizons, and their depth of burial. In addition, the resolution of the imaged reflector is particularly dependent on how well the velocity analysis has been approximated at various seismic processing stages. Therefore, a crucial part for high-resolution reflection seismic imaging is to obtain accurate velocity information that will constrain seismic processing, interpretation and time-to-depth conversion. In structurally complex and crystalline environments (such as the Witwatersrand Basin), the velocity variations make the velocity analysis a challenging task. This is because seismically-derived horizons are fundamentally interpreted from the seismic travel time data that have been corrected for depth using complex velocity analysis. Uncertainties are inherent in seismically-derived velocities. Hence, it may be impossible to draw conclusions based on one set of velocity data.

While downhole geophysics (density and velocity measurements) has been used to better understand the physical properties for seismic studies, there has been little or no focus on relating the seismic velocities to stress and mineral modal abundances. Thus, for better imaging of the deeper reflectors, it is necessary to understand how velocities are influenced by these properties. A fundamental empirical relation between seismic velocity and density in rocks is described by Birch's Law, which generally states that an increase in rock density leads to an increase in seismic velocity (Birch 1961). Further to this, Christensen and Salisbury (1975), Spudich and Orcutt (1980) and Elbra *et al.* (2011) noted the potential influence of effective stress on the seismic velocities, through their studies of crustal rocks.

Furthermore, although the application of 3D seismic data have been able to image thin gold-bearing reefs and crosscutting faults with throws as small as 25 m, the traditional interpretation tools that were used were unable to map the continuity of some of the gold-bearing reefs and small faults because their throws were below the seismic resolution limits (quarter of the dominant wavelength) (Gibson *et al.* 2000). This is because most interpretations were mainly derived from the conventional seismic amplitude displays that seem to suffer from low signal-to-noise ratio. A variety of volumetric techniques and horizon-based seismic attributes have since been developed to improve the interpretation of the seismic data in complex areas. These techniques include: (1) ant-tracking technique that enhances the detection of faults below the seismic resolution limits, (2) edge enhancement techniques that smooth the seismic data prior to seismic horizon picking so as to increase the signal-to-noise ratio of the data, and (3) edge detection attributes that enhance the detection of faults at the horizon levels. These tools are now available in the interpretation software packages provided by oil and gas service companies. The detection of these small-scale faults prior to mining is very important because they may have a number of effects. These include: (1) making the gold-bearing reefs impractical to mine due to the vertical displacements, (2) making the mining

hangingwall unstable in underground workings, and (3) providing conduits for migration of water and flammable gas into underground workings. Faced with such risks, it is necessary to incorporate new interpretations tools to map these faults.

This study, in addition to conducting physical properties, aims to enhance the structural interpretation of the seismic data and derive the strato-structural ore body model of the CLR along the West Wits Line, by integrating 3D seismics, volumetric and horizon-based seismic attribute techniques, geological mapping and information from exploration boreholes.

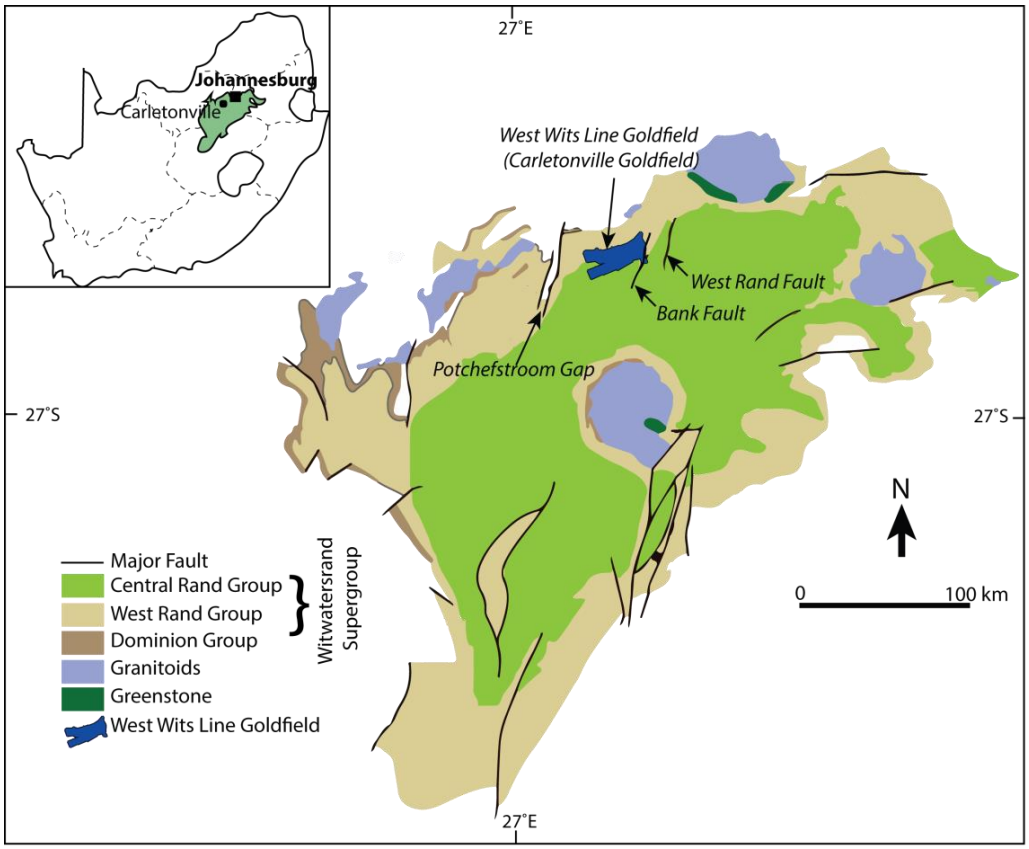


Figure 0.1 A simplified geological map of the Witwatersrand Basin showing the location of the West Wits Line goldfield (Carletonville goldfield) as well as the locations of major faults (after Grové and Harris 2010).

1.1 Aims and objectives of the study

The aim of this study is to better understand the seismic reflectivity of the Carbon Leader Reef (CLR) and to derive a structural model of the West Wits Line (WWL) goldfield from the state-of-the-art interpretation of 3D reflection seismic data.

The main objectives can be outlined as follows:

- Conducting petrographic analysis (polished thin sections and ore blocks) and determining the chemical composition of the various rock units to investigate the effect of mineral composition on seismic velocities.
- Analysing the bulk densities and seismic velocities of approximately 50 drill core samples to determine the acoustic impedance contrast and reflection coefficient at the CLR-hangingwall and CLR-footwall boundaries. The physical property measurements were conducted on drill-core samples obtained from surface and underground boreholes that intersect the reef and its hangingwall and footwall rocks. All the rock samples used for the various analyses were sampled from depths ranging between ~2.5 km and 5 km below the surface.
- Investigating the dependence of seismic velocities on elevated uniaxial stress conditions of up to 65 MPa (corresponding to depths between ~2 km and 3.9 km).
- Seismic interpretation of the Roodepoort shale horizon (located ~350 m below the CLR) to derive a 3D structural model of the WWL goldfield that could be used for CLR mining purposes. The Roodepoort shale (RS) was chosen because of its strong reflective character and close proximity to the CLR.
- Apply seismic attributes (volumetric and horizon-based seismic attributes) to enhance the mapping of horizons and faults with throws below the conventional vertical seismic resolution.

1.2 Study area and mining background

The Witwatersrand gold deposits occur in various ore provinces (goldfields) located on the margins of the basin. These include the Evander, East Rand, Central Rand, West Rand, West Wits Line (WWL), Klerksdorp and Welkom goldfields (Frimmel *et al.* 2005). The West Wits Line goldfield (Fig. 1.2) investigated in this study, also known as the Carletonville goldfield, is situated 60 km south-west of the city of Johannesburg and south of the town of Carletonville.

The West Wits Line goldfield comprises several gold mines that exploit various gold-bearing conglomerate reefs located at deep (~500 m - 1 km) to ultra-deep levels (~4 km). The gold mines mainly exploit the CLR and the Ventersdorp Contact Reef (VCR) at depths between 2.0 km and 4.2 km. The Carbon Leader Reef is the world's deepest gold-bearing conglomerate reef and accounts for ~75% of the gold produced in the WWL goldfield while the VCR accounts for the remaining 25%. The gold mines of interest to this study include the Mponeng and Tau Tona gold mines which are the deepest gold mines in the world and are owned and operated by Anglo Gold Ashanti Ltd. The Mponeng gold mine comprises a twin shaft system consisting of two surface shafts and two sub-shafts. The mine exploits the VCR at depths between 2.4 km and 3.9 km and the CLR between 3.0 km and 4.0 km. The Mponeng lease area is bound to the north by the Tau Tona gold mine and to the east by the Driefontein gold mine, which is owned by Sibanye Gold Ltd. At the Tau Tona gold mine, mining takes place between depths of 1.9 km and 3.9 km. The mine comprises a three shaft system

supported by secondary and tertiary shafts. It mainly exploits the CLR from ~3.5 km to 3.9 km depths. The Driefontein gold mine is a deep to ultra-deep level mine with a maximum operating depth of ~3.4 km. The primary reefs exploited at this gold mine are; the VCR (at depths ranging from 700 m to 2.7 km), CLR (at depths ranging from 2.0 km to 3.3 km) and the Middelvlei Reef (located ~50 m to 75 m above the CLR).

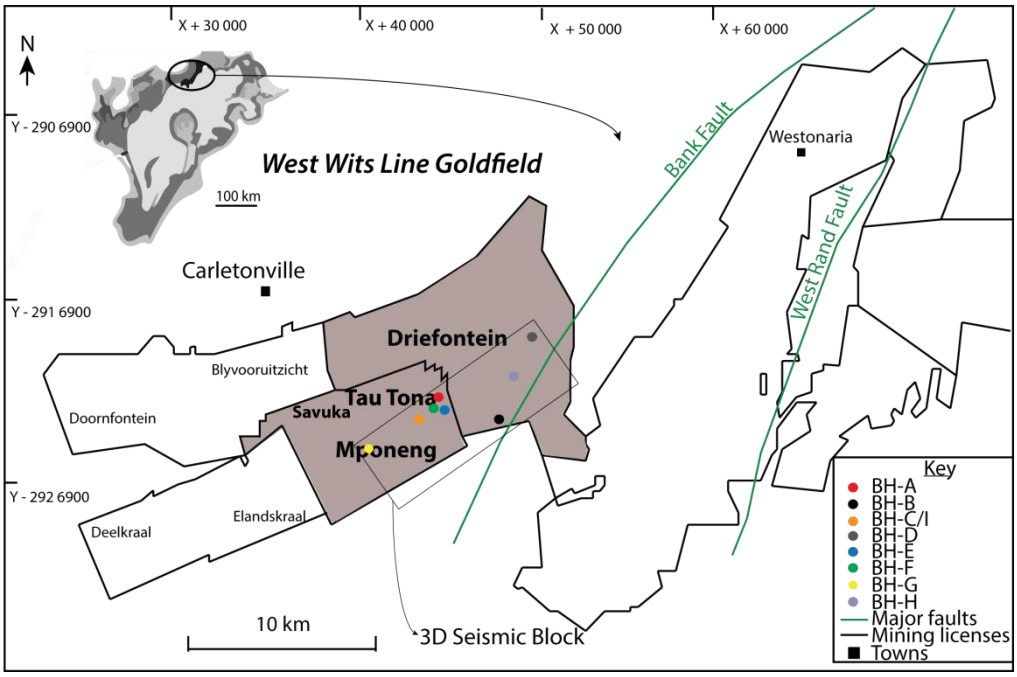


Figure 0.2 The map showing the Witwatersrand Basin and the various gold mines across the West Wits Line goldfield. The north-east trending first-order scale Bank Fault and West Rand Fault are shown. The Bank Fault cuts through the south-east margin of the Driefontein gold mine. The map also shows the locations of the 9 surface and underground boreholes used to derive samples for this study (after Dankert and Hein 2010).

1.3 Chapter descriptions

This dissertation is divided into eleven chapters. The introduction (Chapter 1) highlights the purpose and main objectives of the study, and provides a brief overview of the study area. Chapter 2 provides a review of the geological and structural setting of the Witwatersrand Basin. This chapter summarises the stratigraphy of the CLR and its hangingwall and footwall units. Chapter 3 introduces the principles of the seismic reflection method and its application in mineral exploration. The chapter further investigates the effects of porosity, bulk density, rock composition and applied stress on seismic velocities. Chapter 4 summarizes the acquisition, processing and interpretation of the 3D reflection seismic data previously acquired in the WWL goldfields. Chapter 5 presents the detailed methodology carried out in this study while chapter 6 highlights the contributions of the author in each manuscript. The chapter further gives detailed summaries of each manuscript. Chapters 7-9 present manuscripts that have been published, accepted for publication with minor revisions, or submitted for review.

Chapter 10 presents the final discussion and chapter 11 summarizes the main conclusions and recommendations for future research studies.

2 Geological and structural setting

The sediments of the Witwatersrand Basin were deposited between 3.07 Ga and 2.71 Ga on the north-east of South Africa on the Archaean Kaapvaal Craton (Robb and Meyer 1995; James *et al.* 2003). An understanding of the geological setting of a region is crucial in the interpretation of seismic data for the following reasons: (1) To better understand the geological boundaries that are likely to produce strong seismic reflections in the seismic data and (2) to constrain the structural interpretation based on seismic data.

2.1 Kaapvaal Craton

The Kaapvaal Craton contains a variety of Archaean granite greenstone terranes and much older tonalitic gneisses (3.6 - 3.2 Ga) intruded by various granitic bodies (3.3 - 3.0 Ga; Robb *et al.* 2006). The craton can be divided into two domains, the Mid-Archaean Kaapvaal Shield to the southeast (3.0 - 3.7 Ga) and the Late-Archaean Shield to the northwest (2.5 - 3.0 Ga; De Wit *et al.* 1992). The accretion and stabilization of the Kaapvaal Craton occurred between 3.7 and 2.5 Ga by the emplacement of granitoid batholiths that thickened and stabilized the continental crust during the early stages of magmatism and sedimentation cycles (Robb *et al.* 2006).

2.2 Witwatersrand Basin

The Witwatersrand Basin is an arcuate northeast-trending oval shaped basin that occupies a central position on the Kaapvaal Craton (Robb and Meyer 1995; Frimmel *et al.* 2005). The Witwatersrand Basin was formed during the collision of the Archaean Kaapvaal Craton with the Zimbabwe Craton (Armstrong *et al.* 1991; Robb and Meyer 1995). This collision resulted in the reactivation of old fault planes of the pre 3.07 Ga basement rocks (Frimmel *et al.* 2005).

Figure 2.1 shows the stratigraphy of the Witwatersrand Basin as reported by literature and as observed in the seismic data. The Witwatersrand Basin overlies the clastic sedimentary and volcanic rocks of the Dominion Group (3074 ± 6 Ma, single zircon U-Pb SHRIMP; Armstrong *et al.* 1991). The Dominion Group is not shown on Figure 2.1 because it is beneath our zone of interest and was not imaged by the seismic data. The Witwatersrand Basin is divided into the lower Witwatersrand Supergroup, middle Ventersdorp Supergroup and upper Transvaal Supergroup. The Witwatersrand Supergroup lies unconformably above the Dominion Group (Fig. 2.1) and elsewhere it unconformably overlies the Archaean basement complex (Frimmel *et al.* 2005). This Supergroup, in turn, consists of the lower West Rand and upper Central Rand Groups (Jolley *et al.* 2004; McCarthy 2006; Dankert and Hein 2010).

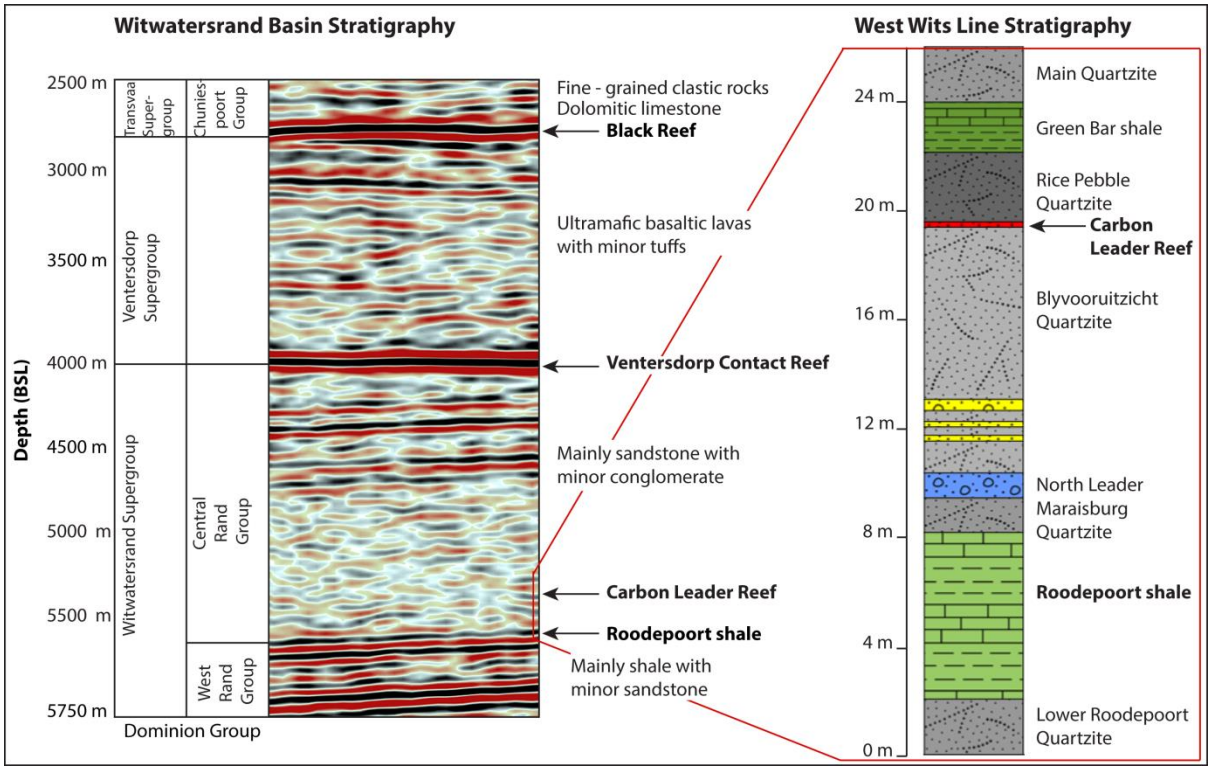


Figure 2.1 Stratigraphy of the Witwatersrand Basin highlighting the location of the strong reflectors throughout the basin. The local stratigraphy at the base of the Central Rand Group and at the top of the West Rand Group along the West Wits Line goldfield is illustrated on the far right, as observed from borehole intersections (after Guy *et al.* 2010).

The West Rand Group (ca. 2985 - 2902 Ma; U-Pb detrital zircon SHRIMP; Kositcin and Krapež 2004) occupies an area of about 42 000 km^2 and has an average thickness of approximately 4.5 km (Frimmel *et al.* 2005). It was deposited in a tectonically stable environment and is largely dominated by marine sediments and minor clastics (Frimmel and Minter 2002; Beach and Smith 2007). The group is divided into three subgroups, namely the Hospital Hill, Government and Jeppestown Subgroups (Table 2.1). The Hospital Hill and Government Subgroups form the lower-most units in the group and are characterized by rock sequences that range from shallow marine quartzites and shales to conglomerates, shale and diamictites (Frimmel and Minter 2002; McCarthy 2006). The upper Jeppestown Subgroup is divided into the Florida Quartzite Formation, Crown Formation and the Roodepoort Formation (Zhao *et al.* 2006).

The lower Florida Quartzite Formation consists of quartzite and small-pebble conglomerate units and is overlain by the Crown Lava Formation, consisting of up to ~250 m of thick basaltic andesite flows (Zhao *et al.* 2006; McCarthy 2006). The top of the Crown Lava Formation is a strong seismic marker due to the significant acoustic impedance contrast between the overlying quartzite units and the underlying basaltic lavas (*see* Fig. 2.1). The base of the overlying Roodepoort Formation is largely made up of quartzites, but contains an erosional disconformity above which the sequence is

dominated by iron-rich shales (McCarthy 2006). The shale unit (Roodepoort shale) coarsens upwards into the quartzites of the Maraisburg Formation (McCarthy 2006). The Roodepoort shale (RS), at the top of the West Rand Group, is a seismically recognizable marker due to the varying physical properties (densities and seismic velocities) of the overlying quartzites and the shale, which produce a high acoustic impedance contrast (*see* Fig. 2.1). The West Rand Group is unconformably overlain by quartzites, conglomerates and shale units of the Central Rand Group (ca. 2902 - 2849 Ma; U-Pb detrital zircon SHRIMP; Kositcin and Krapež 2004).

The Central Rand Group covers an area of about 10 000 km^2 and reaches a maximum thickness of approximately 2.8 km towards the centre of the basin (Viljoen 2009). Its sediments were deposited in braided river systems that combined to form alluvial fans (Wronkiewics and Condie 1987). The alluvial fans narrowed in size over time and resulted in fluvial sediments prograding from the basin margins inward (Wronkiewics and Condie 1987; Moon and Whateley 1989). Most of the gold produced throughout the basin has been extracted from the conglomerate units of the Central Rand Group (McCarthy 2006). These units include the Elsberg, Libanon, Kloof and Kimberley reefs of the Johannesburg Subgroup, and the Bird, Middelvlei, Carbon Leader and North Leader reefs of the Turrfontein Subgroup (De Kock 1964). The Carbon Leader Reef (CLR) occurs at the base of the Central Rand Group, between alternating quartzite units. The CLR and its overlying and underlying units will be discussed in detail in the next section.

Unconformably overlying the upper Central Rand Group is the Ventersdorp Contact Reef (VCR) of the Venterspost Formation (2729 ± 19 Ma; U-Pb detrital zircon SHRIMP; Kositcin and Krapež 2004). The Venterspost Formation comprises altered conglomerate units (siliceous, chloritic and micaceous alteration) as well as quartzites known as the Ventersdorp Quartzite (Zhao *et al.* 2006). The deposition of the Venterspost Formation is the result of compressional tectonics which caused topographic undulations (McCarthy 2006). Work by Tankard *et al.* (1982), van der Westhuizen *et al.* (1991), Frimmel and Gartz (1997), Gibson *et al.* (2004), Gibson *et al.* (2005) and McCarthy (2006) reveals that the VCR is a degradational surface that ended the deposition of the Central Rand Group.

The Ventersdorp Contact Reef is located between 2.5 km and 4.2 km depths below the surface (*see* Fig. 2.1). It is unconformably overlain by the Ventersdorp Supergroup (ca. 2.72 - 2.63 Ga), which comprises the lower ultramafic basaltic lavas of the Klipriviersberg Group, and the metasedimentary and bimodal metavolcanic rocks of the upper Platberg Group (van der Westhuizen *et al.* 1991). The Platberg Group is well developed in the west of the Witwatersrand Basin and consists of a wide range of rock types, including boulders, cobbles, fragments of amygdaloidal lavas and minor quartzite, chert and shale units (Engelbrecht *et al.* 1986). Overlying the Platberg Group is the Pniel Sequence, which consists of the Bothaville and Allanridge Formations (van der Westhuizen *et al.* 1991).

The Black Reef Quartzite Formation unconformably overlies the Ventersdorp Supergroup and forms the base of the Palaeoproterozoic Transvaal Supergroup (ca. 2588±6 Ma; Vos 1975; Krapež 1985; Jolley *et al.* 2004). This silici-clastic unit can be subdivided into a basal conglomerate unit (Black Reef (BLR)) and an upper quartzite unit (Els *et al.* 1994). The quartzite unit is in turn overlain by carbonaceous shale and dolomites of the Transvaal Supergroup (Frimmel *et al.* 2005). On a seismic section the Black Reef appears as a recognizable horizon due to the high acoustic impedance contrast that exists between the overlying dolomites of the Chuniespoort Group and the underlying ultramafic lavas of the Klipriviersberg Group. The Transvaal Supergroup comprises the carbonate (dolomite) and banded iron formation (BIF) succession of the Chuniespoort Group and the overlying clastic sedimentary and volcanic rocks of the Pretoria Group, which reach a thickness of 6 - 7 km (Eriksson *et al.* 2007). Eriksson and Reczko (1995) and Frimmel *et al.* (2005) propose a hiatus of ~80 million years at the end of the formation of the Transvaal Basin/Supergroup, which reflects a glacio-eustatic sea level fall because the unconformity is overlain by glacio-genic diamictites. The rocks of the Witwatersrand Basin have been regionally metamorphosed to greenschist facies (Phillips and Powell 2012). This basin wide metamorphism has yielded mineral assemblages that range from pyrophyllite to chloritoid. This has resulted in shales and sandstones having more aluminous compositions (Phillips and Powell 2012).

Table 2.1 Stratigraphy of the Witwatersrand Supergroup across the West Wits Line goldfield (summarized from Armstrong *et al.* 1991; Robb and Meyer 1995; Zhao *et al*. 2006).

VENTERPOST CONGLOMERATE Formation: Ventersdorp Contact Reef					~2714 Ma
WITWATERSRAND SUPERGROUP	CENTRAL RAND GROUP	TURFFONTEIN SUBGROUP	Mondeor Formation	Quartzite	2894- >2714 Ma
			Elsburg Formation	Quartzite	
			Gold Estates Formation	Quartzite and conglomerate (Kloof Reef, Libanon Reef)	
			Robinson Formation	Quartzite, shale, conglomerate	
		JOHANNESBURG SUBGROUP	Booysens Formation	Quartzite, shale,	
			Krugersdorp Formation	Quartzite, conglomerate (Bird Reef)	
			Luipaardsvlei Formation	Quartzite, conglomerate	
			Randfontein Formation	Quartzite, conglomerate	
			Main Formation	Quartzite (Main Quartzite, Rice Pebble Quartzite), conglomerate (Middelvlei Reef, Carbon Leader Reef), shale (Green Bar Shale)	
			Blyvooruitzicht Formation	Quartzite, conglomerate (North Leader)	
	WEST RAND GROUP	JEPPESTOWN SUBGROUP	Roodepoort Formation	Shale, shaly quartzite	3070-2914 Ma
			Crown Formation	Amygdaloidal lava	
			Florida Quartzite Formation	Quartzite, conglomerate	
		GOVERNMENT SUBGROUP	Witpoortjie Formation	Shale, siltstones, argillaceous quartzite	
			Coronation Shale Formation	Black magnetic shale	
			Promise Quartzite Formation	Sericitic, argillaceous quartzite, shale, conglomerate (Promise Reef)	
		HOSPITAL HILL SUBGROUP	Brixton Formation	Green orthoquartzite, shale	
			Parktown Shale Formation	Shale, quartzite	

2.3 Regional geology of the Carbon Leader Reef

In this section, a review of the stratigraphy surrounding the CLR, which extends from the top of the Main Formation down to the Blyvooruitzicht Formation at the base of the Central Rand Group, is provided (Table 2.1). The stratigraphy associated with the CLR is illustrated in Figure 2.1 as observed from borehole intersections. Table 2.1 summarizes the stratigraphy of the Witwatersrand Supergroup across the West Wits Line.

Along the West Wits Line goldfield the base of the Central Rand Group is defined by the North Leader, a thin but well developed conglomerate unit (McCarthy 2006; Zhao *et al.* 2006). Although the North Leader is successfully exploited in other goldfields in the Witwatersrand Basin (e.g., Welkom and Klerksdorp goldfields) it has neither been mined nor studied in detail in the WWL goldfield (Fletcher 2009). The strata overlying the North Leader consist of quartzites with alternating conglomerate bands, forming the Blyvooruitzicht Quartzite (McCarthy 2006). The Blyvooruitzicht Quartzite consists of a light brown to grey argillaceous quartzite with minimal sulphide mineralization. Together the North Leader and the Blyvooruitzicht Quartzite compose the Blyvooruitzicht Formation. The formation is progressively truncated by an erosional surface beneath the Main Formation.

The overlying Main Formation hosts the economically important CLR conglomerate at its base. The reef is composed of a basal carbon seam of narrow length that is directly overlain by a carbon rich small-pebble conglomerate (Engelbrecht *et al.* 1986). The carbon seam can range in thickness from a mere carbon streak to a solid seam up to 3 cm thick (Grové and Harris 2010). The small pebbles are often scattered within thicker conglomerate units that are intercalated with quartzites (Buck and Minter 1985). Studies conducted by Braun (1987) and Fletcher (2009) subdivided the Carbon Leader Reef into various types of facies, each representing a distinct phase of sedimentation. Facies 3 is the oldest conglomerate package and attains an average thickness of 23.1 cm. It is characterized by a single conglomerate band consisting of smoky quartz and black chert pebbles. Facies 2 is located above facies 3 and is the second oldest conglomerate package. It consists of multiple conglomerate bands separated by internal quartzite bands divided on the basis of pebble type, content, colour and sedimentary structures. The combined average thickness of this unit it 188.9 cm. Facies 1 is located above facies 2 and is the youngest of the three conglomerate facies. Along the WWL this unit can be further subdivided into 3 facies based on pebble type, content, mineral alteration and presence of sulphides. For the purpose of this study the CLR facies will be considered as one sedimentary package because these are too small to be mapped by the surface seismic surveys.

Overlying the CLR is a ~3.5 m thick siliceous quartzite known across the WWL as the Rice Pebble Quartzite (Fletcher 2009). This hangingwall quartzite is overlain by a continuous shale horizon termed the Green Bar shale. The Green Bar shale is persistent throughout most of the Witwatersrand Basin

goldfields and has been correlated with the Cab and Black Bar of the West Rand and the Central Rand goldfields, respectively (Engelbrecht *et al.* 1986). The quartzite unit overlying the Green Bar shale (termed the Main Quartzite) ranges from a medium- to coarse-grained argillaceous quartzite with scattered sulphides and coarse grit (Fletcher 2009). The Main Quartzite is overlain by the economically important Middelvlei Reef which is exploited in the gold mines located in the eastern part of the Bank Fault. The Middelvlei Reef forms the uppermost unit of the Main Formation.

2.4 Structural setting

As previously mentioned, the deformation of the Witwatersrand Basin was controlled by the collision of the Kaapvaal and Zimbabwe Cratons, which reactivated old fault planes of the pre 3.07 Ga basement rocks (Stanistreet and McCarthy 1991; Frimmel *et al.* 2005). The Witwatersrand Basin experienced several stages of deformation that can be distinguished by the division of the various lithostratigraphic units. The basin is fault bounded along its north-western margin and the many fault sets described in the WWL goldfield indicate a complex structural history (De Kock 1964; Engelbrecht *et al.* 1986; Myers *et al.* 1990a, 1990b).

The initial stages of basin formation involved crustal extension at ~3.09 Ga to 3.07 Ga that gave rise to the deposition of the volcano-sedimentary Dominion Group in a low-lying region of the basin (Myers *et al.* 1990b; Armstrong *et al.* 1991; Robb and Meyer 1995; Frimmel and Gartz 1997; Robb *et al.* 1997). The extensional period resulted in the activation of faults and the emplacement of numerous plutons (Westerdam and Coligny) recorded by detrital zircon population (Robb and Meyer 1995). Further basin extension resulted in the deposition of the West Rand Group sediments at ~2.99 Ga to 2.90 Ga. Uplifting and tilting of the West Rand Group sediments syn- to post-erosion occurred at ~2.90 Ga, followed by the unconformable deposition of coarse-grained silici-clastic rocks of the Central Rand Group (Wronkiewics and Condie 1987; Jolley *et al.* 2004). Although it is not clear what caused the tilting of the West Rand Group sediments, it is clear that the tectonic event (Asazi Event at ~2.90 Ma) described by Manzi *et al.* (2013) resulted in the exposure of the clastic and marine sediments of the West Rand Group.

The deposition of the Central Rand Group was synchronous with the compressive deformation event (Umzawami Event at ca 2.73 Ga) described by Dankert and Hein (2010). The Umzawami Event resulted in the formation of a thrust fold belt, in which folding of the topography was synchronous with the formation of thrusts, reverse and flexural-slip faults (Dankert and Hein 2010). The Libanon Anticline and its parasitic folds identified by Manzi *et al.* (2013) as well as macroscopic folds identified by Beach and Smith (2007), and Frimmel and Minter (2002) in their studies of the Welkom and Klerksdorp goldfields confirm the occurrence of the compressional Umzawami Event. The Umzawami

Event was followed by basin extension (Hlukana Extension Event at ~2.70 - 2.64 Ga) during the emplacement of the Ventersdorp lavas and deposition of the Platberg Group (Manzi *et al.* 2013). The extensional tectonics of the basin resulted in the formation of first-, second- and third-order scale faults.

The Bank Fault (BF), one of the first-order scale faults (~400 m - 3 km throw) in the WWL goldfield, cuts through the south-eastern margin of the Driefontein and Mponeng gold mines (*see* Fig. 1 and 2). Manzi *et al.* (2012a) interpreted the Bank Fault as a north-northeast trending listric fault which dips between 65° to 70° at shallow depths (~1.5 km below surface) and 5° to 10° at deeper depths (~5 km below surface). The fault crosscuts the Ventersdorp Supergroup, Central Rand Group and the top of the West Rand Group sediments at a depth of ~5 km below the surface (Dankert and Hein 2010). Second-order scale faults (~25 - 400 m throws) include the north-northeast trending Pretorius Fault (PF) which is dominant in the Mponeng and Tau-Tona gold mines (Heesakkers *et al.* 2011). The Pretorius Fault is a 10 km long oblique strike-slip fault with a maximum throw of ~200 m at the Tau-Tona gold mine (Heesakkers *et al.* 2011). The fault crosscuts the Ventersdorp Supergroup, Central Rand Group and the top of the West Rand Group (Heesakkers *et al.* 2011).

In addition to faults and fractures, the WWL goldfield is intruded by dolerite sills and syenite dykes. These igneous intrusions have been confirmed by exploration boreholes that were drilled within the seismic volume. Mapping the extension of these dykes and sills through seismics is important for mine safety since these features can cause considerable damage in underground workings. For example, when dykes intrude into fault zones they can contribute to rock instability and cause rock bursts, and they can create water pockets that can lead to the flooding of the mine (Litthauer 2009; Manzi *et al.* 2012b).

3 Physical rock properties

The propagation of seismic waves in rock media is characterised by the bulk density and elastic moduli of the rocks that the waves propagate through. These parameters are dependent on several factors such as mineralogy, metamorphic grade, preferred mineral alignment, fractures and chemical composition (Kern and Mengel 2011). To determine the reflectivity of the rocks making up the Witwatersrand Basin stratigraphy, it is first required to understand their physical properties. Studies by Kern (1982), Kern (2011), Elbra *et al.* (2011) and Malehmir *et al.* (2013) show that the bulk densities and seismic velocities of rocks can be determined with minimal error by conducting the necessary laboratory experiments at temperatures and pressures appropriate to the lithosphere.

3.1 Seismic waves

Seismic waves are parcels of elastic strain energy that travel through the Earth's layers. These waves result from low-frequency acoustic energy sources i.e., earthquakes, volcanoes, explosions etc. (Kearey and Brooks 1991; Pater and Lissauer 2001; Kearey *et al.* 2002). In seismic reflection surveys, the sources that are used usually generate short-lived wave pulses that contain a wide range of frequencies. With the exception of the immediate vicinity of the source, the strains associated with the passage of a seismic pulse are miniscule and may be assumed to be elastic (Kearey *et al.* 2002). Based on this assumption, seismic velocities can be determined from the elastic moduli and density of the medium through which they propagation (Kearey *et al.* 2002). Seismic waves can be divided into two types, namely, body waves and surface waves. Body waves consist of compressional and shear waves, while surface waves include Rayleigh and Love waves (Shearer 1996). For the purpose of this study we will only consider body waves.

3.2 Body waves

Body waves are pulses of energy that travel within the Earth, and therefore through rock medium (Shearer 1996; Peng and Zhang 2007). In the seismic reflection method this elastic energy travels in two modes; as primary (P) waves and as secondary (S) waves (Veeken 2007). The P-waves are characterized by particles that have vibration directions that coincide with the travel direction of the wave energy (Fig. 3.1a) (McQuillin *et al.* 1979; Shearer 1996). S-waves are characterized by particles that have vibration directions perpendicular to the travel direction of the wave (Fig. 3.1b) (Kearey *et al.* 2002).

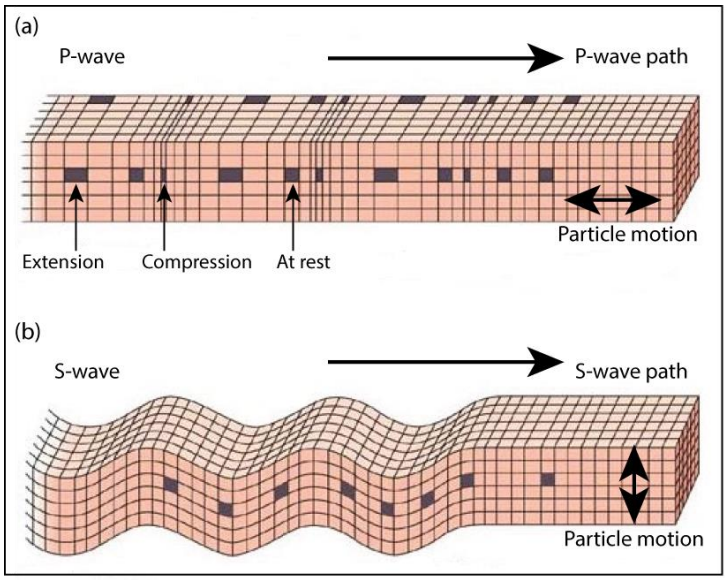


Figure 3.1 Body waves and their propagation directions. (a) Particle motion of P-waves is parallel to the direction of wave propagation. (b) Particle motion of S-waves is perpendicular to the direction of wave propagation (after Veeken 2007).

The P-waves are also referred to as "compressional'' or "dilatational" waves because they produce compression and rarefaction when travelling through a medium. The velocity at which they travel is given by:

$$Vp = \sqrt{\frac{K+(\frac{4}{3})\mu}{\rho}} \quad (1)$$

The velocity of S-waves is given by (Shearer 1996):

$$Vs = \sqrt{\frac{\mu}{\rho}} \quad (2)$$

where K is the bulk modulus (modulus of incompressibility), μ is the shear modulus (modulus of rigidity) and ρ is the density of the material in which the wave travels.

The propagation of P-waves involves compression and shearing, therefore making them sensitive to both the bulk and shear moduli as seen in Equation 1 (Shearer 1996). Since the bulk modulus, shear modulus and density values are always positive, P-waves travel faster than S-waves in the same material.

Figure 3.2 illustrates a hypothetical example of the arrival of P- and S-waves at a seismic station. The propagation velocity of the P- and S-wave ($\mathcal{V}$) is given by:

$$\mathcal{V} = \frac{x}{t} \tag{3}$$

where x is the distance travelled by the wave and t is the time taken (Gadallah and Fisher 2009).

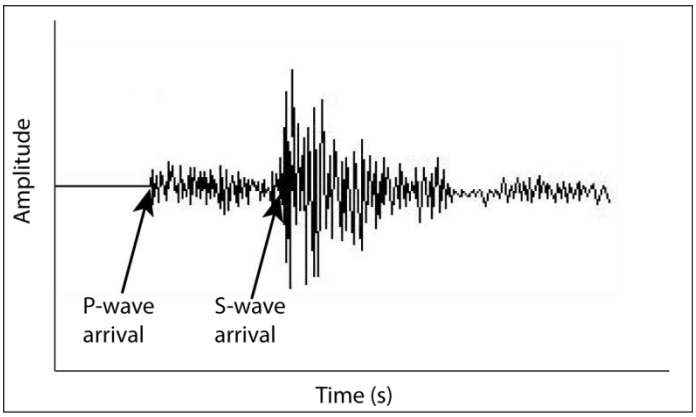


Figure 3.2 Hypothetical example of the arrival of P- and S-waves at a seismic station. The P-waves are the first waves to arrive and the next sets of waves are the S-waves which have a larger amplitude than the P-waves (after Mussett and Khan 2000).

The ratio of P-wave velocity and S-wave velocity (Vp / Vs) in any material is dependant solely on the Poisson's ratio for that material (Kearey and Brooks 1991). The Poisson effect is observed when a material is compressed in one direction and expands in the other two directions perpendicular to the direction of compression. The Poisson's ratio (σ) is the measure of this effect, and its relationship with P- and S-wave velocity is expressed by (Kearey and Brooks 1991):

$$\frac{Vp}{Vs} = \sqrt{\frac{(1-\sigma)}{(\frac{1}{2}-\sigma)}} \tag{4}$$

where Vp and Vs are the compressional and shear waves, respectively.

The Poisson's ratio for consolidated rocks is typically 0.25, therefore Vp~1.7 Vs. As important as the knowledge of the P-wave velocity is, it is a function of three distinct rock properties (bulk modulus, shear modulus and density) and is only a vague indicator of the rock lithology (Kearey *et al.* 2002). The $\frac{Vp}{Vs}$ ratio, however, is not dependent on the density and can thus be used to derive Poisson's ration, which is a more diagnostic lithological indicator (Kearey *et al.* 2002; Peng and Zhang 2007).

3.3 Seismic wave propagation in rocks

As previously mentioned, the propagation velocity of a seismic wave is determined by the physical properties of the medium through which it travels. For a seismic wave travelling through a purely homogenous rock, at any given time, its velocity will be the same in all directions away from the source (Kearey *et al.* 2002; Peng and Zhang 2007). However, most rocks are heterogeneous due to varying mineral compositions, textures (e.g., grain size, grain shape and degree of sorting) and porosities. Different rocks therefore have different elastic moduli and densities, and hence different seismic velocities. Table 3.1 summarizes the typical P-wave velocities in various Earth materials.

Table 3.1 Summary of the P-wave velocities ($\boldsymbol{Vp, in\ km/s}$) of common Earth materials (after Kearey *et al.* 2002).

Rock type	Rock name	$Vp(km/s)$
Unconsolidated materials	Sand (dry)	0.2 - 1.0
	Clay	1.0 - 2.5
Sedimentary rocks	Sandstones	2.0 - 6.0
	Quartzite	5.5 - 6.0
	Limestones	2.0 - 6.0
	Dolomites	2.5 - 6.5
Igneous/Metamorphic rocks	Granite	5.5 - 6.0
	Gabbro	6.5 - 7.0
	Ultramafic rocks	7.5 - 8.5
Other materials	Air	0.3
	Water	1.4 - 1.5
	Petroleum	1.3 - 1.4

Knowledge of the P-wave (Vp) and S-wave (Vs) velocities of rocks encountered in seismic reflection surveys is important for four reasons: (1) For the processing of the data, (2) the conversion of seismic wave two-way travel times into depth; (3) to indicate the subsurface lithologies; and (4) to provide the reflection coefficient of the rocks to be mapped using reflection seismics.

The laboratory measurement of physical properties, of seismic velocities in particular, can be determined from the measurement of the travel-time of high frequency (~1 MHz) acoustic pulses transmitted through cylindrical rock specimens. By using this method the effect on seismic velocities of varying temperature, confining stress, pore fluid pressure and mineral composition can be quantitatively estimated (Kearey *et al.* 2002). Over the past decade a number of studies that integrate reflection seismic methods and physical property measurements have increased (Carlson and Miller 2004; Punturo *et al.* 2005; Kern *et al.* 2009; Elbra *et al.* 2011; Malehmir *et al.* 2012, 2013). These studies have resulted in the improved understanding of the mapping of key ore bodies and subsurface structures. It is emphasized, however, that laboratory measurements of rock samples represents only a small part of the crustal section and may not fully represent the rocks covering the entire survey area. Nonetheless, laboratory measurements of physical rock properties do have some advantages over geophysical logging (e.g., VSP surveys) especially in hardrock environments such as the Witwatersrand Basin. Some of these advantages include (1) the cost effectiveness of measuring individual samples compared to entire holes; (2) a wider variety of measurements that can be conducted in the laboratory environment compared to vertical holes; and (3) the accurate monitoring of testing conditions, e.g., increasing stress and temperature increments. This is particularly important for establishing the overall relations between individual physical properties, e.g., for assessing the influence of temperature, porosity, density and confining stress.

3.4 Effects of bulk density on seismic wave velocities

As shown in Equation 1 and 2, the seismic velocities are dependent on the rock density. The density is defined as the mass of the rock contained in a given volume. It is often referred to as the bulk density. The bulk density is dependent on two main parameters, namely, mineral composition and porosity (Kearey *et al.* 2002). In sedimentary rocks the variation in rock porosity is the primary cause of variations in bulk density. The bulk density therefore tends to increase with depth, due to increased compaction and cementation of the rocks. However, rocks in crystalline environments such as the Witwatersrand Basin have negligible porosity (<2%), thus the mineral composition is considered the main cause for the density variations (Kearey and Brooks 1991). Laboratory measurements of the bulk density for this study are determined by direct measurement of the rock samples. The detailed methodology has been outline in Chapter 5.

3.5 Effects of porosity and stress on seismic velocities

Porosity and stress are considered major influences of seismic velocities. The porosity of a material refers to the total volume in a rock that is occupied by pores and cracks. Porosity results from different geological, physical and chemical processes that take place during the emplacement of a rock and/or during the geological history of the rock (Schön 1996). Porosity is primarily controlled by the size,

shape and sorting of the rock grains. The following relationships between rock grains and porosity exist (Schön 1996; Peng and Zhang 2007):

Grain size: porosity increases with increasing grain size. A dependence results from the increasing effect of surface forces for finer-grained sediments while coarser grains do not interlock as well as finer grains and thus create pores in rocks.

Grain sorting: porosity increases with increased sorting. In poorly sorted sediments the spaces created by large grains is filled by finer material.

Grain shape: porosity increases as grains change shape from well-rounded to angular.

In terms of the effect of stress, laboratory experiments conducted by Peng and Zhang (2007) show that rock porosity decreases with increasing applied stress. These observations enable the use of the velocities, or of velocity-related parameters obtained from seismic reflection surveys, to make *in situ* estimates of the porosity and stress that rocks experience. A porous rock specimen will display significant changes in the velocity as a load is applied, whereas a compact, well cemented sample will show slight or no changes in velocity as a load is applied. In porous rocks defects such as fractures and cracks are closed with increasing stress as the grain-to-grain contact conditions are changed. This results in an initial increase in velocity as the defects are closed, but with time a constant velocity is achieved after the closure of the defects (Wyllie *et al.* 1956; Birch 1961; Walsh and Brace 1964).

3.6 Effects of mineral composition on seismic velocities

The mineralogy of sedimentary rocks also has a strong influence on seismic velocities. The elastic properties of these porous clastic rocks are highly dependent on their porosity and the matrix composition (Schön 1996). Rocks with high clay content, as opposed to quartz or carbonate rich rocks, have significantly reduced velocities and elastic moduli (Schön 1996). These rocks are highly sensitive to depth and stress changes as a result of their porosity. It is observed that velocities of most crystalline rocks tend to increase with increasing bulk density as observed in Figure 3.3 (Milkereit *et al.* 1996). Therefore, in general, the velocities and densities of rocks will increase as they become more mafic or increase in metamorphic grade.

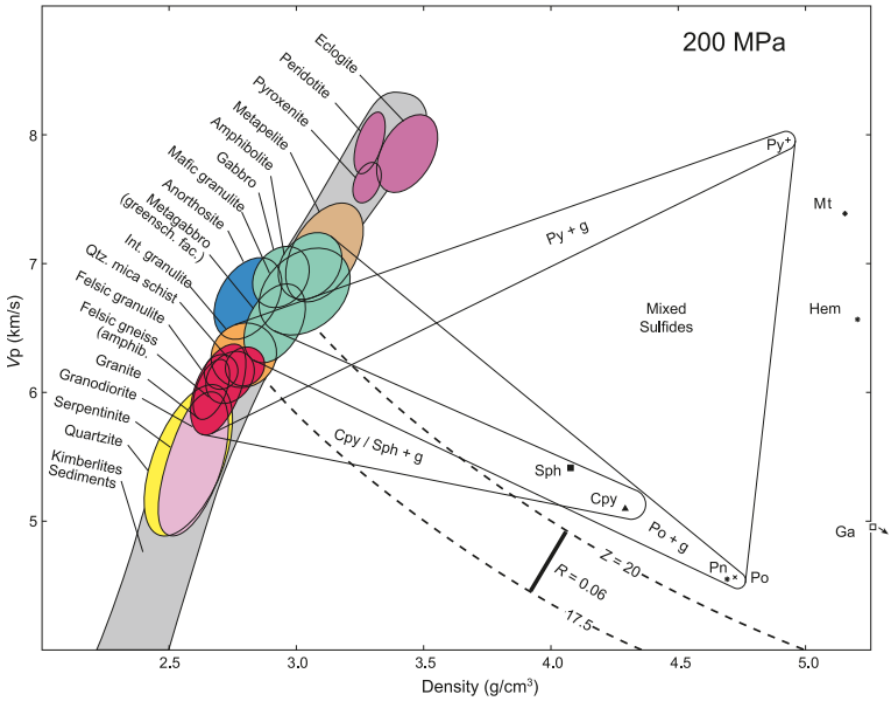


Figure 3.3 Nafe-Drake curve is a plot of compressional wave velocity (Vp) versus density for silicate rocks and sulphide ores. From the diagram it can be seen that quartzites usually have seismic velocities in the range of ~5 - 5.5 km/s and densities of ~2.5 g/cm^3 - 2.7 g/cm^3 (after Salisbury and Snyder 2007).

Previous studies by Milkereit *et al.* (1996), and Salisbury and Snyder (2007) suggest that rocks with high concentration of sulphides should make significantly strong reflectors against rocks that are sulphide deficient in geological settings due to their higher bulk densities. Studies of the physical properties of sulphides have revealed that most sulphide ores occupy the far right field of the Nafe-Drake curve (Salisbury *et al.* 2003; Salisbury and Snyder 2007). Different sulphide ores appear to be associated with different rock types, for example, pyrrhotite is associated with mafic host rocks, while ores that are rich in pyrite and chalcopyrite are associated with felsic host rocks (Milkereit *et al.* 1996). Salisbury and Snyder (2007) also showed that ores that contain pyrite have elevated acoustic impedances compared with their surrounding host rocks thus making them potential reflectors.

4 The 3D seismic reflection method

4.1 Background

The reflection seismic method is a powerful geophysical mineral exploration tool because it provides high-resolution images of subsurface structures. It utilizes the principles of seismology to estimate the properties of the Earth's subsurface from reflected seismic waves. Musset and Khan (2000) define the reflection seismic method as a "dynamic geophysical technique of generating sound waves at a source and recording the time it takes for components of that seismic energy to return to the surface and be recorded by receivers". The principal aim of the reflection seismic method, the 3D reflection seismic method in particular, is to provide high-resolution imaging of the subsurface geology and unravel important information about structures and lithological relationships that control mineral deposits. The 3D reflection seismic method has proven to be a more reliable mineral exploration tool worldwide compared to other geophysical methods such as gravity, magnetics and 2D reflection seismics (Pretorius *et al.* 1994; Milkereit *et al.* 1996; Trickett *et al.* 2004; Salisbury and Snyder 2007; Malehmir *et al.* 2012, 2013). The international success of the 3D reflection seismic method in the oil and gas exploration made it an attractive geophysical tool for deep mineral exploration. South African gold mines adopted the technique in 1980s to image the structurally complex Witwatersrand Basin, which hosts world-class gold-bearing reefs (conglomerate) at great depths (Gibson *et al.* 2000; Salisbury *et al.* 2003). Generally, the 3D reflection method is carried out in four phases; seismic design, acquisition, processing and interpretation.

4.2 Seismic survey design and acquisition

The basic principle of the reflection seismic technique is based on Snell's Law, which describes the behaviour of an incident wave impinging on a boundary between two media having different refractive indices (Kearey *et al.* 2002). In reflection seismics a compressional wave emanating from an energy source (e.g., Vibroseis systems) is incident on an interface between two materials of varying physical properties (Fig. 4.1). The incident wave will either be refracted and continue to travel through the media in the same direction as the incident wave, or it will be reflected and travel from the interface back to the source (Gadallah and Fisher 2009). The reflection of a seismic wave can occur when the wave encounters lithological or structural boundaries such as unconformities, conformities and faults. The energy of the reflected seismic wave is measured by an array of strategically placed receivers (e.g., geophones) which are set up on surface (Gadallah and Fisher 2009).

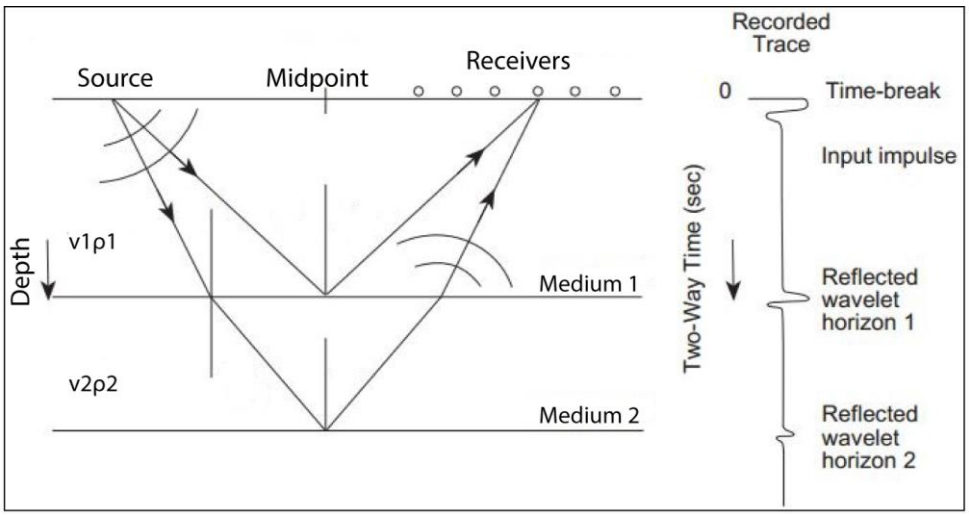


Figure 4.1 Schematic diagram of source-receiver geometry and the signal recorded by receivers. The diagram shows the reflection wave paths over a horizontal interface across which there is an acoustic impedance contrast, where v2ρ2>v1ρ1 or v2ρ2<v1ρ1 (after Salisbury and Snyder 2007). The two-way travel time increases with depth and v1ρ1 and v2ρ2 are the velocity and density for medium 1 and medium 2, respectively.

The amount of energy that is reflected at the geological interface is dependent on the acoustic impedance contrast across the layers (Salisbury *et al.* 2000; Kearey *et al.* 2002; Malehmir *et al.* 2014). The acoustic impedance (Z) is itself dependent on the velocity and density of the two rock units and is defined by:

$$Z = v * \rho \tag{5}$$

where v is the seismic velocity and ρ is the density of the rock (Veeken 2007).

A reflection from a geological interface or structure may be observed if there is a sufficient acoustic impedance contrast between the interface and the surrounding rock units. Therefore, a high acoustic impedance contrast between rocks will result in strong reflections that allow the subsurface geology to be interpreted; while a lower acoustic impedance contrast will result in poor seismic reflections and increased difficulty in interpreting the geology (Bacon *et al.* 2003). Previous studies by Milkereit *et al.* (1996), Salisbury and Snyder (2007) and Chopra *et al.* (2009) suggest that an impedance contrast of at least 2.5 x10^5 g/cm^2 s between two geological entities having different densities (ρ_1 and ρ_2) and velocities (v_1 and v_2) will result in a sufficient seismic reflection. Numerous reflection seismic surveys have shown that most mafic rocks (Z ~20 g/cm^{2}s) can give strong reflections when in contact with felsic rocks, and fresh ultramafic rocks will reflect against most lithologies (Milkereit *et al.* 1996).

The potential of a geological boundary to produce a sufficient reflection is described by the reflection coefficient (RC). The reflection coefficient is a variable that describes how much a wave is reflected by an impedance boundary (Kearey and Brooks 1991; Salisbury *et al.* 2000; Kearey *et al.* 2002). It is defined at the ratio of reflected amplitudes to incident amplitudes (Warner 1990). Thus for a wave that impinges a geological boundary at normal incidence, the reflection coefficient is defined by:

$$R = \frac{\rho 2 v 2 - \rho 1 v 1}{\rho 2 v 2 + \rho 1 v 1} = \frac{Z2 - Z1}{Z2 + Z1} \quad (6)$$

where $\rho 1$, $v 1$, $Z 1$ are the density, P-wave velocity and acoustic impedance of the first layer, respectively and $\rho 2$, $v 2$, $Z 2$ are the density, P-wave velocity and acoustic impedance of the second layer, respectively (Salisbury and Snyder 2007).

Salisbury *et al.* (2003) and Salisbury and Snyder (2007) suggest that for an interface to be detected as a strong horizon by the seismic reflection method it should reflect a minimum of 6% of its incident energy. The Witwatersrand Basin provides good examples of strong and continuous seismic reflectors that are well delineated by the seismic reflection method, such as the Black Reef (BLR), Ventersdorp Contact Reef (VCR) and the Roodepoort shale (RS) (Fig. 4.2). The BLR is imaged as a strong reflector due to a major acoustic impedance contrast between the overlying dolomites (velocity ~5000 m/s velocity and density ~2.84 g/cm) of the Transvaal Supergroup and the underlying basic-ultrabasic Klipriviersberg Group lavas (~6400 m/s velocity and ~2.90 g/cm^3 density). The strong reflection of the VCR is due to a major acoustic impedance contrast between basic to ultrabasic Klipriviersberg lavas (~6400 m/s velocity and ~2.90 g/cm^3 density) and quartzite units at the top of the Central Rand Group (velocity ~5700 m/s and density ~2.67 g/cm^3) and the strong reflection of the Roodepoort shale horizon is the result of the low velocity and density of the overlying quartzite (velocity ~4980 m/s and density ~2.76 g/cm^3) and the high velocity and density (velocity ~5520 m/s and density ~2.87 g/cm^3) of the shale unit.

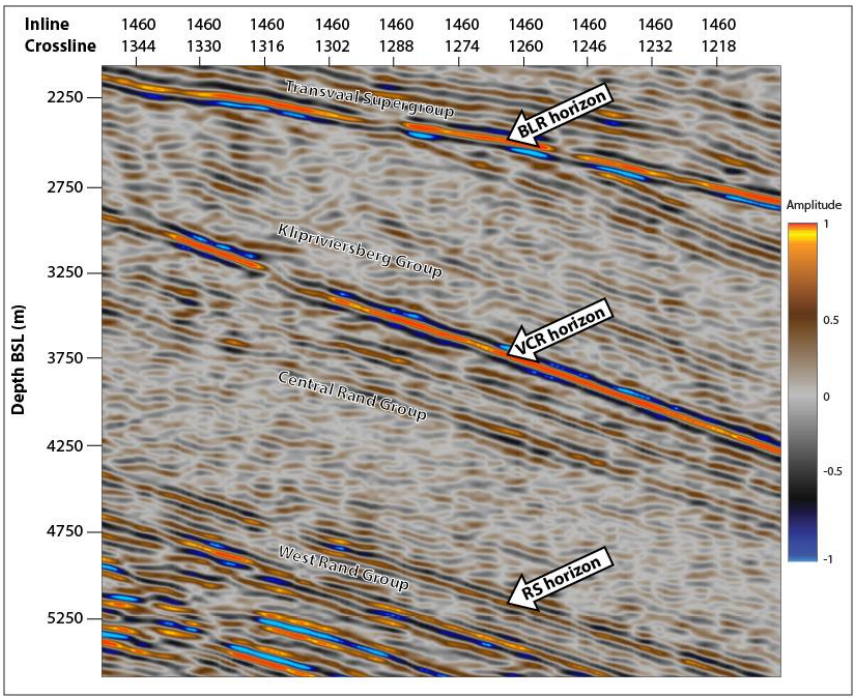


Figure 4.2 Seismic section (amplitude display) across the Mponeng gold mine showing the imaging of the reflective interface between the dolomites of the Transvaal Supergroup and the ultra-mafic to mafic lavas of the Klipriviersberg Group, which coincides with the Black Reef (BLR) horizon; the reflective interface of the Klipriviersberg lavas and the quartzites of the Central Rand Group, which coincides with the Ventersdorp Contact Reef (VCR) horizon; and the reflective boundary of the quartzites of the Central Rand Group and the chloritoid-rich shales of the West Rand Group, which coincides with the Roodepoort shale (RS) horizon.

In addition to acoustic impedance and the reflection coefficient, another parameter which is important in determining whether a horizon will be reflective or not is the depth and geometry of the deposit. Reflection surveys are designed to provide subsurface information at a specific depth of penetration and at a specific degree of resolution in both the vertical and horizontal dimensions (Kearey and Brooks 1991). The vertical resolution refers to the ability to distinguish closely spaced reflectors at different depth levels (tuning thickness) and the horizontal dimension provides the ability to distinguish and recognize two laterally displaced features as two distinct adjacent events (Fresnel zone) (Chopra *et al.* 2006). The resolution of fault and horizon imaging is largely dependent on the signal-to-noise ratio (SNR) of the seismic data. The Earth acts as a low-pass filter by attenuating higher frequencies in seismic signals (Lowrie 1997). This results in an increase in the dominant seismic wavelength with depth and the poor imaging of deeply buried geological features (Lowrie 1997).

The minimum thickness of a tabular deposit that can be determined is estimated from its tuning thickness. The tuning thickness is interpreted as the interval which seismic waves reflecting off the top and bottom surfaces of a horizon constructively interfere (Salisbury and Snyder 2007). This thickness is also known as the Rayleigh limit or one-quarter wavelength criterion which was first proposed by Widess (1973). The minimum thickness (t) is expressed as follows:

$$t = \frac{v}{4f} \quad (7)$$

where v is the average velocity of the rocks and f is the dominant frequency used in the seismic survey (Salisbury and Snyder 2007). Below this thickness the two reflection surfaces (the top and bottom) cannot be resolved and the combined reflection amplitude decreases to that of a single reflector.

When an energy pulse propagates through the Earth's interior it propagates as a wave rather than a beam, thus causing uncertainties about the exact position of an imaged structure (Kearey and Brooks 1991). The horizontal resolution is described by the dimensions of the first Fresnel zone, which is the subsurface area where the reflected waves interfere constructively and their travel paths differ by less than a half wavelength (Yilmaz 2001). The size of the Fresnel zone is dependent on the dominant seismic wavelength and the depth of the interface (Fig. 4.3). For interpreting small features on seismic data, attention is focused on the vertical resolution, as the migration is routinely employed to enhance horizontal resolution (Chopra *et al.* 2006).

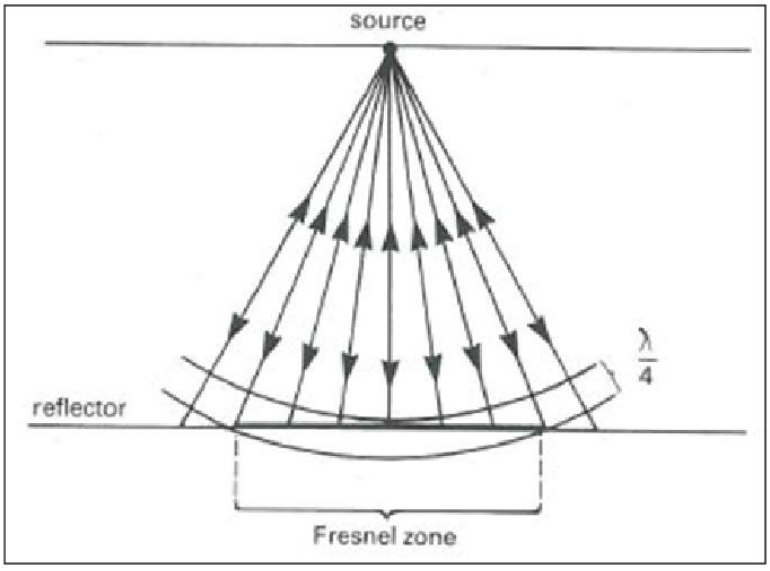


Figure 4.3 Fresnel zone (Kearey and Brooks 1991). The Fresnel zone is the area on a reflector where the energy of the incident ray is returned within a half-wavelength of the central ray. For seismic data with high signal-to-noise ratio the vertical resolution is defined by $\lambda 8$ and by $\lambda 4$ for data with low signal-to-noise where λ is the dominant wavelength of the data. Therefore, the wavelength is essentially the measure of the seismic resolution.

Inversion modelling results reveal that deposits with up to one wavelength across, can still be imaged using the reflection seismic method under ideal conditions, but that smaller deposits will not be detectable due to attenuation (Berryhill 1977). Therefore, deposits that are located deeper in the

subsurface need to be thicker and wider for them to be imaged as strong reflectors (Salisbury and Snyder 2007).

4.3 Seismic data processing

In the 1990s, Anglo Gold Ashanti Ltd and Sibanye Gold Ltd conducted 3D reflection seismic surveys at their gold mines in the West Wits Line goldfield to map potential ore-bearing horizons and subsurface structures. These seismic volumes were initially processed and interpreted by Gibson (1997) and Gibson *et al.* (2000) and later re-processed and merged (post migration) by Manzi *et al.* (2012a) to produce a continuous seamless depth converted prestack time migrated (PSTM) seismic volume. The total merged 3D seismic survey has an east-west extent of 20 km and north-south extent of approximately 15 km and covers a depth of 11 km. The total volume of the survey is 3300 km^3 which makes it the largest seismic survey in the southern African region to date. The processing parameters applied to the data and the details of the merging of the two seismic surveys are summarized in table 4.1 below.

Table 4.1 Summary of the processing parameters for the 2003 Kloof-South Deep and 1994 Leeudoorn 3D seismic data sets and merging with the 1995 Western Ultra-Deep Levels (WUDLs) seismic data (Manzi *et al.* 2012b)

Processing route	**Parameters**
Data reformat	From SEGD to Promax internal format
Trace editing	Air-blast attenuation applied
Geometry application	Source, receiver, offsets, etc., assigned to each trace
Gain recovery: spherical divergence correction	1/(TV ∧ 2), where V ¼ 5500 m/s
Surface consistent spiking deconvolution	Operator design window at 0 m offset: 100-2500 ms, operator length: 120 ms,
	white noise stabilization: 1%
Zero-phase spectral whitening	Eight frequency windows, 500-ms sliding window
3D refraction statics correction	Surface layer V0=1200 m/s (constant), seismic datum elevation: 1500 m a.m.s.l
Statics application	Smooth processing datum
First-pass interactive velocity analysis	Every 600 m in crossline and inline directions
First-pass surface consistent residual statics	Maximum power autostatics, 300-ms time gate around flattened horizons
Interim stack: Leeudoorn and Kloof-South Deep	Data sets stacked separately, 35% stretch mute and 500-ms AGC applied

Prestack phase rotation and time-shift to match Leeudoorn and Kloof data sets	Leeudoorn data: time shift of −8 ms and 90° phase shift
Prestack merge of Kloof-South Deep and Leeudoorn data sets	Refraction statics calculated on the merged data and tied to upholes
Second-pass interactive velocity analysis	Every 600 m in crossline and inline directions
Second-pass surface consistent residual statics application	Maximum power autostatics, 300-ms time gate around flattened horizons
CDP trim statics	Nonsurface consistent CDP statics
DMO velocity analysis	Full 3D Kirchoff DMO using 50-m inline and crossline distance
Prestack time migration (PSTM) flow	
First-pass PSTM velocity analysis	DMO velocities removed and PSTM velocities picked
PSTM	Full 3D Kirchoff using velocity model from smoothed first pass PSTM velocities
Second-pass PSTM velocity analysis	Second pass PSTM velocities picked
NMO correction	Second pass PSTM velocities applied
Stack	
Band-pass frequency filter	Time varient Ormsby zero-phase filter, 0–1400 ms: 15⁄20 − 80⁄90 Hz
Depth conversion	Using interval velocities derived from borehole data and BLR and VCR time horizons
WUDLS data merge	Kloof-South Deep data depth shifted to 1830 m a.m.s.l datum and regridded to match WUDLs orientation

The surveys successfully imaged the entire Witwatersrand Basin stratigraphy as well as key seismic horizons such as the Black Reef, Ventersdorp Contact Reef, Roodepoort shale and Crown Lavas.In this study, the seismic interpretation focused on the Roodepoort shale (located ~350 m below the Carbon Leader Reef).

4.4 Seismic data Interpretation

Seismic interpretation involves the extraction of subsurface geological information from seismic data. The interpretation of the data can aid in identifying subsurface structures and geological properties or in deriving seismic models. After the data have been acquired and processed, seismic sections are interpreted using geological information from surface and underground sources e.g., fault traces or geological contacts. Initial interpretation of 3D seismic data begins with the picking and tracking of strong and laterally continuous seismic horizons at wide line spacing of the vertically (inline and

crossline) and horizontally (time or depth slices) migrated seismic sections. The seismic interpretation is correlated with the geological information from borehole data, surface and underground mapping. The reliability of the seismic interpretation is dependent on the resolution of the 3D seismic data, the availability of boreholes and the skill of the interpreter. The interpretation steps are explained in more detail below.

4.4.1 Seismic sections

A seismic section is a cross section of the Earth that displays seismic data along a profile extracted from a 3D seismic cube. The section is made up of numerous traces with locations given on the x-axis and the time or depth along the y-axis. Seismic horizons are defined as the reflectors (or seismic events) picked on individual profiles. These horizons may represent lithological boundaries, unconformities, or the top or bottom contacts of ore bodies. The seismic amplitude-based interpretation is the simplest seismic attribute used to determine the detectability of any horizon or fault in the seismic data. The amplitude display is dependent on changes in acoustic impedance (see section 3.2) at lithological boundaries and hence provides information about the lithological changes or presence of structures in the data. A seismic horizon can either be picked as a peak (positive amplitude) or a trough (negative amplitude) on a seismic section, depending on the data polarity. A peak is associated with a decrease in acoustic impedance across a lithological boundary and a trough is associated with an increase in acoustic impedance (Brown 1996, 2001). The Roodepoort shale was picked as a trough due to its negative polarity owing to the increase of the acoustic impedance from the hangingwall quartzites to the top of the shale layer.

4.4.2 Autotracking and manual picking

Picking of seismic horizons through interpretation software packages on the seismic sections can be achieved manually (manual picking) or automatically (autotracking). The interpreter needs to decide on the picking technique depending on the polarity of the data and the complexity of the geology.

The autotracking method is considered the most efficient and time conscience horizon picking tool in most interpretation software packages. The basic concept of autotracking is that the interpreter plants seed picks on the inlines or crosslines of the chosen horizon in the 3D seismic data (Johnston and Cooper 2010). These points are then used to initiate the autotracking operation. The algorithm searches for similar features in neighbouring traces and extrapolates the points along the horizon (Johnston and Cooper 2010). In regions of structural complexities and low signal-to-noise ratio of the data the autotracking method may fail to consistently track the horizon. The manual picking method, however, provides the user with full interpretation control, thus allowing them to pick at wide line spacing or at every single inline and crossline, facilitating detailed structural interpretation. When picking, it is important to simultaneously correlate the picks made on the inline with the picks on the

crossline and depth slices to ensure that the horizon is being picked consistently and accurately. The ability to consistently pick a horizon is dependent on the quality of the data. As shown by the solid yellow lines in Figure 4.4a and b, the confidence in picking the Rooderpoort shale horizon was relatively high when the reflective character of the horizon was strong and continuous. The decrease in the quality of the data in structurally complex regions introduced some uncertainties in picking, as shown by the dashed yellow lines in Figure 4.4c.

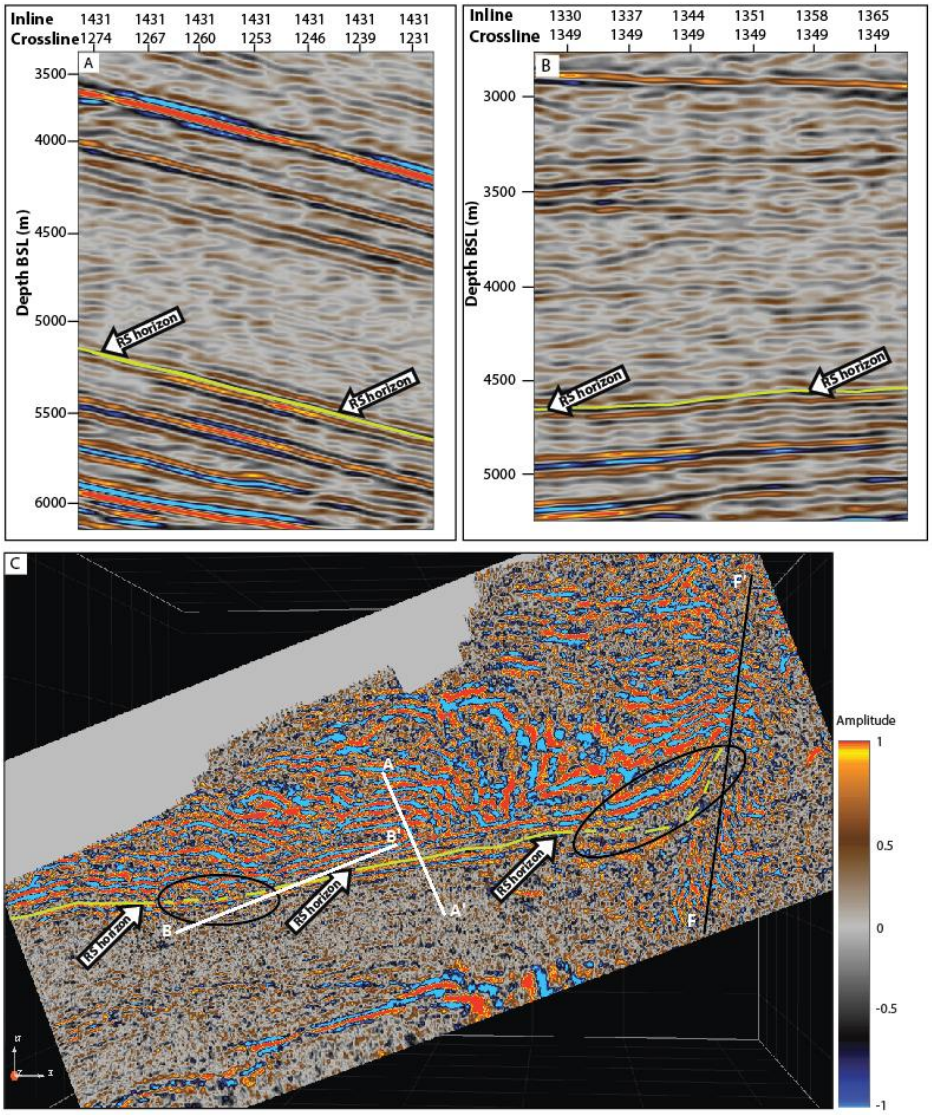


Figure 4.4 Conventional amplitude display seismic sections showing the correlation of the Roodepoort shale (RS) picks on the vertical sections represented by the (a) inline section and (b) crossline section and on the horizontal section represented by (c) the depth slice. The solid yellow lines represent areas where the confidence in picking was high due to the strong and continuous reflection of the horizon. The dashed yellow lines that are highlighted by the black circles in (c) show areas of structural complexity and low confidence in picking. Line A-A' and B-B'' show the location of inline and crossline sections, respectively. F: Fault.

After picking, a structure map (Fig. 4.5) of the horizon can be extracted incorporating first-, second- and third-order scale faults.

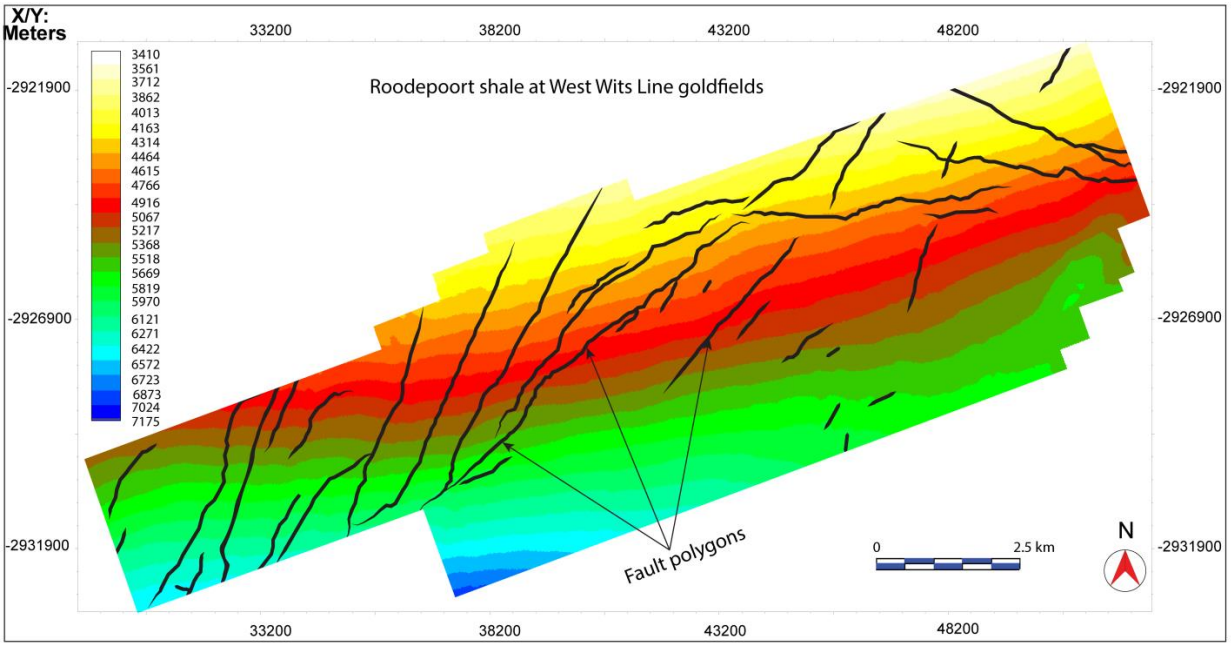


Figure 4.5 Depth structure map of the Roodepoort shale derived from manual picking. The map shows faults of various orientations that crosscut the horizon.

4.4.3 Seismic interpretation of structures

4.4.3.1 Folds

In addition to horizons, structural features can also be interpreted on seismic sections. Fold structures are easily observed in amplitude seismic sections and are characterized by dip changes of the horizons. These structures may form in response to regional compression, subsidence or frictional drag associated with faults (Badley 1985). Folds can be classified into three basic types, anticlines, synclines and monoclines. Anticlines are characterized by two limbs spread apart in a concave downward manner (Fig. 4.6a), whereas the two limbs of a syncline are concave upward (Fig. 4.6b). Monocline folds only have one limb (Fig. 4.6c). Various fold styles can be produced in the same rock sequence when there is a ductility contrast between different materials. Folds may be described in terms of shape, tightness, symmetry, plunge and axial trace (Badley 1985).

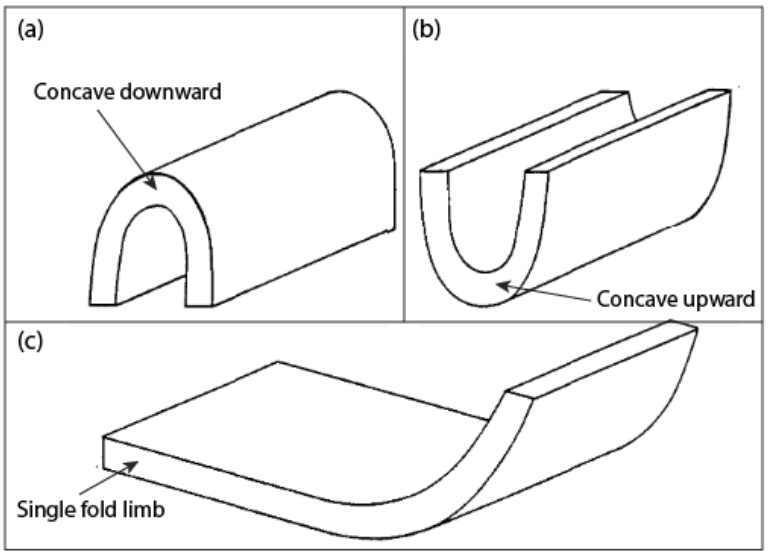


Figure 4.6 Schematic diagrams of basic fold structures. (a) Symmetrical anticline; (b) symmetrical syncline; (c) monocline. The anticline and syncline are characterized by two limbs orientated concave downward or concave upward, respectively. The monocline has only one limb (after Davis and Reynolds 1996).

Numerous folds can be identified in the WWL 3D seismic data. Figure 4.7a and b show anticlinal structures formed by lithological units due to compressive deformation experienced by the Witwatersrand Basin. Figure 4.7a is a depth slice extracted from the amplitude-based seismic volume showing the folding of horizons, but importantly, the image shows that the RS horizon forms a rollover anticline against the Bank Fault. Figure 4.7b shows that the overlying VCR also forms a rollover anticline against the Bank Fault. The anticline possibly formed during the reactivation of the Bank Fault as a normal listric fault during the Platberg Extension Event (Dankert and Hein 2010; Manzi *et al.* 2012b).

Identifying folds during the interpretation of seismic data can help to identify areas of weakness and pathways which fluids might have migrated through and may have used to deposit minerals. Additionally, the identification of folds can help geologists to reconstruct the stresses that the rocks have been exposed to which can ultimately lead to the identification of other important large-scale or small-scale structures. Therefore, their identification can lead to better planning of new drill sites and exploration targets.

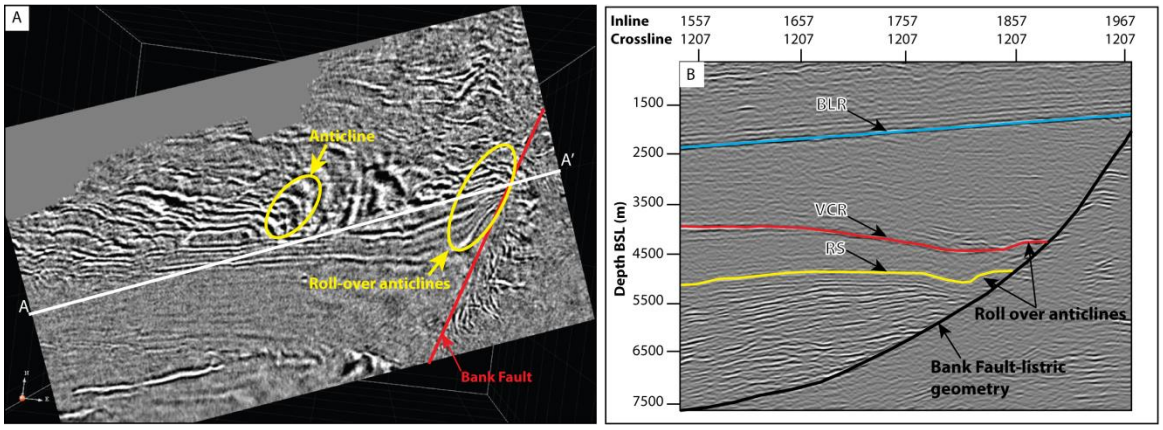


Figure 4.7 Showing examples of folds identified in the seismic data. The depth slice in (a) shows the extent of the first-order scale Bank Fault and the termination of horizons against the fault at 5000 m depth. The yellow circles highlight anticlines and line A-A' shows the location of the crossline in B. The crossline in (b) shows a vertical view of the roll-over anticlines against the Bank Fault.

4.4.3.2 Faults

Along with folds, faults can also be mapped on seismic sections. A fault is a fracture of discontinuity in a volume of rock across which the rock masses on either side have moved relative to one another parallel to the fracture (Davis and Reynolds 1996). The location and geometry of faults can be inferred by the reflection termination and displacement of the horizon on the opposite side of the fault plane (Badley 1985). Various types of faults can be distinguished based on the direction of movement of the hangingwall and footwall blocks. These include normal, reverse/thrust and strike-slip faults.

Normal faults form in response to extensional deformation of the crust, in which the hangingwall rocks move down relative to the footwall rocks (Fig. 4.8) (Davis and Reynolds 1996). There are several types of normal faults, which are distinguished based on different geometries. These include planar normal faults and listric normal faults. Planar normal faults are the most common types of faults in most sedimentary basins and are characterized by consistent dip angles with depth (Park 2004). A graben represents a downthrown block between two normal faults dipping towards each other, and a horst is an upthrown block between two normal faults (*see* Fig. 4.8). A listric normal fault is characterized by a curved fault plane where the dip of the fault is steeper near the surface and becomes progressively shallow with increasing depth. An example of a listric fault in the Witwatersrand Basin is the first-order scale Bank Fault (*see* Fig. 4.7b).

Reverse faults (*see* Fig. 4.8) form in response to compressional deformation of the crustal rocks, in which the hangingwall rocks move up relative to the footwall rocks (Davis and Reynolds 1996). Reverse faults are characterized by relatively steep dips that are greater than ~45°. Thrust faults have the same sense of movement as reverse faults, but with dips of less than ~45°.

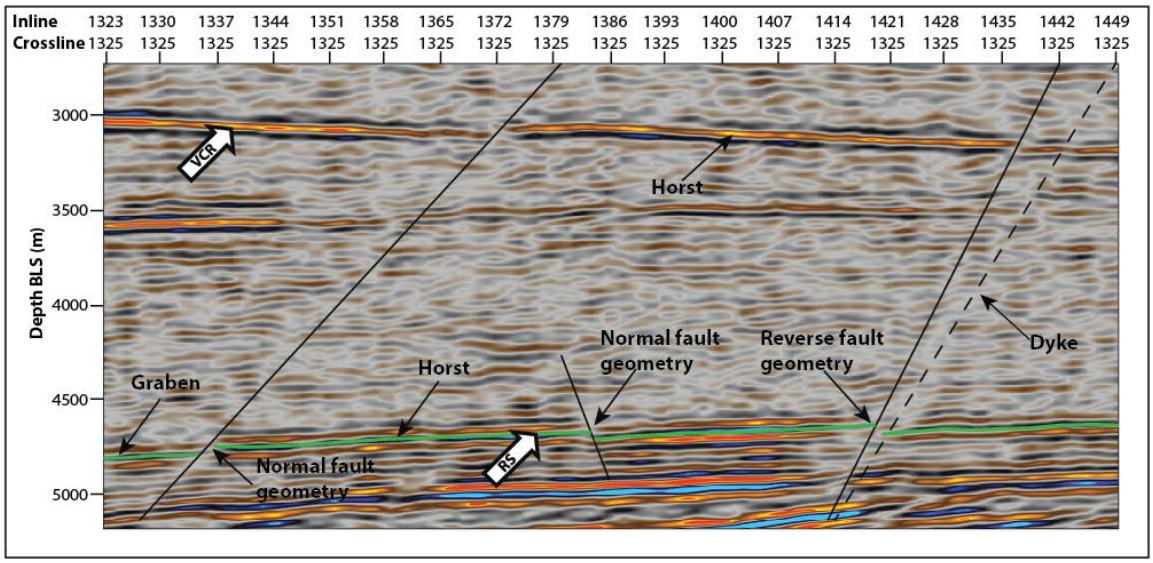


Figure 4.8 Amplitude display seismic section showing various types of faults across the survey areas. These faults crosscut the Roodepoort shale (RS) horizon at the top of the West Rand Group as well as the Ventersdorp Contact Reef (VCR) at the base of the Ventersdorp Supergroup. The seismic section also shows near vertical features (dykes) associated with highly attenuated seismic amplitudes.

Crustal rocks may also move horizontally past each other along nearly-vertical faults (Davis and Reynolds 1996). Faults typical of this movement are known as strike-slip faults. The slip of the fault is defined by the direction of movement of the ground on the opposite side of the fault from the observer. Therefore, movement is described as sinistral when the opposite side moves to the left and dextral when the opposite side moves to the right. In the next section we outline the effects of faults and dykes (vertical igneous intrusions) on mining activities and the importance of identifying them on seismic sections.

4.4.3.3 Effects of faults and dykes on mining activities

Previous seismic interpretation studies conducted by various authors (Gibson *et al*. 2000; Manzi *et al.* 2012a, 2012b) across the Witwatersrand Basin gold mines have identified various faults and dykes that crosscut the key gold-bearing conglomerate reefs (*see* Fig. 4.8). These studies identified faults of varying scales (small to large scale faults) and orientation that directly influence the reef behaviour. Faults have a number of effects on underground mining, which include: (1) displacement of the gold-bearing reefs which may result in loss of mineable ground, (2) compromising the rigidity of the mining hangingwall which may possibly lead to extensive falls of ground, and (3) they may act as conduits for water and methane gas to underground mining levels (Manzi *et al.* 2012a). For example, dykes can create water pockets that can lead to the flooding of the mine and they can transport methane to mining levels where it can cause explosions. Therefore identifying the geometry and extent of faults and dykes on seismic sections is of critical importance.

One of the major limitations of the conventional WWL 3D seismic data is its inability to image thin dykes (*see* Fig. 4.8), nearly-vertical faults and faults with throws of less than 25 m. This is because they fall below the dominant wavelength of the seismic resolution limit (see section 3.2; Chapter 8). These features may appear as subtle amplitude disturbances in the seismic section and are difficult to correlate using conventional interpretation. Seismic attributes are then applied to the data or interpreted horizons to enhance the mapping of subtle geological information.

4.4.4 Seismic attributes

Seismic attributes are derived from the seismic data and mathematical manipulation of seismic wave components such as amplitude, frequency and phase (Sheriff 1991). They are used in the enhancement of seismic features that are below the recommended seismic resolution criteria (one quarter of the dominant wavelength), thus providing accurate and detailed information on structural, stratigraphic and lithological parameters of the seismic data (Taner 1979). Seismic attributes have been classified in many different ways by several authors (Sheriff 1991; Brown 1996; Taner 1979). Here, seismic attributes are grouped into two types, namely, volumetric and horizon-based seismic attributes.

4.4.4.1 Volumetric seismic attributes

Amplitude

As previously mentioned, the amplitude attribute is the most basic and widely used attribute in the interpretation of seismic data. It is expressed as the maximum amplitude value at a specific area along a horizon picked from a 3D volume. The amplitude attribute correlates strongly with variations in porosity because this property has a direct effect on the velocity and density of the seismic reflections observed at boundaries where the acoustic impedance (product of velocity and density) significantly changes. Although the amplitude attribute is widely used in the interpretation of the structural architecture of an area, one of its major limitations is that it fails to clearly image minor lithological changes within thin horizons below the tuning thickness (one quarter of the dominant seismic wavelength), as observed in Figure 2.1 and Figure 4.9. The poor imaging of the CLR is due to minor lithological changes in the hangingwall (Rice Pebble Quartzite) and footwall units (Blyvooruitzicht Quartzite).

Instantaneous attributes

Instantaneous attributes are computed from the complex seismic trace, which is defined as:

$$CT(t)=T(t) + iH(t) \quad (8)$$

Where CT(t) is the complex trace, T(t) is the seismic trace, H(t) is the Hilbert's transform of T(t) and H(*t*) is a 90° phase shift of T(*t*) (Subrahmanyan and Rao 2008). These attributes are determined from every sample and represent variations in different instantaneous parameters such as trace envelope, frequency and phase (Taner 2001). All instantaneous attributes reveal important information in the seismic data. For example, the instantaneous phase provides information of the continuity or discontinuity of events and is thus the best indicator of the lateral continuity of seismic reflectors. The instantaneous phase is also used in the computation of instantaneous frequency. The instantaneous frequency provides information on the bed thickness and variations of the lithology (Subrahmanyan and Rao 2008). This attribute is also useful in indicating the edges of low impedance thin beds.

Edge enhancement

The edge enhancement attribute is used to enhance the spatial continuity of features (horizons and faults) in the seismic data. This attribute decreases the noise in the data by using local dip estimates of the reflection layers (Randen and Sønneland 2000). This attribute smooths the data, reducing noise levels, and therefore allows small amplitude changes to be detected. Hence, even subtle faults that are usually difficult to detect on seismic data are evident (Fig. 4.9a and b). The edge enhancement technique was applied to the seismic volume to smooth the data and reduce the noise before the ant-tracking attribute was applied.

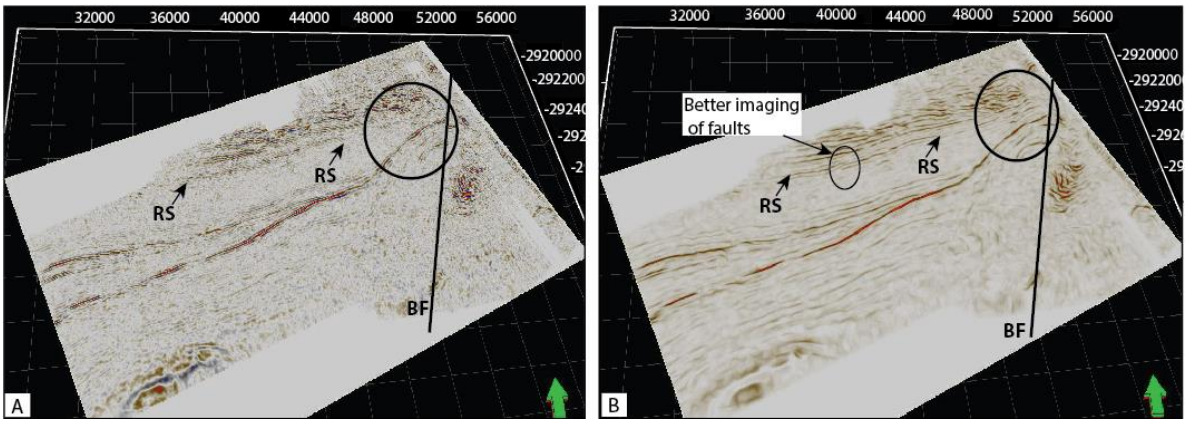


Figure 4.9 Depth slices at 5000 m showing (a) the amplitude display and (b) edge enhancement display.

Comparison of the amplitude depth slice in Fig. 4.9a and the edge enhancement depth slice in Fig. 4.9b it can be seen that the noise in the data has been significantly attenuated. The partial imaging of the lateral continuity of the RS horizon in Fig. 4.9a has been significantly improved in Fig. 4.9b. The edge enhancement attribute has highlighted the roll over anticline formed by the RS horizon against the Bank Fault (BF), which was only partially imaged in the amplitude display. The edge enhancement attribute, however, can sometimes over smooth the data and ultimately smooth important faults and

fractures. The ant-tracking attribute was applied to identify and track subtle faults and fractures in the seismic volume.

Ant-tracking

The ant-tracking attribute is a very powerful edge enhancement tool that is applied to processed 3D seismic data to enhance the detection of fault and fracture networks throughout the seismic cube (Pedersen *et al.* 2002). The ant-tracking technique is based on the idea of ant-colony systems to determine discontinuities (e.g., faults) in 3D seismic data (Basir *et al.* 2013). The ant-tracking technique uses the principles of "swarm intelligence", which explain how ants find the shortest path between their nest and the food by communicating with each other using a chemical substance known as pheromone (Ngeri *et al.* 2015). When searching for food ants leave pheromone trails to direct other colony members to the food that they have found. The colony members that follow reach the food by sniffing this pheromone. Through this processes the ants find the most efficient trail from nest to food (Pedersen *et al.* 2002; Cox and Seitz 2007).

Similarly, in the Petrel software computer coded "ant agents" search for and enhance fault networks, this allows automatic fault extraction from the output ant-track attribute volume (Fig. 4.10). The general workflow of the ant-tracking technique involves the application of structural smoothing filters (e.g., median and mean filters) to the seismic volume followed by the application of discontinuity attributes, i.e., variance and edge enhancement. The resultant ant-track volume is shown in Figure 4.10. The ant-tracking technique has proved to better map horizons and structures compared to the amplitude and the edge enhancement attributes. The antrack volume has highlighted fractures that are associated with the Bank Fault and that had not been previously mapped by the amplitude or the edge enhancement techniques. The identification of these fractures will aid in reducing the risks of weak hangingwalls and thus reduce rock burst and fall of ground at the mining level.

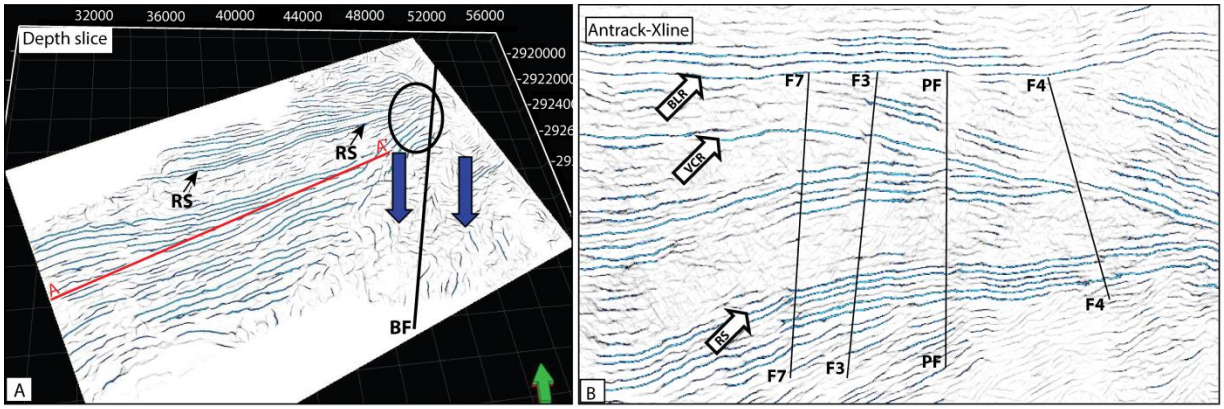


Figure 4.10 Resultant (a) depth slice at 5000 m and (b) antrack crossline (xline) extracted from the antrack volume. The depth slice shows the improved imaging of the Roodepoort shale and enhancement of fractures associated with the Bank Fault. The crossline shows the improved imaging of the Black Reef (BLR), Ventersdorp Contact Reef (VCR) and the Rooderpoort shale (RS) horizons. The crossline also shows the improved mapping of faults to shallow depths (VCR and BLR levels).

4.4.4.2 Horizon-based seismic attributes

Horizon-based seismic attributes, originally described by Dalley *et al.* (1989), have been used with great success in the Witwatersrand Basin to enhance the detection of sub-seismic faults at the horizon level (Manzi *et al.* 2012a, 2013). These attributes are applied directly to the picked surface to enhance the detectability of faults and unravel complex fault geometries.

The biggest difficulty faced when applying seismic attributes on the picked seismic horizon is their sensitivity to the variability in reflector waveform as well as to seismic noise. In order to reduce the effects of noise introduced during picking, post-fault interpretation smoothing parameters such as the mean and median smoothing algorithms, were applied to the picked Roodepoort shale surface. These smoothing algorithms are used in seismic interpretation to detect subtle faults, to filter-out the isolated horizon noise, and to separate gross structural configurations (long wavelength) from faults and dykes (short wavelength). They also provide an optimum resolution for the identification and location of faults, eliminate errors resulting from false complex geometries created by conventional picking around faults, and thus minimize unrealistic fault-horizon geometries. Figure 4.11a below shows the RS shale surface as obtained from conventional picking methods and Figure 4.11b shows the RS surface after the mean and median smoothing algorithms have been applied. The application of the smoothing parameters has improved the quality of the data and significantly attenuated the noise while retaining the faults. In addition, filtering of the data has enhanced the continuity of faults that were partially picked on the conventional surface and has enhanced some of the subtle faults not detected on the conventionally picked surface.

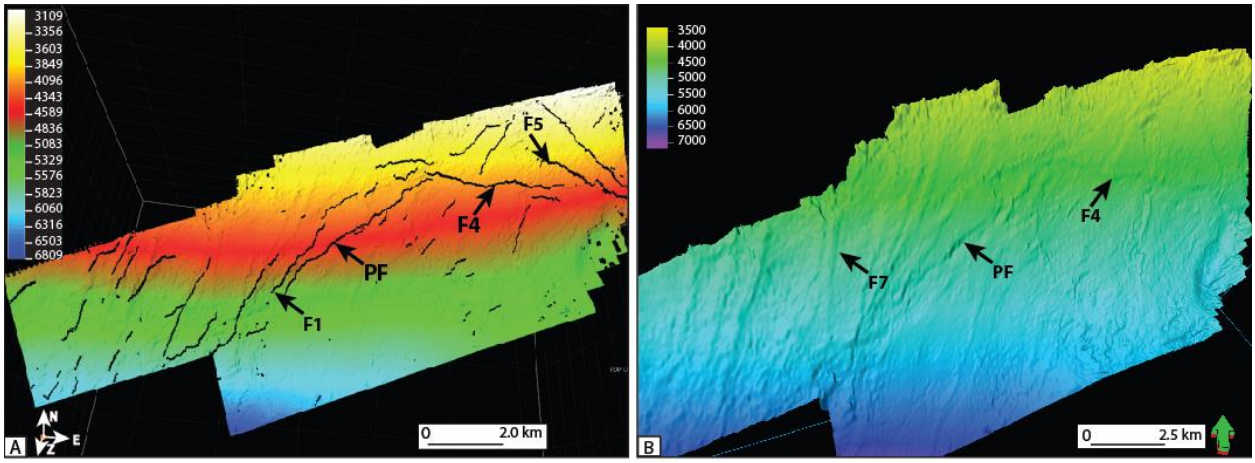


Figure 4.11 Roodepoort shale surface obtained from (a) conventional picking and (b) smoothed Roodepoort shale surface. The application of the smoothing operators has reduced the noise and spikes in the data.

Furthermore, another advantage of applying the mean and median smoothing algorithm post-picking is that filtering only occurs within the horizon rather than across the faults. However, care must be taken not to filter out the faults and dykes, since these operators are capable of filtering-out noise in addition to real faults and dykes, which can significantly affect the fault geometry. In this study the dip, dip-azimuth and edge detection horizon-based seismic attributes were applied to the Roodepoort shale surface.

Dip-amplitude and dip-azimuth

As described by Rijks and Jauffred 1991, the dip and azimuth are essentially the magnitude and direction of the time gradient vector calculated at each sample of the interpreted horizon. This is achieved by fitting a plane through neighbouring points in the data and posting the computed values at the central data point (Fig. 4.12).

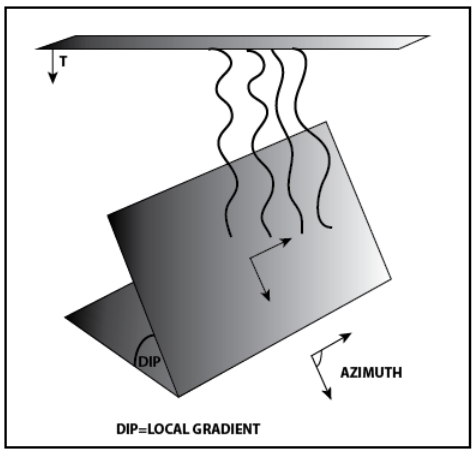


Figure 4.12 Schematic representation of how the dip and azimuth are calculated in seismic data.

In mathematical terms this can be expressed as follows:

$$Dip - amplitude = \sqrt{\left(\frac{dt}{dx}\right)^2 + \left(\frac{dt}{dy}\right)^2} \quad (9)$$

$$Dip - azimuth = arctan\left(\left(\frac{dt}{dx}\right) \Big/ \left(\frac{dt}{dy}\right)\right) \quad (10)$$

where $\frac{dt}{dx}$ and $\frac{dt}{dy}$ are the dip in the x and y direction, respectively.

The dip and dip-azimuth attributes are applied to the picked seismic horizon and are able to resolve subtle faults with vertical displacements below 25 m (Fig. 4.13). Both attributes have different capabilities and limitations in terms of fault enhancement and should be compared constantly during interpretation.

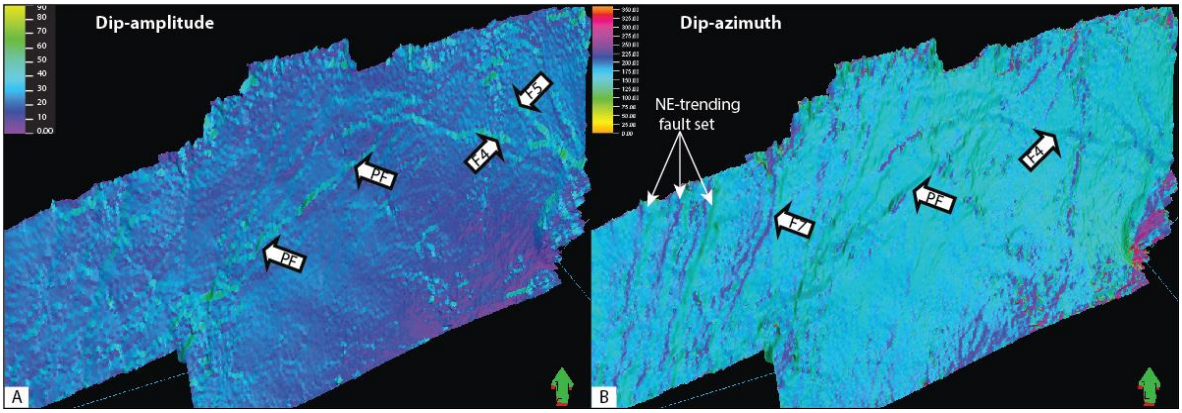


Figure 4.13 Seismic attributes computed for the Roodepoort shale horizon. (a) Dip attribute display, showing the clear mapping of the Pretorius Fault (PF) and the Fault (F4) and Fault 5 (F5) (colour bar given in degrees). (b) Dip-azimuth display, showing the extent of the PF, Fault 7 (F7) and Fault 4 (F4) (colour bar is given in degrees). The dip-azimuth map also shows the extent of some NE-trending faults on the western margin of the map.

As much as the dip and dip-azimuth maps reveal types and degree of faulting not observed on conventionally interpreted surfaces they do have a few short comings. For example, the dip-amplitude map fails to clearly image faults with apparent dips that are similar to that of the horizon, and the dip-azimuth map cannot image faults with similar dip directions to that of the horizon. To overcome the limitations of conventional interpretations as well as the dip-amplitude and dip-azimuth attributes, the edge detection attribute is applied to the seismic data after applying the dip-amplitude and dip-azimuth attributes.

Edge detection attribute

The edge detection attribute is considered to be one of the most reliable discontinuity enhancement techniques used in the interpretation of seismic data. The technique is a useful means of enhancing important fault characteristics such as fault continuity, connectivity and fault cross-cutting relationships. The attribute combines dip and azimuth variations that are normalized to the local noise of the interpreted horizon (Rijks and Jauffred 1991). This means that the edge detection attribute is able to detect minor changes in the signal amplitude allowing it to provide optimum imaging of faults with throws as small as 25 m. Edge-detection attributes surpass the ability of dip, dip-azimuth and other discontinuity enhancements techniques in highlighting (with the help of the manipulation of the colour bar) intricate structural details of horizons. In some studies (Manzi *et al.* 2012a; Manzi *et al.* 2013) the edge detection attribute could detect faults that had throws less than 5 m. The detection of faults with such small vertical displacement is important for the designing accurate mine plans and ensuring that reef displacement and poor ground conditions are anticipated ahead of mining. Figure 4.14 below shows the result of the application of the edge detection attribute to the Roodepoort shale surface. The white arrows indicate the enhancement of faults partially imaged by the dip and dip-azimuth maps and the red arrows show new faults that have been enhanced by the edge detection technique.

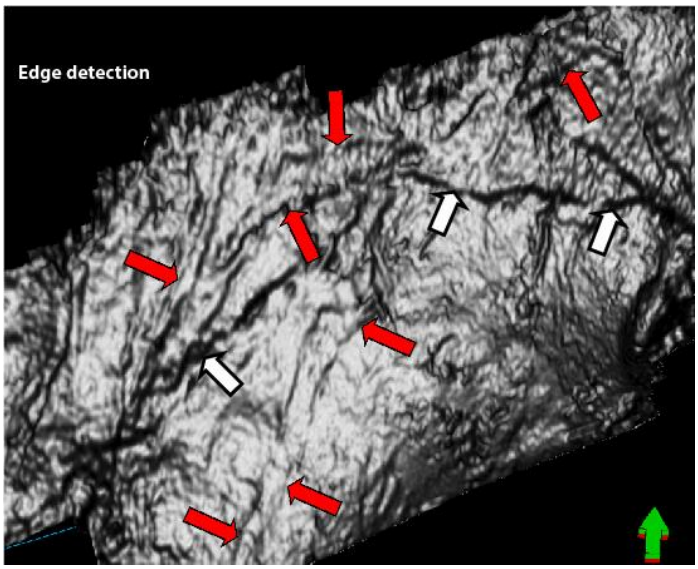


Figure 4.14 Roodepoort shale edge detection attribute map. The white arrows show faults which were clearly mapped by the dip and dip-azimuth maps in figure 14.11a and b and the red arrows show newly enhanced faults, which were not mapped by the dip-amplitude and dip-azimuth displays.

The application of the edge detection attribute to the RS surface has resulted in the (1) enhancement of faults with throws less than 25 m that were not detected on the conventionally interpreted amplitude seismic sections, (2) better imaging of faults that were partially mapped by the dip and dip-azimuth attributes and (3) enhancement of fault cross-cutting relationships as well as fault continuity and connectivity. Therefore, only relying on conventional interpretation methods to reveal intricate

structures and their relationships could result in a biased interpretation and inaccurate mine development plans that could compromise mine workers safety.

5 Methodology

This study used a multidisciplinary approach incorporating the aspects of geology, geochemistry and geophysics. To achieve the primary aims and objectives of this study the following procedures were followed: core-logging and sampling, thin-section and polished block microscopy, chemical analysis (XRF and XRD), physical property measurements (bulk density, seismic wave velocities and applied stress) and the interpretation of 3D reflection seismic data.

5.1 Core-logging and sampling

The diamond drilling method was used in the recovery of borehole core used in this study. Unlike rotary drilling which produces rock chips, diamond drilling produces solid core samples from the subsurface that can be extracted and examined on the surface for petrographic, structural and mineralogical studies. This method provides an accurate assessment of the deposit as fewer particles are likely to contaminate the core samples.

The drill-core samples used in this study were obtained from 9 boreholes (Fig. 5.1). Of the 9 boreholes, 8 (BH-A, BH-B, BH-C, BH-E, BH-F, BH-G, BH-H and BH-I) intersect the CLR and its associated hangingwall and footwall units and 1 (BH-D) intersects the Roodepoort shale and its surrounding rock units. These boreholes were selected based on their positioning within the 3D seismic volume (Fig 5.2), whether they intersected the CLR or RS shale stratigraphy and their availability. Refer to Appendix A for full borehole logs.

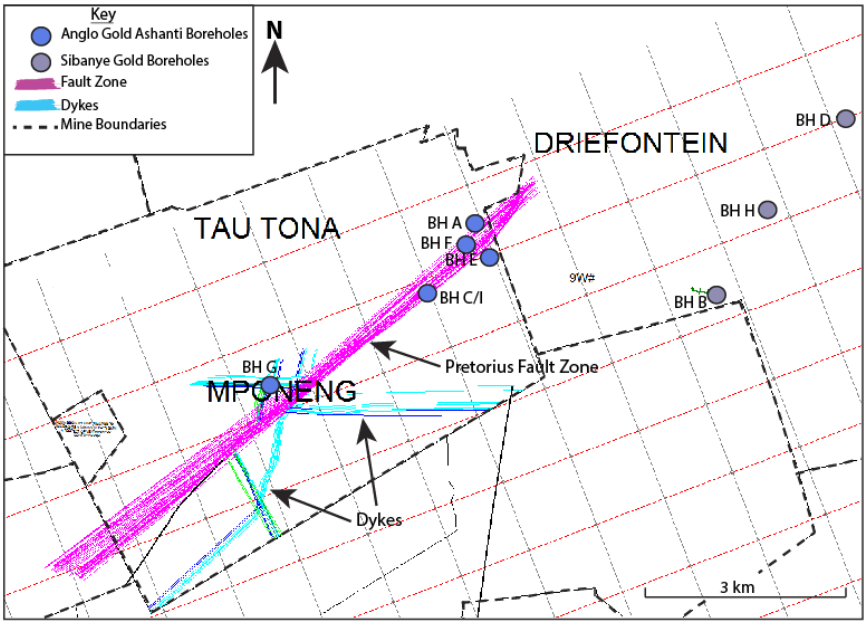


Figure 5.1 The map showing the location of the boreholes used for the physical property measurements and used to constrain the interpretation of the seismic data. The 9 boreholes are located within the Anglo Gold Ashanti Ltd and the Sibanye Gold Ltd mining boarders, but most importantly within the seismic volume. The map also shows the optimum mapping of the Pretorius Fault and dykes by underground geological mapping method.

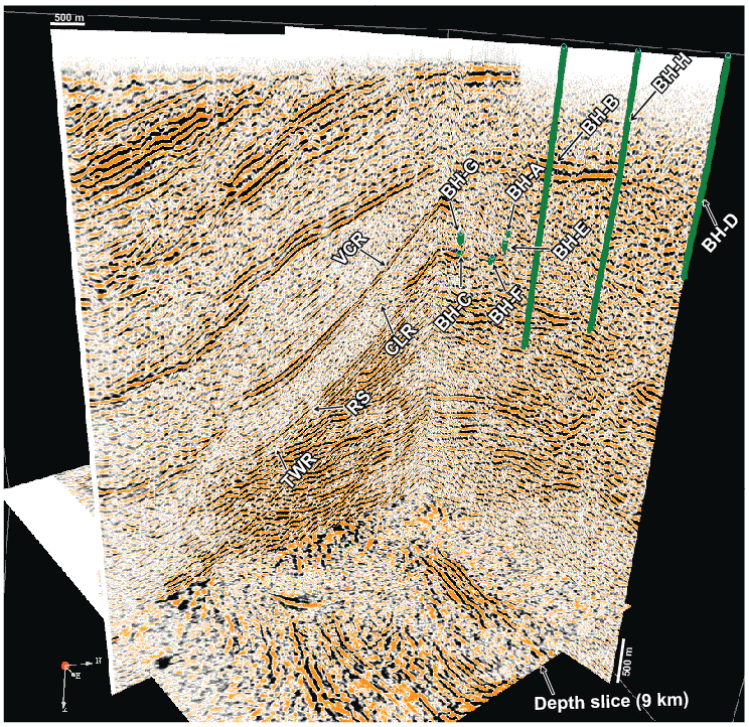


Figure 5.2 3D visualization of the migrated seismic volume covering Anglo Gold Ashanti and Sibanye Gold mines along the West Wits Line Goldfields, showing strong seismic reflectors and location of boreholes (BH-A to BH-H). VCR: Ventersdorp Contact Reef, TWR: Top of the West Rand, RS: Roodepoort shale, CLR: Carbon Leader Reef.

Detailed core logging was based on physical observation of the stratigraphic units. Firstly, the core logging was done to identify the rock units that constitute the hangingwall and footwall of the Carbon Leader Reef (CLR) conglomerate. Secondly, it was done to identify zones of alteration, changes in colour, textures and mineralogy, and the presence of structures at a macroscopic level. For detailed analysis of the core, logging was done at a 5 cm by 5 cm scale. This was done to ensure that subtle changes in the geological characteristics of the core were not missed and that accurate depths were measured at the contacts that separate each unit and at the location of the CLR conglomerate. Particular interest was given to rock units situated in the immediate hangingwall and footwall of the CLR conglomerate (~10 m above and below the CLR conglomerate). These units include the Main Quartzite, Green Bar shale and Rice Pebble Quartzite which constitute the hangingwall, the CLR conglomerate and the footwall Blyvooruitzicht Quartzite unit. Full-core (36 mm diameter) and half-core (18 mm diameter) samples were obtained from the hangingwall and footwall at 1 m intervals. This equidistant sampling allowed detailed analyses of the geophysical, physical and geochemical parameters of the different rock units within a particular borehole. More than one sample was obtained from each unit if the unit showed significant mineralogical and textural differences. A total of 50 drill core samples were used in this study.

Once sampling of the core was complete, the samples were prepared for petrographic, geochemical and rock physical property analyses. The samples used in geochemical analyses were crushed to

achieve a 1 mm particle size. The sample was then separated into four quarters. One quarter was used for the X-ray Diffraction (XRD) analysis and another for X-ray Fluorescence (XRF) analysis, while half the sample was saved. The XRF and XRD analyses were used to conduct elemental and chemical analysis of materials.

5.2 X-ray Fluorescence (XRF)

XRF is the emission of X-rays from a material that has been bombarded with high energy X-rays or gamma rays. A sample is exposed to a beam of X-rays emitted from a cased tube with either tungsten or molybdenum. A beam of X-rays is emitted from a tube to the sample and these result in an increased energy or excitement of electrons in atoms in the sample. The excited electrons will be displaced in the atom and their vacant positions will be filled by electrons that move from higher energy levels to lower energy levels. This movement of electrons from higher energy levels to lower energy levels releases a quantum of energy which is characteristic of each element in the sample. It is this quantum of energy that is referred to as the X-ray fluorescence.

The XRF method is able to detect elements from Calcium (Ca) to Uranium (U), to about 100 ppm. XRF detects both major and trace elements present in a rock sample. Major elements refers to elements whose concentration in a sample is greater than 1% (10000 ppm) and trace elements are chemical elements that have a concentration of less than 0.1% (1000 ppm).

The following steps were carried out in preparing samples for trace and major element analysis:

1. Mill rock samples to no less than 50 microns (or to a very fine powder).
2. Weigh 9g (or two teaspoons) of the sample and pour it into a mortar (Fig. 5.3a).
3. Add 4 drops of polyvinylalcohol solution to the sample and mix together with a pestle in order to consolidate the fine powder (Fig. 5.3a and b).
4. Empty the sample into a mould and place it in the stainless steel cylindrical sample holder.
5. Place the sample holder in the centre of the pellet presser (Fig. 5.3c and d)
6. Apply 10 kPa pressures to compress the sample (Fig. 5.3e).
7. Remove the sample from the pellet press and from the sample holder.
8. The sample is then placed in the Axios PANanalytical major and trace element analyser (Fig. 5.3f).
9. Repeat steps 1-8 for all the samples.

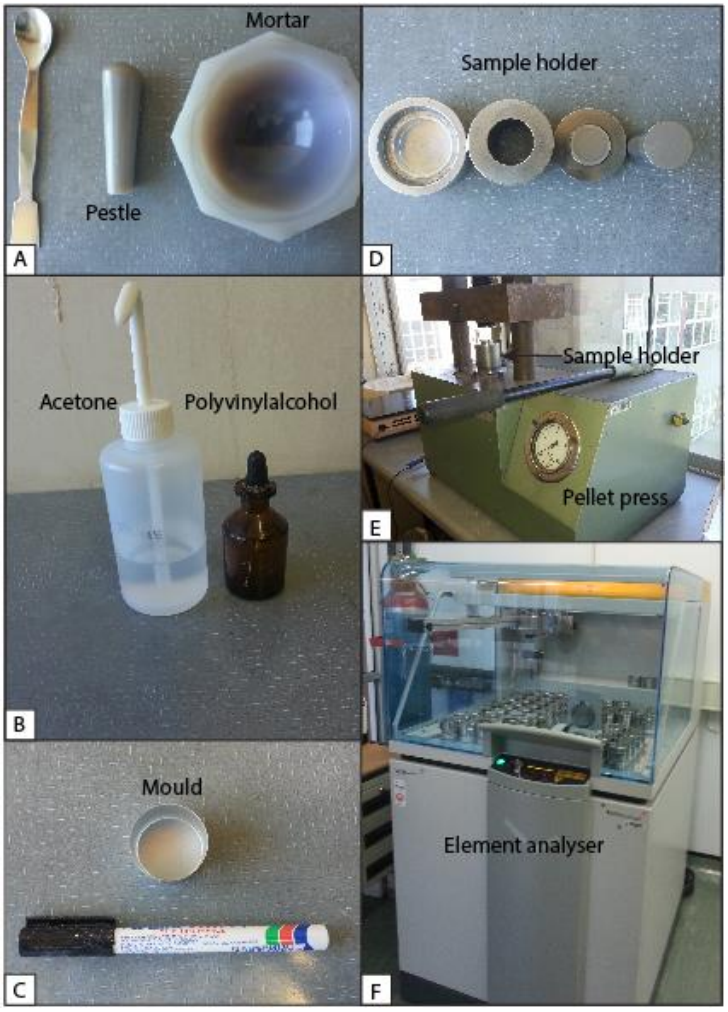


Figure 5.3 Apparatus used in conducting the XRF analysis. (a) Pestle and mortar used to the grind sample, (b) Polyvinylalcohol is used to thicken the texture of the sample, (c) Mould is used as a holding dish after the sample has been consolidated, (d) Sample holder is used to keep the sample confined and make sure that it is evenly flattened at the top when the pellet is made, (c) Pellet press machine used to compress the sample and (d) Axios PANanalytical machine which performs the analysis for both the major and minor elements.

This analysis was conducted in the XRF lab in the Bernard Price Building at the University of the Witwatersrand. The comprehensive data is presented in Appendix B for boreholes BH-A, BH-C, BH-E, BH-F, BH-G and BH-I. Due to the late arrival of boreholes BH-B, BH-D and BH-H and the mal functioning of the handheld XRF analyser, the chemical compositions of these boreholes were not determined (n.d.).

5.3 X-ray Diffraction (XRD)

The -1 mm sample saved for XRD was further divided into two halves. One half was saved and the other half was further ground into a fine powder. XRD was used in the characterization of crystalline materials and the determination of their crystal structure. This analysis is based on the premise that each crystalline solid has its own unique diffraction pattern, which is used for its identification. The detection of crystalline solids in a given sample is measured in percentage. By definition quartzites are composed of >90% quartz. Therefore, the peaks of any other solids present in the sample will not

be prominent and will be overshadowed by the quartz peaks. Furthermore, solids present in quantities of <5% will be undetectable. To overcome this, the Sodium polytungstate (SPT) mineral separation method was conducted on all samples from boreholes (BH) BH-A, BH-C, BH-E, BH-F, BH-G and BH-I.

5.3.1 Sodium polytungstate (SPT) mineral separation

Sodium polytungstate is an inorganic salt that when mixed with distilled water becomes a light yellow heavy liquid. This solution is used to separate materials of different density through their buoyancy. The SPT mineral separation process is based on the premise that materials with densities higher than the liquid will sink and materials with densities lower than the liquid will float.
In this study, the SPT method was used to separate out the heavier and less abundant minerals and alteration minerals from the lighter and more abundant silicates.

The following steps were carried out:

1. Write sample name on two test tubes and add a 1 g sample to one tube.
2. Weight 410 g of SPT stock in a beaker and add 30 ml of distilled water. Stir continuously while adding distilled water to make sure the solution maintains a watery consistency. The quantity of solution should be ~200 ml.
3. Pour 30 ml SPT solution into the test tube that contains the sample. Close the test tube lid tightly and shake. Make sure that there is no sample remaining at the bottom of the test tube.
4. Place the test tube in the Rotofix 32A Centrifuge, making sure that it is properly secured. Adjust the operating time on the centrifuge to 10 minutes and switch it on.
5. Remove the test tube from the centrifuge upright.
6. Pour off the floating material into another test tube. Rinse both tubes with distilled water at least 3 times.
7. Place the test tubes with rinsed samples into a crate and place them in the Gallenkamp Incubator oven to dry for ~24 hours at 34°c.
8. Repeat steps 1-7 for all of the samples until the required amount of float and sink has been generated.

The SPT mineral separation was conducted in the Geo-luminescence lab in the School of Geosciences at the University of the Witwatersrand.
The separation of heavy and light minerals was repeated 5 times for all of the samples. The samples were then sent to the laboratory for XRD analysis. The results reveal that silica was the dominant crystalline solid detected in all the samples and the peaks of the heavy minerals were not detected. This information can form the basis for studies that are concerned with the crystalline structure of quartz. Refer to Appendix C for full XRD report.

5.4 Polished thin sections and ore blocks (petrography)

The 20 samples used for the petrographic analysis were selected from eight boreholes to represent the different lithological units or distinct mineralogical changes in the stratigraphy.

An area of interest was marked on the hand sample and polished thin sections and ore blocks were created. Polished thin sections were made from all of the samples. The advantage of polished thin sections compared to unpolished thin sections is that you can analyse mineralization in reflected light. Ore minerals (oxides and sulphides), unlike normal minerals, are not transparent in thin section, i.e., they are opaque. Therefore reflected light is used in the identification and characterization of these opaque minerals in a sample and their textural relationships. Polished blocks were made from mineralized samples from the Rice Pebble Quartzite unit and the conglomeritic reef in order to identify the types and forms of mineralization. Photographs of the thin sections and polished blocks were taken using a polarising stereomicroscope and point-counting microscope with a digital camera output.

5.5 Physical property measurements

5.5.1 Density

Density measurements of every core sample were carried out using a Sartorius digital analytical balance (model E5500S, 5500 g maximum). A hook was attached underneath the balance and a nylon string was tied to it. A bucket filled with water was placed underneath the balance. The core samples were weighed in air in order to obtain a Wa (weight in air) value, then tied with the nylon string and submerged in water to obtain a Ww (weight in water) value to be used to calculate the density of the rock specimen. This analysis was based on Archimedes' principle which indicates that the buoyant force exerted on a body that is submerged in a fluid is equal to the weight of the fluid that the body displaces.

The following steps were carried out during this experiment:

1. Measure the weight of the sample in air by placing the sample on top of the balance.
2. Tie the nylon string around the sample then submerge it in water. Make sure that the sample is fully submerged then record its weight. Using Equation 11 to calculate the density of the rock specimen:

$$\rho = \frac{Wa}{(Wa - Ww)} \quad (11)$$

3. Repeat steps 1-3 for all the core samples.

Different rocks will have varying densities as a result of differences in mineralogy and porosity. The density range for the most abundant rock forming minerals is 2.2 to 3.5 g/cm^3 and ore minerals is 4.0 to 8.0 g/cm^3 (Schön 1996).

It was expected that the rock samples in this study would not differ greatly in density as they have similar mineralogy's. Because the samples are from a crystalline environment and have undergone metamorphism very little porosity was expected, no attempt was made to saturate the samples before the measurements. As a result of the degree of metamorphism that the sample have undergone, the difference between the sample weight in air (Wa) and the sample weight in water (Ww) was expected to be small due to the low porosity.

5.5.2 Seismic velocities

P- and S-wave velocities were obtained from the measurement of arrival times of waves propagating through full core samples. Measurement of arrival times was achieved by using receiver and transmitter transducers, and the results were displayed on an ultrasonic oscilloscope. The wave travels from the transmitter to the receiver and the reflection amplitude is plotted against time. The resultant wave is displayed on the Tektronix TDS 2012C two channel digital storage oscilloscope. The following steps were followed in carrying out for this analysis:

1. Core samples from each of the rock units were cut flat on both ends. Outmost care was taken in selecting homogeneous samples in order to obtain the most accurate arrival times.
2. Measure the length (L) of each sample and record it. The core length is very crucial because the shorter the core the greater the wave interference between the transmitter and receiver and this can yield inaccurate results.
3. Lubricate both ends of the sample with grease. This is done in order to increase the contact of the sample with the transmitter and receiver.
4. Place the sample on the receiver and place the transducer on top of the sample (Fig. 5.4a and 5.4b). Special care was taken to ensure that the sample is placed in the centre of the transducers so as to ensure wave propagation through the entire cross sectional area of the sample.
5. Adjust the oscilloscopes vertical scale (amplitude) and voltage so that the P-wave arrival time (Tp) can be recorded (Fig. 5.4b insert).
6. The Vp can now be calculated using the following formula below:

$$Vp = \frac{L}{Tp} \quad (12)$$

7. Move the cursor to the start of the S-waves and read off the arrival time Ts (Fig. 5.4b insert).
8. Calculate the S-wave velocity using the formula below:

$$Vs = \frac{L}{Ts} \quad (13)$$

9. Repeat steps 1-8 for all the samples.

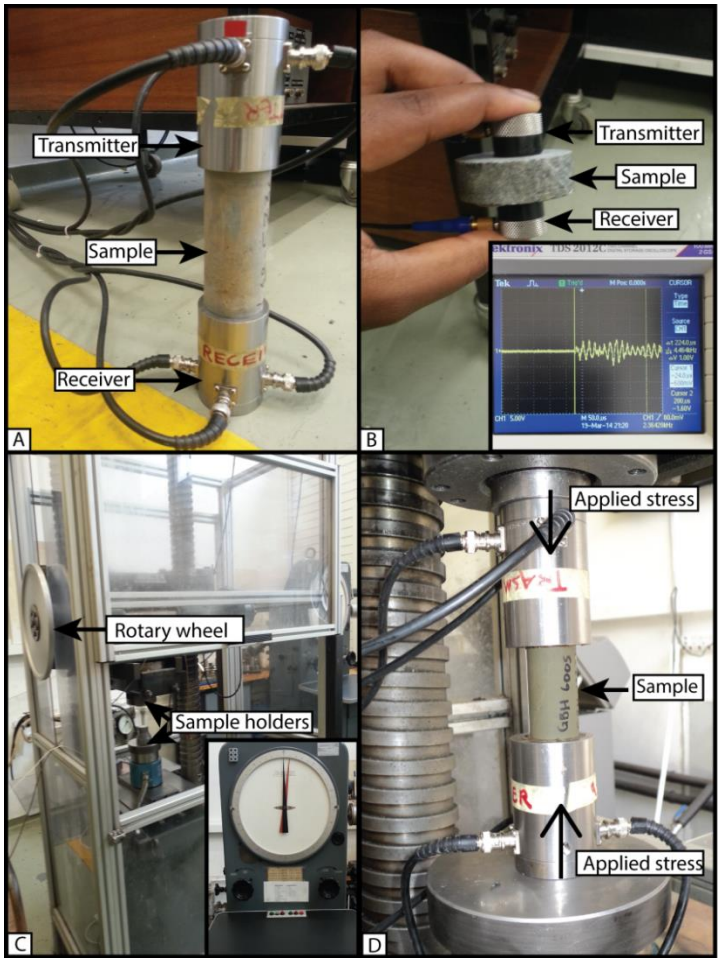


Figure 5.4 Ultrasonic velocity measurement apparatus at ambient (a and b) and elevated stresses (c and d). (a) Larger transducer (diameter=32 mm, 0.5 MHz) set used to measure seismic velocities for large samples (b) smaller transducer (diameter=16 mm, 0.5 MHz) set used to measure seismic velocities for smaller samples. (c) The uniaxial compressional loading is produced by hydraulic pistons that are driven by a computer controlled load holding pump. The induced load is monitored on a stress measuring gauge (insert in c). (d) The image shows the placement of the sample between the transducers positioned on pistons within the chamber.

All the petrophysical analyses were carried out in the Rock Mechanics Lab in the School of Mining Engineering at the University of the Witwatersrand.

5.5.3 Applied stress

Unconfined uniaxial compressive tests were carried out on full-core samples. This procedure was used to test the strength of a rock when a load was applied in one direction without any lateral strain. An AMSLER compression testing machine was used to measure the response of P- and S-wave velocities with increased confining pressure. The core samples were confined to room and incrementally elevated uniaxial compressive pressures from 0 MPa to 60 MPa, at 10 MPa intervals.

Each cylindrical core sample was placed between the transducers and placed on pistons in a stainless steel chamber (Fig. 5.4 c and d). The load was applied on the samples by adjusting the length of the chamber using motors attached above it. The stress readings were displayed on the measuring gauge and recorded (Fig. 5.4c insert).

5.6 Interpretation of 3D seismic reflection data

Chapter 8 and 9 provide the detailed methodology for the interpretation of the 3D seismic data across the West Wits Line goldfields (*see* Fig. 5.2 for the 3D seismic cube).

6 Scientific contributions

6.1 Authorship statement

This chapter presents a summary of the three papers which constitute the main focus of the study. A summary of each paper is provided, highlighting its main objectives, methods, results and conclusions. A description of the candidate's contribution and the contribution of each author to each paper is summarized below.

Chapter 7: *Nkosi N. Z., Manzi M.S.D., Drennan G.R. and Yilmaz H. 2016. Experimental measurements of seismic velocities on core samples and their dependence on mineralogy and stress, Witwatersrand Basin (South Africa),* ***accepted****, Studia Geophysica et Geodaetica.*

The candidate was responsible for the following:

- Logging and sampling of 9 boreholes provided by AngloGold Ashanti Ltd and Sibanye Gold Ltd.
- Crushing and milling of samples for X-ray Fluorescence and X-ray Diffraction geochemical analysis. The candidate created pressed pellets for the X-ray Fluorescence analysis. With the help of Dr. M. Evans, the candidate conducted the SPT mineral separation method that was required before the X-ray Diffraction analysis could be conducted. The X-ray Fluorescence analysis was conducted by Marlin Padayachee at the Bernard Price Building at the University of the Witwatersrand. The candidate was responsible for the interpretation of the data. The X-ray Diffraction analysis was conducted and interpreted by Dr. R.P. Forbes from the School of Chemistry at the University of the Witwatersrand.
- The interpretation of all polished thin-sections and polished blocks. The petrography material was made by Mr C. Majola and Mr M. Cebekhulu at the School of Geosciences at the University of the Witwatersrand.
- All physical property measurements, calculations and interpretation including density measurements, P- and S-wave velocity measurements, Uniaxial Compressive strength measurements.
- The candidate did all the figures and graphs in the manuscript and the comments from Dr M Manzi helped to improve their quality.
- The writing of the manuscript was done by the candidate. Dr M. Manzi and Prof. G. Drennan improved the quality of the paper with their comments and suggestions.

Chapter 8: *Nkosi N. Z., Manzi M. S. D. 2016. 3D seismic attributes for structural mapping and enhancement of deep gold mining: A Case study from the West Wits Line goldfields, South Africa,* ***accepted****, Exploration Geophysics.*

The candidate was responsible for the following:

- Importing the 3D reflection seismic data in the form of a SEGY file onto the Kingdom Suite software for initial interpretation. The coordinate system used was the LO27 (Cape Datum) format, which is the South African national coordinate system.
- Creating a base map after the coordinates of the seismic survey were loaded.
- Importing more than 6000 deviating boreholes that were drilled on the various mining properties, into the seismic volume. Special care was taken to ensure that each borehole was imported with its correct well data (e.g., x and y coordinates, elevation, inclination, azimuth and formation tops) for accurate correlation with seismic horizons and structures (faults, dykes and sills).
- Selecting the boreholes that intersected the stratigraphy from the Black Reef to the top of the West Rand Group or from the Ventersdorp Contact Reef to the top of the West Rand Group, to constrain the depth location of the Roodepoort shale horizon.
- The manual picking of the Roodepoort shale seismic horizon on the conventional seismic sections at wide line and close line spacing.
- The mapping of all faults and dykes in the seismic volume. For each fault, the candidate was responsible for the following: (1) measuring its vertical displacement (throw), (2) measuring its apparent dip angle and (3) determining its dip direction, type and trend. The structural interpretation was guided by Dr M. Manzi.
- The exporting of the seismic data, picked horizon and structures from the Kingdom Suite software and importing them onto the Petrel software for the application of seismic attributes and creation of fault surfaces.
- Applying the volumetric attributes (e.g., edge enhancement and ant-tracking) to the seismic volume and horizon-based attributes (e.g., dip, dip-azimuth and edge detection) to the picked horizon to enhance the detection of subtle or sub-seismic faults.
- Interpreting and comparing the depth slices and horizontal sections from the conventional amplitude-based seismic volume, edge enhancement volume and the antrack volume. The candidate also interpreted and compared the fault mapping results of each horizon-based attribute.
- With the help of Dr M. Manzi created the 3D structural model of the West Wits Line goldfields incorporating fault surfaces.
- The writing of the manuscript and all figures were done by the candidate and the comments and suggestions made by Dr M. Manzi remarkably improved the quality of the manuscript.

Chapter 9: *Manzi M.S.D, Cooper G., Malehmir A., Durrheim R. and Nkosi Z. 2015. Integrated interpretation of 3D seismic data to enhance the detection of the gold-bearing reef: Mponeng Gold mine, Witwatersrand Basin (South Africa).* ***Geophysical Prospecting 63, 881-902, doi:10.1111/1365-2478.12273.***

The candidate was responsible for:

- Logging of all the boreholes used in this study. This involved (1) identifying the CLR and its hangingwall and footwall units, (2) identifying the major and minor mineral components of each unit and (3) identifying appropriate samples to use for the physical property measurements.
- The interpretation of all polished thin-sections and polished blocks, for the microscopic analysis of the minerals that constitute each rock unit. The petrography material was made by Mr C. Majola and Mr M. Cebekhulu at the School of Geosciences at the University of the Witwatersrand.
- Conducting all the physical property measurements at ambient stresses which included, bulk density measurement and ultrasonic measurements of the P- and S-wave velocities of each sample. With the help of Dr M. Manzi and Mr A. Carpede the P-wave velocities of each sample were measured at elevated stress levels, up to 65 MPa.
- The calculation of the reflection coefficients at the boundaries between the CLR and its hangingwall and footwall units.
- The candidate was also responsible for making the velocity vs density and the P-wave velocity vs pressure graphs.

6.2 Summary of papers

Manuscript 1 titled "*Experimental measurements of seismic velocities on core samples and their dependence on mineralogy and stress, Witwatersrand Basin (South Africa)."* (Chapter 7) integrates physical rock property measurements such as bulk densities and seismic wave velocities with mineralogy and chemical analyses. This is done to better understand the seismic reflective nature of the world's deepest gold-bearing horizon, the Carbon Leader Reef (CLR), within the seismic volume interpreted in this study.

To test the reflectivity of the Carbon Leader Reef CLR against adjacent rock units a series of physical rock property measurements were carried out on drill-core samples from boreholes that intersect the CLR. The analyses carried out in this paper involved:

- The Physical and petrographic observation of the various rock units to identify distinct textures, mineral assemblages as well as macro- and micro-structures present in the hangingwall, footwall and reef samples.
- Conducting X-ray Fluorescence (XRF) to determine the chemical composition of each rock unit.
- Measurement of the bulk density and seismic wave velocities at atmospheric and elevated stresses to investigate the dependence of seismic velocities on mineralogy and increased uniaxial stress.

The results show that seismic wave velocities are dependent on the mineral and chemical composition of the rocks. Seismic velocities generally increase with increasing bulk density of the sample. The CLR has slightly higher bulk density and velocity values compared to the overlying Main Quartzite and Rice Pebble Quartzite and the underlying Blyvooruitzicht Quartzite units. The slightly higher bulk density and velocity values of the CLR may be attributed to its higher concentration of pyrite compared to the other quartzitic units. The similarities in the mineral composition and chemical signature of the quartzite units, which primarily consists of quartz, chert, chlorite, chloritoid, a sericite dominated matrix and pyrite is responsible for the similarities of their seismic velocities. The chloritoid-rich Green Bar shale has the highest bulk density and velocity owing to its fine-grained nature, modal mineralogy and pyrite content. A direct relationship between seismic velocities and silica and iron content was therefore established. It was observed that seismic velocities decrease with increasing silica content and increase with increasing iron content. The Green Bar shale has the highest iron values and lowest silica values in the entire CLR stratigraphy, and hence the highest seismic velocities.

Reflection coefficient values were calculated for the boundaries of the CLR with the overlying and underlying rock units using these physical property measurements. Values are below the minimum required reflection coefficient of 0.06 to produce a sufficient reflection between the rock units. This suggests that the reflection seismic method might not be able to directly image the Carbon Leader Reef as a strong reflector, as seen in the 3D seismic cube interpreted in this study.

To investigate the dependence of seismic wave velocities on applied stress, samples were subjected to elevated stresses of up to 65 MPa (equivalent to 3 km-4 km below the surface). Seismic velocities increase with progressive loading up to ~25 MPa, after which the seismic wave velocities remain constant. The rapid increase in seismic velocities at lower stress regimes (0 - 25 MPa) can be associated with the closure of microdefects (Birch 1961; Walsh and Brace 1964). At higher stress regimes (above 25 MPa) the velocity remains the same with increasing load due to the compaction and closure of microdefects being complete.

Manuscript 2 titled "*Structural mapping in the West Wits Line goldfields (South Africa) using integrated seismic attributes."* (Chapter 8) shows the advantage of applying state-of-the-art volumetric and horizon-based seismic attributes to enhance faults that are not detectable using conventional seismic interpretation methods.

To achieve the objectives of the study, the re-processed and merged 3D seismic data covering the West Wits Line goldfields were interpreted. These data were acquired in the 1990s and cover the Mponeng, Tau Tona and Driefontein gold mines. The merged surveys include the Western Ultra Deep Levels (WUDLs) and Driefontein seismic surveys. The outcome of the merging of the 3D data sets was a continuous seamless depth-converted prestack time migrated (PSTM) seismic volume that

covers a region of approximately 3300 km^3 (Manzi *et al.* 2012a) The seismic volume images the entire Witwatersrand Basin stratigraphy from the surface to a depth of ~11 km. This includes the imaging of high acoustic impedance boundaries, which coincide with key horizons in the basin, i.e., the Black Reef, Ventersdorp Contact Reef and the Roodepoort shale. As observed on the 3D seismic cube, the Carbon Leader Reef is not mapped as a strong seismic reflector. This is due to its thickness (~1 m) which is below the vertical seismic resolution limit (25 m) and low acoustic impedance contrast between it and its hangingwall and footwall rock units. Here, we interpret the Roodepoort shale (RS) horizon, which is the strongest and closest seismic reflector (located ~350 m below the CLR) to the commercial Carbon Leader Reef.

The initial interpretation of the seismic data involved the picking of the RS horizon and associated faults on conventional amplitude display seismic sections. The seismic sections provided information about the first-order scale Bank Fault (65°-70° dip; 2.0 - 2.5 km normal throw; 800 m sinistral offset), the second-order scale Pretorius Fault (75° - 80° dip; 40 - 500 m normal throw; 200 m horizontal displacement) and a number of third-order scale normal and thrust faults with varying dips, strikes and throws that displace the stratigraphy by tens of metres. Although the seismic section provided the opportunity to interpret structures that cross-cut the RS, the technique did not allow for full exploitation of the data. This is because faults with throws below 25 m were not detected on the amplitude display sections. To overcome this, seismic attributes were applied to the seismic data to enhance the detection of these features.

The ant-tracking volumetric attribute was applied to the seismic volume to track the continuity of faults. Not only did this technique improve the imaging of faults in structurally complex regions, it improved the imaging of the lateral continuity of the strong reflectors. The better imaging of faults enabled us to track them across stratigraphic levels to shallower depths, thus constraining the structural history of the goldfield. For example, the ant-track volume shows that these faults crosscut and offset the RS at the top of the West Rand Group (ca. 2.985 - 2.902 Ga), the CLR at the base of the Central Rand Group (ca. 2.902 - 2.849 Ma) and the VCR at the base of the Ventersdorp Group (ca. 2.720 - 2.630 Ga). The normal geometry (extension) of these faults can be attributed to the Platberg-Hlukana age extension event (2.70 - 2.64 Ga). More importantly, the first-, second- and third-order scale faults do not breach the base of the Transvaal Supergroup (ca. 2.58 - 2.20 Ga), thus constraining the tectonic evolution to between 2.71 Ga and 2.58 Ga. This work confirms previous studies by Gibson *et al.* (2000), Gibson (2004), Dankert and Hein (2010) and Mambane *et al.* (2011).

Furthermore, examination of the seismic sections reveal near vertical features which can be attributed to dykes, which are known to have negative impacts on mining activities in the Witwatersrand Basin gold mines. The dykes and faults in the basin are known to be possible transport conduits for methane gas from the source to mining levels. Therefore, mapping these structures could aid in reducing the risk of methane explosions in mines (Manzi *et al.* 2012a).

Horizon-based seismic attributes, such as dip, dip-azimuth and edge detection on the RS horizon data, have enhanced the imaging of subtle or sub-seismic faults that could have an effect on mine production and stope development. The application of the edge detection attribute, in particular, enhanced the detection of intersecting and crosscutting faults with variable orientations and throws compared to the dip and dip-azimuth attributes. The edge detection maps enhanced the fault architecture in a way that would not have been possible using conventional interpretation techniques. Finally, a model of the structural framework across the WWL goldfields was derived from the interpretation of the 3D reflection seismic data coupled with borehole logs and underground mapping information. This model can be factored into future CLR exploration plans and should be regularly updated as the mining operation expands and moves to deeper levels.

Manuscript 3 titled "*Integrated interpretation of 3D seismic data to enhance the detection of the gold-bearing reef: Mponeng Gold mine, Witwatersrand Basin (South Africa)."* (Chapter 9) investigates the poor seismic reflectivity of the CLR by conducting physical property measurements such as bulk densities and seismic velocities on the CLR and its surrounding rock units, and using them to obtain reflectivity values of the CLR. The study then uses modified complex trace attributes to enhance the detection of the non-seismic Carbon Leader Reef and incorporates borehole data to constrain its depth location.

Since the acquisition of the 1995 seismic survey, covering the Mponeng gold mine located in the WWL goldfield, over 100 exploration boreholes have been drilled to intersect the CLR ore body (at depths ranging between 1.5 km and 4.2 km) to test the ore grade. These boreholes intersected prominent rock units in the hangingwall (Green Bar shale and Rice Pebble Quartzite) and footwall (Blyvooruitzicht Quartzite), which are distinct CLR marker horizons. For a horizon to have a strong and continuous reflection on a seismic section, a reflection coefficient of the order of 0.06 between major geological boundaries is suggested (Salisbury *et al.* 2000), given that the seismic data have a high signal-to-noise ratio and the target horizon has a suitable geometry to be detected by reflection seismic methods (Milkereit *et al.* 1996). To understand the poor reflectivity of the CLR ultrasonic measurements of P-and S-wave velocities as well as bulk density measurements were conducted on drill-core samples collected from four boreholes that intersect the CLR within the seismic volume.

Results show that the bulk density values obtained for the CLR, the hangingwall and footwall quartzite samples are similar. The average density values for the CLR, hangingwall and footwall quartzite are 2.80 g/cm^3, 2.79 g/cm^3 and 2.75 g/cm^3, respectively. The similarities in the bulk densities of the rocks may be associated with their similar mineral compositions. The Green Bar shale unit, however, has a relatively higher density (mean= 3.05 g/cm^3) compared to the CLR and its surrounding quartzites. The higher density of the Green Bar shale may be the result of its finer grain size and high iron and magnesium content (Krapež 1985). In addition to the similar bulk density values of the quartzite units, similar P-wave velocity values were also observed. The average P-wave velocity values obtained for the CLR, Rice Pebble Quartzite and the Blyvooruitzicht Quartzite samples are 5395 m/s, 5195 m/s

and 5063 m/s, respectively. The Green Bar shale has an average P-wave velocity of 5508 m/s, which is higher than its footwall rocks. It is observed that the P-wave velocities increase with increasing density and pyrite content and decrease with increasing quartz content. The reflection coefficient value of ~0.02 was obtained between the CLR-Rice Pebble Quartzite and CLR-Blyvooruitzicht Quartzite geological boundaries, which are below the suggested minimum of 0.06 required to produce a strong reflection. This means that the quartzite units surrounding the CLR do not produce a sufficient acoustic impedance contrast to produce an observable reflection on seismic sections. As a result of the insignificant impedance contrast (and low reflection coefficient values) at the boundaries between the CLR and its hangingwall and footwall units and its thickness (~1 cm) it is difficult to identify, pick and to track the CLR horizon throughout the West Wits Line goldfield using conventional amplitude-based interpretation tools.

Seismic attributes can be used in this situation to enhance the lateral continuity of the CLR. However, the main issue with conventional instantaneous attributes based on wavelet amplitude is that they cannot resolve thin beds below the tuning thickness. This is because the amplitude has a direct relationship with bed thickness, i.e., the amplitude decreases as the thickness of the bed decreases. Conventional instantaneous attributes also fail to detect thin beds that occur within rock units of similar velocity and density (typical of the CLR stratigraphy) owing to their sensitivity to lithological changes. With this in mind, a new seismic instantaneous attribute (amplitude-independent) was derived from conventional instantaneous attributes that sharpens the seismic trace and measures the wavelet character rather than lithological changes. The amplitude-independent seismic attributes were successful in highlighting the lateral continuity and shape of the CLR in greater detail than achieved by traditional amplitude displays. Due to the high levels of noise introduced to the data by applying these seismic attributes, borehole data were used to constrain the interpretation.

A 3D CLR model was derived by computing the difference between the Ventersdorp Contact Reef (located ~700 m above the CLR) and the Crown Lavas (located 600 m below the top of the West Rand Group), which are detected as strong reflectors throughout the seismic volume. The resultant CLR model was confirmed by the amplitude-independent seismic attribute and borehole intersections. Finally, horizon-based seismic attributes were applied to the CLR surface and successfully imaged a number of major faults across the goldfields. The edge detection technique enabled the mapping of subordinate faults associated with the major structures, as well as dykes that have a direct effect on mining activities and safety.

7. Manuscript 1

The manuscript has been modified according to journal standards.

Experimental measurements of seismic velocities on core samples and their dependence on mineralogy and stress, Witwatersrand Basin (South Africa)

Nomqhele Z. Nkosi[1*], Musa S.D Manzi[1], Gillian R. Drennan[1], Halil Yilmaz[2]

[1] University of the Witwatersrand, School of Geosciences, Johannesburg, South Africa.

[2] University of the Witwatersrand, School of Mining Engineering, Johannesburg, South Africa.

Email: 464950@students.wits.ac.za; Musa.Manzi@wits.ac.za; Gillian.Drennan@wits.ac.za; Halil.Yilmaz@wits.ac.za

Abbreviated title: Seismic properties of hard rocks

ABSTRACT

Physical property measurements were integrated with mineralogical analyses to better understand the nature of the seismic reflectivity of the deepest (> 3.5 km depth) gold ore body (Carbon Leader Reef). The CLR lies at depths between 3.5 km and 4.5 km below the surface. Over 50 drill core samples were selected for geochemical analyses, density and seismic velocity measurements. Ultrasonic measurements were conducted at ambient and elevated stresses, using transducers operating at 0.5 MHz. The study reveals that P-wave velocities generally increase with increasing bulk density. The CLR conglomerate, the gold-bearing reef, has slightly higher P-wave velocity (~ 5070 m/s-5468 m/s) and density values (~ 2.78 g/cm^3) amongst the quartzitic units, possibly due to its massive pyrite content. The quartzite hangingwall and footwall rocks to the Carbon Leader Reef exhibit similar P-wave velocity (~ 5028 m/s-5480 m/s and ~ 4777 m/s-5211 m/s, respectively) and density values (~ 2.68 g/cm^3 and 2.66 g/cm^3). The reflection coefficients calculated at the interface between the Carbon Leader Reef conglomerate and its hangingwall and footwall units range between ~ 0.02 and 0.05 which is below the required minimum reflection coefficient value of 0.06 to produce a strong reflection between two lithological boundaries. This suggests that seismic reflection methods might not be able to directly image the Carbon Leader Reef, as observed from its poor reflectivity in the 3D seismic data. Samples were also subjected to stresses of up to 65 MPa to simulate *in situ*-like conditions and investigate the dependence of seismic velocities on applied stresses. P-wave velocities increase with progressive loading, but at different rates in shale and quartzite rocks as a result of the presence of micro-defects.

INTRODUCTION

The Witwatersrand Basin in South Africa hosts some of the world's deepest gold mines which have significantly contributed to the economic growth in South Africa. The basin has been mined for over 122 years and produced over 35% of the gold ever mined in the recorded history of humankind. Most of the gold is hosted in quartz-pebble conglomerates (~ 1 m thick) and carbon rich seams *(Frimmel and Minter, 2002; Buck and Minter, 2014)*. The discovery of the various goldfields was the result of the integration of various geological and geophysical methods such as geological field mapping, drilling, gravity and magnetic geophysical methods. In the late 1980s, gold mines adopted seismic reflection techniques, widely used in the petroleum industry, to map deeply buried gold-bearing reefs located at depths of ~ 2.5 km - 4.0 km, which is typical of gold deposits from the basin *(Gibson et al. 2000; Pretorius et al. 2003; Malehmir et al. 2012; Manzi et al. 2012; Manzi et al. 2013; Malehmir et al. 2014; Manzi et al. 2014)*. The 3D seismic reflection method has proven to be more effective when compared to the 2D reflection seismics. For example, 2D seismic data are difficult to interpret, particularly in regions of complex mining, whereas 3D seismic data provide more accurate mapping of depths, dip and strike of essential horizons and subsurface structures. The integration of 3D seismic data with borehole information have proven to provide better interpretations of the Witwatersrand Basin gold reefs *(Manzi et al. 2012; Malehmir et al. 2013; Manzi et al. 2013)* and have provided mines with more reliable geological models for mine planning and design.

Though borehole geophysical measurements provide essential information about physical properties of mineralized zones, their host rocks and associated lithological units, a detailed and direct laboratory approach to measuring physical properties (e.g. seismic velocities, bulk densities and porosity) of Witwatersrand Basin conglomerate reefs and their host rocks has not been done. The laboratory measurements of physical properties, seismic velocities in particular, associated with ore deposits and their host rocks are crucial in interpreting seismic data collected at the surface for mineral exploration purposes. Over the past decades, there has been an increasing trend in integrating reflection seismic studies with various physical property measurements for improved understanding of the mapping of major ore-bearing horizons and subsurface structures, e.g. faults, dykes and sills *(Pretorius et al. 1994; Gibson et al. 2000; Salisbury et al. 2000; Milkereit et al. 1996, 2004; Malehmir and Bellefleur, 2009; Elbra et al., 2011; Malehmir et al. 2011; Dobróka and Molnár, 2012; Wood et al.,*

2012; Malehmir et al. 2013; Malehmir et al. 2014; Manzi et al. 2015).

In this paper, we provide a detailed investigation of the physical properties and geological characteristics of one of the world's deepest and richest gold-bearing reef in the Witwatersrand Basin, the Carbon Leader Reef (CLR) conglomerate. Our primary aim is to understand the seismic reflective nature of the CLR conglomerate and its associated hangingwall (H/W) and footwall (F/W) units. To achieve this we conducted laboratory measurements of ultrasonic velocities and bulk densities of the various lithologies.

Previous studies *(Christensen, 1965; Castagna et al. 1985; Carlson and Miller 2004; Punturo et al. 2005; Kern et al. 2009; Elbra et al. 2011; Malehmir et al. 2012, 2013)* have conducted laboratory measurements on hand samples or samples obtained from boreholes to understand physical properties (bulk density and seismic velocities) of rocks that might not be easily measured in boreholes. As efficient and insightful as laboratory measurements can be it should be noted that physical properties obtained from the laboratory are not *in situ* and only represent the immediate borehole surroundings. Therefore, they may not be fully representative of the rocks covering the entire survey area. The advantages of laboratory measurements over borehole measurements in hard rock environments, such as the Witwatersrand Basin, are that laboratory measurements are (1) cheaper and more affordable due to the analysis of individual core samples rather than entire holes, and (2) various measurements can be conducted on core samples that may be difficult to achieve in narrow holes.

Laboratory physical property studies provide first-hand information about the mineral assemblages and densities of rocks and how they may affect seismic wave propagation. According to general observations, average seismic velocities of crystalline rocks increase with increasing density and thus with increasing metamorphic grade, e.g. rocks with higher sulphide content will have higher velocities due to their high density *(Milkereit et al. 2004; Salisbury and Snyder, 2007).* The phenomenon that seismic velocities increase with applied stress is well known and has been highlighted by a number of studies *(Wyllie et al. 1956; Birch, 1961; Walsh and Brace, 1964).* The dependence of seismic velocities to stress is mainly controlled by the presence of micro-defects (micro-fractures, grain

contacts) which close under the effect of differential stress, thereby increasing the rigidity of the material *(Birch, 1961; Walsh and Brace, 1964; Christensen, 1965; Best, 1997).* Studies by *Schön (2004)* on the velocity-stress relationships show a higher stress effect for coarse-grained rocks and a lower effect for fine-grained rocks owing to larger and smaller pore spaces, respectively. From the physical property data, it is possible to derive the seismic impedance and reflection coefficients for various lithological units and their boundaries.

Reflection seismic studies *(Milkereit et al. 2004; Salisbury and Snyder, 2007; Malehmir et al. 2013)* show that an impedance contrast (velocity x density) of at least 2.5 x 10^5 g/cm^2s between two adjacent geological boundaries will result in a sufficient reflection. Therefore, according to *Salisbury et al. (2000)* a minimum reflection coefficient of 0.06 is required between two lithological boundaries in crystalline environments. The Carbon Leader Reef conglomerate is not mapped as a prominent horizon in the 3D seismic data from the Witwatersrand Basin *(Manzi et al. 2015)*, and the reason for its poor seismic reflectivity is still not fully understood.

Summarily, the main objectives of this study include (1) providing information about the mineral assemblages and chemical composition of the various rock units at ambient stress conditions and investigating the effect on seismic velocities, (2) measuring bulk densities of the various rock samples and investigating their relationship with seismic velocities, and (3) analysing seismic velocity and bulk density data to obtain the reflection coefficients at the CLR conglomerate interface with adjacent hangingwall and footwall rock units. Furthermore, we present data obtained from velocity-stress analysis conducted on full core samples to investigate the dependence of seismic velocities on applied stresses and the role of micro-defects. Moreover, the paper provides information about seismic velocities of three rock units that constitute the Top of the West Rand Group (TWR) namely; Maraisburg Quartzite, Roodepoort shale (RS) and the Lower Roodepoort Quartzite. This information will help us understand the basic acoustic properties and the strong reflection of the RS which may provide essential information in understanding the seismic properties of the overlying CLR conglomerate. This information will aid in better understanding the structure, extent and physical state of the CLR conglomerate and thus improve future mine planning and development.

Location of the study area

The samples used in this study were obtained from borehole intersections from Mponeng and Tau-Tona gold mines, two of Anglo Gold Ashanti's gold mining operations, situated in the Carletonville Goldfield (also known as the West Wits Line Goldfield) within the Witwatersrand Basin (Fig. 1 and 2). The West Wits Line (WWL) Goldfield is situated 60 km south-west of Johannesburg (Fig. 1 and 2) on the northern margin of the basin *(Dankert and Hein, 2010)* and boasts the highest grade of Carbon Leader Reef. The CLR conglomerate is amongst the most economically important gold-bearing conglomerates in the WWL and is responsible for ~ 75% of the gold produced while the Ventersdorp Contact Reef (VCR) accounts for the remaining 25%. The Mponeng and Tau-Tona gold mines are amongst the deepest gold mines in the world, with maximum operating depths of ~ 4.0 km and 3.9 km, respectively *(Manzi et al. 2012).* Both mining operations currently exploit the CLR conglomerate, which is mined at depths of ~ 3.5 km-4.0 km striking at 075° and dipping basinward at 20°S. A smaller number of samples were obtained from Sibanye Gold's shallow to ultra-deep Driefontein gold mine. This mine exploits various tabular gold deposits, including the CLR conglomerate at depths ranging from 600 m to 3.3 km. This WWL goldfield is dominated by extensional faults such as the Bank Fault and West Rand Fault (*see* Fig. 1) *(Dankert and Hein, 2010; McCarthy, 2006)*. The West Rand Fault separates the WWL Goldfield from the West Rand Goldfield, and the Bank Fault divides the WWL Goldfield into two sections (*see* Fig. 2) *(Robb and Robb, 1998)*. As a result of faulting, a change in strike from east to west in the western part and north to east in the eastern part is observed *(McCarthy, 2006).*

Geological setting

The geology of the West Wits Line Goldfield in the Witwatersrand Basin (Fig. 3) has been studied in great detail by a number of authors, including *De Kock (1964), Coward et al. (1995), Robb and Meyer (1995), Jolley et al. (2004), McCarthy (2006), Beach and Smith (2007) Fletcher (2009), Viljoen (2009)* and *Dankert and Hein (2010).* The Witwatersrand Basin has been described by *Armstrong et al. (1991)* and *Robb and Meyer (1995)* as having been formed during collision of the Archaean Kaapvaal Craton with the Zimbabwe craton between 3.07 and 2.71 Ga. The collision reactivated old fault planes of pre 3.07 Ga basement rocks *(Myers et al. 1989; Stanistreet and McCarthy, 1991)* and resulted in the basin occupying a central position on top of the Archaean granite-greenstone

basement *(Frimmel et al. 2005).* In addition to fault reactivation, new faults, bedding-parallel shear zones and overturning were generated from deformation experienced by the Witwatersrand Basin *(Phillips and Powell, 2012)*. Several stages of basin development can be distinguished in the Witwatersrand Basin based on the various lithostratigraphic units present *(Frimmel and Gartz, 1997).* The first stage involved crustal extension accompanied by deposition of bimodal volcanics and sediments of the 2.25 km thick Dominion Group (3.09-3.07 Ma; *Armstrong et al. 1991; Frimmel and Gartz, 1997; Dankert and Hein, 2010).* The second stage of basin formation is reflected by epicontinental-style sedimentation of the West Rand Group *(Moon and Whateley, 1989)* whereas the third stage involved compression and uplift of the hinterland, which led to the deposition of the fluvial sediments of the Central Rand Group (2.89-2.71 Ma; *Hayward et al. 2005*).

The Central Rand and West Rand Groups constitute the Witwatersrand Supergroup and are unconformably overlain by the ultramafic basaltic lavas of the Klipriviersberg Group (Fig. 3), which represent a period of extension and promoted deposition of the Ventersdorp Supergroup *(Frimmel and Gartz, 1997)*. The Ventersdorp Supergroup hosts the Ventersdorp Contact Reef at its base (formerly known as the Ventersdorp Conglomerate Formation), which has contributed significantly to gold production in the Witwatersrand Basin *(Manzi et al. 2012)*. This supergroup is composed of the lower Klipriviersberg, Platberg and upper Pniel Groups *(Van der Westhuizen et al. 1991)*. Precipitation of marine material resulted in the accumulation of the Transvaal Supergroup carbonates (2.6-2.4 Ga old) that unconformably overlie the Ventersdorp Supergroup *(Frimmel and Gartz, 1997)*. The rocks of the Witwatersrand Basin have been regionally metamorphosed to greenschist facies *(Phillips and Powell, 2012)*. This basin wide metamorphism has yielded mineral assemblages that range from pyrophyllite-chloritoid and has resulted in shales and sandstones having more aluminous compositions *(Phillips and Powell, 2012).*

This study focuses on the CLR conglomerate of the Central Rand Group, which hosts some of the most important and richest gold-bearing reefs in the Witwatersrand Basin. The Central Rand Group is interpreted as having been deposited in a braided river system which combined to form alluvial fans *(Wronkiewics and Condie, 1987)*. The CLR conglomerate is a pebble conglomerate unit underlain by a thin carbon seam, known as the Carbon Leader *(Engelbrecht et al. 1986; Grové and Harris, 2010)*.

The thickness of the Carbon Leader can range from a mere streak up to ~ 3 cm thick. Along the WWL, the CLR is characterized by three conglomerate facies each representing a different phase of sedimentation *(Fletcher, 2009).* Facies 3 is the oldest conglomerate package and attains an average thickness of 23.1 cm. It is characterized by a single conglomerate band consisting of smoky quartz and black chert pebbles. Facies 2 is located above facies 3 and is the second oldest conglomerate package. It consists of three conglomerate bands divided on the basis of pebble type, content, colour and sedimentary structures. The combined average thickness of this unit it 188.9 cm. Facies 1, the youngest of the three conglomerates facies, is located above facies 2 and ranges between 7 cm and 26.3 cm in thickness. Along the WWL this unit can be further subdivided into 3 facies based on pebble type, content, mineral alteration and presence of sulphides *(Fletcher, 2009).* In this study the various CLR conglomerate facies will be considered as one sedimentary package.

Gold mineralization occurs in the conglomerate bands or in the fibrous or columnar structures that occur in the carbon seam. The H/W to the CLR conglomerate consists of two quartzite units and a prominent shale horizon. The immediate H/W is defined by a ~ 3.5 m thick light to dark grey siliceous quartzite, known as the Rice Pebble Quartzite *(McCarthy, 2006; Fetcher, 2009).* Overlying the Rice Pebble Quartzite is the Green Bar shale, which covers ~ 85 % of the WWL *(Fletcher, 2009).* The Green Bar shale is overlain by the Main Quartzite which consists of a light bluish green to grey siliceous quartzite. The CLR conglomerate unconformably overlies the Blyvooruitzicht Formation, which is the lowest formation in the Central Rand Group, and consists of a semi-siliceous to siliceous quartzite with sporadic conglomerate bands at its base *(McCarthy, 2006).* The uppermost unit of the West Rand Group is known as the Maraisburg Quartzite and represents progradation of a fluvial braid-plain signalling the onset of the Central Rand Group Sedimentation. The feldspathic quartzites at the TWR are underlain by iron-rich shale, known as the Roodepoort shale (RS). The footwall (F/W) of the RS consists of a thin shaly quartzite unit that separates the Roodepoort shales from a series of basaltic andesite flows referred to as the Crown Lavas *(McCarthy, 2006; Fetcher, 2009).*

3D SEISMIC CUBE

The 3D seismic data covering our study areas in the West Wits Line goldfields were acquired in 1995 *(Gibson et al. 2000)*. The detailed information regarding the data acquisition, processing and

interpretation is reported by *Manzi et al. (2012)*. The primary goal of the seismic survey was to image the VCR ore body and geological features that offset it. The VCR consists of conglomerates with varying clast sizes in a quartzite matrix. The ore body rarely exceeds ~ 1.5 m in thickness and is too thin to be directly detected by surface reflection seismics. The Ventersdorp lavas have higher density and seismic velocity; therefore, it is the Ventersdorp-Quartzite contact that gives rise to a strong seismic reflection observed in the 3D seismic volume (Fig. 4). A secondary goal was to image the CLR ore body which lies at depths between 2.5 km-4.0 km, making it the world's deepest ore body. Unfortunately, the CLR ore body does not appear as a strong seismic reflector within the 3D seismic volume, probably because it is too thin (~ 1.5 m) and occurs at the contact between quartzitic units with similar mineralogy *(Manzi et al. 2015)*. The seismic survey also mapped a large variety of reflectors, including the RS and the TWR at depths of ~ 5 km and ~ 6 km, respectively. The boreholes chosen for this study are located within the 3D seismic volume, cutting through the CLR ore body through the RS to the TWR (Fig. 4).

ROCK SAMPLES AND METHODS

Over 50 drill core samples (obtained from diamond drilling) from boreholes (BH-A, BH-B, BH-C, BH-E, BH-F, BH-G, BH-H and BH-I; *see* Fig. 2) that intersect the CLR conglomerate and its associated hangingwall and footwall units of the Central Rand Group were investigated. These boreholes were chosen because of their better positioning within the 3D seismic volume (*see* Fig. 4). Samples consisting of both full core (ø= 32 mm) and half core (ø= 16 mm) segments ranged from 60 mm to 80 mm in length. The core segments were collected from five rock units representing the main lithologies covering a depth range from 2.7 km to 4.0 km (Fig. 5). These litho-types consist of the CLR conglomerate, the Rice Pebble Quartzite, the Green Bar shale and the Main Quartzite units which make up the H/W, and the Blyvooruitzicht footwall quartzite. In addition, borehole BH-D that intersects the TWR stratigraphy (Maraisburg Quartzite, Roodepoort shales and Lower Roodepoort Quartzite units; *see* Fig. 2) was also investigated. In most cases, samples used for the analyses of seismic velocities, mineralogy and chemical composition were taken from the same drill core interval. In some cases, samples used for modal mineralogy and geochemistry were taken from parts adjacent to the core considered close enough to have the same compositions as the samples used for seismic velocity measurements.

A total of 9 borehole cores were logged to (1) identify rock units that constitute the H/W and F/W of the CLR conglomerate and RS, and (2) identify changes in colour, zones of alteration and mineralization, change in textures, mineralogy and presence of macro-fractures. In order to supplement core-logging results, the characterization of each rock unit was achieved by using thin section and polished block microscopy. The advantage of polished thin sections compared to unpolished thin sections is that they enable detailed analysis of mineralization in reflected light. The polished blocks were created from highly mineralized units (e.g. Rice Pebble Quartzite and CLR conglomerate) to identify the types and forms of mineralization and their relationship to mineralogy.

Basic physical properties, such as bulk density (ρ) and seismic velocities were measured for all the samples. Measurements of the density were carried out using a Sartorius digital analytical balance (model E5500S, 5500 g maximum) with a 10-mg resolution. The density of each sample was determined using Archimedes' principle which is based on weighting water saturated and dry samples in air and in water *(Rybach and Buntebarth, 1981)*.

The ultrasonic velocities (P- and S-wave) were measured on more than 50 dry cylindrical samples using an ultrasonic pulse transmission technique *(Kern, 1982, Kern, 2011; Elbra et al. 2011; Malehmir et al. 2013; Manzi et al. 2015)* with transducers operating at 0.5 MHz. The experimental procedure of the ultrasonic velocities is summarized in Figure 6. Each sample was cut flat and greased on both ends before being placed between the two transducers to improve the energy transmission between the transmitter and receiver (Fig 6a). Summarily, an electrical pulse is converted into a stress pulse that travels through the cylindrical sample and is converted to an electrical signal and displayed on an oscilloscope (Tektronix TDS 2012C two-way channel digital storage oscilloscope; Fig. 6b). A smaller set of transducers (Fig. 6b) was used to measure the ultrasonic velocities of few poorly developed CLR conglomerate samples with inadequate length and shape, and half core samples. The P- and S-wave arrival times were picked up on the oscilloscope, along with the sample lengths, were used to calculate the P- and S-wave velocities.

To better investigate the dependence of seismic velocities on stress, the P-wave velocities were

measured for the samples using the ultrasonic device and a uniaxial stress system at ambient and elevated stresses of 65 MPa (equivalent to a maximum depth of ~ 3.9 km). A maximum compressive stress of 65 MPa was applied to rock segments so as not to reach the yield strength of each cylindrical piece while attempting to close majority of the micro-defects in each sample. Each cylindrical core sample was placed between a transmitter and receiver and positioned on pistons in a stainless steel cylindrical chamber (Fig. 6c and d). The uniaxial compressional loading is produced by hydraulic pistons that are driven by a computer controlled load holding pump. The induced load is monitored on a stress measuring gauge (Fig. 6c). It was not possible to measure all the samples at elevated stresses as some lacked the correct size and geometry required for equal stress distribution. The transducer and receiver piezoelectric sensors used in this study to measure velocities were chosen based on their desirable shape and size that enabled easy placement of full drill core samples between them. As a result of the sensitivity of the transducers to noise, velocity measurements were conducted at times where there was the least amount of movement near the laboratory, and the measurements were repeated at least 3 times for every sample. It was paramount for this study to cut samples flat on either end so that the sample sits flat on the transducers. This also prevented premature fracturing of samples at elevated stress conditions due to unequal stress distribution.

RESULTS

This section presents results from the physical property measurements (bulk density and seismic velocities), modal mineralogy and geochemistry analyses of meta-quartzites and shales that make up the hangingwall and footwall of the CLR conglomerate. Although seismic velocities of various units from the Witwatersrand Basin are known *(see Malehmir et al. 2014)*, this is the first study, to our knowledge, to incorporate seismic velocities, densities, mineralogy and geochemistry in the goldfields. Previous studies have highlighted common relationships observed between seismic velocities, physical properties and the influence of mineralogy *(Rybach and Buntebarth, 1981, 1984; Christensen and Mooney, 1995; Kern et al. 2009; Carlson and Miller, 2004; Chang et al. 2006; Malehmir et al. 2011; Nováková et al. 2012; Barrett and Froggatt, 2012; Malehmir et al. 2013; Manzi et al. 2015).* The mineral constituents of the CLR conglomerate and its associated units were determined from physical observation of minerals from drill core samples, polished thin sections and polished blocks. X-ray fluorescence (XRF) was carried out on 21 samples (from boreholes that

intersect the CLR conglomerate) in order to supplement the petrography results. Seismic wave velocities for each rock sample were compared based on their response to density, mineral and chemical composition of each sample.

Mineralogy

Table 1 provides a summary of the main mineralogy and geochemistry of the rock samples. The CLR conglomerate, one of the most economically important auriferous horizons along the WWL, attains various thicknesses throughout the 8 boreholes investigated in this study. Its thickness can range from 5-10 cm where it occurs as a single band or can be up to ~ 1.5 m where it occurs as a package of alternating conglomerate units. This conglomerate unit consists of closely packed white/smoky quartz and dark grey chert pebbles, adhered by a dark grey to black fine-grained silica-rich matrix. Mineralization in the CLR conglomerate occurs largely in stringers of pyrite and to a lesser degree as disseminated to slightly massive primary and secondary pyrite around pebbles. Overlying the CLR conglomerate is the Rice Pebble Quartzite. It is characterized by medium to coarse grit consisting of white/smoky quartz and dark grey chert. Its matrix can range from dark grey to light bluish grey argillaceous quartzite. Pyrite mineralization in the Rice Pebble Quartzite is characterized by disseminated euhedral crystals and anhedral nodules. A sharp contact separates the Rice Pebble Quartzite from the overlying ~ 2 m thick chloritoid-rich siltstone, known as the Green Bar shale. This shale layer is one of the most consistent markers in the Central Rand Group. Minor disseminated pyrite mineralization occurs in the Green Bar shale. The Main Quartzite forms the immediate H/W of the underlying Green Bar shale. It consists of coarse to medium-grained light blue-grey quartzite, which grades into a grittier quartzite with ~ 4 mm sized chert and quartz pebbles. Pyrite mineralization is concentrated in dark grey-black scattered stringers. The CLR conglomerate F/W is composed of a relatively mono-mineralic medium-grained argillaceous quartzite unit. This unit is known as the Blyvooruitzicht Quartzite. None to very minor mineralization is observed in this unit.

In thin section, the Main Quartzite sample (Fig. 7a) is dominated by fractured quartz grains, tabular chlorite and chloritoid crystals and a sericite matrix. The inequigranular quartz crystals have rugged edges and show undulatory extinction. Figure 7b shows the sample in reflected light. We observe mainly anhedral pyrite grains which occur as disseminated aggregates between grain boundaries

and fractures. The Green Bar shale appears very fine-grained in cross polarized light (Fig. 7c). The shale sample is largely characterized by randomly orientated chlorite and chloritoid crystals ranging from ~ 0.5-1 µm in size. Sericite crystals form the groundmass and generally have low birefringence compared to surrounding minerals. The larger mica crystals have high order colours (e.g. pink, blue and orange). This unit is characterized by significant layering (Fig. 7d). These layers range from planar to radical and are filled with quartz and muscovite crystals. Tiny pyrite crystals, ranging from ~ 0.3-0.5 µm in size, occur as disseminated aggregates that are concentrated in the quartz and muscovite lenses (Fig. 7c and d). Pyrite crystals may be euhedral or anhedral, although some crystals exhibit both primary and secondary mineralization features with both straight and irregular edges. Some of the pyrite also occurs in fractures with chlorite crystals.

The lower Rice Pebble Quartzite (Fig. 8a and b) is largely made up of quartz (~ 90-97 %), chloritoid (~ 5-7 %) and to a lesser amount sericite (<3 %). The polycrystalline quartz crystals exhibit strained textures and undulating extinction. Quartz subgrains are observed between larger crystals as evidence of subgrain rotation and recrystallization during deformation. Unlike the Main Quartzite and Green Bar shale which have low pyrite content, the pyrite mineralization in the Rice Pebble Quartzite ranges from moderate to high (Fig. 8b). The pyrite mineralization occurs in fractures and between quartz grain boundaries (Fig. 8b) as euhedral or anhedral crystals. The CLR conglomerate consists of interlocking quartz and chert grains with strained texture (Fig. 8c) set in a sericite matrix. Disseminated euhedral and anhedral pyrite crystals occur between fractures and grain boundaries, along with minor magnetite (Fig. 8d). The underlying Blyvooruitzicht Quartzite (Fig. 9a) is defined by coarse to medium-grained quartz crystals (~ 77-89 %), sericite groundmass (~ 8-20 %) and minor randomly scattered chloritoid crystals (~ 3-7 %). A slight increase in sericite is observed in this rock unit compared to the Main Quartzite and Rice Pebble Quartzite. The quartz crystals in the Blyvooruitzicht Quartzite are significantly fractured compare to the other H/W quartzites. Minimal sulphide mineralization (<5 grains per sample) is observed in the Blyvooruitzicht Quartzite in borehole BH-A (Fig. 9b), BH-E, BH-F, BH-H and BH-I, and none is observed in borehole BH-B, BH-C, BH-D and BH-G. The similar mineralogy amongst the quartzite units may cause them to have similar physical properties; however, varying pyrite content may have a stronger effect on physical property variations.

Seismic velocity - mineralogy dependence

The propagation of the seismic waves through the rock is dependent on many factors, including mineral constituents, grain shape, grain size and porosity. Table 2 summarizes the P- wave velocity, average bulk density, impedance contrast and reflection coefficient results for full- and half-core segments from the 9 boreholes obtained from our analyses. The results of the P- and S-wave velocities and bulk densities measured at ambient stresses from 4 boreholes (BH-A, BH-B, BH-C and BH-D) are shown in Figure 10. Figure 10a-c represents boreholes that intersect the CLR conglomerate and the associated H/W and F/W units, whereas Figure 10d represents borehole BH-D which intersects the Roodepoort shale horizon and its associated Maraisburg Quartzite (H/W) and Lower Roodepoort Quartzite (F/W) units. The velocity and bulk density measurements were conducted for all samples from all the boreholes, but only boreholes that contain the entire lithological succession are presented graphically (borehole BH-E to BH-I are not presented graphically). Borehole BH-D, for example, is the only borehole that intersects the top of the West Rand Group at ~ 5-6 km. This borehole provides an opportunity to investigate the role that the deeply-buried rocks play on the physical properties. Although the results for S-wave velocity measurements are provided, these are not discussed due to problems in picking their first time arrival. Figure 9c shows the P- and S-wave first arrivals resulting from the Blyvooruitzicht Quartzite sample in Figure 9a and b. As observed from the waveform in Figure 9c, it was difficult to accurately identify the arrival time of the S-wave due to the complexity of the wave.

Our mean bulk density measurements across all the boreholes range from 2.66 g/cm^3 to 3.15 g/cm^3 and mean P-wave velocity values range from 4777 m/s to 5914 m/s. The Green Bar shale horizon exhibits the highest bulk density values in the range of 2.89 g/cm^3 to 3.15 g/cm^3. This fine-grained, chloritoid-rich shale unit lies to the far right of the velocity-density curve (Fig. 10a-c) owing to the differences in texture, mineral assemblage (clays, chlorite, chloritoid, and pyrite) and chemical composition from the quartzite units (*see* Figure 6-8). In addition to its high bulk density values, the Green Bar shale exhibits higher P-wave velocity values (5124 m/s-5914 m/s) than the Main Quartzite (4970 m/s-5443 m/s), Rice Pebble Quartzite (5028 m/s-5480 m/s) and the Blyvooruitzicht unit (4777 m/s-5211 m/s). The high P-wave velocity values of the Green Bar shale correspond to the low SiO_2

(42.39 wt. %-62.78 wt. %) and higher FeO^T (8.78 wt. %-13.01 wt. %) contents as seen in Figure 11a and b. The low silica content is in agreement with the minimal quartz and chert crystals observed in the Green Bar shale and the high iron may be due to the presence of chlorite, chloritoid and clay minerals (*see* Fig. 7c).

Unsurprisingly, the bulk densities obtained from the core samples representing the quartzite units (Main Quartzite, Rice Pebble Quartzite and Blyvooruitzicht) show little variation and lie to the left of the velocity-density curves (Fig. 10a-c) due to their similar mineral compositions; those consist mainly of quartz and chert which are slow and dense minerals. For example, in borehole BH-B, core samples from the Main Quartzite (Vp ~ 5423 m/s and ρ ~ 2.69 g/cm^3), Rice Pebble Quartzite (Vp ~ 5307 m/s and ρ ~ 2.68 g/cm^3) and Blyvooruitzicht Quartzite (Vp ~ 5108 m/s and ρ ~ 2.66 g/cm^3) show only slight changes in seismic velocity and bulk density values. Interestingly, the Rice Pebble Quartzite has lower P-wave velocity and slightly lower density when compared to the overlying Main Quartzite, owing to the presence of chert grit in the Rice Pebble Quartzite which slows down seismic waves. However, the Main Quartzite and the Rice Pebble Quartzite have relatively higher seismic velocity and bulk density values than the Blyvooruitzicht Quartzite. The slightly higher P-wave velocity of the Rice Pebble Quartzite may be due to the lower silica (average ~ 89.15 wt. %) and higher FeO^T (~ 4.32 wt. %) content when compared to the Blyvooruitzicht Quartzite unit (SiO_2 ~ 90.97 wt. % and FeO^T ~ 1.19 wt. %) (Fig. 11a and b). Furthermore, the distinct clustering of rock samples into distinct fields (Fig. 11) based on mineral content is a clear indication that mineralogy, which is a function of chemical composition and metamorphic grade, has a major effect on seismic wave propagations.

The CLR conglomerate in borehole BH-A, BH-B and BH-C exhibits slightly higher bulk density values than its hangingwall and footwall quartzites (Table 2). For example, the CLR conglomerate sample in borehole BH-B has a density of 2.83 g/cm^3, while the Main Quartzite, Rice Pebble Quartzite and the Blyvooruitzicht Quartzite have densities of 2.69 g/cm^3, 2.68 g/cm^3 and 2.66 g/cm^3, respectively. The slightly higher density of the CLR conglomerate may be due to a higher concentration of pyrite (*see* Fig. 8b). Similar trends of increasing seismic velocity with bulk density are observed in borehole BH-A and BH-B, which show a clear dependence of seismic velocities on density. Amongst the quartzitic units, the CLR conglomerate has the highest velocity values (5070 m/s and 5468 m/s) when

compared to the Main Quartzite (5423 m/s), Rice Pebble Quartzite (5028 m/s and 5307 m/s) and the Blyvooruitzicht Quartzite (4916 m/s and 5108 m/s).

To better understand the nature of the seismic reflectivity of the main geological boundaries, reflection coefficients were calculated at the Rice Pebble Quartzite-CLR conglomerate interface and the CLR conglomerate-Blyvooruitzicht Quartzite interface. Furthermore, reflection coefficients were calculated at the Main Quartzite-Green Bar shale interface and the Green Bar shale-Rice Pebble Quartzite interface to determine whether strong seismic reflections can be produced at these interfaces. The rock samples used for these calculations were obtained as close as possible to the contacts of the adjacent rock units. According to *Salisbury and Snyder (2007)* reflection coefficients of RC ±0.06 are required to cause the strong seismic reflections. The reflection coefficient values of RC ~ 0.02 at CLR conglomerate-Rice Pebble Quartzite interface suggest that reflection seismics would not be successful in mapping the CLR conglomerate as a strong seismic reflector. Similar conclusions can be drawn for the interface between CLR conglomerate and Blyvooruitzicht Quartzite, which exhibits a RC of ~± 0.01-0.05 (Table 2). In contrast, reflection coefficient values (RC ~ 0.06-0.14) obtained at the Main Quartzite-Green Bar shale and Green Bar shale-Rice Pebble Quartzite interface (RC ~ 0.06-0.11) suggest that it might possible to map the Green Bar shale as a strong reflector using seismic reflection methods. Similarly, the interface between Maraisburg Quartzite and Roodepoort shale (RC=±0.07) as well as between the Roodepoort shale and Lower Roodepoort Quartzite (RC=±0.06) may produce strong reflections.

Seismic velocity - stress dependence

The variation of physical properties of rocks under the influence of stress is of fundamental importance for the interpretation of seismic data, particularly at great depths. Several qualitative ideas exist describing the stress dependence of seismic velocity, e.g., such that pore volume reduces with increasing stress, thus increasing velocity can be measured on the rock sample *(Birch, 1961). Walsh and Brace (1964)* explain the stress dependence of this phenomenon by the closure of macro- and micro-cracks.

To test the dependence of seismic velocities on stress, the P-wave velocities were measured for the

samples using the ultrasonic device and a uniaxial stress system at ambient and elevated stresses of 65 MPa (equivalent to a maximum depth of ~ 3.9 km). A maximum compressive stress of 65 MPa was applied to rock segments so as not to reach the yield strength of each cylindrical piece while attempting to close majority of the micro-defects in each sample. Figures 12a and b show the dependence of P-wave velocities on bulk density and mineralogy at ambient and elevated stresses. At elevated stresses, we can see that all the samples have a higher velocity than at ambient stresses. We also note two distinct clusters in both graphs where the quartzite samples (quartz saturated) and shale samples (quartz depleted) cluster separately. These results support the dependence of seismic waves on mineral composition. Figures 12c and d show results of P-wave velocities as a function of uniaxial compressive stress for boreholes BH-A (the borehole intersects the CLR conglomerate and its H/W and F/W) and BH-D (the borehole intersects the Roodepoort shale and its H/W and F/W). When the seismic velocity behaviour is compared amongst the rocks in borehole BH-A (Fig. 12c) at ambient and elevated stresses, a consistent initial increase in P-wave velocity is observed. This behaviour is evident at stresses between 0 MPa to ~ 20 to 25 MPa. This gradual increase in velocity with increasing stress may be due to the closure of micro-defects (pore spaces) during loading *(Birch, 1961; Walsh and Brace, 1964)*. However, beyond stresses of ~ 25 MPa the P-wave velocities become constant. As the load is applied and the stress is increased, the micro-defects are closed (porosity reduced) until the velocity is independent of the applied stress *(Christensen, 1965)*.

The fine-grained Green Bar shale exhibits a smaller variation in velocity (~ 246 m/s) compared to the medium to coarse-grained quartzite units (Rice Pebble Quartzite ~ 426 m/s and Blyvooruitzicht ~ 538 m/s) and the CLR conglomerate (~ 385 m/s). This may be due to the absence of significant micro-cracks and fractures in fine-grained rocks as a result of increased grain-to-grain contact compared to coarser rocks *(Schön, 2004)*. Figure 12d shows a velocity-stress relationship between the TWR rock units. A slight initial increase in velocity at low stresses (0-20 MPa) is shown for the Roodepoort Quartzite and Maraisburg Quartzite with P-wave velocity increasing from 5373 m/s-5628 m/s and 4922 m/s-5075 m/s, respectively. The Lower Roodepoort Quartzite exhibits a slightly higher increase in velocity from 4977 m/s at ambient stresses to 5474 m/s at 30 MPa. The velocity becomes independent of the applied stress at a higher stress (~ 30 MPa-65 MPa).

DISCUSSION

In this paper, we have investigated the dependence of seismic velocities on mineralogy, chemical composition and applied stress on CLR conglomerate and TWR borehole intersections. Investigations of the mineral constituents of each rock unit were made from the physical observation of drill-core samples as well as thin section and polished block microscopy. The CLR stratigraphy is largely dominated by quartzite units that range from fairly mono-mineralic (Main Quartzite and Blyvooruitzicht Quartzite) to highly altered (Rice Pebble Quartzite), and consists of a chloritoid-rich shale unit in the hangingwall. Pyrite mineralization is prominent in the hangingwall units where it can be disseminated or massive closer to the reef and strictly disseminated further up stratigraphy.

Seismic velocity – mineralogy

The quartzite units display no distinct differences in mineralogy and chemical composition throughout the CLR borehole intersections. This is supported by the ultrasonic P-wave velocity data, which indicate minor velocity variations amongst the quartzite units within each borehole under laboratory conditions (ambient stress conditions). These slight variations are mainly due to mineralogical similarities such as quartz, chert, chlorite, chloritoid, a sericite groundmass and sulphides. On average, the P-wave velocities in the quartzite samples (including the CLR conglomerate samples) range between 4552 m/s and 5480 m/s at ambient stress conditions. The data reveal that the average velocity (from borehole BH-A to C) in the CLR is ~ 5209 m/s while the Rice Pebble Quartzite, Main Quartzite and Blyvooruitzicht Quartzite exhibit lower velocities (5199 m/s and 5202 m/s and 5036 m/s, respectively). The P-wave velocity values concur with measurements conducted by *Weder 1994* on the quartzite samples from the Central Rand Group. Our results reveal that samples dominated by quartz and chert, which are represented by quartzites and conglomerates in this study, are associated with low seismic velocities compared to samples that are deficient in quartz and chert. Amongst these quartzite samples the Blyvooruitzicht Quartzite exhibits the highest quartz and chert content hence, its lower velocity compared to the hangingwall quartzites. According to *Kern et al. (2009)* and *Schön (1996)* rocks dominated by quartz and chert exhibit low seismic velocities because these minerals are slow and dense. The effects of quartz and chert on seismic velocities are further supported by high silica content as observed from XRF results. It can be noted that the higher the silica content in the quartzite sample the lower its seismic velocity (Fig. 12a). Although there are no distinct differences observed between the cores from the various mines we do observe that there are differences in

texture and pyrite content within the individual boreholes. In most cases, the quartzite samples located furthest away from the CLR (Blyvooruitzicht Quartzite and Main Quartzite) show coarser grain size and are slightly altered, while the Rice Pebble Quartzite samples (immediate H/W to the CLR) show a slightly finer grain size (although they contain some quartz and chert grit) and are more altered. Thus, the P-wave velocities tend to increase as the rock becomes finer in grain size and increases in metamorphic grade.

Contrary to the low seismic velocities of the quartzite units, the finer grained chloritoid-rich Green Bar shale exhibits higher average velocity (5685 m/s) compared to all its adjacent hangingwall and footwall quartzite units. This is probably due to its fine grained texture, high iron and low silica values. Studies by *Kern et al. (2009)* confirm that rocks with high iron content have high seismic velocities. High seismic velocities associated with high iron content in rocks have also been investigated by *Krapež (1985)*.

This study also shows that seismic velocities in our rock samples are sensitive to variations in mineralogy, grain size and presence of fractures, preferred mineral alignment and density as well as by the applied stress. These observations concur with studies done by *Kern et al. (2001, 2009) Kuusisto et al. (2006) and Elbra et al. (2011)*. The CLR conglomerate samples consisted of quartz and chert pebbles and the Rice Pebble Quartzite samples were characterized by quartz and chert grit, which provided slight variations in the measured seismic velocities. Therefore, as proposed by *Kern et al. (2011)*, the P-wave velocities of the samples were measured more than three times to ensure accuracy.

As mentioned earlier, the pyrite content of the CLR is relatively higher than that of its H/W and F/W quartzite units. In general, the bulk density as a function of velocity shows that P-wave velocities tend to increase with the increase in bulk densities, probably owing to the presence of high pyrite content in most samples. This concurs with studies of massive sulphide ores conducted by *Salisbury et al. (2003)*, which suggest that some sulphide ores are characterized by high bulk densities and seismic velocities. *Salisbury et al. (2003)* further noted that the velocity-density field may be affected by the end-member properties of sulphides such as pyrite, pyrrhotite and chalcopyrite (*Milkereit et al. 1996;*

Salisbury and Snyder 2007). Our general observation of increasing P-wave velocity with bulk density also follows Birch's Law or the Nafe-Drake trend (*Birch 1961; Nafe and Drake 1963*).

It is possible that the variations in seismic velocities in our measurements were partially controlled by anisotropy, since the measured velocities were along the z direction. This is common in seismic velocity studies in the hard rock environments (e.g., Milkereit et al. 1996; Salisbury and Snyder, 2007). It was not possible to study anisotropy in our samples due to inadequate sizes of the samples and sensors.

To lithologically and seismically explain the nature of seismic reflectors observed in the 3D seismic data (*see* Fig. 4), we have calculated the reflection coefficients of various pairs of lithological units down the boreholes using the velocities measured under laboratory conditions as described above. *Salisbury et al. (2003)* and *Salisbury and Snyder (2007)* show that for an interface to be detected as a strong seismic reflector it should reflect a minimum of 6% of its incident energy. Therefore, reflection coefficients of Rc > ±0.06 are required to cause the strong seismic reflections. The reflection coefficients (Table 2) computed in the current study indicate that the contact between the CLR-Rice Pebble Quartzite interface (Rc ~ 0.02 at depth ~3901 m) and the CLR-Blyvooruitzicht Quartzite (Rc ~ 0.05 at depth ~3903 m) cannot produce strong seismic reflections, particularly at depths between 2 km and 3.9 km, as observed in the seismic data. These results also indicate that low reflection coefficients, observed throughout the boreholes, at the contact between Rice Pebble Quartzite-CLR and the CLR-Blyvooruitzicht Quartzite could be the main reason for the poor seismic reflectivity of the CLR conglomerate. These results are not surprising since the Rice Pebble Quartzite, CLR and Blyvooruitzicht Quartzite units share mineralogical similarities. The reflection coefficients at the contact between H/W Main Quartzite and the Green Bar shale (Rc ~ 0.06-0.14 at depth ~3897 m), Green Bar shale and F/W Rice Pebble Quartzite (Rc ~ 0.06-0.11 at depth ~3899 m) suggest that the top or bottom of the Green Bar shale unit can be detected using reflection seismics, provided it has the appropriate thickness and geometry. The reflection coefficients obtained at the Maraisburg Quartzite-Roodepoort shale interface (Rc ~ 0.07) suggest that these contacts can produce strong

seismic reflections. This is further confirmed by strong seismic reflections associated with the top of the RS on the 3D seismic data (see Fig. 4).

Seismic velocity - applied stress

To investigate the effects of micro-fracturing and applied stress, P-wave velocities for samples were measured at elevated stresses from 0 MPa to 65 MPa (corresponding to depths of ~2-3.9 km). Generally, we observe that the seismic velocity as a function of differential stress shows a nonlinear-type behaviour, at least over a limited stress interval. For example, seismic velocities for all the rock samples increase with increasing applied stresses. In general, the highest stress effect is found for coarse-grained rocks (quartzites and conglomerate), and the lowest for fine-grained rocks (shale). At higher stress regimes (~20-65 MPa), the velocity increase is smaller than in the lower stress regime (0-20 MPa). Both boreholes (BH-A and BH-D) confirm the distinct increase in P-wave velocity with increasing stress, particularly in the lower stress regime. In the stress range of 0 MPa-20 MPa, the velocity gradients of the various rock types differ. For example, the Green Bar shale has a smaller velocity gradient compared to the quartzitic units, owing to variations in mineralogy, grain size, and its low permeability.

The velocity variations observed between the quartzitic samples might be a result of the degree of alteration within the units. For example, the F/W Blyvooruitzicht is the least altered unit and has the highest variation of velocity with applied stress from 0 MPa to 65 MPa. This is followed by the Rice Pebble Quartzite which is characterized by a black to dark grey quartzitic matrix with chert and quartz grit. The CLR conglomerate is the most altered quartzite unit and has the smallest velocity variation than the immediate H/W and F/W quartzites. From the data it can be observed that rocks that have been metamorphosed to a higher degree will show less velocity variations at higher stresses than less metamorphosed rocks. Although the quartzite and conglomerate samples do not show visible fracturing, it is possible that the samples contain micro-fractures that are not visible. Therefore, future studies should be aimed at studying the importance of micro-cracks and their preferential orientations as well as their relationships to seismic velocities.

The Roodepoort shale sample also exhibits a smaller velocity gradient at lower stress ranges, of 0

MPa-20 MPa, compared to the Lower Roodepoort Quartzite. The increase of P-wave velocity with stress in the lower stress regime is associated with closure of large pores and micro-fractures *(Birch, 1961; Walsh and Brace, 1964)*. The closure of microdefects improves the contact between rock forming minerals *(Schön, 2004)*. At higher stresses above ~20 MPa, the velocity stress relationship becomes linear. The velocity remains constant with applied stress probably due to the compaction of microdefects and mineral aggregates being complete. As the porosities throughout the core were extremely low (<1%), the sharp increase in velocities in the lower stress regimes was probably due to compaction and the closing of macro-and micro-cracks. The micro- and macro cracks in our samples may have been induced by drilling or stress release in rocks during the extraction of the core. The low porosity throughout our samples at different depth interval indicates that the micro fracturing was not drilling induced.

CONCLUSIONS

We have collected and measured P- wave velocities from more than 50 full- and half-core samples from Carbon Leader Reef and Top of the West Rand borehole intersections along the West Wits Line. Our study has integrated the measurement of physical rock properties (bulk density and seismic velocities) with mineralogy and geochemistry to better understand the nature of seismic reflectivity within the 3D seismic cube. Our analyses involved (1) physical and petrographic observation of various rock units to identify textures, mineral assemblages and structures present in the H/W and F/W, (2) conducting X-ray fluorescence to understand the chemical composition of each rock unit, and (3) measurement of physical rock properties such as bulk density and P- and S-wave velocities to study the dependence of seismic velocities to mineralogy and uniaxial stress.

Our data show that seismic velocities are significantly affected by mineral and chemical composition of rocks. Minerals such as quartz and chert are slow and dense; therefore they exhibit low seismic velocities. In contrast, the presence of sulphides (mainly pyrite), results in faster seismic velocities. It is then no surprise that quartz-rich rocks such as CLR conglomerate, Main Quartzite, Rice Pebble Quartzite, Blyvooruitzicht Quartzite, Maraisburg Quartzite and Lower Roodepoort Quartzite have lower velocities compared to iron-rich rocks such as the Green Bar and Roodepoort shales. From the density measurements, it was observed that the shale samples have higher bulk density values than

quartzite samples. Minor density variations are observed between the quartzite samples, possibly due to their mineralogical similarities. Generally, the measured velocities for most of our samples show a positive correlation with bulk density.

The significant effect of velocity on grain sizes and micro-fractures was evident in the velocity vs. stress measurements. An initial increase in velocity with applied uniaxial stress can be associated with closure of microdefects at lower stress regimes. According to these results, P-wave velocities sharply increase with uniaxial stress, especially within the first ~20 MPa, with only a slight linear increase in velocity at higher stresses (>20 MPa). P-wave velocities show that the pressurized quartzite samples have relatively larger velocity gradients and are more sensitive to elevated stresses than the fine-grained shale samples. The measurement of seismic velocity response to elevated stresses enables us to simulate the prevailing stress conditions at relevant mining levels.

This study has provided evidence that the poor seismic reflection nature of the CLR conglomerate is due to combination of its size, depth and the low reflection coefficient between its H/W and F/W quartzite units. This study improves our understanding of the physical properties of the CLR conglomerate and the Top of the West Rand Group stratigraphy, which is important for constraining the acquiring, processing and interpretation of future reflection seismic surveys in the Witwatersrand Basin.

ACKNOWLEDGEMENTS

This research was sponsored by Thuthuka Funding (NRF), CIMERA (Centre of Excellence for Integrated Mineral and Energy Resource Analysis), CGG, Shell South Africa, Anglo Gold Ashanti Ltd and Sibanye Gold Ltd. We would like to thank Halil Yilmaz, Edward Thomas, Rob Burnett, Simone Hartmann and Felicia Shumba for the major role they played in locating and providing borehole core used in this project. Various laboratory help provided by Andrew Carpede and Musa Cebekhulu from the Rock Mechanics Laboratory at the University of the Witwatersrand is also acknowledged.

REFERENCES

Armstrong R., Compston W., Retief E., Williams I. and Welke H., 1991. Zircon ion microprobe studies bearing on the age and evolution of the Witwatersrand triad. *Precambrian Res.,* **53**, 243-266.

Barrett P.J. and Froggatt C.P., 2012. Densities, porosities, and seismic velocities of some rocks from Victoria Land, Antarctica. *N. Z. J. Geol. Geophys.,* **21** (2), 175-187.

Beach A. and Smith R., 2007. Structural geometry and development of the Witwatersrand Basin, South Africa. In: *Deformation of the Continental Crust: The Legacy of Mike Coward,* Geol. Soc. London Spec. Pub., pp. 533-542.

Best A.I., 1997. The effect of pressure on ultrasonic velocity and attenuation in near-surface sedimentary rocks. *Geophys. Prospect.,* **45**(2), 345-364.

Birch F., 1961. The velocity of compressional waves in rocks to 10 kilobars, Part 1. *J. Geophys. Res.,* **65** (4), 1083-1102.

Buck S.G. and Minter W.E.L., 2014. Placer formation by fluvial degradation of an alluvial fan sequence: the Proterozoic Carbon Leader placer, Witwatersrand Supergroup, South Africa. *J. Geol. Soc.,* **142**, 757-764.

Carlson R. and Miller J., 2004. Influence of pressure and mineralogy on seismic velocities in oceanic gabbros: Implications for the composition and state of the lower crust. *J. Geophys. Res.,* **109**, B09205.

Castagna J., Batzle M. and Eastwood R., 1985. Relationship between compressional - wave and shear - wave velocities in clastic silicate rocks. *Geophys.,* **50**, 571-581.

Chang C., Zoback M. and Khaksar A., 2006. Empirical relations between rock strength and physical properties in sedimentary rocks. *J. Pet. Sci. Eng.,* **51,** 223-237.

Christensen N., 1965. Compressional wave velocities in metamorphic rocks at pressures to 10 kilobars. *J. Geophys. Res.,* **70**, 6147-6162.

Christensen N.I. and Mooney W.D., 1995. Seismic velocity structure and composition of the continental crust: A global view. *J. Geophys. Res.,* **100**, 9761-9788.

Coward M.P., Spencer R.M. and Spencer C.E., 1995. Development of the Witwatersrand Basin, South Africa. *Geol. Soc. London, Spec. Pub.,* **95** (1), 243-269.

Dankert B.T. and Hein K.A., 2010. Evaluating the structural character and tectonic history of the

Witwatersrand Basin. *Precambrian Res.,* **177**, 1-22.

De Kock W. P., 1964. *The geology and economic significance of the West Wits Line*. In: Haughton S.H.,The geology of some ore deposits in southern Africa, Vol. 1, pp. 323- 386, eds. Geol. Soc. S. Afr.

Dobróka M. and Molnár J., 2012. New petrophysical model describing the pressure dependence of seismic velocities. *Acta Geophys.,* **60**, 371-383.

Elbra T., Karlqvist R., Lassila I., Hæggström E. and Pesonen L., 2011. Laboratory measurements of the seismic velocities and other petrophysical properties of the Outokumpa deep drill core samples, eastern Finland. *Geophys. J. Int.,* **184**, 405-415.

Engelbrecht C.J., Baumbach G.W., Matthysen J. and Fletcher P., 1986. *The West Wits Line*, in Mineral deposits of southern Africa, Vol. 1, pp. 599-648, eds. Anhaeusser C.A. & Maske S. Geol. Soc. S. Afr.

Fletcher, P. (2009). Carbon Leader Reef West Wits Line internal report.

Frimmel H.E. and Gartz V.H., 1997. Witwatersrand gold particle chemistry matches model of metamorphosed, hydrothermally altered placer deposits. *Miner. Dep.,* **32,** 523-530.

Frimmel H.E. and Minter W.E.L., 2002. Recent developments concerning the geological history and genesis of the Witwatersrand gold deposits, South Africa. *Soc. Econ. Geol Spec. Pub.,* **9**, 17-45.

Frimmel H.E., Groves D.I., Kirk J., Ruiz J., Chesley J. and Minter, W.E., 2005. The formation and preservation of the Witwatersrand goldfields, the world's largest gold province. *Econ. Geol. 100th Ann.*, 769-717.

Gibson M.A.S., Jolley S.J. and Barnicoat A.C., 2000. Interpretation of the Western Ultra Deep Levels 3D seismic survey. *The Leading Edge,* **19**, 730-735.

Grové D. and Harris C., 2010. O - and H - isotope study of the Carbon Leader Reef at the Tau Tona and Savuka mines (Western Deep Levels), South Africa: Implications for the origin and evolution of Witwatersrand Basin fluids. *S. Afr. J. Geol.,* **113** (1), 1-14.

Guy B.M., Beukes N.J. and Gutzmer J., 2010. Paleoenvironmental controls on the texture and chemical composition of pyrite from non-conglomeritic sedimenatary rocks of the mesoarchaean Witwatersrand Supergroup, South Africa. *S. Afr. J. Geol.,* **113** (2), 195-228.

Hayward C.L., Reimold W.U., Gibson R.L. and Robb L.J., 2005. Gold mineralization within the Witwatersrand basin, South Africa: evidence for a modified placer origin, and the role of the

Vredefort impact event. In: MacDonald I., Boyce A.J., Butler I.B., Herrington R.J. and Polya D.A. (Eds.), *Mineral Deposits and Earth Evolution*. Geological Society of London Special Publication*,* **248**, pp. 31-58.

Jolley S.J., Freeman S.R., Barnicoat A.C., Phillips G.M., Knipe R.J. and Pather A., 2004. Structural controls on Witwatersrand Gold mineralization. *J. Struct. Geol.,* **26**, 1026- 1086.

Kern H., 1982. P- and S-wave velocities in crustal and mantle rocks under the simultaneous action of high confining pressure and high temperature and the effect of the rock microstructure. In: Schreyer W. (Eds.), *High pressure researchers in geosciences*. Schweizerbart, Stuttgart, 15-45.

Kern H., Popp T., Gorbatsevich F., Zharikov A., Lobanov K.V. and Smirnov Yu.P., 2001. Pressure and temperature dependence of VP and VS in rocks from the superdeep well and from surface analogues at Kola and the nature of velocity anisotropy, *Tectonophysics,* **338,** 113–134.

Kern H., Mengel K., Strauss K.W., Ivankina T.I., Nikitin A.N. and Kukkonen I.T., 2009. Elastic wave velocities, chemistry and modal mineralogy of crustal rocks sampled by the Outokumpu scientific drill hole: Evidence from lab measurements and modelling. *Phys. Earth. Planet. Inter.,* **175**, 151-166.

Kern H. 2011. Measuring and modelling of P- and S-wave velocities on crustal rocks: a key for interpretation of seismic reflection and refraction data. *Geophys. J. Int.,* **2011,** 530728. dx.doi.org/10.1155/2011/530728.

Krapež B., 1985. The Ventersdorp Contact placer: a gold-pyrite placer of stream and debris- flow origins from the Archaean Witwatersrand Basin of South Africa. *Sedimentology.,* **32**, 223-234.

Kuusisto M., Kukkonen I.T., Heikkinen P. and Pesonen L.J., 2006. Lithological interpretation of crustal composition in the Fennoscandian Shield with seismic velocity data, *Tectonophysics,* **420,** 283–299.

Malehmir A. and Bellefleur G., 2009. 3D seismic reflection imaging of volcanic-hosted massive sulfide deposits: Insights from reprocessing Halfmile Lake data, New Brunswick, Canada. *Geophysics.,* **74**, B209-B219.

Malehmir A., Dahlin P., Lundberg E., Juhlin C., Sjöström H. and Högdahl K., 2011. Reflection seismic investigations in the Dannemora area, central Sweden: insights into the geometry of

polyphase deformation zones and magnetite-skarn deposits. *J. Geophys. Res.,* **116**, B11307.

Malehmir A., Durrheim R., Bellefleur G., Urosevic M., Juhlin C. and White D., 2012. Seismic methods in mineral exploration and mine planning: a general overview of past and present case histories and a look into the future. *Geophysics.,* **77**, WC173-WC190.

Malehmir A., Andersson M., Lebedev M., Urosevic M. and Mikhaltsevitch V., 2013. Experimental estimation of velocities and anisotropy of a series of Swedish crystalline rocks and ores. *Geophys. Prospect.,* **61**, 153-167.

Malehmir A., Koivisto E., Manzi M., Cheraghi S., Durrheim R. and Bellefleur R., 2014. A review of reflection seismic investigations in three major metallogenic regions: The Kevitsa Ni-Cu-PGE district (Finland), Witwatersrand goldfields (South Africa), and the Bathurst Mining Camp (Canada). *Ore Geol. Rev.,* **56**, 423-441.

Manzi M.S.D., Gibson M.A.S., Hein K.A.A., King N. and Durrheim R.J., 2012. Application of 3D seismic techniques to evaluate ore resources in the West Wits line Goldfield and portions of the West Rand Goldfield, South Africa. *Geophysics.,* **77**, WC163-WC171.

Manzi M.S.D., Hein K.A.A., King N. and Durrheim R.J., 2013. Neoarchaean tectonic history of the Witwatersrand Basin and Ventersdorp Supergroup: New Constraints from high resolution 3D seismic reflection data. *Tectonophysics,* **590**, 94-105.

Manzi M.S.D., Hein K.A.A., Durrheim R.J. and King N. 2014. The Ventersdorp Contact Reef model in the Kloof Gold Mine as derived from 3D seismics, geological mapping and exploration borehole datasets. *Int. J. Rock Mech. Min. Sci.,* **66**, 97-113.

Manzi M., Cooper G., Malehmir A., Durrheim R. and Nkosi Z., 2015. Integrated interpretation of 3D seismic data to enhance the detection of the gold-bearing reef: Mponeng Gold mine, Witwatersrand Basin (South Africa). *Geophys. Prospect.,* **63**, 881-902.

McCarthyT.S., 2006. The Witwatersrand Supergroup. In Johnson M. R., Anhaeusser C. R. and Thomas R.J. *The geology of South Africa*. *Geol. Soc. S. Afr.,* 155-186.

Moon C. J. and Whateley M. K., 1989. Witwatersrand conglomerate gold: West Rand. In Evans A. M. (Eds.), *Introduction to mineral exploration*, Blackwell science. **91**, 258-291.

Milkereit B., Eaton D., Wu J., Perron G., Salisbury M., Berrer E.K. and Morrison G., 1996. Seismic imaging of massive sulphide deposits: Part II. Reflection seismic profiling. *Econ. Geol.,* **91**, 829-834.

Milkereit B., Adam E., Bohlen T., Salisbury M. and Eaton D., 2004. 3D sesmic imaging for massive sulfide exploration. *EAGE 66th Conference and Exhibition, Paris, France, 7-10 June, extended abstract Z-99.*

Myers R.E., McCarthy T.S. and Stanistreet R.E., 1989. A tectono-sedimentaryreconstruction of the development and evolution of the Witwatersrand Basin with particular emphasis on the Central Rand Group. *S. Afr. J. Geol.,* **93**, 211-223.

Nováková L., Sosna K., Brož M., Najser J. and Novák P., 2012. The matrix porosity and related properties of a leucocratic granite from the Krudum Massif, west Bohemia. *Acta geodyn. Geometer.,* **9** (168), 521-540.

Phillips N. and Powell R., 2012. Origin of Witwatersrand gold: a metamorphic devolatilisation-hydrothermal replacement model. *Appl. Earth Sci.,* **120**, 112-129.

Pretorius C.C., Steenkamp W.H. and Smith R.G., 1994. Developments in data acquisition, processing, and interpretation over ten years of vibroseismic surveying in SouthAfrica, in *Proceedings of the 15th CMMI Congress,* J. *S. Afr. Inst. Min. Metall.,* **3**, 249-258.

Pretorius, C.C., Muller, M.R., Larroque, M. and Wilkins, C.A., 2003. Review of 16 years of hardrock seismics on the Kaapvaal Craton. In: Eaton D.W., Milkereit B. and Salisbury M.H. (Eds.), *Hardrock seismic exploration*. *Soc. Explor. Geophys*., **10**, 247-68.

Punturo R., Kern H., Cirrincione R., Mazzoleni P. and Pezzino A., 2005. P- and S wave velocities and densities in silicate and calcite rocks from the Peloritani Mountains, Sicily (Italy): The effect of pressure, temperature and direction of wave propagation. *Tectonophysics,* **409**, 55-72.

Robb L. and Meyer F., 1995. The Witwatersrand Basin, South Africa: Geological framework and mineralization processes. *Ore Geol. Rev.,* **10**, 67-94.

Robb L.J. and Robb V.M., 1998. Gold in the Witwatersrand Basin. In: Wilson M.G.C. and Anhaeusser C.R*. The Mineral Resources of South Africa*. *Geol. S. Afr.,* **16**, 294-349.

Rybach L. and Buntebarth G., 1981. Relationship between the petrophysical properties density, seismic velocity, heat generation and mineralogical constitution. *Earth Planet. Sci. Let.,* **57**, 367-376.

Rybach L. and Buntebarth G., 1984. The variation of heat generation, density and seismic velocity with rock type in the continental lithosphere. In: Cermak V., Rybach L. and Chapman D.S. (Eds.),

Terrestrial heat flow and the structure of the lithosphere. *Tectonophysics.,* **103**, 335-344.

Salisbury M.H., Milkereit B., Ascough G., Adair R., Matthews L. and Schmitt D.R., 2000. Physical properties and seismic imaging of massive sulphides. *Geophysics* **65**, 1882-1889.

Salisbury M. and Snyder D., 2007. Application of seismic methods to mineral exploration. In: Goodwell, W. D. (Eds.), *Mineral deposits of Canada: a synthesis of major deposit types district metallogeny, the evolution of geological provinces and exploration methods*, *Geol. Ass. Can. Min. Dep. Div Spec. Publ.*, **5**, 971-982. Schön J. H., 2004. Physical properties of rocks: fundaments and principles of petrophysics, Handbook of geophysical exploration seismic exploration, **18**, 59-76, 133-233.

Stanistreet I.G. and McCarthy T.S., 1991. Changing tectono-sedimentary scenarios relevant to the development of the Late Archaean Witwatersrand Basin. *J. Afr. Earth Sci.,* **13,** 65-81.

Van der Westhuizen W.A., De Bruiyn H. and Meintjes P.G., 1991. The Ventersdorp Supergroup: an overview. *J. Afr. Earth Sci.,* **3**, 83-105.

Viljoen M., 2009. The life, death and revival of the Central Rand goldfield. *Special Publication for the World Gold Conference*, 131-138.

Walsh J. B. and Brace W., 1964. A fracture criterion for brittle anisotropic rock. *J. Geophys. Res.,* **69** (16), 3449-3456.

Wood G., O'Dowd C., Cosma C. and Enescu N., 2012. An interpretation of surface and borehole seismic surveys for mine planning at the uranium deposit, northern Saskatchewan, Canada. *Geophysics,* **77**, WC203-WC212.

Wronkiewicz D. and Condie K.C., 1987. Geochemistry of Archaean shales from the Witwatersrand Supergroup, South Africa: source-area weathering and provenance. *Geochim. Cosmochim. Acta.,* **51**, 2401-2416.

Wyllie M.R.J., Gregory A.R. and Gardner G.H.F., 1956. An experimental investigation of factors affecting elastic wave velocities in porous media. *Geophysics,* **23** (3), 459-493.

LIST OF TABLES

Table 1 Summary of the main mineralogy and geochemistry of rock samples. SiO_2 and FeO^T are the silica content and total iron, respectively, in each sample. Not determined (Nd.).

BH Name	Rock type	Description	Mineralization	SiO2 (wt. %)	FeO^T (wt. %)
BH A	Green Bar shale	Fine-grained rock dominated by tiny chloritoid crystals.	Tiny disseminated pyrite crystals.	62.11	9.53
	Rice Pebble Qtzt.	Quartz grains set in a sericitic matrix.	Euhedral disseminated pyrite.	90.28	3.50
	CLR	Strained quartz grains in a sericite matrix.	Anhedral pyrite (2-3 µm size) occurs in fractures and grain boundaries.	Nd.	Nd.
	Blyvooruitzicht Qtzt.	Polycrystalline quartz crystals in a sericite matrix. Tabular chloritoid crystal as clusters.	No mineralization observed.	90.42	1.36
BH-C	Green Bar shale	Fine grained with quartz and pyrite laminations.	Pyrite occurs in quartz lenses as tiny disseminated aggregates.	61.52	9.51
	Rice Pebble Qtzt.	Angular quartz crystals in sericite matrix.	Disseminated euhedral and anhedral pyrite (1.0-1.5 µm).	86.67	6.03
	CLR	Sub-rounded to angular polycrystalline quartz in a sericite dominated matrix.	Massive pyrite (1.0-2.0 µm).	Nd.	Nd.
	Blyvooruitzicht Qtzt.	Highly fractured quartz crystal set in a sericite matrix. Tabular chloritoid crystals occur as clusters.	No mineralization observed.	91.87	1.33
BH-E	Main Qtzt.	Fractured quartz grains set in an altered sericite matrix.	Anhedral pyrite occurs in grain boundaries.	90.21	2.81
	Green Bar shale	Fine grained sample with randomly scattered chloritoid. Quartz and muscovite filled lenses.	Tiny disseminated pyrite occurs in the quartz lenses.	62.31	9.36
	Rice Pebble Qtzt.	Strained quartz grains in sericite matrix.	Anhedral disseminated pyrite grains (1.0-1.4 µm).	89.56	3.28
	Blyvooruitzicht Qtzt.	Strained and interlocking quartz crystals.	No mineralization observed.	90.78	2.05
BH-F	Main Qtzt.	Highly fractured quartz crystal set in an altered sericite matrix. Random clusters of chloritoid crystals.	Anhedral pyrite crystals (1.0-1.2 µm) occur in grain boundaries.	89.65	4.79
	Rice Pebble Qtzt.	Angular interlocking quartz crystals.	Anhedral pyrite occurs in grain boundaries and fractures.	90.65	3.55

	Blyvooruitzicht Qtzt.	High degree of fractured quartz and sericitization.	No pyrite mineralization observed.	91.02	0.74
BH-G	Green Bar shale	Fine grained with lenses of quartz and pyrite.	Tiny disseminated pyrite.	42.39	13.01
	Rice Pebble Qtzt.	Angular interlocking quartz crystals.	Anhedral pyrite occurs in grain boundaries and fractures.	90.22	4.29
	Blyvooruitzicht Qtzt.	Highly fractured quartz. Tabular chloritoid crystals	A single fractured pyrite grain.	90.24	0.79
BH-I	Green Bar shale	Fine grained sample with radical quartz and pyrite lenses.	Tiny disseminated quartz crystals.	62.78	8.78
	Rice Pebble Qtzt.	Interlocking quartz crystals.	Anhedral pyrite crystals	87.49	5.25
	Blyvooruitzicht Qtzt.	Highly fractured quartz.	No mineralization observed.	91.46	0.86

Table 2 Summary of bulk density (ρ), P-wave velocity (Vp), acoustic impedance (Z) and reflection coefficient (Rc) measured at ambient stress for 9 boreholes. The Z is calculated from the product of the velocity and density and the Rc = $(\rho_2 Vp_2 - \rho_1 Vp_1) / (\rho_2 Vp_2 + \rho_1 Vp_1)$. Quartzite (Qtzt.); Carbon Leader Reef (CLR).

BH Name	Sample Type	Sample thickness (mm)	Velocity (Vp, m/s)	Density (ρ, g/cm^3)	Z (*10^5, g/cm^{2}s)	[Rc]
BH-A	Green Bar shale	60	5636	3.00	16.91	0.10
	Rice Pebble Qtzt.	60	5028	2.72	13.70	0.02
	CLR	60	5070	2.83	14.36	0.04
	Blyvooruitzicht Qtzt.	60	4916	2.71	13.32	
BH-B	Main Qtzt.	80	5423	2.69	14.59	0.05
	Green Bar shale	80	5537	2.89	16.00	0.06
	Rice Pebble Qtzt.	80	5307	2.68	14.22	0.02
	CLR	80	5468	2.74	14.97	0.05
	Blyvooruitzicht Qtzt.	80	5108	2.66	13.59	
BH-C	Green Bar shale	60	5882	3.01	17.71	0.10
	Rice Pebble Qtzt.	60	5263	2.76	14.53	0.02
	CLR	60	5088	2.77	14.03	0.01
	Blyvooruitzicht Qtzt.	60	5085	2.71	13.78	
BH-D	Maraisburg Qtzt.	80	4980	2.76	13.75	0.07
	Roodepoort shale	80	5518	2.87	15.84	0.06
	Lower Roodepoort Qtzt.	80	4977	2.81	13.99	
BH-E	Main Qtzt.	60	4970	2.71	13.47	0.14
	Green Bar shale	60	5914	3.00	17.74	0.09
	Rice Pebble Qtzt.	60	5458	2.73	14.90	
	Blyvooruitzicht Qtzt.	60	5211	2.70	14.07	-
BH-F	Main Qtzt.	60	5209	2.73	14.22	-
	Rice Pebble Qtzt.	60	5172	2.72	14.07	-
	Blyvooruitzicht Qtzt.	60	5042	2.71	13.66	-
BH-G	Green Bar shale	31	5124	3.15	16.14	0.04
	Rice Pebble Qtzt.	60	5195	2.87	14.91	
	Blyvooruitzicht Qtzt.	60	4959	2.72	13.49	-
BH-H	Main Qtzt.	80	5041	2.69	13.56	0.11
	Green Bar shale	80	5594	3.04	17.01	0.07
	Rice Pebble Qtzt.	80	5480	2.72	14.90	
	Blyvooruitzicht Qtzt.	80	4777	2.68	12.80	
BH-I	Green Bar shale	60	5769	3.13	18.06	0.11
	Rice Pebble Qtzt.	60	5263	2.75	14.47	
	Blyvooruitzicht Qtzt.	60	5150	2.77	14.27	

LIST OF FIGURES

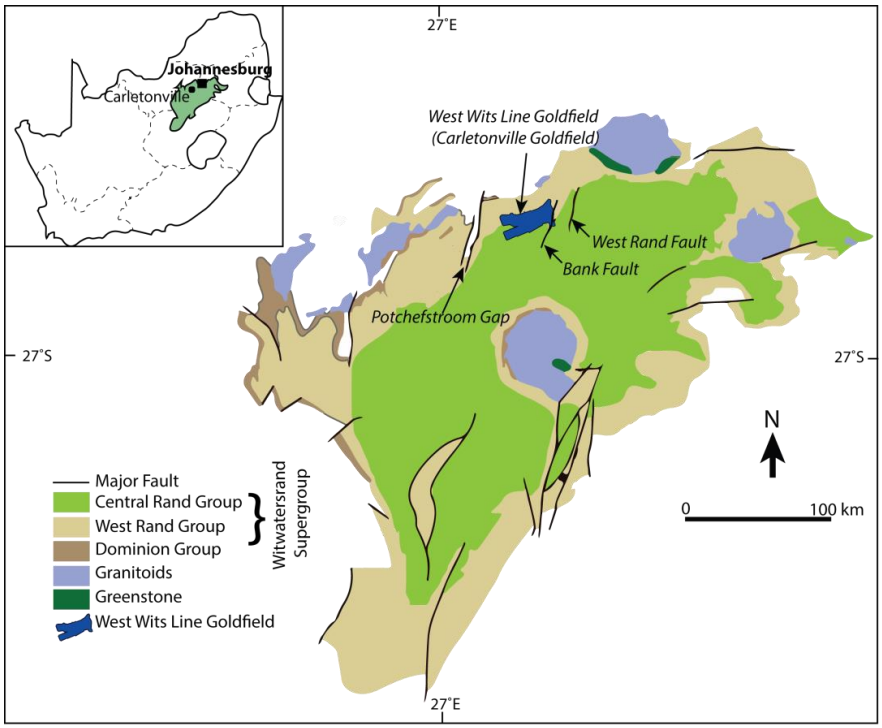


Figure 1 A simplified geological map of the Witwatersrand Basin with older sediment cover, showing the location of the West Wits Line Goldfield (Carletonville Goldfield) (after Grové and Harris 2010).

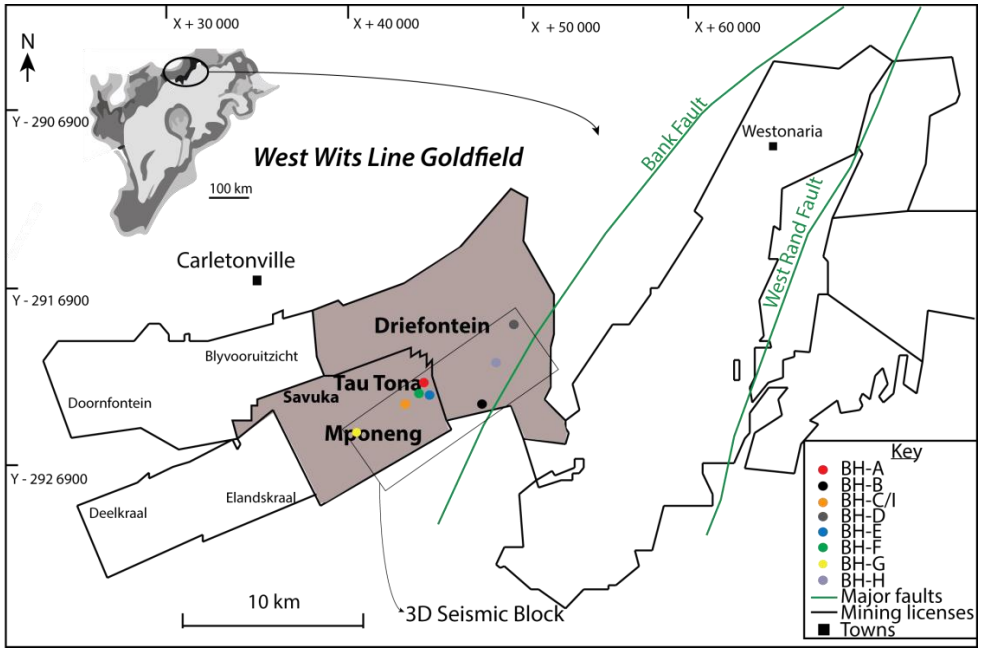


Figure 2 The map showing the location of 9 boreholes within the Anglo Gold Ashanti Ltd and Sibanye Gold Ltd mining boarders, along the West Wits Line Goldfield. Note that all the 9 boreholes lie within the 3D seismic block covering the two mines. Note that boreholes BH-C and BH-I are deflections (after Dankert and Hein 2010).

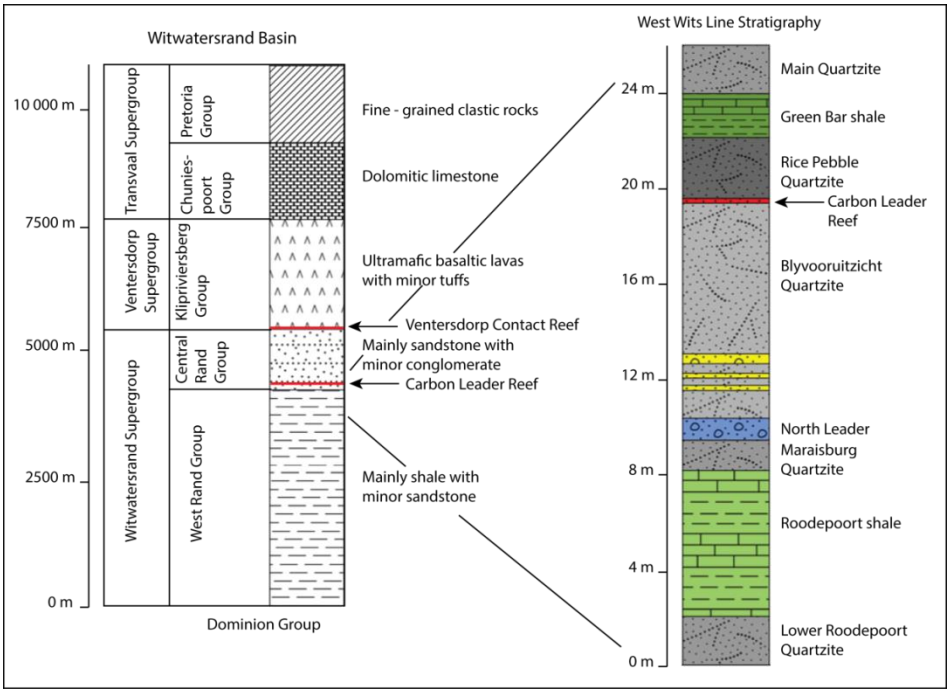


Figure 3 Generalized stratigraphic column of the Witwatersrand Basin and the West Wits Line Goldfield with particular emphasis on the CLR conglomerate and the Roodepoort shale stratigraphy (after Guy *et al.* 2010).

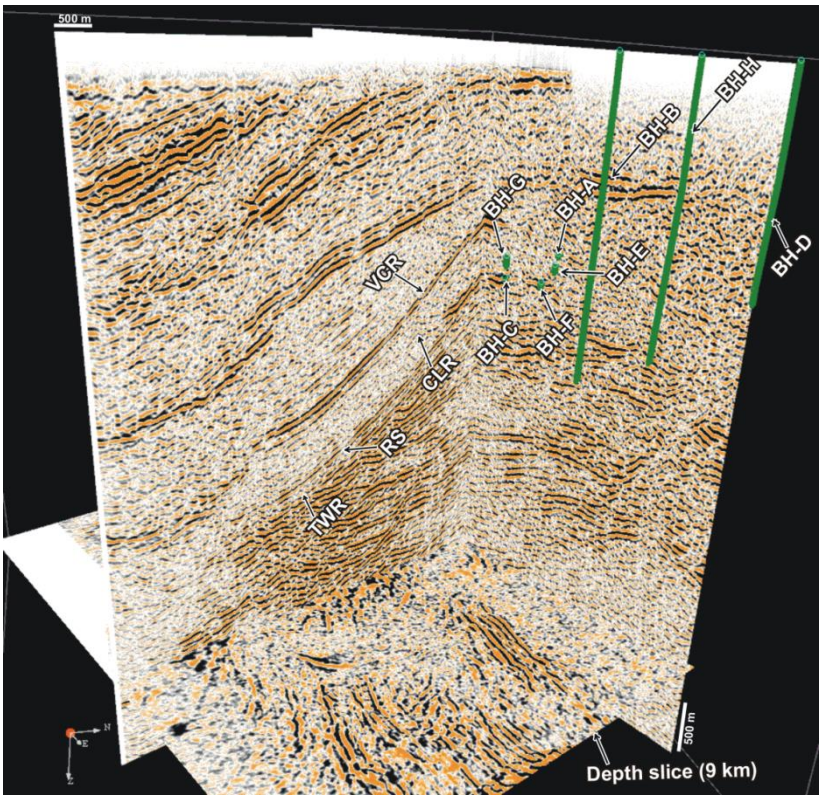


Figure 4 3D visualization of the migrated seismic volume (see 3D seismic block Fig. 2) covering Anglo Gold Ashanti Ltd and Sibanye Gold Ltd mines along the West Wits Line Goldfields, showing strong seismic reflectors and location of boreholes (BH-A to BH-H). VCR: Ventersdorp Contact Reef, TWR: Top of the West Rand, RS: Roodepoort shale, CLR: Carbon Leader Reef.

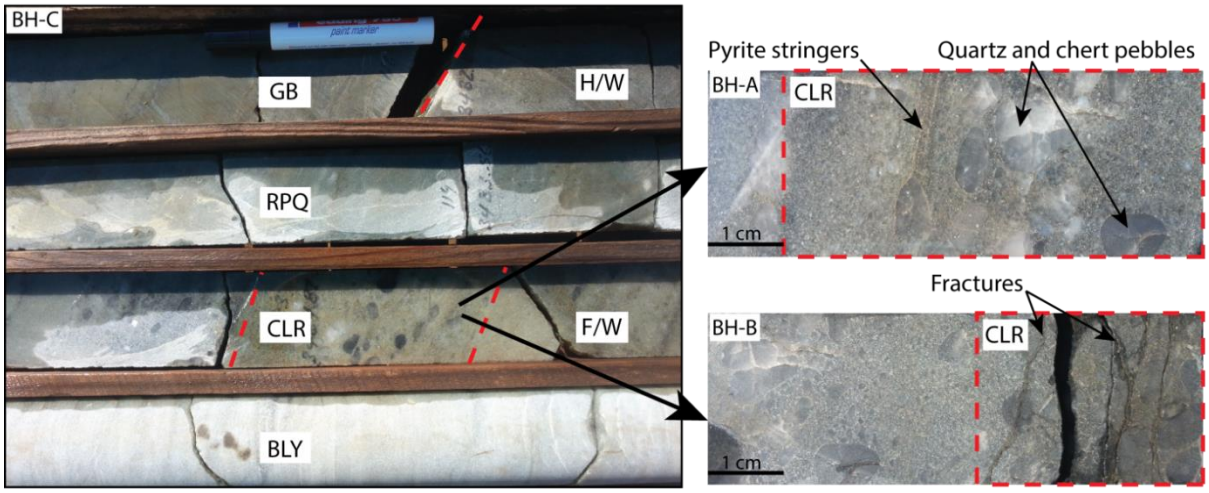


Figure 5 Borehole drill-core showing the CLR conglomerate and its hangingwall (Green Bar shale and Rice Pebble Quartzite) and footwall (Blyvooruitzicht Quartzite) lithostratigraphic units. Note that boreholes BH-A and BH-B show the poor development of the Carbon Leader Reef (CLR) conglomerate. GB: Green Bar shale, H/W: Hangingwall, RPQ: Rice Pebble Quartzite, CLR: Carbon Leader Reef, F/W: Footwall, BLY: Blyvooruitzicht Quartzite.

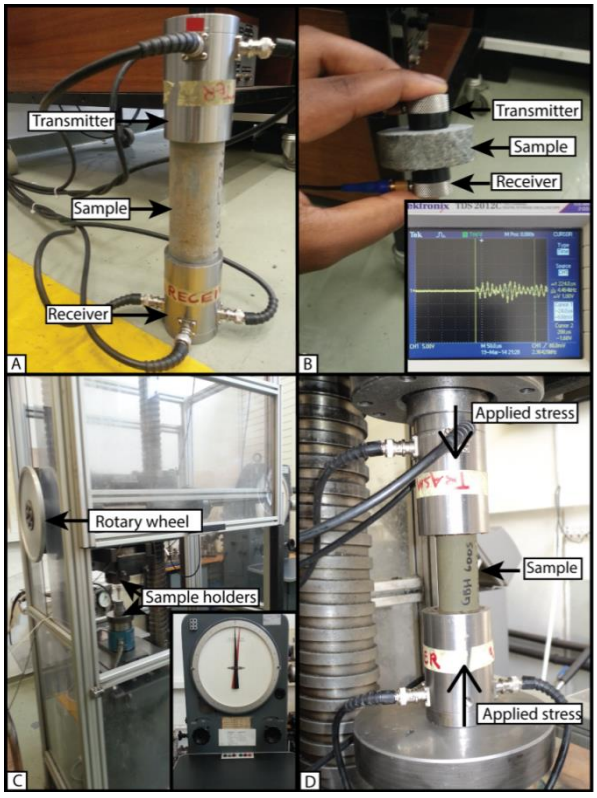


Figure 6 Ultrasonic velocity measurement apparatus at ambient (a and b) and elevated stresses (c and d). (a) Larger transducer (diameter=32 mm, 0.5 MHz) set used to measure seismic velocities for large samples (b) smaller transducer (diameter=16 mm, 0.5 MHz) set used to measure seismic velocities for smaller samples. (c) The uniaxial compressional loading is produced by hydraulic pistons that are driven by a computer controlled load holding pump. The induced load is monitored on a stress measuring gauge (insert in c). (d) The image shows the placement of the sample between the transducers positioned on pistons within the chamber.

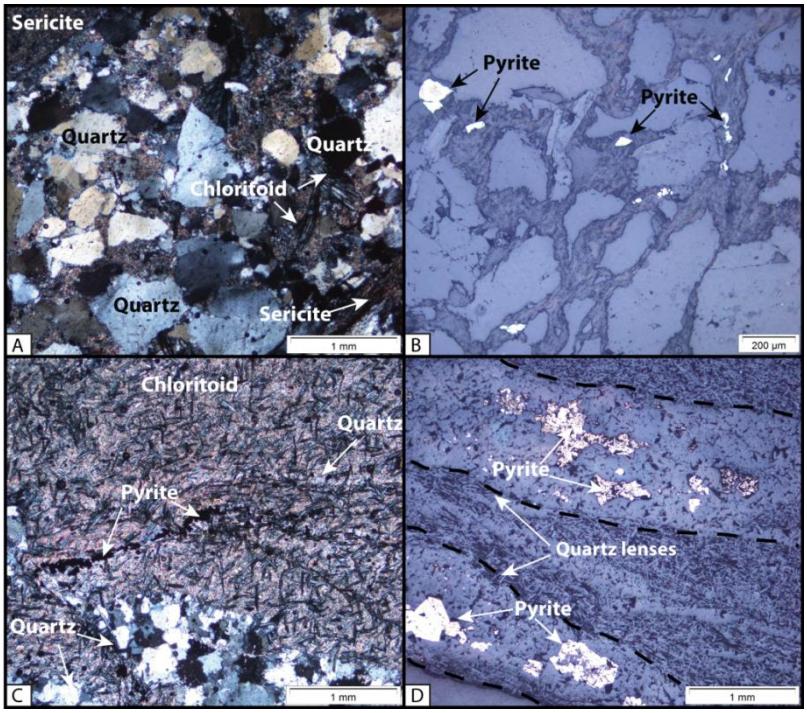


Figure 7 Thin section of the hangingwall Main Quartzite in (a) cross polarized and (b) reflected light, and the Green Bar shale in (c) cross polarized and (b) reflected light. Sulphides occur within the groundmass in the Main Quartzite (b) and the sulphides in the Green Bar shale (d) occur within the quartzite lenses.

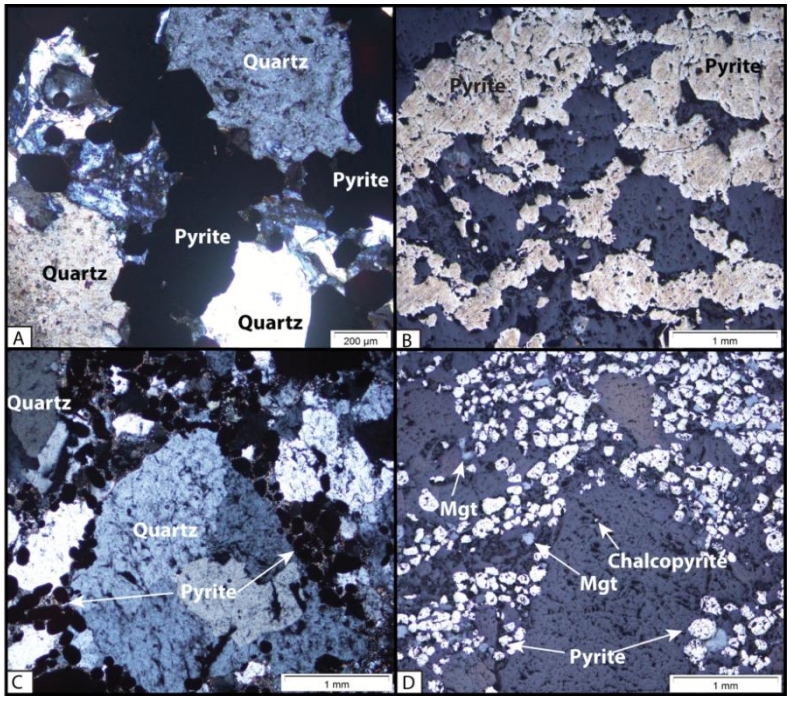


Figure 8 Thin sections and polished blocks of the Rice Pebble Quartzite and Carbon Leader Reef conglomerate from photo microscopy analysis. A and C show views of the thin sections in reflected light and B and D shows the polished blocks in reflected light.

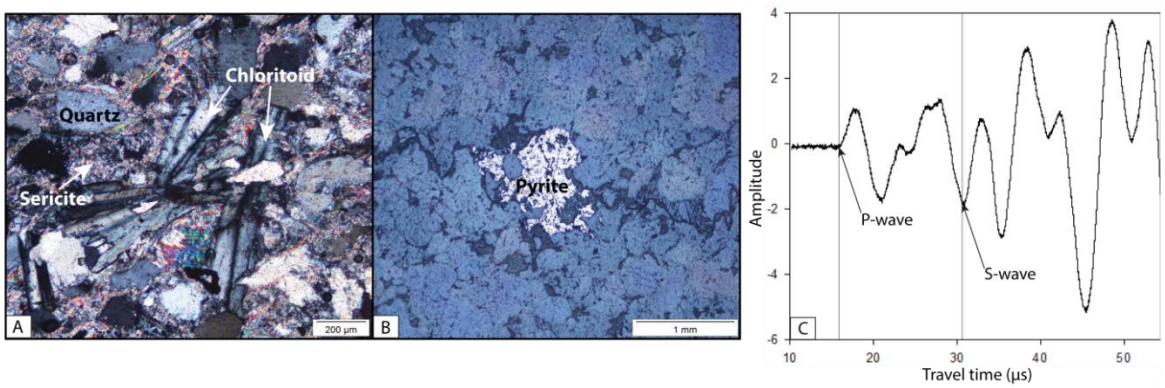


Figure 9 Thin section of the Blyvooruitzicht footwall in (a) cross polarized light and (b) reflected light. The thin sections show the dominant minerals such as quartz, chloritoid and sericite and (c) the amplitude versus travel time graph shows the response of seismic wave velocities to these dominant minerals. The amplitude versus travel time graph also shows the clear identification of the P-wave arrival time compared to the S-wave arrival time.

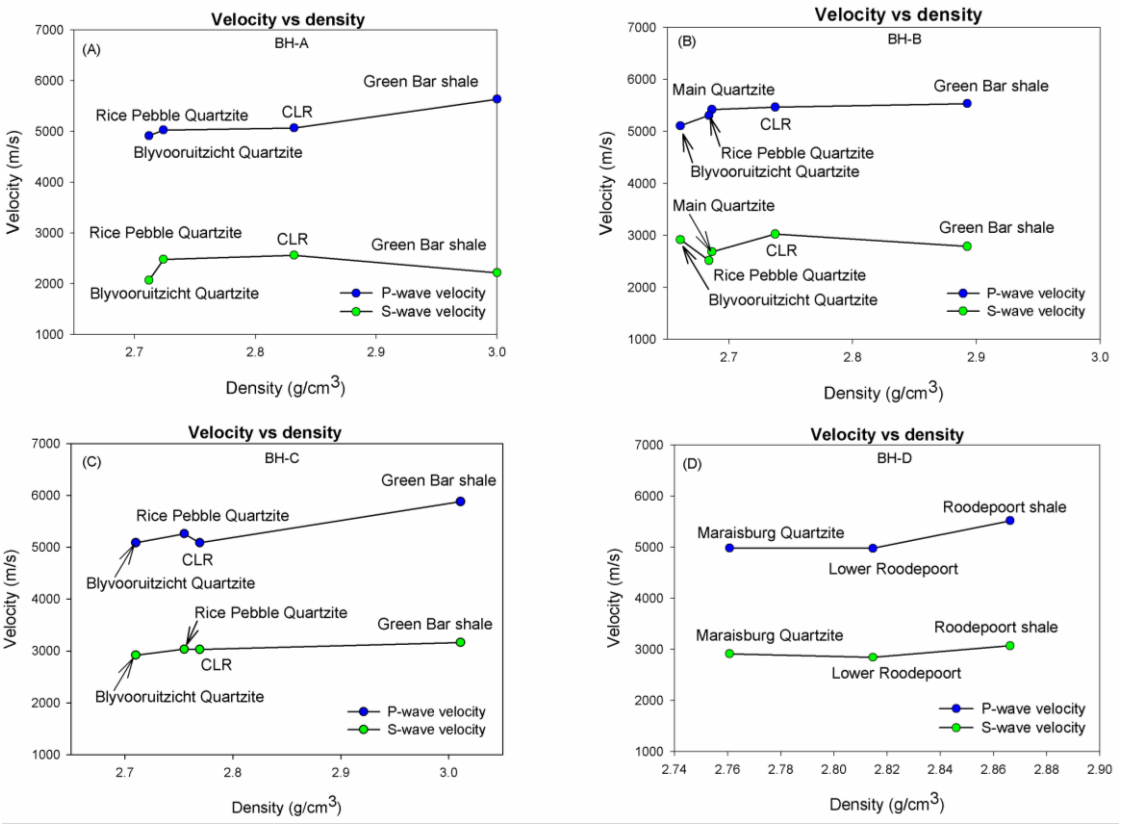


Figure 10 Graphs of P- wave and S-wave velocities obtained using the ultrasonic device at ambient stresses from (a) BH-A, (b) BH-B, (c) BH-C and (d) BH-D. Borehole BH-A to BH-C represent the Carbon Leader Reef (CLR) conglomerate intersections and borehole BH-D represents the Roodepoort shale intersection. The calculated Vp error ranges from 0.1 to 0.3 for the measured samples.

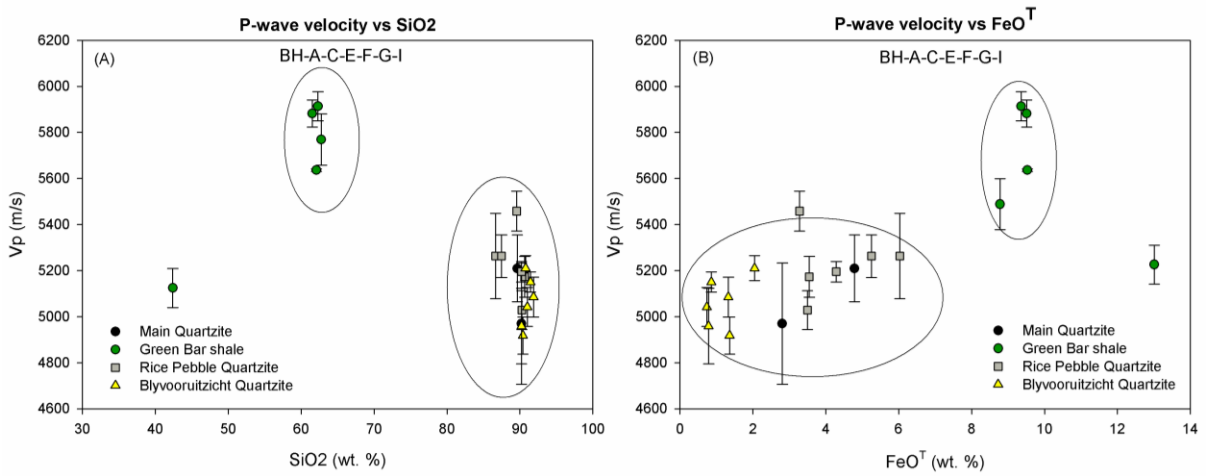


Figure 11 Graph of (a) P-wave velocity versus SiO_2 (Vp) and (b) P-wave velocity versus FeO^T for the Carbon Leader Reef hangingwall and footwall lithologies from borehole BH-A, BH-C, BH-E, BH-F, BH-G and BH-I. Higher P-wave velocities correspond to lower SiO_2 and higher FeO values, while lower P-wave velocities correspond to higher SiO_2 and lower FeO values. The horizontal and vertical bars indicate standard deviations obtained from multiple measurements of the same sample or from similar type samples. The calculated Vp error ranges from 0.1 to 0.3 for the measured samples.

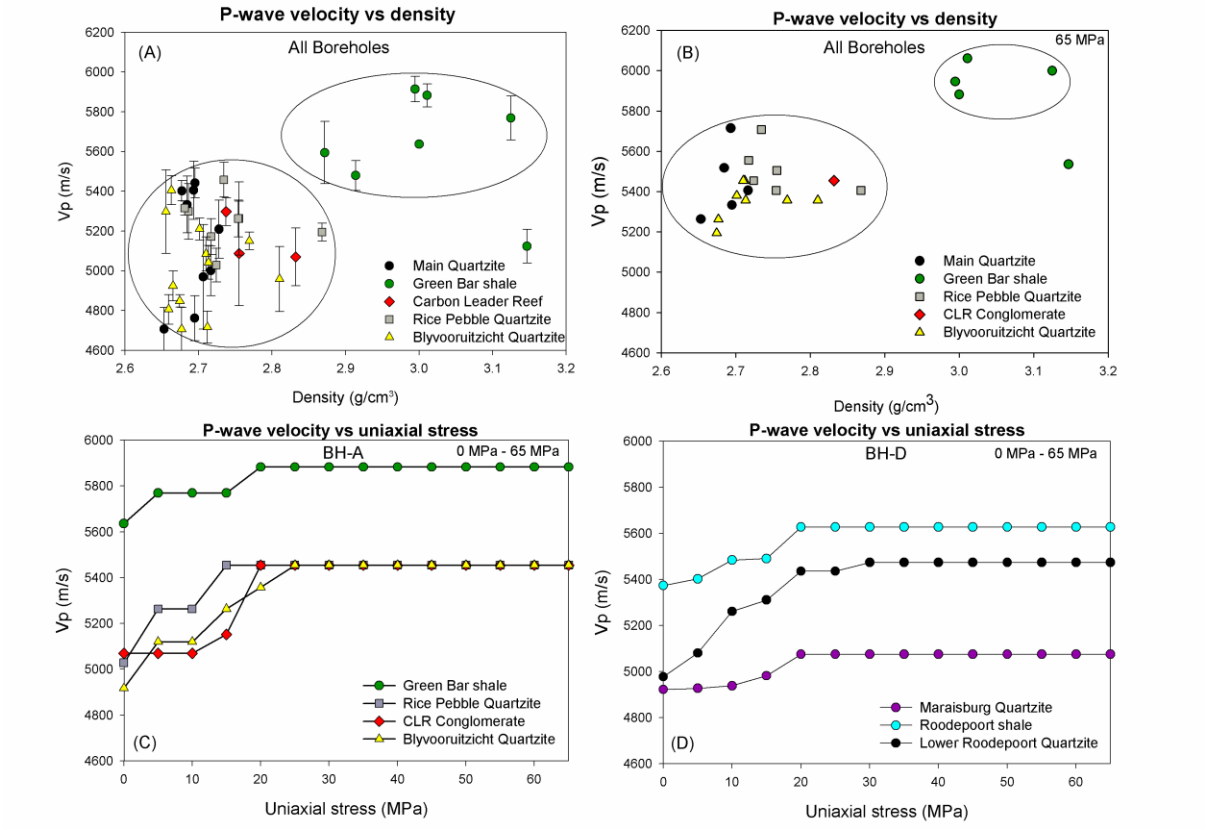


Figure 12 A comparison of P-wave velocity (Vp) versus density (a) ambient and (b) elevated stresses, showing an increase in velocities of the samples with increasing stress. The effect of uniaxial stress is further shown by (c) borehole BH-A and (d) BH-D where the seismic velocities increase as the stress is increased and becomes constant above ~20 - 25 MPa. The horizontal and vertical bars indicate standard deviations obtained from the measurements of similar type samples or repeated measurements. The calculated Vp error ranges from 0.1 to 0.3 m/s for the measured samples.

8. Manuscript 2

The manuscript has been modified according to journal standards.

3D seismic attributes for structural mapping and enhancement of deep gold mining: A Case study from the West Wits Line goldfields, South Africa

Nomqhele Z. Nkosi[1*], Musa S.D. Manzi[1]

[1] University of the Witwatersrand, School of Geosciences, 1 Jan Smuts Avenue,

Braamfontein 2000, Johannesburg, South Africa.

Abstract

Volumetric and horizon-based seismic attributes were carried out on the West Wits line goldfields (South Africa) using 3D seismic data covering a total volume of approximately 3300 km^3. This study was aimed at improving the delineation of minor faults that crosscut the gold-bearing horizons in the goldfield using different seismic attributes. The 3D seismic data have delineated faults that crosscut and displace the key horizons by tens to hundreds of metres, leading to the delineation of the ore resources in faulted areas of the mines. In particular, the ant-tracking technique has provided better stratigraphic and structural imaging in complex faulted areas, relative to conventional interpretation methods. Other improvements include more accurate mapping of the depths, dip, and strike of the key seismic horizon (Roodepoort shale) using the edge detection attributes, yielding a better understanding of the interrelationship between fault activity, reef distribution, and the relative chronology of tectonic events. The integration of the 3D reflection seismic data, seismic attributes and information from borehole logs and underground mapping has provided better imaging and modelling of important fault systems that might have a direct effect on mining. This information could be used for future mining planning and designs to (1) assess and mitigate the risks posed by mining activities and (2) improve the resource evaluation of the gold-bearing reefs in the West Wits Line goldfields.

Keywords: Faults, Imaging, Interpretation, Mining geophysics, Mineral exploration, Mining , Seismic reflection, Dip, Azimuth

1. Introduction

Almost 40% of the gold ever mined has come from the Witwatersrand Basin, which still contains about 45% of the world's unmined reserves (Frimmel and Minter, 2002; Viljoen, 2009). The gold is hosted within the thin conglomerate units (10 cm - 5 m thick), known as reefs and carbon rich seams (up to 3 cm thick) (Moon and Whateley, 1989; Gibson et al., 2000; Frimmel et al., 2005). The gold-bearing ore bodies are located in the various goldfields across the basin, at depths between 500 m and 4.2 km (Krapež, 1985; Vieira and Durrheim, 2002; Safonov and Prokofèv, 2006). Initially, geological and ore body models developed for mine planning and designs were based on geological field mapping, drilling, and interpretation of gravity and magnetic data (Durrheim, 1986; Stevenson et al., 2003). However, these methods were unable to map deeply buried strata and complex fault geometries required to produce detailed geological and structural models of deep ore bodies (Pretorius et al., 1994; Stevenson et al., 2003). In order to delineate targets as deep as 3.0 km - 4.2 km and to increase the mapping resolution of faults in the structurally complex Witwatersrand Basin, the mining industry adopted the 3D reflection seismic method, which is widely used in the petroleum industry (Pretorius et al., 1994; Salisbury et al., 2003).

The success of this technique is due to its ability to provide high-resolution images of ore bodies and subsurface structures, and greater penetration that can be achieved with sufficient resolution, compared with other geophysical methods (Bacon et al., 2003). This technique has not only played a major role in the exploration for ore deposits worldwide but also in constraining the tectonic history of the basin (Pretorius et al., 2003; Jolley et al., 2004; Duff et al., 2012; Malinowoski et al., 2012; Malehmir et al., 2012, 2013; Manzi et al., 2012a, 2013). Although boreholes have provided first-hand information about the subsurface geology, the information is only limited to the vicinity of the borehole. However, the integration of 3D reflection seismic data with borehole information has proven to provide

better interpretations of the subsurface horizons (Manzi et al., 2012a, 2013; Malehmir et al., 2013).

In the 1990s, Anglo Gold Ashanti Ltd and Sibanye Gold Ltd conducted 3D reflection seismic surveys at their gold mines in the north-western part of the Witwatersrand Basin to map potential ore-bearing horizons and subsurface structures. Figure 1 shows a geological map of the Witwatersrand Basin as well as the boundaries of the 3D seismic surveys acquired by the two mining companies along the West Wits Line (WWL) goldfields. These 3D seismic cubes were processed and merged (post-migration) to produce a continuous seamless cube (Manzi et al., 2012b). The reflection seismic surveys covered the Mponeng and Tau-Tona gold mines owned by Anglo Gold Ashanti Ltd as well as the Driefontein gold mine, owned by Sibanye Gold Ltd, as shown in Figure 2. The 3D seismic survey successfully imaged the entire Witwatersrand Basin stratigraphy from the surface through the Transvaal Supergroup, Ventersdorp Supergroup, Witwatersrand Supergroup to the crystalline basement onto which the sedimentary units were deposited . The seismic survey also successfully imaged the seismic reflectors that occurred at major geological boundaries. A seismic section from the WWL goldfields showing the strong geological boundaries, such as the Black Reef (BLR), the Ventersdorp Contact Reef (VCR) and the Roodepoort shale (RS) is shown in Figure 3. 3D seismic interpretations of the strong and continuous ore horizons, such as the BLR and VCR have provided excellent structural models for mine planning and design (Manzi et al., 2012a, 2013). However, such interpretations have not been conducted for the Carbon Leader Reef (CLR), which is the most economic gold-bearing horizon in the basin. The reason for this is that, the CLR is a poor seismic reflector, due to its size (~1.5 m thick), depth location (~2.5 to 4.2 km)and its low acoustic impedance contrast (product of velocity and density) (Nkosi et al*.,* submitted).

Furthermore, conventional 3D seismic interpretation has its own limitations. For example, features such as thin dykes, near-vertical faults and minor faults with vertical throws less than 25 m cannot be seen on a seismic section because they are below the conventional vertical seismic resolution (~ 25 m or quarter of the dominat wavelength). The seismic resolution limit is determined by the seismic wavelength, which depends on the seismic velocity of the rock unit and the frequency of the seismic wavelet. Studies conducted by Widess (1973), Chopra et al. (2006) and Chopra et al. (2009) suggest that seismic data with a dominant frequency of 60 Hz and low signal-to-noise ratio (SNR) can delineate faults with minimum vertical throws of ~25 m, while seismic data with high SNR can delineate faults with vertical throws as small as ~5 m. The SNR is the amplitude ratio between the strength of the real signal and the level of noise recorded during the field survey. On the conventional seismic section (amplitude), faults with large vertical throws (≥25 m) can be identified by the displacement of reflectors, whereas faults with smaller vertical throws (<25 m) appear as minor disturbances in the seismic waveform and are often difficult to correlate using conventional interpretation of seismic cross-sections. Seismic attributes are then used in obtaining better insight into fault and fracture systems and their relationships (Neves et al., 2004). The application of seismic attributes in hydrocarbon and mineral exploration to enhance interpretation of 3D seismic data has been used worldwide (Taner et al., 1979; Dalley et al., 1989; Sheriff, 1991; Rijks and Jauffred, 1991; White, 1991; Brown, 1996; Basir et al., 2013).

In this study, we provide a detailed 3D seismic interpretation of the Roodepoort shale (RS), which is located at approximately 350 m below the poorly reflective CLR ore body. We achieve this by using horizon-based seismic attributes, such as dip, dip-azimuth and the edge detection attributes, to map faults and dykes that fall below the vertical seismic resolution limit (quarter of the dominant wavelength). We also use the volumetric attributes (e.g., amplitude, edge enhancement and ant-tracking) to better map the continuity of these

faults and dykes along sections and depth slices, and we compare these results with conventional interpretation techniques. Finally, we present a structural framework model of the mining area incorporating the RS horizon and fault surfaces.

2. Lithological setting

The Mesoarchaean Witwatersrand Basin sediments were deposited on the Archaean Kaapvaal Craton (ca. 3.6 - 3.2 Ga). The basin is defined by a basement of volcanics and sediments of the Dominion Group (ca. 3074 ± 6 Ma; Myers et al., 1990b). This group is unconformably overlain by the Witwatersrand Supergroup which is subdivided into the lower West Rand and upper Central Rand groups, as shown in Figure 3 (Jolley et al., 2004; McCarthy, 2006; Dankert and Hein, 2010).

The West Rand Group is largely dominated by marine sediments and minor clastics (2.99 - 2.90 Ga; Kositcin and Krapež, 2004), whereas the Central Rand Group (CRG) consists of quartzite, conglomerate and shale units (2.90 - 2.85 Ga) (Frimmel et al., 2005). The shale horizons are the most consistent units in the entire stratigraphy. They are primarily chlorite-rich horizons interbedded with magnetic shale (Frimmel and Minter, 2002). The Roodepoort shale unit is located at the top of the West Rand Group (Fig. 3) and it is a strong seismic marker due to the acoustic impedance contrast between itself and surrounding quartzite units (Nkosi et al., submitted).

The unconformably overlying Central Rand Group hosts a number of economically viable gold-bearing reefs that have been mined throughout the history of the Witwatersrand Basin, including the Elsberg, Kloof, Libanon, North Leader, Middelvlei and the Carbon Leader Reef (De Kock, 1964). The Carbon Leader Reef, the deepest known gold-bearing reef in the

world, occurs as a package of alternating conglomerate units that are interbedded within highly altered to mono-mineralic quartzite units.

The Central Rand Group is unconformably overlain by the Ventersdorp Contact Reef of the Venterpost Formation (2.73 ± 19 Ga; Kositcin and Krapež, 2004). Overlying the VCR is the late-Achaean Ventersdorp Supergroup, comprising ultramafic to mafic lavas of the Klipriviersberg Group, metasediments and bimodal volcanics of the Platberg and Pniel groups (van der Westhuizen et al., 1991). Finally, the Ventersdorp Supergroup is overlain by the Black Reef Formation (BLR), which occurs at the base of the early Proterozoic Transvaal Supergroup (Fig. 3) (Jolley et al., 2004).

1. Structural setting

2.4. Structural setting

The detailed structural setting of the Witwatersrand Basin is reported by Coward et al., (1995), Frimmel and Gartz (1997), Jolley et al. (2004) and Dankert and Hein (2010) so only a brief overview is given here. Summarily, the Witwatersrand Basin experienced several stages of deformation that can be distinguished by the division of the various lithostratigraphic units. The basin is fault boundedbound by the Potchefstroom gap along its north-western margin and the many fault sets described in the WWL goldfield indicate a complex structural history (De Kock, 1964; Engelbrecht et al., 1986; Myers et al., 1990a, 1990b).

The first stages of basin formation involved crustal extension that prompted the deposition of the Dominion (3086 - 3074 Ma) and West Rand Groups (2.99 - 2.90 Ga) (Myers et al., 1990b; Armstrong et al., 1991; Frimmel and Gartz, 1997; Robb et al., 1997). Uplifting and tilting of the West Rand Group sediments syn- to post-erosion occurred at ~2.90 Ga, followed by the unconformable deposition of coarse-grained siliciclastic rocks of the Central Rand Group (Wronkiewics and Condie, 1987; Jolley et al., 2004). The deposition of the Central Rand Group was synchronous with the compressive deformation event (Umzawami Event at ca 2.73 Ga) described by Dankert and Hein (2010). The Umzawami Event was followed by basin extension (Hlukana Extension Event at ~2.70 - 2.64 Ga) during the emplacement of the Ventersdorp lavas and deposition of the Platberg Group (Manzi et al., 2013).

The extensional tectonics of the basin resulted in the formation of first-, second- and third-order scale faults. The Bank Fault (BF), one of the first-order scale faults (~400 m - 3 km vertical throw) in the WWL goldfield, cuts through the south-eastern margin of the Driefontein and Mponeng gold mines, as shown in Figures 1 and 2. Manzi et al. (2012a) interpreted the Bank Fault as a north-northeast trending listric fault which dips between 65° and 70° at shallow depths (~1.5 km below surface) and 5° to 10° at deeper depths (~5 km below surface). The fault crosscuts the Ventersdorp Supergroup, Central Rand Group and the top of the West Rand Group at a depth of ~5 km below the surface (Dankert and Hein, 2010).

Second-order scale faults (~25 - 400 m vertical throws) include the north-northeast trending Pretorius Fault (PF) which is dominant in the Mponeng and Tau-Tona gold mines (Heesakkers et al., 2011). The Pretorius normal Fault is a 10 km long oblique strike-slip fault with a maximum vertical throw of ~200 m at the Tau Tona gold mine (Heesakkers et al.,

2011). The fault crosscuts the Ventersdorp Supergroup, Central Rand Group and the top of the West Rand Group (Heesakkers et al., 2011).

In addition to faults and fractures, the WWL goldfield is intruded by dolerite sills and syenite dykes. These igneous intrusions have been confirmed by exploration boreholes that were drilled within the seismic volume. Mapping the extension of these dykes and sills through seismics is important for mine safety since these features can cause considerable damage in underground workings. For example, when dykes intrude into fault zones they can contribute to rock instability and cause rock bursts, and they can create water pockets that can lead to the flooding of the mine (Litthauer, 2009; Manzi et al., 2012b).

2. 3D seismic survey

As previously shown in Figures 1 and 2, the Western Ultra Deep Levels (WUDLs) 3D seismic survey covers the Mponeng and Tau-Tona gold mines and the Driefontein seismic survey covers the Driefontein gold mine to the west of the Bank Fault. As mentioned earlier, the two seismic surveys were re-processed and merged (post-migration) to produce a continuous seamless depth-converted prestack time migrated (PSTM) seismic volume covering the WWL goldfields (Manzi et al., 2012a). The merged survey is by far the largest 3D seismic survey in southern Africa and covers a total volume of approximately 3300 km^3. The seismic volume is about 11 km deep, and extends for 20 km in the east-west direction, and approximately 15 km in the north-south direction, as shown in Figure 4.

The 3D seismic surveys were designed to delineate the gold-bearing ore bodies, at a depth range of 2.7 km to 4.2 km, and to map first-order to third-order scale structures that crosscut

the ore bodies. The survey successfully imaged the entire Witwatersrand Basin stratigraphy from the surface through the Transvaal and Ventersdorp Supergroups to the base of the Witwatersrand Basin (~11 km in depth). As shown in Figure 4, strong seismic markers, such as the BLR, VCR, RS and the top of the WRG, were easily mapped by the seismic technique because these occur at boundaries with high acoustic impedance contrasts between their overlying and underlying rocks. Interpretation of the RS was of particular interest in this study because it is the closest strong seismic marker to the most economic gold-bearing ore body, the CLR, which is a poor seismic reflector. The RS occurs at a major and laterally extensive acoustic impedance contrast between low-velocity, low-density quartzite units (~4980 m/s velocity and ~2.76 g/cm^3 density; Nkosi et al., submitted) and the high-velocity, high-density RS (~5520 m/s velocity and ~2.87 g/cm^3 density; Nkosi et al., submitted). In other words, the strong reflection denotes the top of the RS. Figure 4 clearly shows the poor imaging of the CLR throughout the entire survey area and the good imaging of the VCR and RS markers, located above and below the CLR, respectively. The poor seismic reflection associated with the CLR may be due to its thickness (~1 m), which is below the conventional vertical seismic resolution limit, and the low reflection coefficient (~0.03; Nkosi et al., submitted) between hangingwall and footwall quartzite units of the CLR.

3. Seismic attributes

As stated earlier, the quality of the seismic interpretation is dependent on the signal-to-noise ratio of the datasets. Although the 3D seismic interpretation steps undertaken by Gibson et al. (2000) and Manzi et al. (2012a) offered the gold mines with reliable geological models, the conventional interpretation techniques did not allow for exploitation of the data to its full potential. However, sophisticated volumetric seismic attribute analysis, implemented in the new and advanced interpretation software packages, can be used to enhance the detection

of these features in the data. Seismic attributes are derived from the seismic data and mathematical manipulation of seismic wave components such as amplitude, frequency and phase (Sheriff, 1991).

In this study, we tested test different volumetric attributes (e.g., amplitude, edge enhancement and ant-tracking) and horizon-based attributes (e.g., dip, dip-azimuth and edge detection) to enhance the mapping of subtleminor geological information throughout the seismic volume and conventional interpreted horizons. The edge enhancement attribute is used to enhance the spatial continuity of features (horizons and faults) in the seismic data. This attribute decreases the noise in the data by using local dip estimates of the reflection layers (Randen and Sønneland 2000).The edge enhancement attribute smooths the seismic data, reducing noise levels, and therefore allowing small amplitude changes to be detected. The ant-tracking, in particular, has been effectively will be applied to the seismic cube to help us map the continuity of sub-seismic geological features and understand the structural framework of the goldfield. The amplitude measures the seismic acoustic impedance and thus helps to identify changes in lithological characteristics in the data (Sheriff 1991).

The ant-tracking attribute, defined by Pedersen et al. (2002), is an edge enhancement tool that is applied to the processed 3D seismic data to enhance the delineation of fault and fracture networks throughout the seismic cube. The technique uses the principles of “swarm intelligence” to search and enhance fault networks from spatial discontinuity seismic attributes like variance and edge enhancements, and allows automatic fault extraction from the output ant-track attribute volume. Generally, the ant-tracking workflow involves pre-processing of seismic data by surface smoothing filters (e.g., median and mean filters) followed by the application of discontinuity attributes (Pedersen et al., 2002). The final volume is tracked by computer coded agents, which follow fault like structures discontinuities

while avoiding discontinuous noise like features. Ant-tracking has been used in the petroleum industry for improved fault detection and reservoir characterization (Pedersen et al., 2002; Basir et al., 2013). The attribute reveals geological features, relationships, and structural patterns in the 3D seismic data that may not be easily noticeable on the conventional amplitude displays.

Horizon-based seismic attributes, originally described by Dalley et al. (1989), have been used in the Witwatersrand Basin to enhance the detection of sub-seismic faults at the horizon level. Dalley et al. (1989) and Rijks and Jauffred (1991) have shown that the dip and azimuth attributes can highlight faults having displacements less than the size of the seismic wavelet. The dip and azimuth are essentially the magnitude and direction of the gradient vector, computed at each sample of the interpreted horizon (Rijks and Jauffred, 1991). The edge detection attribute combines dip and azimuth variations that are normalized to the local noise of the interpreted horizon (Manzi et al., 2012a). These attributes are powerful tools used to enhance structural continuities and to determine the cross-cutting relationships between faults. This study is, to our knowledge, the first to use the combination of ant-tracking and edge detection seismic attributes to enhance the delineation of faults at depths of 2.5 km - 4.5 km.

4. Methodology

The interpretation of seismic data was conducted using the Seismic Micro-Technology (SMT) Kingdom Suite and Petrel software packages. These packages provided 3D visualization and interpretation of structural and stratigraphic features, enabling the mapping of strong seismic reflectors and faults at great depths and in geologically complex regions. The seismic interpretation workflow began with horizon picking, 3D seismic definition and

mapping of faults and other structures using the Seismic Micro-Technology (SMT) Kingdom Suite software. On seismic sections, the horizons were picked either as a peak or trough depending on the data polarity. The confidence in picking the seismic reflector was dependent on the SNR ratio of the data and structural complexities of the area. Thus, in structurally intricate areas and regions of poor SNR, careful picking of the reflector and faults was required.

The Roodepoort shale is characterized by the clear wavelets and continuous phase thus allowing confident picking of the horizon. To ensure the accurate mapping of the RS reflector, seismic sections were initially interpreted at wide line spacing. The Roodepoort shale horizon was picked as a trough due to its negative polarity owing to the increase of the acoustic impedance from the overlying quartzites (~4980 m/s velocity and ~2.76 g/cm^3 density) to the top of the shale layer (~5520 m/s velocity and ~2.87 g/cm^3 density). After the picking of the RS at wide line spacing, infill picks were made at a close line spacing (e.g., at every tenth, fifth and first inline and crossline), facilitating detailed structural interpretation. The location and vertical throw of each fault was controlled by the seismic amplitude character and displacement of the RS reflector. Volumetric attributes (e.g., amplitude, edge enhancement and ant-tracking) were extracted for each section and horizon-based attributes were applied to the picked horizon to enhance the detection of minor or sub-seismic faults. Prior to the application of the ant-tracking attribute using the Petrel software, the 3D seismic volume was conditioned using different structural smoothing filters (e.g., median, mean and laplacian filters) in order to eliminate noise and increase the SNR of the data horizon. The ant-tracking technique is known to be CPU-intensive (Ngeri et al., 2015) and it takes time to run. The running time for this attribute is dependent on the structural complexity (e.g., number of faults) in the data, and the parameters used. With this in mind, we first applied the ant-tracking algorithm to a small area in the data to test the various parameters of the ant-

tracking attribute. After achieving a successful result the ant-tracking attribute was then applied to the entire data set.

Although more than 100 surface and underground borehole data were utilized to control our seismic interpretation, only few (~10) of these intercepted the RS (4.0 km - 4.5 km depth) and used as control for the RS interpretation and modelling. The surface boreholes were drilled on a widely-spaced grid (~1 km), while underground boreholes were drilled in a tight grid (~100 m), and more than 80% of these were stopped as soon as they intersected the gold-bearing horizons (VCR and CLR) above the RS. The shortage of boreholes at the RS level caused uncertainties in the picking of the RS reflector in the structurally complex areas. The mistie (~100) computed between seismically-defined RS horizon and borehole control was observed across the survey area (Figure 5). The depth mistie grid showed that there was a consistent error in the depth conversion. Such misties between the seismic horizon and borehole control suggest that the velocity analysis used for migration and time-to-depth conversion of the seismic data was not optimum. Furthermore some depth misties of several meters occurred where boreholes were drilled in faulted areas.

The occurrences of discontinuities and displacement of reflectors, suggesting the presence of faults, were manually picked. Initially, faults were delineated at every fifth inline and crossline and then at every single seismic line to ensure that minor faults were not missed.

5. Results

7.1 Seismic interpretation

Interpretation of the geological structures from the 3D seismic reflection data acquired in crystalline environments is often ambiguous and challenging because of the complex geology. Here, we used existing geologic information to reduce the ambiguity and focused our interpretation in the northern part of the 3D seismic cube, where most of the data have high SNR. The depth-structure map in Figure 6 shows the interpreted RS horizon and the location of the inline section shown in Figure 5 and the crossline sections shown in Figure 7 and 8. The RS reflector is well mapped in the area covered by the interpretation. The amplitude display of the seismic section in Figure 5 exhibits a strong and continuous reflection that is associated with the Roodepoort shale across most of the WWL goldfields.

At a regional scale, the RS exhibits a fairly variable strike and apparent dip across the study area possibly due to tilting during deformation. The RS seismic horizon strikes in a north-easterly direction and has an average dip of 22°SE. At depths between 3.7 km and 4.0 km the RS dips at approximately 20° - 22° south-east and at approximately 10° to 16° south-east at depths of 5.3 km - 5.7 km (*see* Fig. 5).

The RS is crosscut by second-order to third-order scale faults such as the Pretorius Fault (PF), Fault 1 (F1), Fault 2 (F2), Fault 3 (F3), Fault 4 (F4) and Fault 5 (F5), as shown in Figure 7 and 8. The most dominant feature is the Pretorius Fault, which is a north-northeast trending, second-order scale normal fault that steeply dips at ~75° - 80° to the west (Figure 7). As observed in the seismic data, the PF displays a variable vertical throw across the survey area, reaching a maximum vertical throw of 500 m and a minimum of 40 m in the north-eastern and south-western areas, respectively. The PF is part of a ~750 m wide Pretorius Fault Zone (PFZ), which has associated subordinate normal faults that displace the RS horizon by a vertical throw as small as 25 m. The third-order scale F1 is a north-south

trending and westerly dipping (~70°) reverse fault that displaces the RS by 25 m - 30 m at a depth of approximately 4.6 km.

The F2 (west of the F1) is a second-order scale, north-east trending and an easterly dipping (~70°) normal fault. The fault has a variable vertical throw across the RS surface and reaches a maximum vertical throw of 60 m and a minimum of 30 m. Further to the west of the seismic section in Figure 7, the RS reflector is crosscut by the third-order scale, north-south trending and westerly dipping (~65°) fault (F3). The F3 is normal in form and has a vertical throw of ~35 m at approximately 5 km below the surface. However, at shallower depths the F3 is not seismically mapped as a clear discontinuity but rather as an amplitude disturbance on a seismic section. The disturbance may have been caused by dyke intrusions or mine infrastructures. In addition, there is no observed offset of the lithological units observed at these depths. Further to the western margin of the survey area, the RS is crosscut by a series of north-northeast trending faults (*see* Figure 6). The fault network consist of normal and thrust faults that dip at approximately 40° - 65° in an easterly direction and displace the RS by up to ~50 m. However, due to structural complexity and low SNR in these areas, the full extent of these faults across the RS surface could not be picked with confidence.

On its eastern side, the RS is crosscut by a second-order scale, north-west trending reverse fault (F4), dipping at an average of 63° to the east (Figure 8). The apparent dip angle of F4 slightly increases from ~55° to ~65° in the west and east, respectively. The F4 attains vertical throws in the range of 50 m - 100 m, with the largest vertical throws (~80 m - 100 m) observed further west of Figure 8 and at depths of 4.3 km - 4.5 km below the surface. Further to the east, the RS is crosscut by an east dipping reverse fault (F5) with vertical throws between 50 m - 60 m. At depths of 4.8 km to 5 km, F5 displaces the RS by a

maximum vertical throw of 100 m and it is subsequently truncated by the first-order scale Bank Fault.

The geometry of the Bank Fault and its timing of activity have been described by several authors (e.g., Gibson et al., 2000; Dankert and Hein, 2010; Manzi et al., 2013). Our interpretation of the fault is in agreement with that reported by Gibson et al. (2000) and Manzi et al. (2013) that the Bank Fault and its subordinate scale normal faults (e.g., Pretorius Fault) were likely formed during the Platberg Extension (2.70 - 2.64 Ga; Dankert and Hein, 2010). Moreover, the nature and timing of activity of the seismically mapped minor reverse faults in the WWL have previously been discussed by Dankert and Hein (2010). The mapping of these structures is critical for the mines as they may represent losses of mineable ground and potential safety hazards, as they may cause instabilities in the hangingwall leading to poor ground conditions. The geometry, depth positions and apparent dips of some of these structures have been confirmed by underground mapping and drilling (Dankert and Hein, 2010). Future mine development plans will need to be updated to take these new structural parameters into account, since this horizon is proximal to commercial gold deposits (mainly Carbon Leader Reef).

By further examining the inline and crossline sections, we notice that the sections are, in some parts, characterized by high amplitude anomalies that cannot be confirmed with underground mapped geological features (*see* Figure 7 and 8). We interpret these strong reflections to have been caused by developmental infrastructures (shaft, excavations and stopes), resulting from a high acoustic-impedance contrast between rocks and the air. This is possible since some parts of the seismic arbitrary lines were extracted from the mined out areas.

Furthermore, seismic sections exhibit some continuous near vertical features which are associated with highly attenuated seismic amplitudes across the survey areas. We attribute these seismic reflections to igneous intrusions (dykes), known to exist in the Witwatersrand Basin (Litthauer, 2009; Manzi et al., 2012b). The reason for the attenuation of the seismic amplitude, instead of strong reflections known to be associated with dykes and sills, may have been caused by the interaction of dykes with known methane gas within the basin, which is known to highly attenuate the seismic amplitude (Priest et al., 2005). The majority of these dykes strike north to north-northeast with thicknesses that vary from 1 m to 90 m. However, the ones that can be mapped by our 3D seismic data have a minimum thickness of 25 m, which is the vertical resolution limit of our data. Methane gas conduits (or gas escape features) from similar geologic environments elsewhere in the world are known to produce similar continuous low-amplitude seismic lineaments (*see* Dvorkin and Uden, 2004; Priest et al., 2005). The existence of the methane gas in the Witwatersrand basin is confirmed by the studies undertaken by Wanger et al. (2012) where they sampled these gases from fracture water during exploration drilling within these deep underground gold mines. These hydrocarbons have been found to have a strong correlation with dykes and faults (*see* Wanger et al., 2012; Manzi et al., 2012b). Most importantly, these geological features crosscut the RS, which is among the primary candidates considered to be the rock sources for hydrocarbons (mainly methane gas) within the basin. Therefore mapping these features is important for the mitigation of risks associated with methane explosions in the mines (Manzi et al., 2012b).

7.2 Ant-tracking

In seismic interpretation, it is essential to delineate geological features that are below the seismic resolution because they make the reefs impractical to mine and hence affect production. Following the traditional seismic interpretation of faults on the seismic sections,

we carefully applied a series of volumetric attributes to enhance the delineation of faults with vertical displacements below the traditional resolution criteria.

The smoothed conventional amplitude seismic volume shown in Figure 9a was used as input data (amplitude display) to compute the ant-tracking volumetric attribute and Figure 9b is the resultant volume. Figure 9b shows how the application of the ant-tracking technique has markedly improved the resolution in the data, and the minor continuous geological features can be more easily identified. It is also clear that the ant-tracking technique has enhanced the lateral continuity of the RS horizon within the ant-track volume. Another improvement in structural mapping is noted in Figure 9b, where the PF and its subordinate faults are better identified than on the conventional amplitude display in Figure 9a. We also see that most of the faults that crosscut the RS reflector can be tracked up the stratigraphy to crosscut the CLR and intersect the VCR at ~2.5 km. The PF crosscuts and offsets the West Rand Group, Central Rand Group and Ventersdorp Supergroup, but does not breach the base of the Transvaal Supergroup; normal displacement on the BF predates deposition in the Transvaal Basin, therefore restricting the tectonic evolution of the faults to pre-2.58 Ga. Again, this work confirms previous studies of Gibson et al. (2000), Gibson (2004), Dankert and Hein (2010) and Mambane et al. (2011).

Due to the high noise levels in conventional seismic sections it was difficult to extrapolate faults to shallower depth levels. Although the ant-tracking technique has successfully highlighted faults that crosscut the RS horizon, some of these faults cannot be tracked up stratigraphy to the overlying Central Rand Group and Ventersdorp Supergroup. This may suggest that these faults have vertical throws below the level required to see them at the other stratigraphic levels (mainly VCR and BLR) on the seismic sections. The other possible explanations for poor correlation of structures between stratigraphic levels could be (1) the large vertical separation between horizons, (2) poor reflectivity of markers within the

stratigraphic levels, and (3) the large range in dip angles of faults between the seismic horizons. Therefore, the linkage of displacements on the RS, VCR and BLR levels sometimes was uncertain. However, there are many fault traces that can be confidently projected from the VCR to the BLR horizons. These may represent faults that were reactivated during the post-BLR deformation event described by Coward et al. (1995), Gibson et al. (2000) and Dankert and Hein (2010).

To further enhance the structural and stratigraphic interpretation, we extracted depth slices from the conventional seismic volume (Figure 10a), the smoothed seismic volume using edge enhancement algorithms (Figure 10b) and the ant-tracking volume (Figure 10c). The amplitude depth slice reveals the partial mapping of the RS horizon and faults, while the smoothed seismic volume and ant-tracking technique successfully highlights minor faults that have vertical throws of less than 25 m, as well as stratigraphic features that manifest themselves through minor changes in the seismic waveform. The smoothed seismic volume in Figure 10b and ant-tracking technique in Figure 10c also show better continuity of horizons and the termination of the RS against the Bank Fault in the east, compared to the conventional amplitude display. The ant-tracking attribute, in particular, proved to be an excellent tool to map faults and the continuity of horizons when compared to the amplitude and the edge enhancement techniques. From Figure 10c we observe that the RS horizon forms a rollover anticline against the Bank Fault, which is dissected by numerous fractures that are not clearly defined in the amplitude display. The formation of the anticline is interpreted to have occurred during the reactivation of the Bank Fault as a normal listric fault during the Platberg Extension Event (Dankert and Hein, 2010; Manzi et al., 2012b). Most importantly, the ant-tracking depth slice shows the better mapping of the fractures associated with the Bank Fault Zone, which were not clear on both the conventional amplitude and edge enhancement displays.

7.3 Horizon based attributes

In order to test the feasibility of seismic horizon resolution of minor structures, we applied 3D horizon-based seismic attributes. Unfortunately, variability in reflector waveform, as well as seismic noise, can cause difficulties when extracting attributes on the picked horizons. In order to minimize the effects of noise introduced during picking, we applied post-fault interpolation smoothing operators such as the mean and median smoothing algorithms to the Roodepoort shale surface. These smoothing algorithms are used in seismic interpretation to detect minor faults, to filter-out the isolated horizon noise, and to separate gross structural configurations (long wavelength) from faults and dykes (short wavelength). They also tend to maximize the resolution for the identification and location of faults, eliminate errors resulting from false complex geometries created by conventional picking around faults, and thus minimize unrealistic fault-horizon geometries. The advantage of applying this algorithm post-picking is that filtering only occurs within the horizon rather than across the faults. However, care must be taken not to filter out the faults and dykes, since these operators are capable of filtering-out noise in addition to real faults and dykes, which can significantly affect the fault geometry. Figure 11a shows the depth structure map of the Roodepoort shale horizon obtained from conventional picking (manual picking) and Figure 11b shows the Roodepoort shale horizon after applying the surface smoothing tools. From the first inspection of the two surfaces, it can be seen that the data quality in Figure 11a has been significantly improved through filtering and the noise in the data have been attenuated while retaining the faults, as shown in Figure 11b.

Further inspection of the conventionally picked RS surface shows that the western part of the surface is more structurally unstable compared to the eastern part. The western part of

the RS surface is dominated by north-northeast trending faults while the eastern part of the surface is dominated by north-west and minor north-east trending faults. It is important to note that the areas characterized by low SNR were near the survey boundaries (mainly northern part of the survey), implying that the poor quality of the data was due to low fold-of-coverage and poor migration at the edges of the investigated volume. We did not interpret the south-west region of the survey area due to low SNR, owing to complex fault geometries. The highly faulted south-western flank of the seismic survey is believed to be the result of the Vredefort impact structure that affected the Witwatersrand Basin (~2.02 Ga, Gibson et al., 1997). In the areas that were interpretable in the south-western flank, we noticed fault regimes being more prominent in one direction, a phenomenon that of course is controlled by the tectonic activity in the area.

For detailed analysis of the study area, the smoothed RS depth structure map in Figure 11b was divided into two blocks, namely Block A (covering the western part of the survey area) and Block B (covering the eastern part of the survey area). To illustrate how different attributes enhance structural mapping resolution, we display dip, dip-azimuth and edge detection attribute maps for the RS horizon. Although the smoothed depth structure map in Figure 11b has better mapping resolution than the conventional display in Figure 11a, we do not see many illuminations of faults and dykes as observed in the dip, dip-azimuth and edge detection maps.

In Figure 12a-c, we indicate several normal faults that have been delineated by seismic attributes. For example, the dip attribute display in Figure 12b has been successful in imaging the PF fault more clearly than achieved by the smoothed depth structure map in Figure 12a. The dip map, however, does not achieve the best results in mapping the north-northeast trending faults compared to the azimuth map in Figure 12c. There are several

plausible reasons why this happened: (1) the faults have small displacements that fall below the resolution of the seismic wavelet, (2) the apparent dip angle of the faults are close to that of the horizon (*see* Rijks and Jauffred, 1991), and (3) the faults are associated with multiple movements that do not cause significant vertical displacements of the seismic waveform but instead cause simple warping of the interface. Most importantly, for this study, is that minor faults with complex geometries can be better mapped using volumetric attributes than conventional interpretations.

The azimuth attribute computed for the RS horizon has shown some degree of faulting that was not observed in the depth structure map and dip attribute map. To compare between the azimuth and dip maps, the dip attribute map could only clearly enhance the Pretorius Fault whereas the azimuth attribute map has highlighted a number of faults, including the (1) Pretorius Fault, (2) F1, (3) F2, (4) F7 and (5) the N-NE Fault set. Although slightly detected on the smoothed RS surface, the azimuth attribute map has intensified the appearance of the N-NE Fault set and revealed that there could be at least three north-northeast trending faults in this region, parallel to each other. Most importantly, the azimuth attribute map has identified a north-south trending fault (F9) in the southern part of the map, which has not been detected by either conventional picking or dip attributes. Furthermore the edge detection map in Figure 12d hints at the presence of more than three north-northeast trending faults in the N-NE Fault set region. Further south of the edge detection attribute map F10 trending in the same north-south direction as F9 has been enhanced.

The dip and azimuth attributes computed for Block B of the RS surface have been successful in enhancing the detection of faults not clearly seen on the eastern side of the smoothed RS surface shown in Figure 13a-13c. By analysing the dip attribute map in Figure 13b, we take note of the enhancement of F5 and F11 which consist of two fault segments

trending in the north-west direction. Importantly, the edge detection map in Figure 13d has enhanced the north-east trending fault (F13), which is not clearly detectable by conventional picking, the dip, or the azimuth attribute maps. The F13 crosscuts the F11 and F5 on the eastern margin of the RS surface, as well as the F1 and PF in the central regions of the surface. Further inspection of the edge detection map shows that F1 is displaced north of its original position by F13. Thus F13 is younger than the F1, F5 and the F11. It is worth noting that the 3D edge detection maps reveal very detailed fault networks that are not easily seen on the dip and azimuth attribute maps.

The final result of this research has been the development of a regional strato-structural model of the study area defined from conventional and attributes analysis (Figure 14). The model displays VCR orebody paleotopography, fault geometries (i.e., dip angles, strike, and dip directions), dykes, and continuity of structures across the mines in the study areas.

6. Discussion

In this paper, we have applied volumetric and horizon-based attributes to the 3D reflection seismic data from the West Wits Line goldfields to better enhance the delineation of geological features with throwvertical throws below the recommended seismic resolution criteria. We achieved this by interpreting the uppermost reflective unit of the West Rand Group, the Roodepoort shale (~5 km below the surface) because it is a strong seismic marker and it is proximal to the commercial but non-seismic reflective Carbon Leader Reef deposit. With the exception of the low SNR of the data in the south-western part of the surveyed area due to low-fold-of coverage, poor migration and structural complexity, the overall quality of the seismic data was good, providing good delineation of faults. Knowing

the structural architecture associated with this deposit can not only enhance the understanding of the tectonic evolution of the goldfields near specific gold mines but can be used to guide future exploration of the Carbon Leader Reef and other economic auriferous conglomerate reefs within the basin.

As demonstrated in this study, the strong seismic reflection associated with the Roodepoort shale is caused by a significant acoustic impedance contrast at the quartzite-shale boundary. Thus, it is the top of the RS that is directly imaged on the seismic data. Initial interpretation of the top of the RS was achieved through conventional picking of the horizon on seismic sections followed by picking of faults where discontinuities occurred. The integration of the seismic data with the borehole data was key to constraining the depth location of the RS horizon and understanding many of the reflections that occur above and below the RS seismic reflector. The conventional interpretation of the RS depth structure map provides a first pass analysis of the first-order scale structures dominating the WWL goldfields but lacked the resolution to map the subtleminor geological features (second-and third-order scale faults).

In general, the RS depth structure map is characterized by numerous steeply dipping (~65° - 80°) faults as well as amplitude anomalies that coincided with the location of stopes and shaft infrastructures. The faults in Block A trend predominantly north-east and some are too complex to identify on the migrated cross sections. These include complex multi-segments of the PFZ (40 m - 500 m throwvertical throw). The area covered by Block B is predominantly dissected by steeply dipping (~65° - 80°) normal and reverse faults with varying throwvertical throws (40 m - 500 m throwvertical throw) and orientations. On a small scale, the main outcome of the volumetric attributes and horizon-based edge detection attributes has been an improved detection of the structural architecture of the horizon that

had not been mapped adequately in the conventional depth-structure map. In particular, the ant-tracking technique has revealed the continuity of some of the small- and large-scale faults in the 3D seismic volume, including the previously known, seismically active Pretorius Fault. The seismic activity of this fault has been confirmed by a number of seismic events that have occurred along the fault zones (Durrheim et al., 2005; Linzer et al., 2007; Heesakkers et al., 2011; Riemer and Durrheim, 2012). The identification of the dual nature of the Pretorius Fault concur with studies by van der Westhuizen et al. (1991), Beach and Smith (2007) and Dankert and Hein (2010) and that the Witwatersrand Basin underwent inversion tectonics during and after the deposition of the Central Rand Group (extension to compression) and the Ventersdorp Supergroup (compression to extension). This information can be incorporated into mine planning and designs so as to mitigate various hazards facing miners, such as rock falls and rock-bursts associated with mine seismic events. In addition to the mapping of the geometry, the identification of the subordinate (small-scale) faults associated with the PF is important as they are likely to cause weak ground conditions during mining. Furthermore, the variations in dip angles and throwvertical throws of the structures, the constraints on fault orientations and timing of activity across the mining areas, are significant and must also be factored into mine planning and development.

On average, boreholes drilled from underground have a good tie (0 - 20 m) with the RS reflector, although the RS at some depths is slightly deeper than the actual depths of the borehole formation tops. The depth misties have been interpreted to be attributed to the greater distance between these boreholes, and errors in the velocity field used for depth conversion and/or borehole deviation at depth. From the ant-tracking techniques, it is also observed that many of these faults crosscut the top of the West Rand Group, Central Rand Group and the VCR at the base of the Ventersdorp Supergroup. As mentioned before, these faults displace the RS and VCR by hundreds of metres but do not crosscut the BLR at the base of the Transvaal Supergroup. This implies that these faults were active prior to the

deposition of the BLR. Thus, the vertical extent of these faults can be used during mining activities that occur between the BLR and top of the West Rand Group. In addition, the seismic data have mapped methane gas conduits (dykes) features which are associated with high attenuation of seismic amplitudes. While the dykes associated with methane gas and water in the basin have been confirmed by seismic, borehole and stable isotope data, it should be noted, however, that the existence of these dykes cannot be validated without confirming with underground mapped data. Some authors (e.g., Cook, 1998; Manzi et al., 2012b; Wanger et al., 2012) have suggested dykes and faults as possible conduits for the migration of methane gas from various sources (e.g., shale units, coal seams and mantle) to the mining levels in the Witwatersrand goldfields. The proposed general idea is that: methane migrates from the source to mine workings through faults and fractures, either as a gas or dissolved in saline ground water. However, the sources of these methane gases still remain unclear. Nevertheless, considering that the faults that have been identified in this study crosscut both the RS and the economic horizons, the RS could be the most probable candidate for the source of methane. Continuing the research, we plan on using stable carbon and nitrogen isotope data from the gold mines to provide an explanation regarding the interaction between gas-water-fracture and methane explosion in deep underground gold mines. This could assist in mitigating risks faced by miners in the mines, which are caused by methane explosions.

The application of horizon-based seismic attributes, including dip, dip-azimuth and edge detection to the data have successfully imaged a number of faults that were not visible on the seismic sections and depth structure map. Comparison of the dip and azimuth attribute displays show that the azimuth attribute display provides better delineation of faults relative to the dip attribute display. The edge detection attribute, in particular, has several advantages over the dip and dip-azimuth maps, including mapping faults with variable orientation and vertical throws and variable colour tables that maximize the usefulness of

this attribute. The application of these techniques to old 3D seismic data can reduce structural risks in strategic mine planning. For example, several structures interpreted through traditional picking by previous workers in the mining areas were found not to exist, whereas many new structures were identified. Finally, these attributes enhanced the accuracy in positioning and projecting traditionally picked surfaces to the 3D RS topographic map. Although we have made an attempt to constrain our structural interpretation with borehole data, there is still some ambiguity in the dip and spatial positioning of the interpreted fault surfaces. These may be the result of low SNR of the seismic data and the poor velocity model used for prestack time migration. A new velocity field and prestack depth migration could improve the quality of the structural mapping resolution. Our final structural model can be used for the CLR exploration projects and it can be factored into future mine development strategies for better placement of shafts and improved life-of-mine planning. The high degree of structural resolution afforded by this interpretation at the RS level will guide future exploration drilling activities in the seismically transparent CLR and enable the layout of tunnels and stopes to be optimized.

7. Conclusion

We have developed a 3D lithological and strato-structural modelstructural model of the Roodepoort shale by integrating 3D seismic data, seismic attributes, borehole logs and underground mapping information. Seismic attributes were used to enhance faults not detectable on the conventional seismic sections. Volumetric and horizon-based seismic attributes were applied to the data for qualitative interpretation of complex structural patterns throughout the seismic volume and interpreted horizons. The ant-tracking attribute was used to identify and track the continuity of faults throughout the seismic cube. Applying the ant-tracking attribute to our data improved the imaging of (1) strong seismic reflectors, such as the Black Reef, Ventersdorp Contact Reef and the Roodepoort shale throughout the seismic volume, (2) faults in structurally complex regions allowing us to confidently track

them to shallower depths. Horizon based attributes, such as dip, dip-azimuth and edge detection were used to image faults with displacements below the seismic resolution limit. These techniques were not only successful in imaging subtleminor structures which were partially detected on conventional seismic sections, but also imaged structures that were seismically invisible on the amplitude display sections. Furthermore the seismic attribute technique improved the lateral continuity of faults on the Roodepoort shale surface, which aided in characterizing fault continuity and determining cross-cutting relationships. The application of various seismic attributes has enhanced a larger number of faults which intersect the top of the West Rand Group, some with offsets below 25 m that were undetected by manual picking. Therefore only relying on conventional interpretation methods to reveal structures and their relationships could result in a biased interpretation and inaccurate mine development plans that could compromise workers safety. Underground mapping and structural mapping from vertical borehole data had given no indication of such minor faults crosscutting the RS and the horizons above. Interpretation of seismic data using seismic attributes has proven to provide considerably more detail than was possible with conventional seismic interpretation and borehole data.

This model will aid in understanding the structural framework of the Carbon Leader Reef located at the base of the Central Rand Group ~350 m above the top of the West Rand Group.

Acknowledgements

We would like to thank Anglo Gold Ashanti Ltd, Sibanye Gold Ltd, CIMERA (Centre of Excellence for Integrated Mineral and Resource Analysis) and Thuthuka Funding (NRF) for sponsoring this research. We also thank IHS Kingdom for providing the Kingdom Suite® interpretation software and Schlumberger for providing the Petrel® interpretation software.

References

Armstrong, R., Compston, W., Retief, E., Williams, I. and Welke, H., 1991, Zircon ion microprobe studies bearing on the age and evolution of the Witwatersrand triad: *Precambrian Research,* **53**, 243-266.

Bacon, M., Simm, R. and Redshaw, T., 2003, 3-D seismic interpretation, first ed. Cambridge University Press, 84, 102-117, 146.

Basir, H. M., Javaherian, A. and Yaraki, M. T., 2013, Multi-attribute ant-tracking and neural network for fault detection: a case study of an Iranian oilfield: *Journal of Geophysics and Engineering*, **10**. doi:10.1088/1742-2132/10/10/015009.

Beach, A. and Smith, R., 2007, Structural geometry and development of the Witwatersrand Basin, South Africa, *in* A. C. Ries, R. W. H. Butler, and R. Graham, eds., *Deformation of the continental crust: The Legacy of Mike Coward: Geological Society, Special Publication*, **272**, 533-542.

Brown, A. R., 1996, Seismic attributes and their classification: *The Leading Edge*, **10**, 1090.

Chopra, S., Castagna, J. and Portniaguine, O., 2006, Seismic resolution and thin-bed reflectivity inversion: *CSEG Recorder,* 19-25*.*

Chopra, S., Castagna, J. and Xu Y., 2009, Thin-bed reflectivity inversion and some applications: *First Break*, **27**, 17-24.

Cook, A. P., 1998, The occurrence, emission, and ignition of combustible strata gases in Witwatersrand gold mines and Bushveld platinum mines, and means of ameliorating related ignition and explosion hazards: Final project report, project GAP 504, Safety in Mines Research Advisory Committee, 89.

Coward, M. P., Spencer, R. M. and Spencer, C.E., 1995, Development of the Witwatersrand Basin, South Africa: *Geological Society of London, Special Publication* **95** (1), 243-269.

Dalley, R. M., Gevers, E. C. A., Stampfli, G. M., Davies, D. J., Gastaldi, C. N., Ruijtenberg, P. A. and Vermeer, G. J. O., 1989, Dip and azimuth displays for 3D seismic interpretation: *First Break*, **7**, 86-95.

Dankert, B. T. and Hein, K. A., 2010, Evaluating the structural character and tectonic history of the Witwatersrand Basin: *Precambrian Research,* **177**, 1-22.

De Kock, W. P., 1964, The geology and economic significance of the West Wits Line, *in* S. H. Haughton, eds., *The geology of some ore deposits in southern Africa: Geological Society of South Africa,* **1**, 323-386.

Duff, D., Hurich, C. and Deemer, S., 2012, Seismic properties of the Voisey's Bay massive sulphide deposit: Insights into approaches to seismic imaging: *Geophysics*, **77**, WC59-WC68. doi:10.1190/GEO2011-0483.1.

Durrheim, R. J., 1986, Recent reflection seismic developments in the Witwatersrand basin, *in* M. Barazangi, and L. Brown, eds., *Reflection seismology, a global perspective: geodynamics series. Washington: American Geophysical Union*, **13**, 77-83.

Durrheim, R. J., Spottiswoode, S. M., Roberts, M. K. C. and van Z. Brink A., 2005, Comparative seismology of the Witwatersrand Basin and Bushveld Complex and emerging technologies to manage the risk of rock bursting: *The Journal of the South African Institute of Mining and Metallurgy*, **105**, 409-416.

Dvorkin, J. and Uden, R., 2004, Interpreter's corner—seismic wave attenuation in a methane hydrate reservoir: *The Leading Edge*, **23**, 730-732.

Engelbrecht, C. J., Baumbach, G. W., Matthysen, J. and Fletcher, P., 1986, The West Wits Line, *in* C. A. Anhaeusser, and S, Maske, eds., *Mineral deposits of southern Africa*, **1**, 599-648.

Frimmel, H. E. and Gartz, V. H., 1997, Witwatersrand gold particle chemistry matches model of metamorphosed, hydrothermally altered placer deposits: *Mineralium Deposita,* **32**, 523-530.

Frimmel, H. E. and Minter, W. E. L., 2002, Recent developments concerning the geological history and genesis of the Witwatersrand gold deposits, South Africa: *Society of Economic Geologists, Special Publication,* **9**, 17-45.

Frimmel, H. E., Groves, D. I., Kirk, J., Ruiz, J., Chesley, J. and Minter, W. E., 2005, The formation and preservation of the Witwatersrand goldfields, the world's largest gold province: *Economic Geology 100th Ann.*, 769-717.

Gibson, R. L., Armstrong, R. A. and Reimold, W. U., 1997, The age and thermal evolution of the Vredefort impact structure: A single-grain U-Pb zircon study: *Geochimica et Cosmochimica Acta*, **61**, 1531-1540. doi:10.1016/S0016-7037(97)00013-6.

Gibson, M. A. S., Jolley, S. J. and Barnicoat, A. C., 2000, Interpretation of the Western Ultra Deep Levels 3D seismic survey: *The Leading Edge,* **19**, 730-735.

Gibson, M. A. S., 2004, Goldfields KEA 3D Seismic Project: Final Report. Unpublished report to Gold Fields Mining, 52.

Heesakkers, V., Murphy, S. and Reches, Z., 2011, Earthquake rupture at focal depth, part 1: Structure and rupture of the Pretorius Fault, Tau-Tona mine, South Africa: Journal of *pure and applied geophysics*, **168**, 2395-2425.

Jolley, S. J., Freeman, S. R., Barnicoat, A. C., Phillips, G. M., Knipe, R. J. and Pather, A., 2004, Structural controls on Witwatersrand Gold mineralization: *Journal of Structural Geology,* **26**, 1026-1086.

Kositcin, N. and Krapež, B., 2004, SHRIMP U-Pb detrital zircon geochronology of the late Archaean Witwatersrand Basin, relation between zircon provenance age spectra and basin evolution: *Precambrian Research*, **129**, 141-168. doi:10.1016/j.precamres.2003.10.011.

Krapež, B., 1985, The Ventersdorp Contact placer: a gold-pyrite placer of stream and debris-flow origins from the Archaean Witwatersrand Basin of South Africa: *Sedimentology*, **32,** 223-234.

Linzer, L. M., Bejaichund, M., Cichiwicz, A., Durrheim, R. J., Goldbach, O. D., Kataka, M. O., Kijko, A., Milev, A. M., Saunders, I., Spottiswoode, S. M. and Webb, S. J., 2007, Recent research in seismology in South Africa: *South African Journal of Science*, **103**, 419-426.

Litthauer, A., 2009, *Geochemistry of the Dykes in the Carletonville Goldfield*: MSc thesis, University of the Free State.

Malehmir, A., Durrheim, R., Bellefleur, G., Urosevic, M., White, J., Milkereit, B. and Campbell, G., 2012, Seismic methods in mineral exploration and mine planning: A general overview of past and present case histories and a look into the future: *Geophysics*, **77** (5), WC173-WC190.

Malehmir, A., Koivisto, E., Manzi, M., Cheraghi, S., Durrheim, R. and Bellefleur, R., 2013, A review of reflection seismic investigations in three major metallogenic regions: The Kevitsa Ni-Cu-PGE district (Finland), Witwatersrand goldfields (South Africa), and the Bathurst Mining Camp (Canada): *Ore Geology Reviews*, **56**, 423-441. doi:10.1016/j.oregeorev.2013.01.003.

Malinowoski, M., Schetselaar, E. and White, D. J., 2012, 3D seismic imaging of volcanogenic massive sulphide deposits in the Flin Flon mining camp, Canada: part 2—forward modelling: *Geophysics*, **77**, WC81-WC93. doi:10.1190/GEO2011-0474.1.

Mambane, P. W., Hein, K. A. A., Twemlow, S. G. and Manzi, M. S. D., 2011, Pseudotachylite in the south boundary fault at the Cooke Shaft, Witwatersrand Basin, South Africa: *South African Journal of Geology*, **114**, 109-120.

Manzi, M. S. D., Gibson, M. A. S., Hein, K. A. A., King, N. and Durrheim, R. J., 2012a, Application of 3D seismic techniques to evaluate ore resources in the West Wits line

Goldfield and portions of the West Rand Goldfield, South Africa: *Geophysics,* **77**, WC163-WC171.

Manzi, S. D., Durrheim, R. J., Hein, A. A. and King, N., 2012b, 3D edge detection seismic attributes used to map potential conduits for water and methane in deep gold mines in the Witwatersrand Basin, South Africa: *Geophysics*, **77** (5), WC133-WC147.

Manzi, M. S. D., Hein, K. A. A., King, N. and Durrheim, R. J., 2013, Neoarchaean tectonic history of the Witwatersrand basin and Ventersdorp Supergroup: new constraints from high resolution 3D seismic reflection data: *Tectonophysics*, **590**, 94-105. doi:10.1016/j.tecto.2013.01.014.

McCarthy, T. S., 2006, The Witwatersrand Supergroup, *in* M. R. Johnson, C. R. Anhaeusser, and R. J Thomas, eds., *The geology of South Africa*: G*eological Society of South Africa,* 155-186*.*

Moon, C. J. and Whateley, M. K., 1989, Witwatersrand conglomerate gold: West Rand, *in* A. M. Evans, eds., *Introduction to mineral exploration*, Blackwell science, **91**, 258-291.

Myers, R. E., McCarthy, T. S., Bunyard, M., Cawthorn, R. G., Falatsa, T. M., Hewitt, T., Linton, P., Myers J. M., Palmer, K. J. and Spencer, R., 1990a, Geochemical stratigraphy of the Klipriviersberg Group volcanic rocks: *South African Journal of Geology*, **93**, 224-238.

Myers, R. E., McCarthy, T. S. and Stanistreet, I. G., 1990b, A tectono-sedimentary reconstruction of the development and evolution of the Witwatersrand Basin, with particular emphasis on the Central Rand Group: *South African Journal of Geology*,**93**, 180-201.

Neves, F. A., Zahrani, M. S. and Bremkamp, S., 2004, Detection of potential fractures and small faults using seismic attributes: *The Leading Edge*, **23**, 903-906.

Pedersen, S. I., Randen, T., Sonneland, L. and Steen, O., 2002, Automatic 3D Fault Interpretation by Artificial Ants: 64th Meeting, EAEG Expanded Abstracts, G037.

Pretorius, C. C., Steenkamp, W. H. and Smith, R. G., 1994, Developments in data acquisition, processing, and interpretation over ten years of south vibroseismic surveying in South Africa: Proceedings of the XVth CMMI Congress: *South African Institute of Mining and Metallurgy*, **3**, 249-258.

Pretorius, C. C., Muller, M. R., Larroque, M. and Wilkins, C., 2003, A review of 16 years of hardrock seismic of the Kaapvaal Craton, *in* D. W. Eaton, B. Milkereit, M. H. Salisbury, eds., *Hardrock Seismic Exploration: Geophysical Developments*, **10**: *Society of Exploration Geophysicists*, 247-268.

Priest, J. A., Best, I. A. and Clayton, C. R. I., 2005, Attenuation of seismic waves in methane gas hydrate-bearing sand: *Geophysical Journal International*, **164**, 149-159.

Riemer, K. L. and Durrheim, R. J., 2012, Mining seismicity in the Witwatersrand Basin: monitoring, mechanisms and mitigation strategies in perspective: *Journal of Rock Mechanics and Geotechnical Engineering,* **4** (3), 228-249.

Rijks, E. J. H. and Jauffred, J. C. E., M., 1991, Attribute extraction: An important application in any detailed 3D interpretation study: *The Leading Edge*, **10**, 11-19.

Robb, L. J., Charlesworth, E. G., Drennan, G. R., Gibson, R. L. and Tongu, E. L., 1997, Tectono-metamorphic setting and paragenetic sequence of Au-U mineralisation in the Archaean Witwatersrand Basin, South Africa, Australian Journal of Earth Sciences: *An International Geoscience Journal of the Geological Society of Australia*, **44** (3), 353-371. doi:10.1080/08120099708728317.

Safonov, G. Yu. and Prokofèv, V. Yu., 2006, Gold-bearing reefs of the Witwatersrand Basin: a model of syn-sedimentation hydrothermal formation: *Geology Ore Deposits*, **48**, 415-447.

Salisbury, M. H., Harvey, G. W. and Mathews, L., 2003, The acoustic properties of ores and host rocks in hardrock terranes, *in* D. W. Eaton, B. Milkereit, M. H. Salisbury, eds., *Hardrock Seismic Exploration: Geophysical Developments*, **10**: *Society of Exploration Geophysicists*, 9-19.

Sheriff, R. E., 1991, Encyclopedic Dictionary of Exploration Geophysics. SEG, Tulsa.

Stevenson, F., Higgs, R. M. A., Durrheim, R. J., 2003, Seismic imaging of precious and basemetal deposits in South Africa, *in* D. W. Eaton, B. Milkereit, M. H. Salisbury, eds., *Hardrock Seismic Exploration: Geophysical Developments*, **10**: *Society of Exploration Geophysicists*, 141-156.

Taner, M. T., Koehler, F. and Sheriff, R. E., 1979, Complex seismic trace analysis: *Geophysics* **44**, 1041-1063.

van der Westhuizen, W. A., De Bruiyn, H. and Meintjes, P. G., 1991, The Ventersdorp Supergroup: an overview: *Journal of African Earth Sciences,* **3**, 83-105.

Vieira, F. M. and Durrheim, R. J., 2002, Probabilistic mine design methods to reduce rock burst risk: *Journal of the South African Institute of Mining and Metallurgy*, 231-42.

Viljoen, M., 2009, The life, death and revival of the Central Rand goldfield: *Special Publication for the World Gold Conference*, 131-138.

Wanger, G., Moser, D., Hay, M., Mynent, S., Onstott, T. C. and Southam, G., 2012, Mobile hydrocarbon microspheres from > 2-billion-year-old carbon-bearing seams in the South African deep subsurface: *Geobiology*, **10**, 1472-4669.

White, R.E., 1991, Properties of instantaneous seismic attributes: *The Leading Edge*, **10**, 26-32.

Widess, M.B., 1973, How thin is thin bed?, *Geophysics*, **38**, 1176-1180.

Wronkiewicz, D. and Condie, K. C., 1987, Geochemistry of Archaean shales from the Witwatersrand Supergroup, South Africa: source-area weathering and provenance. Department of Geosciences, New Mexico: *Institue of Mining and Technology. Geochimica et Cosmochimica Acta*, **51**, 2401-2416.

LIST OF FIGURES

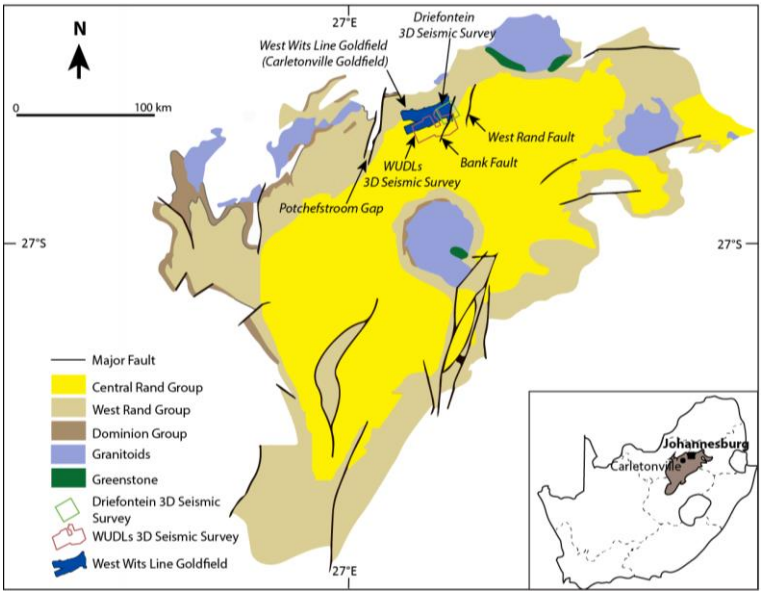


Fig. 1 Location map of the West Wits Line goldfields as well as the boundaries of the Western Ultra Deep Levels (WUDLs) and Driefontein 3D seismic survey of the Witwatersrand Basin, South Africa (after Smith et al., 2013). The insert shows the location of the Witwatersrand Basin in South Africa.

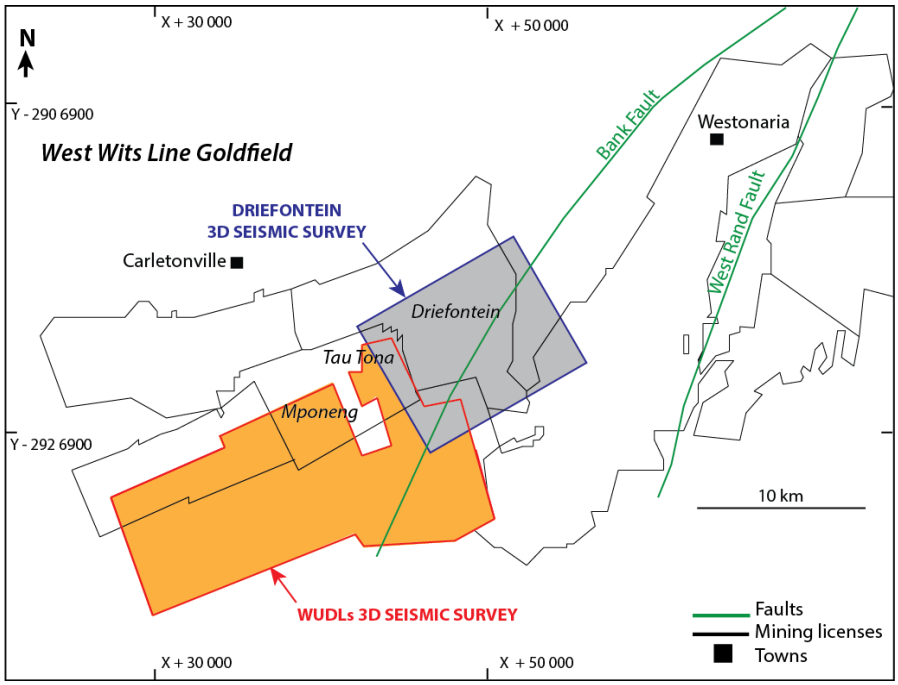


Fig. 2 Location of the Western Ultra Deep Levels (WUDLs) and Driefontein 3D seismic surveys covering the Mponeng, Tau-Tona and Driefontein gold mines along the West Wits Line goldfields (after Dankert and Hein, 2010).

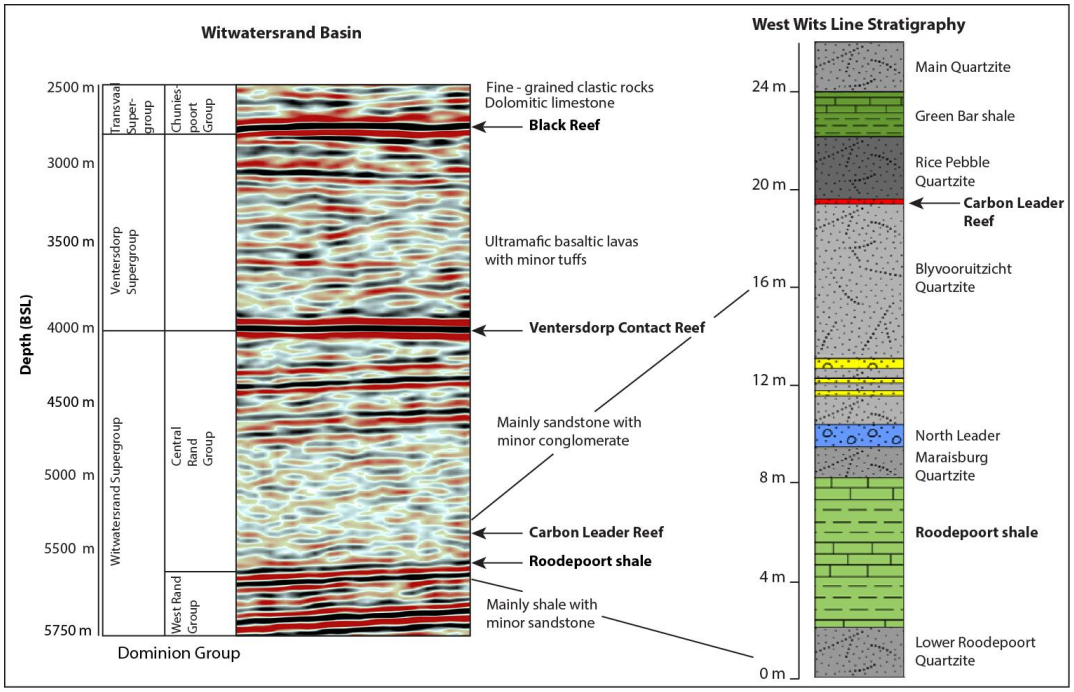


Fig. 3 Stratigraphy of the Witwatersrand Basin highlighting the location of strong seismic reflectors throughout the basin. The local stratigraphy at the base of the Central Rand Group and at the top of the West Rand Group along the West Wits Line is illustrated on the far right, as observed from borehole intersections (after Guy et al., 2010).

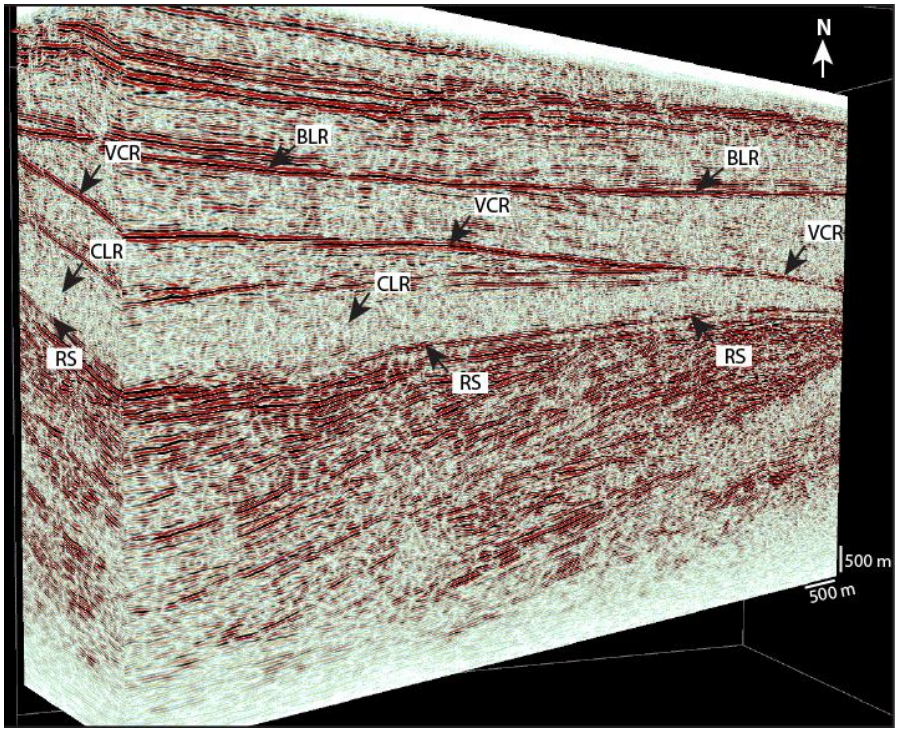


Fig. 4 Extent of the seismic volume along the West Wits Line showing strong seismic imaging of the Black Reef (BLR), Ventersdorp Contact Reef (VCR) and Roodepoort shale (RS) and the poor imaging of the Carbon Leader Reef (CLR).

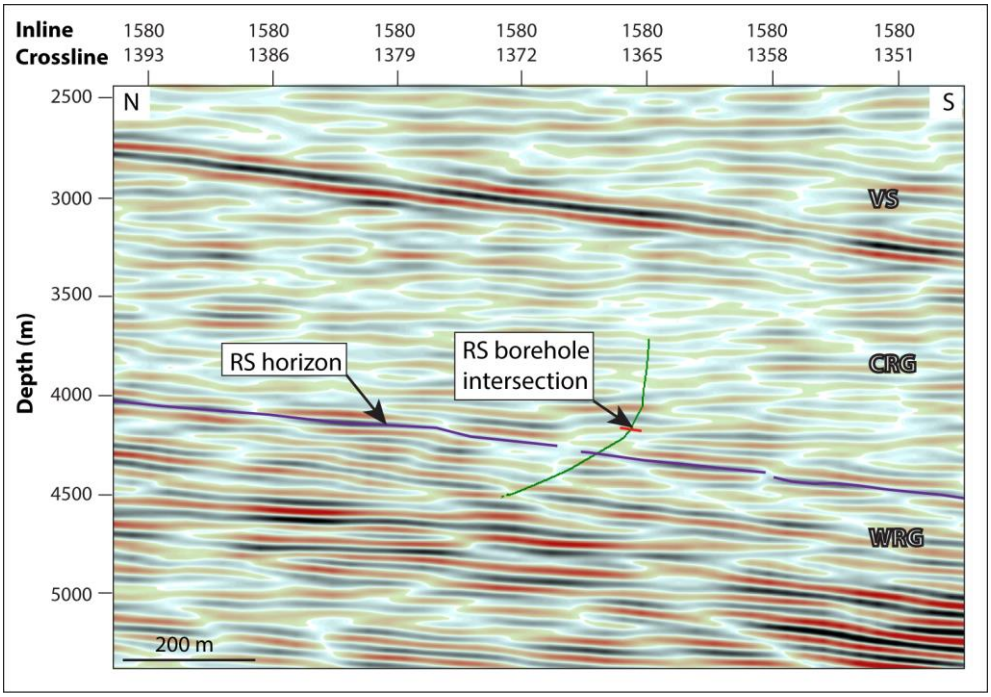


Fig. 5 West-east seismic section (amplitude display line A-A') showing the strong appearance of the Roodepoort shale (RS) at the top of the West Rand Group. The seismic section shows the depth mistie between the RS borehole intersection and the location of the RS horizon in the seismic volume. The borehole shown in the section is one of the few boreholes that intersect the West Rand Group along the West Wits Line goldfield.

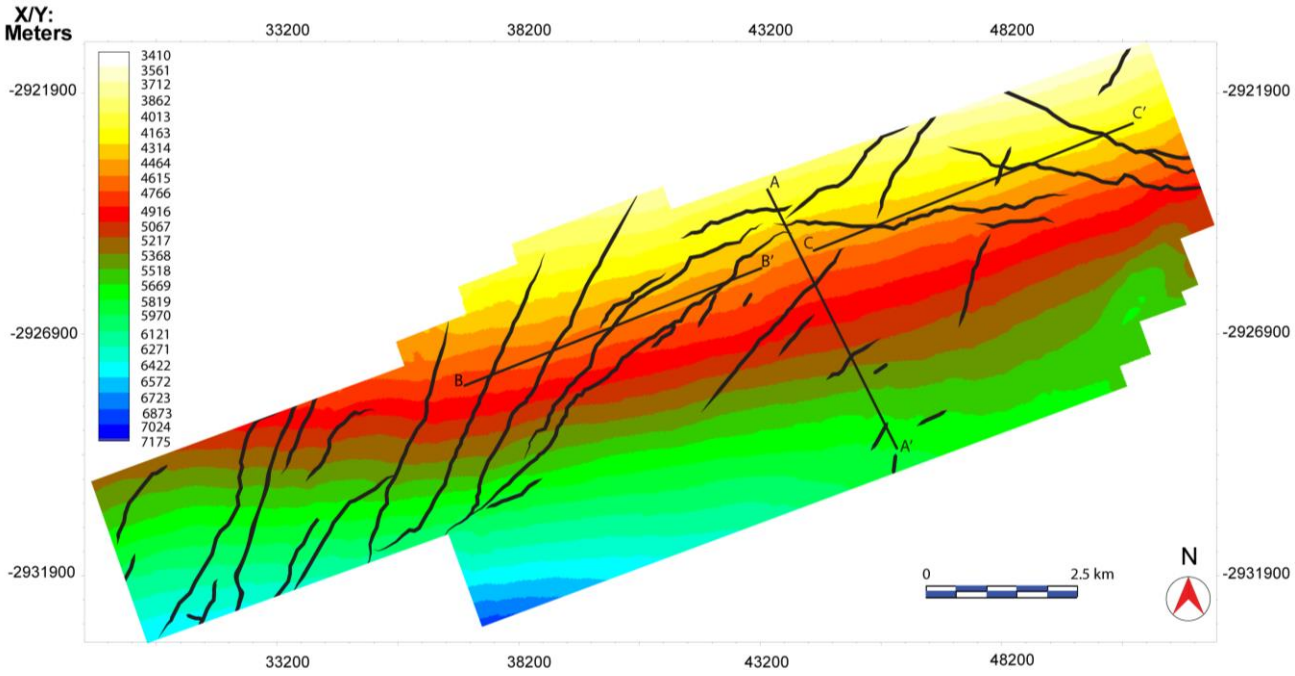


Fig. 6 Depth structural map of the Roodepoort shale derived from conventional picking. The map shows faults striking in various directions and the location of inline and crossline sections discussed in the main text.

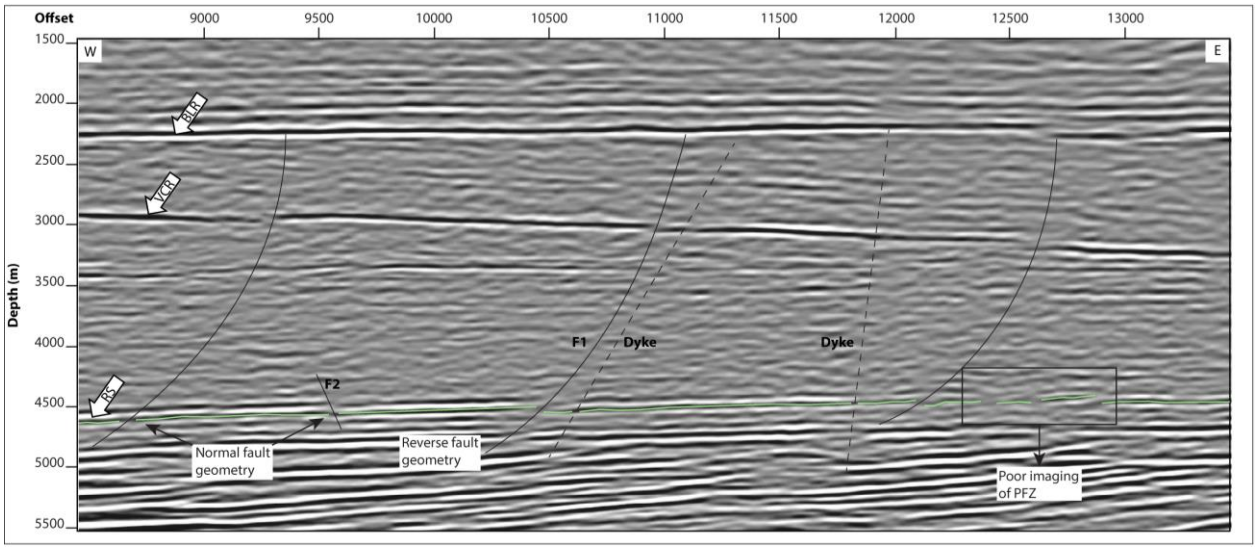


Fig. 7 Amplitude display seismic section (line B'-B'') showing the Pretorius Fault (PF), Fault 1 (F1), Fault 2 (F2) and Fault 3 (F3) cross-cutting the Roodepoort shale (RS) at the top of the West Rand Group. The solid lines indicate various faults while the dashed lines indicate dykes cross-cutting the stratigraphy. The oval shape highlights an area of high amplitude and the square shape encompasses a zone of the poorly imaged Pretorius Fault Zone (PFZ). Due to the low signal-to-noise of the amplitude display it is difficult to track faults and dykes up stratigraphy to the Ventersdorp Contact Reef (VCR) and the Black Reef (BLR) levels.

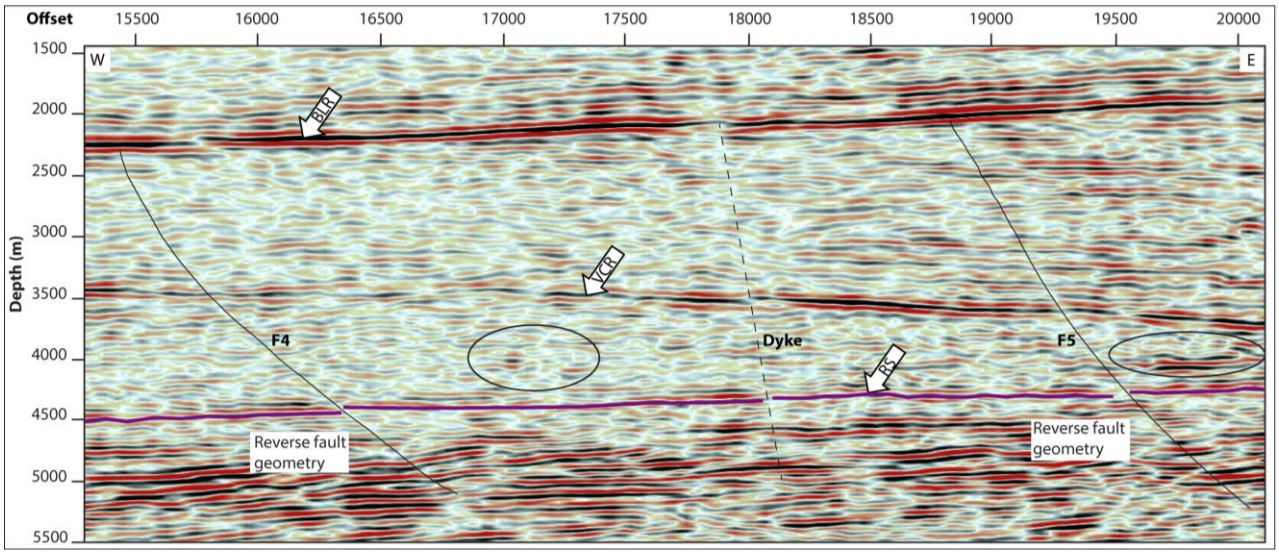


Fig. 8 Amplitude display seismic section (line C'-C'') showing the easterly dipping Fault 4 (F4) and Fault 5 (F5) cross-cutting the Roodepoort shale (RS) horizon at the top of the West Rand Group. The solid black lines highlight faults and the dotted lines show location of dykes in the stratigraphy. The circles encompass high amplitude areas that do not correspond to any horizon. Due to the low signal-to-noise of the amplitude display it is difficult to track faults and dykes up stratigraphy to the Ventersdorp Contact Reef (VCR) and the Black Reef (BLR) levels.

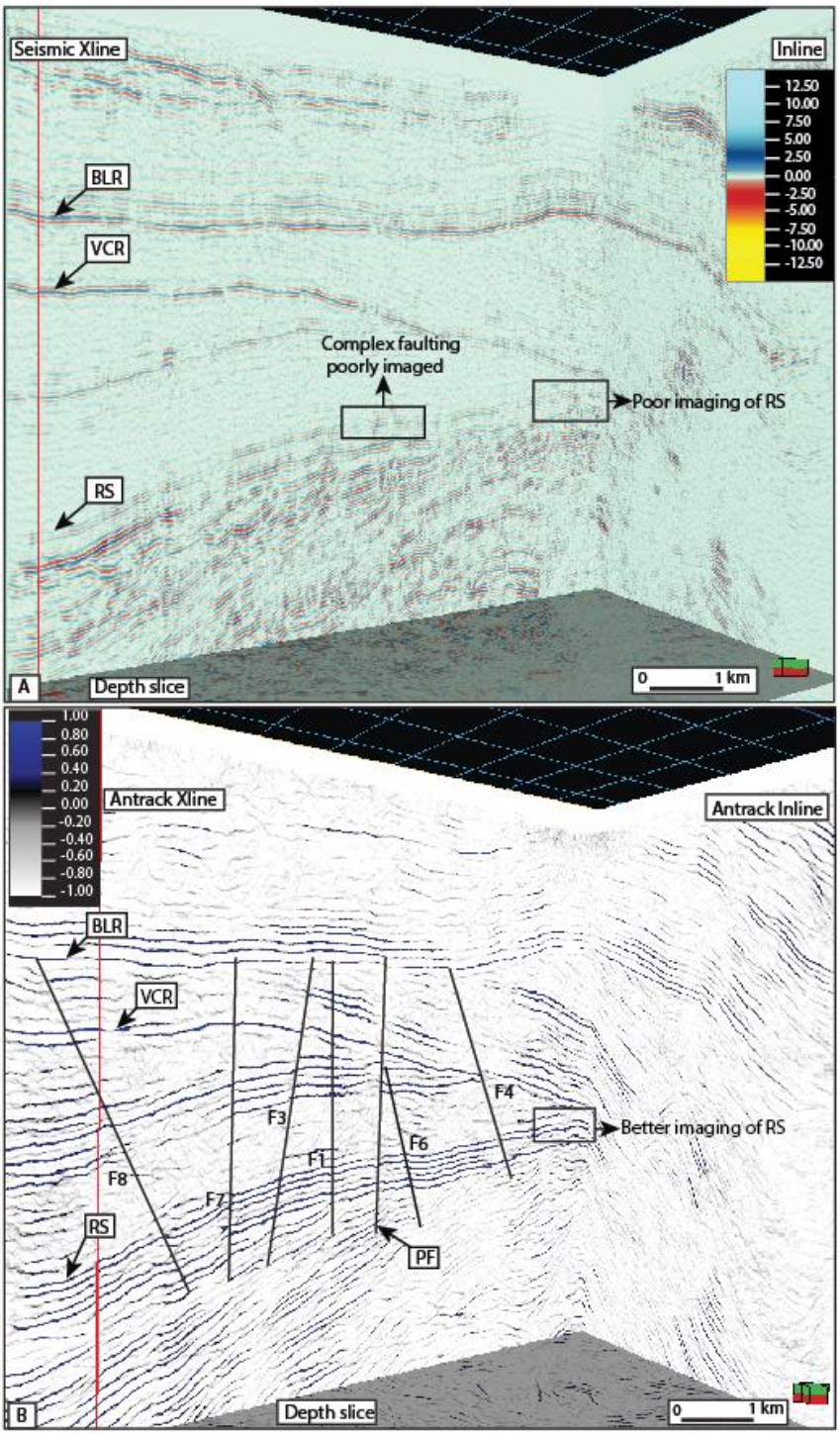


Fig. 9 Seismic inline, crossline (Xline) and depth slice showing the (a) regional continuity of the Black Reef (BLR), Ventersdorp Contact Reef (VCR) and Roodepoort shale (RS) before ant-tracking attribute is applied and (b) after the application of the ant-tracking algorithm. Note that the amount of noise in the data has been considerably attenuated resulting in the better imaging of the various seismic reflectors and the enhancement of faults in the antrack volume.

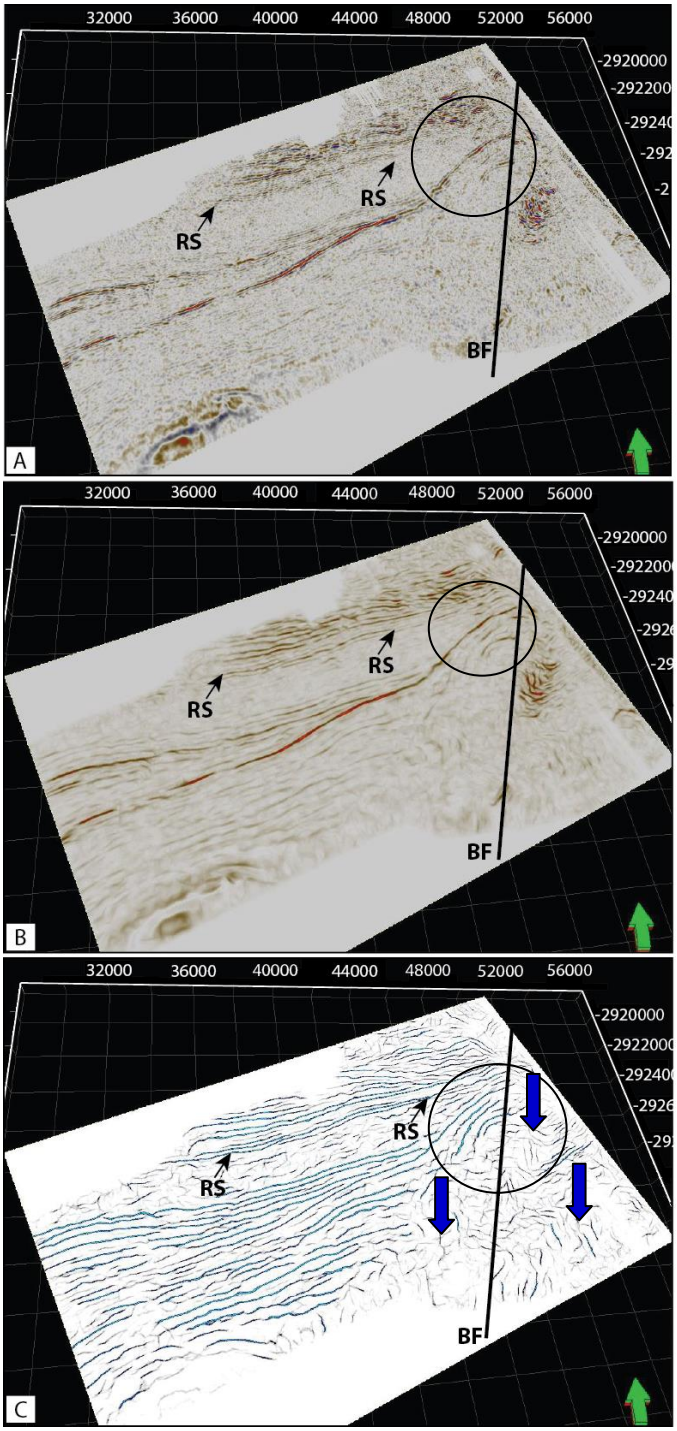


Fig. 10 Depth slices showing (a) the conventional seismic amplitude display, (b) edge enhancement display and (c) the ant-tracking attribute. Circle highlights the rollover anticline position and the blue arrows show the enhancement of fractures and minor faults. RS: Roodepoort shale, BF: Bank Fault.

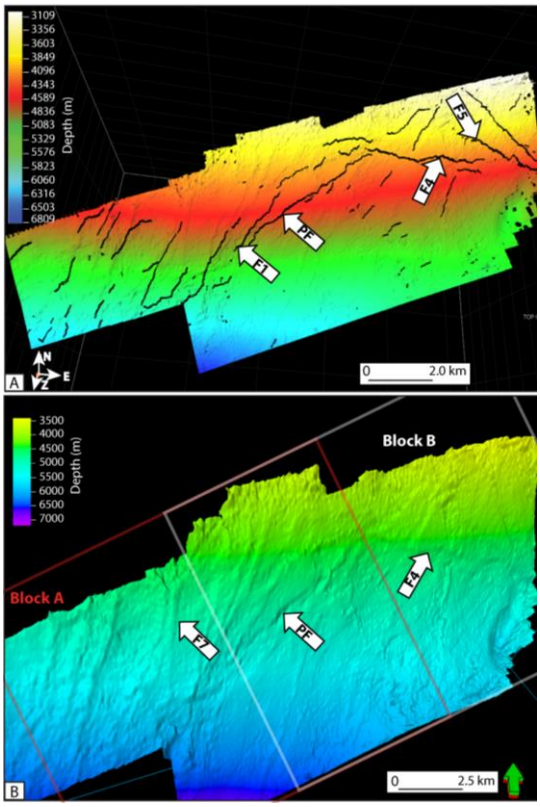


Fig. 11 Top of the West Rand surfaces obtained from (a) conventional picking and (b) smoothed top of the West Rand surface. The red square represents the boundary for Block A and the white square represents the boundary for Block B.

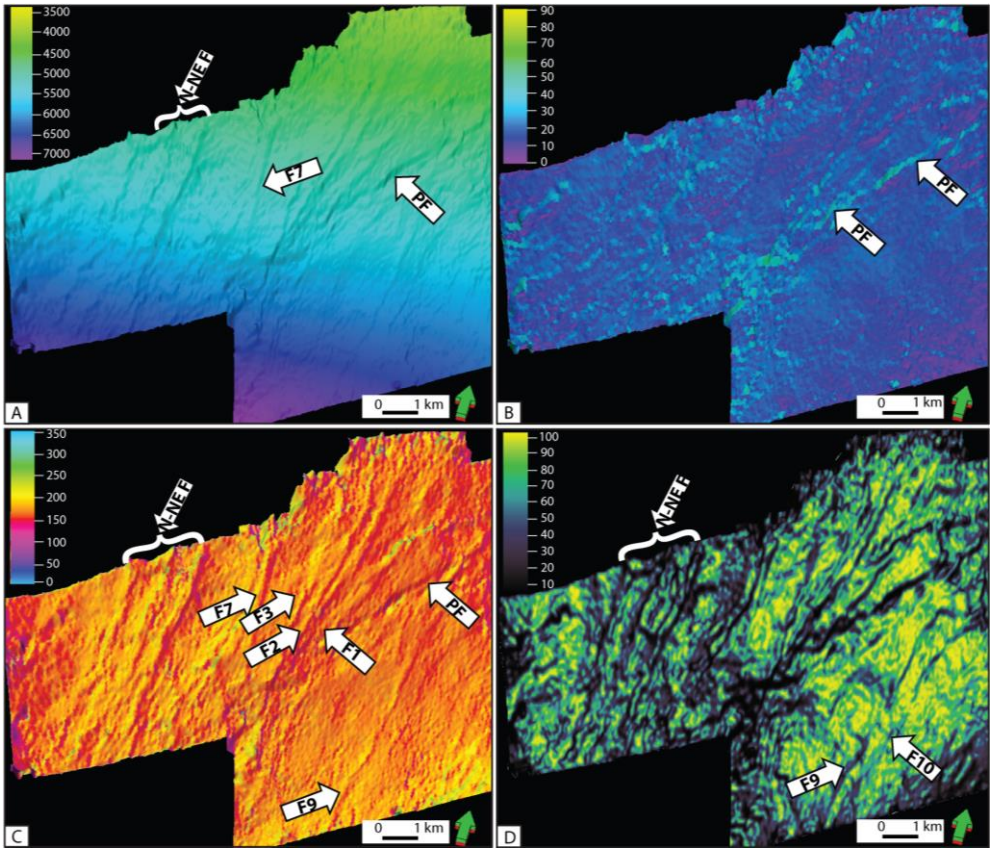


Fig. 12 Seismic attributes computed for the top of the West Rand horizon (block A). (a) The top of the West Rand smoothed surface (colour bar represents depth in metres). (b) Dip attribute display, showing the extent of the Pretorius Fault (PF) (colour bar given in degrees). (c) Azimuth attribute display, showing the enhancement of various faults on the western side of the RS surface (colour bar given in degrees). (d) The edge detection attribute display, clearly enhancing the north-northeast trending fault set and the north-south trending Fault 9 and Fault 10 ((colour bar given in percentages). The north-northeast trending fault set consists of more than 3 faults: north-northeast Fault-set (N-NE F-set), Pretorius Fault (PF), Fault 1 (F1), Fault 2 (F2), Fault 3 (F3), Fault 7 (F7), Fault 9 (F9) and Fault 10 (F10).

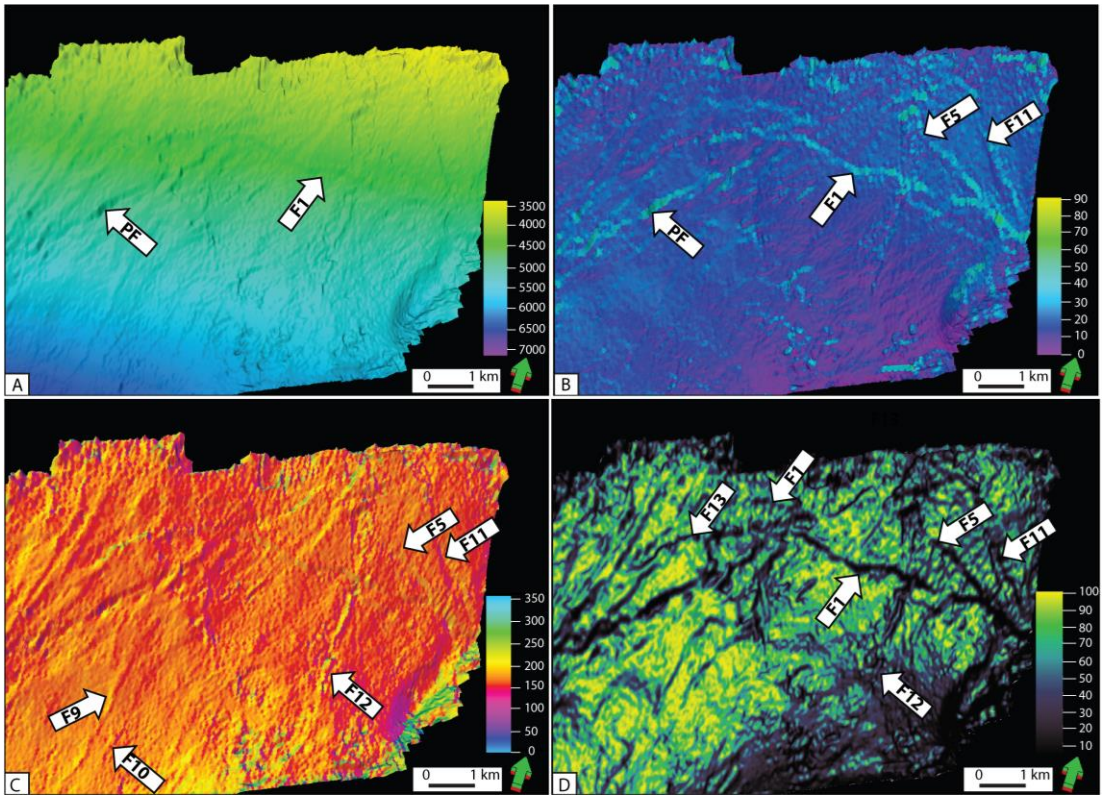


Fig. 13 Seismic attributes computed for the top of the West Rand horizon (block B). (a) The top of the West Rand smoothed surface (colour bar represents depth in metres). (b) Dip attribute display, showing the northeast trending Pretorius Fault (PF), northwest trending F1 as well as F5 and F11 (colour bar given in degrees). (b) Azimuth attribute display, showing the enhancement of the F10 and F12 (colour bar given in percentages). (c) The edge detection attribute display clearly shows the northeast trending F13 as well as the north-northeast trending F12. The edge detection map also enhances a displaced segment of F1 further north: Pretorius Fault (PF), Fault 1 (F1), Fault 5 (F5), Fault 9 (F9) and Fault 10 (F10), Fault (F10), Fault 11 (F11), Fault 12 (F12) and Fault 13 (F13).

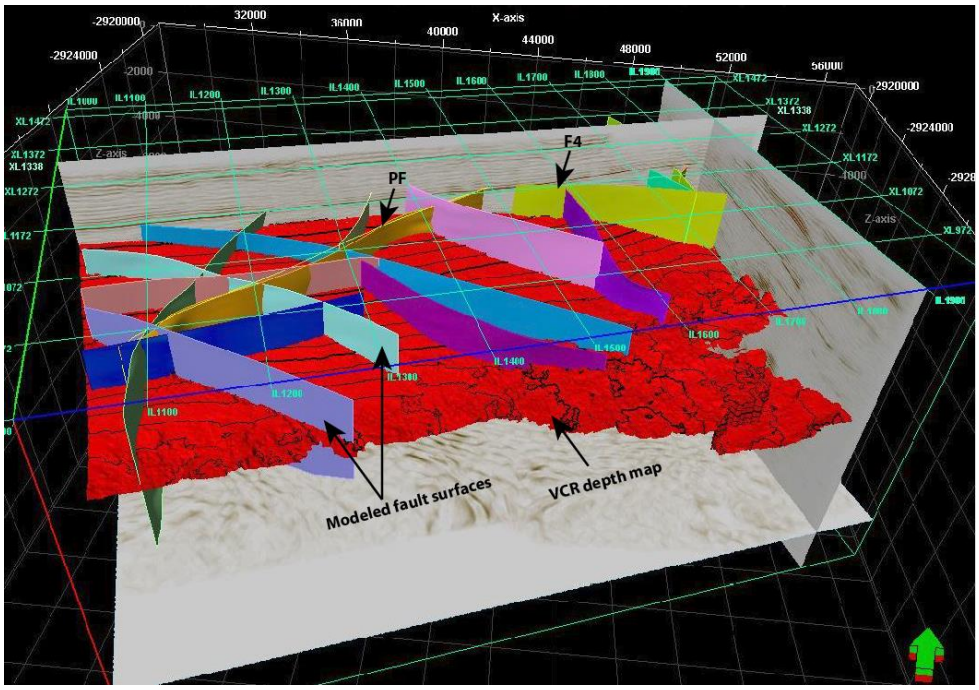


Fig. 14 3D structural model of the mining area incorporating the VCR ore body, second-order scale Pretorius Fault (PF) and subordinate faults.

9. Manuscript 3

The manuscript has been modified according to journal standards.

Geophysical Prospecting

EAGE EUROPEAN ASSOCIATION OF GEOSCIENTISTS & ENGINEERS

Geophysical Prospecting, 2015, **63**, 881–902 doi: 10.1111/1365-2478.12273

Integrated interpretation of 3D seismic data to enhance the detection of the gold-bearing reef: Mponeng Gold mine, Witwatersrand Basin (South Africa)

Musa Manzi[1]*, Gordon Cooper[1], Alireza Malehmir[2], Raymond Durrheim[1,3] and Zamaswazi Nkosi[1]

[1]*University of the Witwatersrand, School of Geosciences, Johannesburg, South Africa,* [2]*Uppsala University, Department of Earth Sciences, Uppsala, Sweden, and* [3]*Council for Scientific and Industrial Research (CSIR), Johannesburg, South Africa*

Received November 2014, revision accepted March 2015

ABSTRACT

We present an integrated approach to the seismic interpretation of one of the world's deepest gold ore body (Carbon Leader Reef) using three-dimensional seismic data, ultrasonic velocity measurements at elevated stresses, and modified instantaneous attribute analysis. Seismic wave velocities of the drill-core samples (quartzite, shale, and conglomeratic reef) from the mine are sensitive to uniaxial stress changes, i.e., they slowly increase with increasing pressure until they reach maximum value at 25 MPa. For all the samples, seismic velocities are constant above 25 MPa, indicating a possible closure of microcracks at stress corresponding to 1.0 km–1.5 km. A reflection coefficient of 0.02 computed between hanging wall and footwall quartzites of the Carbon Leader Reef ore body suggests that it may be difficult to obtain a strong seismic reflection at their interface. Our modified seismic attribute algorithm, on the other hand, shows that the detection of the lateral continuity of the Carbon Leader Reef reflector can significantly be improved by sharpening the seismic traces. Three-dimensional seismic data reveal that faults with throws greater than 25 m that offset the Carbon Leader Reef can clearly be seen. Faults with throws less than 25 m but greater than 2-m throw were identified through horizon-based attribute analysis, while most dykes and sills with thickness less than 25 m were invisible. The detection of the lateral continuity of the Carbon Leader Reef reflector and its depth position is greatly improved by integrating the modified instantaneous attributes with controls from borehole observations. The three-dimensional visualization and effective interpretation of the Carbon Leader Reef horizon shows a host of structurally complex ore body blocks that may impact future shaft positioning and reduce its associated risks.

Key words: Witwatersrand Basin, Carbon Leader Reef, physical properties, seismic attributes.

INTRODUCTION

The Witwatersrand Basin in South Africa is one of the best known gold-producing provinces in the world. It has produced about one-third of the gold ever mined, worldwide.

The Witwatersrand gold ore bodies occur in fluvial conglomerate beds called reefs. Extensive gently dipping tabular deposits are found at several stratigraphic levels; thus, mining may take place at different levels in a mining district or mine (Krapež 1985; Jolley *et al.* 2004; Erismann 2007). Since the 1980s, hundreds of 2D seismic surveys and tens of 3D

* E-mail: musa.manzi@wits.ac.za

c 2015 European Association of Geoscientists & Engineers

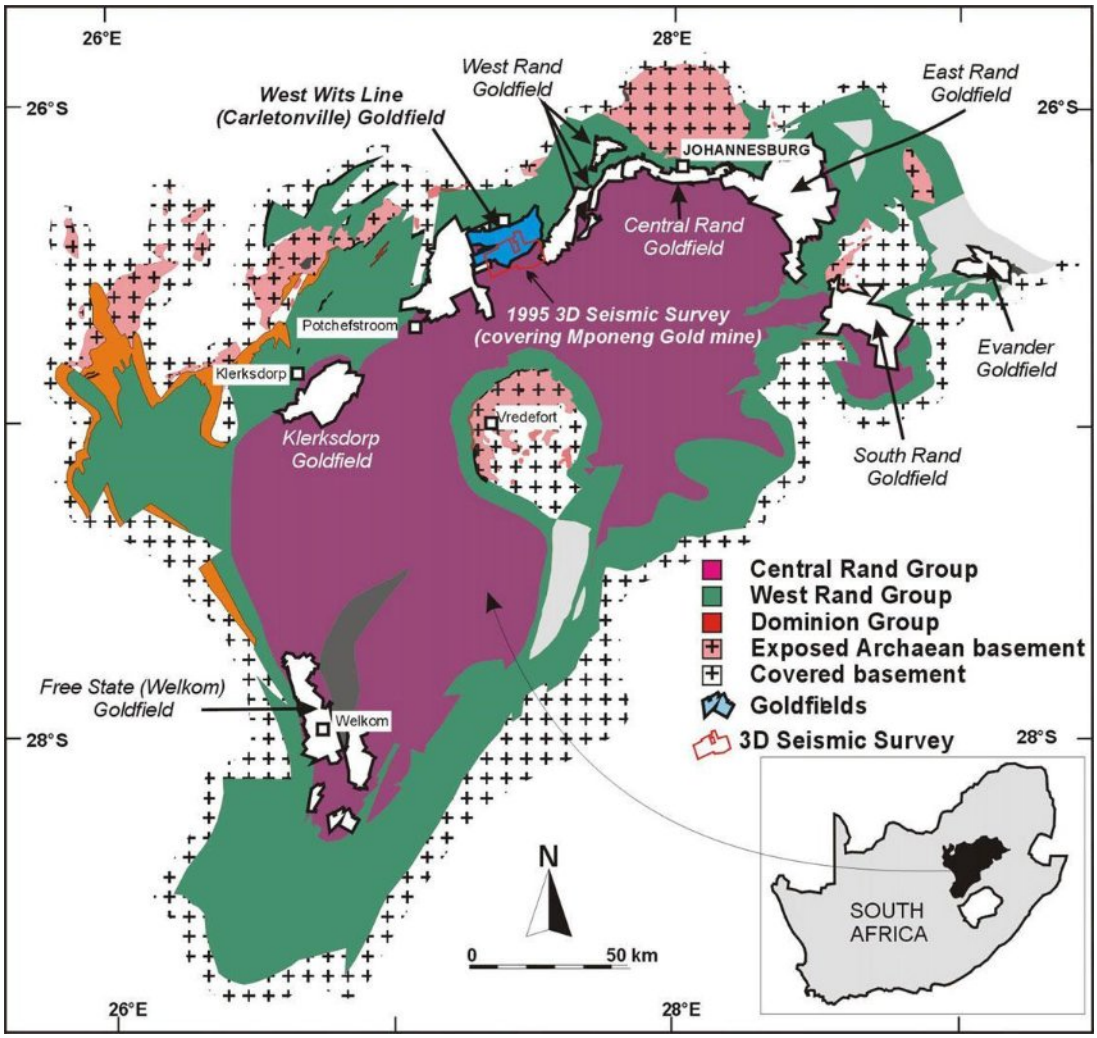


Figure 1 The location map of the West Wits Line (Carletonville) goldfields of the Witwatersrand Basin in South Africa (modified after Dankert and Hein 2010).

seismic surveys have been acquired across the gold mines of the Witwatersrand Basin to delineate the deep-buried gold-bearing reefs and other subsurface structures such as faults and dykes (Pretorius, Jamison, and Irons 1989; Campbell and Crotty 1990; Pretorius *et al.* 2003; Malehmir *et al.* 2012a; Malehmir *et al.* 2014). The 3D reflection seismic method is now applied worldwide for the mineral exploration, as well as for routine mine planning and development (Malehmir *et al.* 2012b; Koivisto *et al.* 2012; Urosevic, Bhat, and Grochau 2012; White and Kjarsgaard 2012; Wood *et al.* 2012; Kukkonen *et al.* 2012; Juhojuntti *et al.* 2012; Malehmir *et al.* 2014). In the Witwatersrand Basin and Bushveld Complex of South Africa, the technique has been mainly used to image major structures such as faults and folds that might bring gold and platinum bearing strata up to mineable depths (Pretorius *et al.* 1989; Trickett, Duweke, and Kock 2004; Manzi *et al.* 2014). South Africa, to our knowledge, has acquired more hard-rock seismic data than the rest of the world (Manzi *et al.* 2014).

In 1995, AngloGold Ashanti acquired 3D seismic data (Gibson 1997; Gibson, Jolley, and Barnicoat 2000) for mine planning at the Mponeng Gold mine in the northwestern part of the Witwatersrand Basin (Figs. 1 and 2). The 3D seismic reflection survey was acquired by Compagnie Gen´erale´ de Geophysique´ (CGG) and processed by Velseis Processing Pty. (Gibson 1997; Gibson *et al.* 2000). To date, this is the largest 3D survey acquired in Southern Africa, covering an area of about 300 km^2 (15 km by 20 km; Fig. 2). The objective of the survey was to image the formations above and below

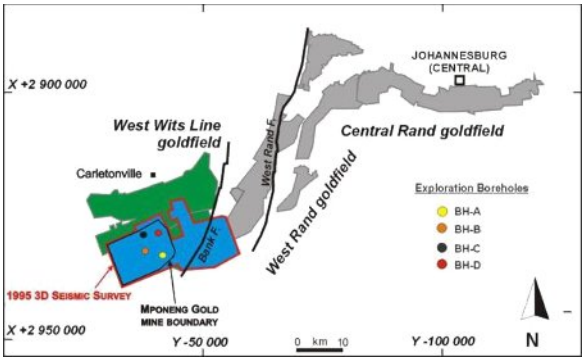


Figure 2 The location map showing the 3D seismic survey covering Mponeng Gold mine within the West Wits Line goldfields (modified after Dankert and Hein 2010).

the Ventersdorp Contact Reef (VCR, 1.5-m thick) and the Carbon Leader Reef (CLR, 1.0-m thick), at depths ranging from 2.7 to 4.2 km (Fig. 3; Gibson *et al.* 2000). The survey successfully imaged the entire stratigraphy from surface through the Ventersdorp Supergroup to the base of the Witwatersrand Basin (11 km in depth) and successfully imaged one of the key gold-bearing reefs, i.e., the VCR (see Gibson *et al.* 2000). The VCR, which is deposited approximately 900 m above the CLR, is a strong seismic reflector because it occurs at the reflective interface between basic to ultrabasic Klipriviersberg lavas and clastic sediments of the Central Rand Group.

The high-resolution imaging of the VCR enabled AngloGold Ashanti to better understand the structural framework of the VCR at depths between 2.5 km and 3.5 km below the surface (Fig. 3), resulting in a coherent model for the development of the region and some indication of the prospectivity of unmined ground. However, the deepest and richest gold-bearing conglomerate reef in the basin, the CLR, is not seismically detectable (Fig. 4) because it is too thin and occurs within quartzitic units where there is no significant acoustic impedance contrast with the surrounding units and the re-flection coefficient (RC) is minimal (see also Gibson *et al.* 2000).

The VCR is now largely mined out, and AngloGold Ashanti is assessing the feasibility of deepening Mponeng Gold mine to access CLR reserves below 4 km depth (below 42 mining level in Fig. 3). The new project is aimed at accessing the CLR located about 900 m below the VCR (Fig. 3). A new deep (4.5 km) vertical shaft (shaft 13 in Fig. 3) to exploit deeper portions of the ore body in the Mponeng Gold mine represents a huge investment before the underground development commences. AngloGold Ashanti is sufficiently concerned about structural sterilization and complexity of the lease area around the shaft sites. Therefore, it is envisioned that the interpretation of the existing 3D seismic data will help to derive an ore-body model for the CLR, and to identify and minimize geological risks ahead of drilling.

Integration of seismic velocity measurements with seismic reflection methods has played a key role in understanding seismic structures in mineral exploration (e.g., Salisbury *et al.* 2000; Malehmir *et al.* 2006, 2007, 2011, 2013, 2014; Malehmir and Bellefluer 2009; Dehghannejad *et al.* 2010, 2012; Bellefleur, Malehmir, and Muller¨ 2012; Juhojuntti *et al*. 2012; Kukkonen *et al.* 2012; Malinowski, Schetselaar, and White 2012; White and Kjarsgaard 2012; Wood *et al.* 2012). Although numerous reflection seismic surveys have been conducted in the Witwatersrand Basin (e.g., Pretorius, Steenkamp, and Smith 1994; Gibson *et al.* 2000; Manzi *et al.* 2012b, 2013, 2014; Malehmir *et al.* 2014), direct measurements of the seismic velocity have not previously been performed on core samples of the hanging wall (H/W) and footwall (F/W) of the gold-bearing horizons. While the seismic velocities and bulk densities of the Ventersdorp lavas (above the VCR) and quartzites (below the VCR) are known, the velocities and densities of the rocks above and below the CLR have not been examined, making it difficult to model the acoustic and elastic behaviour of this conglomerate reef. It is thus important to understand the seismic velocities associated with CLR and its host rocks in order to better understand the nature of the poor seismic reflection and better constrain our seismic interpretation. While sonic velocity and density logs are optimum for this purpose, these measurements have been limited due to their high cost, owing to the great depth of the CLR and other gold-bearing horizons.

Seismic attributes have widely been used in hydrocarbon exploration to enhance the interpretation of 3D seismic data (Taner, Koehler, and Sheriff 1979; Sheriff 1991; White 1991; Brown 1996; Rock Solid Images 2003). The conventional seismic attributes (mainly instantaneous attributes) were first utilized by Manzi *et al.* (2013) in the Witwatersrand Basin to enhance the detection of thin gold-bearing conglomerate reefs of the South Deep Gold mine that fell below the vertical seismic resolution limit (equivalent to a quarter of the dominant wavelength). However, these attributes have not been effective to directly image the CLR due to its extremely low thickness and the small acoustic impendence contrast with enclosing quartzite units. Amplitude-based seismic attribute interpretations, in particular, have been shown to be ineffective when interpreting thin beds in the seismic data (Taner *et al.* 1979). Manzi *et al.* (2013) demonstrated that though instantaneous phase–based seismic attribute analysis can help to delineate

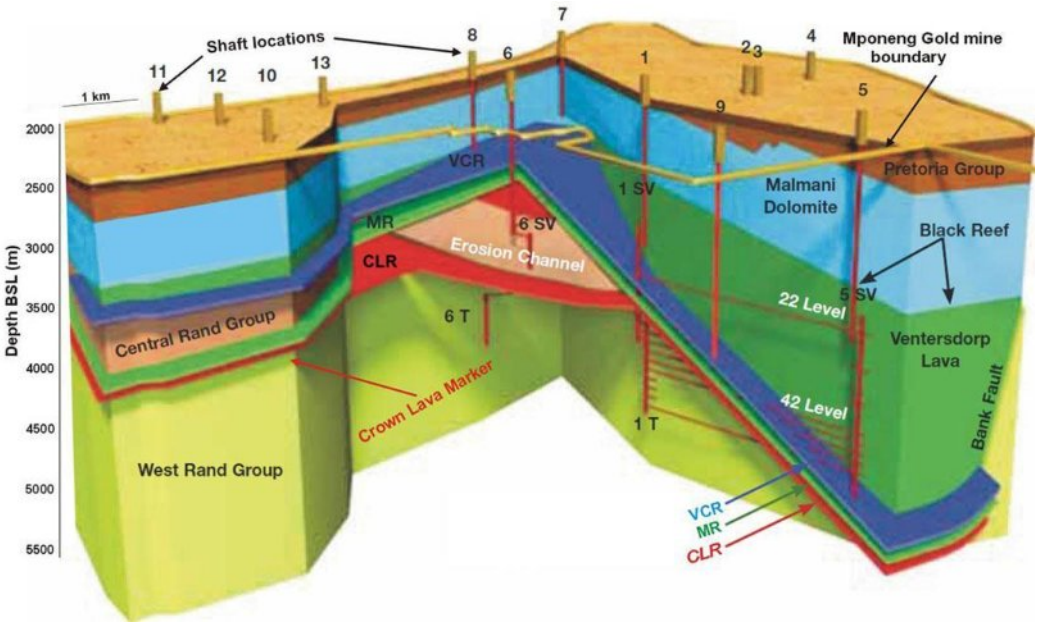


Figure 3 A 3D sketch of the mine lease showing shaft locations, mining levels and stratigraphic units of the study area. VCR: Ventersdorp Contact Reef; MR: Middelvlei Reef; CLR: Carbon Leader Reef.

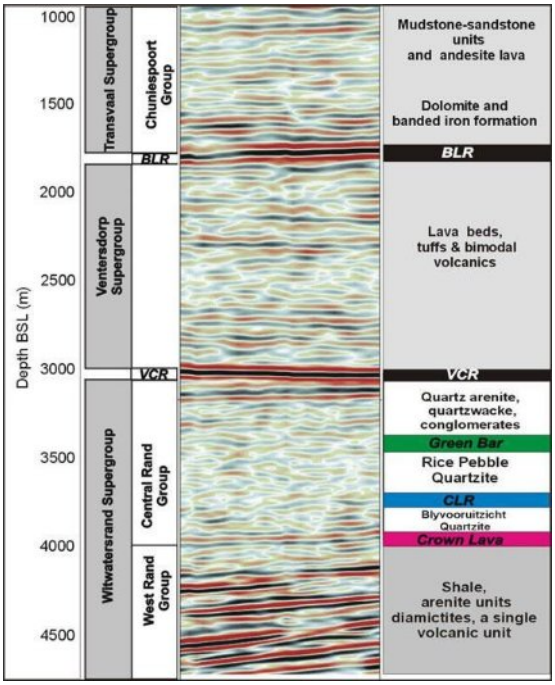


Figure 4 The summary of the stratigraphy of the West Wits Line goldfields (modified after Frimmel *et al*. 2005).

subtle variations in lithology, they are sensitive to noise, resulting in low-amplitude seismic reflections being wrapped with high-frequency dipping coherent noise.

In this study, we use high-resolution 3D seismic data (Gibson 1997; Gibson *et al.* 2000) acquired in the goldfield, covering the Mponeng Gold mine, to enhance the seismic interpretation of the CLR reflector and develop its ore-body model. To achieve this goal, we present new amplitude-independent seismic attributes that enhance the shape character of the CLR and detect its lateral continuity. We also use standard horizon-based attributes (Gibson *et al.* 2000; Manzi *et al.* 2012b) to enhance the interpretation of small faults (throw less than 25 m) that have a direct impact on mine planning decisions. To understand the seismic reflectivity of the CLR, we conduct ultrasonic velocity measurements (both P-wave and S-wave) on drill-core samples of the CLR and its host rocks. Finally, we constrain the seismic interpretation and ore-body model using exploration boreholes.

MPONENG GOLD MINE

General information

Mponeng Gold mine is situated in the West Wits Line gold-field of the Witwatersrand Basin (South Africa) and is one of the largest mines. Mponeng Gold mine is owned and operated by AngloGold Ashanti, which is today one of the world's largest gold-producing companies (Dankert and Hein 2010; Manzi *et al.* 2014). With mining taking place at depths be-tween 2.4 km and 4.2 km below the surface, Mponeng Gold

mine is currently the world's deepest mine. The mine lies to the west of the Bank Fault, a major NNE-trending listric fault with a maximum throw of 2.5 km (see Fig. 2). The mine exploits the CLR (which constitutes about 75% of the ore reserve) and VCR (which constitutes about 20% of the ore re-serve) through a twin-shaft system housing two surface shafts and two sub-shafts. The CLR is a narrow conglomerate band (up to 1-m thick), rich in both hydrocarbons and gold. The reef is reported to have been deposited during a transgressive (expansive) stage of basin development and its depositional environment is considered to reflect tidal marine conditions (Dankert and Hein 2010).

Geological setting

The geological setting of the West Wits Line goldfield is documented by many authors, including Coward, Spencer, and Spencer (1995), Gibson *et al.* (2000), Jolley *et al.* (2004), Beach and Smith (2007), and Dankert and Hein (2010). A 3D sketch showing the main lithological units (including the CLR) at the Mponeng Gold mine is presented in Fig. 3. The simplified stratigraphy around the CLR in the Carletonville Gold-field is shown in Fig. 4. In summary, the Witwatersrand Super-group unconformably overlies the Dominion Group, which is subdivided into the (lower) West Rand and (upper) Central Rand groups (McCarthy 2006; Dankert and Hein 2010). The Central Rand Group is covered by lavas of the Ventersdorp Supergroup, with the VCR of the Venterspost Formation at the base. The Ventersdorp magmatic activity was followed by the continuous deposition of a relatively thin Black Reef Formation, which is the basal lithostratigraphic unit of the Transvaal Supergroup (Beach and Smith 2007).

The target horizons are found in the Central Rand Group (1.5-km thick), which hosts several economically viable conglomerate horizons along the West Wits Line goldfield. The sediment deposition of the Central Rand Group is thought to be controlled by fault-related uplift to the east (Frimmel *et al.* 2005). The CLR is located at the base of the Central Rand Group (Figs. 3 and 4) and varies in thickness from a mere carbon streak to a solid seam of carbon up to 20-cm thick, to a multiple-band medium-pebble conglomerate some 200 cm thick (Jolley *et al.* 2004). The CLR has a low angle of unconformity. The F/W to the CLR consists of a package of conglomerates, known as the "Footwall bands of the CLR." The multiple-band CLR facies is defined as a gold-bearing reef containing more than one conglomerate band separated by internal quartzite bands (Frimmel *et al.* 2005). These F/W bands are characterized by lenses of conglomerates, separated by grey argillaceous quartzites, referred to as Blyvooruitzicht Quartzite (Figs. 3 and 4).

The H/W of the CLR consists of the uniform siliceous grey quartzite units, termed the Rice Pebble Quartzite (Figs. 3 and 4; McCarthy 2006). Overlaying the Rice Pebble Quartzite is the Green Bar, chloritoid shale occurring over most of the Witwatersrand Basin. Most importantly, for the purpose of this study, the CLR is embedded between the uniform H/W quartzite units (Rice Pebble Quartzite) and uniform F/W quartzite units (Blyvooruitzicht Quartzite) of the Cen-tral Rand Group, hence its poor seismic reflectivity.

Structural setting

The studies undertaken by Coward *et al.* (1995), Beach and Smith (2007), Dankert and Hein (2010), Jolley *et al.* (2007), and others confirm that the West Wits Line experienced more than one episode of deformation. The Witwatersrand Basin underwent inversion tectonics during and after deposition of the quartzite and conglomerate units (some auriferous) of the Central Rand Group, from extension to compression, i.e., positive inversion (Beach and Smith 2007; Dankert and Hein 2010), and then from compression to extension (i.e., negative inversion) during deposition of the Ventersdorp Super-group (Van der Westhuizen *et al.* 1991; Gibson *et al.* 2000). The basin is characterized by major listric faults and their related drag folds, which are attributed to extensional tectonics that occurred during the deposition of the Ventersdorp Supergroup (ca. 2709–2643 Ma) (Coward *et al.* 1995; Vermaakt and Chunnet 1994; Gibson *et al.* 2000; Beach and Smith 2007).

One of the most important structures in Mponeng Gold mine is the NNE-trending Pretorius Fault Zone (PFZ, maximum throw 500 m) (Fig. 5). The delineation of the PFZ is important for both mine safety and planning. It has been interpreted as a growth fault with several phases of movement (Dankert and Hein 2010). The PFZ is surrounded by a series of smaller normal faults that are likely to cause poor ground conditions when mining (i.e., unstable rock found in mining operations in proximity to a fault). These will also have an impact on mine safety and development scheduling. This type of faulting cannot be detected by surface drilling and presents a major challenge to mine planning. Most normal faults are of Pilanesberg (1.30 Ga) to Ventersdorp (2.60 Ga) ages. Moreover, minor thrust faults and their associated subordinate structures are observed throughout the mine. The nature

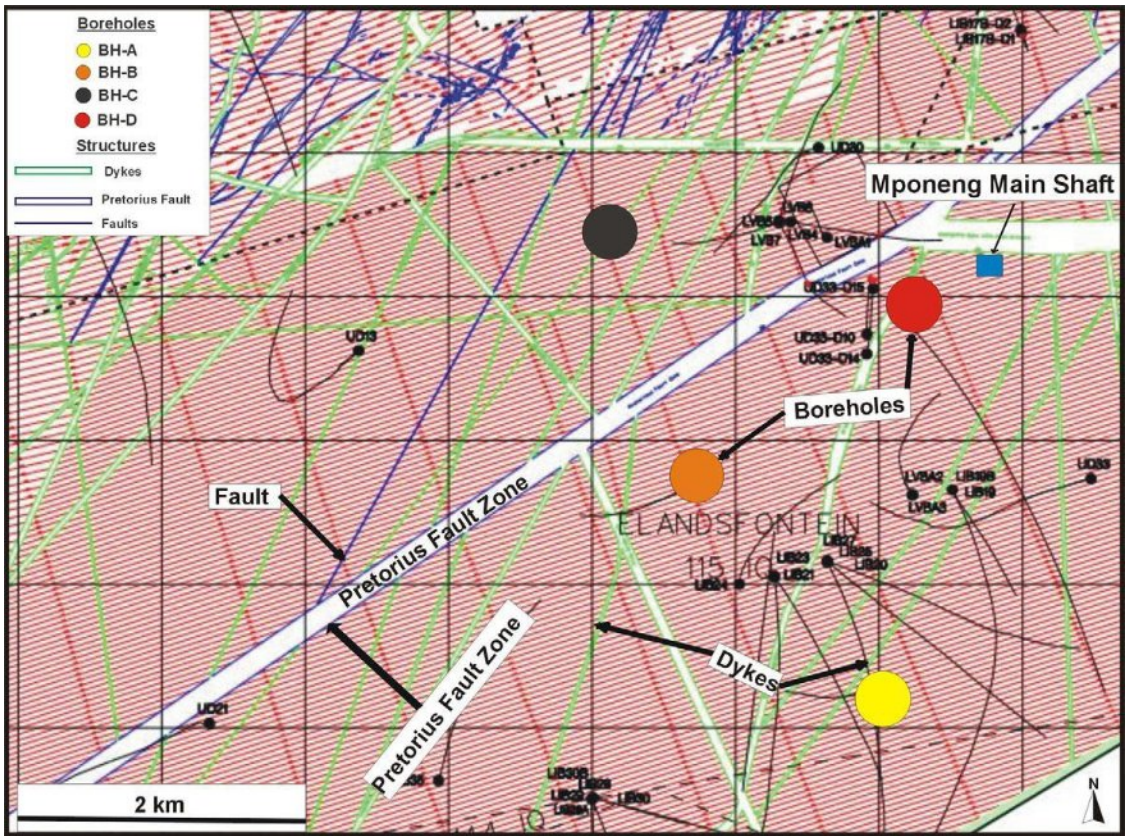


Figure 5 The optimum mapping of faults and dykes by underground geological mapping method. Note that underground mapping has identified a number of dykes and sills that were not mapped seismically (modified after Frimmel *et al.* 2005).

and controls on the reactivation of these faults in the West Wits Line have previously been discussed by Dankert and Hein (2010).

The mining area is also invaded by dolorite sills and syenite dykes of four different ages: Karoo (150 Ma), Pilanesberg (1.30 Ga), Transvaal (2.20 Ga), and Ventersdorp (2.60 Ga). The majority of these dykes strike north to north–northeast with thicknesses that vary from 1 m to 90 m (Fig. 5). Intrusive sills, although rare, have been identified in the borehole data used in this study and may be laterally continuous over several hundreds of metres. These sills often intrude along or close to the lava/quartzite contact (VCR ore body), thus removing or interrupting substantial portions of the reef (Jolley *et al.* 2007; Dankert and Hein 2010).

PHYSICAL PROPERTY MEASUREMENTS

Methodology

Since the acquisition of the 1995 3D seismic survey, at least 200 exploration boreholes have been drilled to the CLR ore zones (depths ranging from 1.5 km to 4.2 km) to test the ore grade. These have provided the stratigraphic control in the H/W (Rice Pebble Quartzite) and F/W (Blyvooruitzicht Quartzite) of the CLR. To obtain an observable reflection, a RC of the order of 0.06 (typical of the contact between a mafic rock and a felsic rock) between the major geological boundaries is suggested (Salisbury *et al.* 2000), provided that the seismic data have good signal-to-noise ratio (SNR) and the target has a suitable geometry/shape for detection by surface seismic methods (Malehmir *et al.* 2012b). To better understand the nature of seismic reflectivity of the CLR in the Mponeng mining area, core samples of the H/W to the F/W were collected for ultrasonic measurements from four exploration boreholes (BH-A, BH-B, BH-C and BH-D; Fig. 5) that intersect the CLR within the seismic volume.

The boreholes are located down-dip of Mponeng Main Shaft (see blue box in Fig. 5). Boreholes BH-B, BH-C, and BH-D are 3.5-km, 3.7-km, and 3.9-km deep, respectively, whereas BH-A is the deepest (4.7 km) borehole in the entire Witwatersrand goldfields, penetrating through the dolomitic

rocks of the Transvaal Supergroup and the ultramafic lavas of the Ventersdorp Supergroup into the Crown Lava of the West Rand Group (see Fig. 4). The holes were initially drilled vertically but, at depths between 2.5 km and 3.5 km, were deviated by a few degrees towards west. To our knowledge, no downhole geophysical measurements have been conducted in these holes. Cores sampled from the holes were logged in detail for better stratigraphic understanding. Lithologies were characterized using X-ray diffraction for their mineralogy and optical examination of thin sections for petrology and micro-structures.

For our measurements, the core samples were cut into cylinders with a diameter of 30 mm and length ranging be-tween 55 mm and 60 mm. Bulk density and porosity measurements were carried out using an Sartorius digital balance (model E5500S, 5500 g maximum) with 10-mg resolution using the Archimedes principle (i.e., weighing water-saturated and oven-dried samples in air and in water). The experimental setup developed for ultrasonic measurements uses pulse transmission (using P-wave or S-wave transducers) to measure P-wave and S-wave velocities (see Malehmir *et al.* 2013). The ultrasonic apparatus consists of two pairs of piezo-sensors that operate as a transmitter and a receiver, respectively, a precise impulse generator (Panametrics 5058 PR with up to 900 V), and a digital oscilloscope (Tektronix TDS 2012c connected to a PC). We chose these transducers because of their availability, and they allow easy fluid coupling to the sample. The resonance frequency of the sensors is 0.5 MHz for P-wave and S-wave transducers at both room and elevated uniaxial stresses (up to 500 MPa). The contact between transducers and sample was improved using ordinary lubricating grease. Two sets of transducers (0.5 MHz) were used for ultrasonic measurements: a bigger set and a smaller set. The smaller set was particularly utilized in the atmospheric pressure conditions. The bigger set, on the other hand, was used under uniaxial stress conditions because of their appropriate size and geometry. Most of the samples could not be measured for seismic wave velocities at elevated uniaxial stresses because the bulk of the samples were too small to fit into the sample chamber. Since the Witwatersrand rocks have under-gone different episodes of deformations, we did not expect significant porosity in our hard rock samples (e.g., Malehmir *et al.* 2013).

The seismic velocities were measured at elevated uniaxial stresses using the AMSLER compression testing system (Zimmer, Prasad, and Mavko 2002). To elevate uniaxial stress on the samples, a stainless-steel cylindrical chamber was used, into which the samples, connected to the transducers, were placed. The chamber has an adjustable length, whereas the cylinder has a diameter of 48 mm, suitable to hold core samples. The uniaxial compressional loading is produced by a hydraulic cylinder that is driven with a computer-controlled load holding pump. The change in sample height was measured with 1.5-μm resolution during the compression with a digimatic indicator. The sample length change was less than 0.1% at the highest pressures, i.e., 50 MPa–60 MPa, and thus was considered negligible and neglected for velocity calculations. The error analysis that we took into account was the picking of arrival times, which gave error estimates of about 2% for the P-wave values, and about 3% for the S-wave values. Another source of error was the surface condition of samples. Since the sample ends were polished by hand, this may have resulted in some of the samples not being perfectly parallel, thus causing nonlinearity in our measurements.

Velocity versus density results

Average P-wave and S-wave velocities and densities of 14 selected drill cores are presented in Table 1. The P-wave and S-wave velocities and bulk density measurements from two boreholes (BH-A and BH-B) are plotted in Fig. 6(a, b). We do not present results from the two other boreholes because they do not contain all the samples from the F/W and H/W of the CLR. We also do not discuss the results for the S-wave velocities due to difficulties experienced in accurately picking up the first arrival and waveform of transmitted S-wave in S-wave ultrasonic measurements on many samples. This has a significant impact on the accuracy of S-wave velocity and quality factor.

Our density values range between 2.70 g/cm^3 and 2.83 g/cm^3. The P-wave velocities range between 4918 m/s and 5870 m/s. There was no depth dependence observed in our seismic velocity and bulk density measurements. The Green Bar samples, the best and most continuous shale markers in the Central Rand Group, differ most from the other samples exhibiting higher values of density (3.01 g/cm^3 in BH-A and 3.00 g/cm^3 in BH-B). These samples lie far to the right of the velocity–density curve controlled by the properties of iron formation, euhedral and anhedral pyrite, which is fast and dense compared with quartz and cherts of the quartzite units.

In both BH-A and BH-B, the samples from Rice Pebble Quartzite and Blyvooruitzicht Quartzite show minor variations of the P-wave velocity, S-wave velocity, and density with average values of 5100 m/s, 2200 m/s and 2.7 g/cm^3, respectively (Table 1). For example, the samples from Rice Pebble Quartzite (P-wave velocity of 5260 m/s and

Table 1 Results of ultrasonic and bulk density measurements at atmospheric pressure and temperature.

Borehole (BH) Name	Depth (m)	Sample	Thickness (m)	Mineral composition	Vp (m/s)	Vs (m/s)	Density (g/cm^3)
BH-A	3427	Green Bar	3.00	Clay, quartz, chlorite	5550	2190	3.01
	3431	Rice Pebble Quartzite	3.35	Quartz, chert crystals, pyrite	5260	2360	2.75
	3436	CLR	0.20	Chert, quartz, pyrite,	5870	3390	2.77
	3438	Blyvooruitzicht Quartzite	7.20	Quartz, chert grit	5080	1910	2.71
BH-B	3660	Green Bar	2.8	Clay, quartz, and pyrite	5570	2500	3.00
	3664	Rice Pebble Quartzite	7.00	Quartz, chert and pyrite	5080	2250	2.72
	3669	CLR	0.25	Chert, quartz, quartzite, pyrite	4920	2480	2.83
	3673	Blyvooruitzicht Quartzite	6.75	Quartz, chert and quartz grit	4920	2070	2.71
BH-C	3757	Green Bar	1.60	Silt and clay, quartz, chlorite	5560	2240	3.10
	3758	Rice Pebble Quartzite	2.95	Quartz, chert, pyrite	5360	2460	2.80
	3763	Blyvooruitzicht Quartzite	5.65	Quartz, chert, pyrite	5080	2130	2.80
BH-D	3668	Green Bar	1.30	Silt and clay, quartz, chlorite	5350	1350	3.11
	3671	Rice Pebble Quartzite	2.50	Quartz and chert, pyrite	5080	2170	2.90
	3671	Blyvooruitzicht Quartzite	6.60	Quartz, chert grit	5170	2100	2.80

density of 2.75 g/cm^3) and Blyvooruitzicht Quartzite (P-wave velocity of 5080 m/s and density of 2.71 g/cm^3) of BH-A show no distinct differences in P-wave velocity and density values and have a reflection coefficient of 0.028 (Fig. 6a). These results are not surprising since Rice Pebble Quartzite and Blyvooruitzicht Quartzite units have similar mineral com-positions such as quartz and cherts, which are slow and dense compared with the euhedral and anhedral pyrites of the Green Bar. Based on these measurements, these two quartzite units cannot be easily distinguished from each other. However, a slightly higher P-wave velocity value for Rice Pebble Quartzite (P-wave velocity of 5260 m/s) may be due to disseminated euhedral and anhedral pyrite grains, which is not present in the unmineralized quartzite of Blyvooruitzicht unit.

Interestingly, the sample of the reef (CLR) from BH-A ex-hibits relatively higher values for P-wave velocity (5870 m/s) and density (2.77 g/cm^3) than the Rice Pebble Quartzite (density of 2.75 g/cm^3 and P-wave velocity of 5260 m/s) and Blyvooruitzicht Quartzite (density of 2.71 g/cm^3 and P-wave velocity of 5080 m/s; see Table 1). Even so, the small thick-ness of the CLR and minor velocity and density variations between the CLR and host rocks are unlikely large enough to produce noticeable reflections. The slightly higher velocity values may be attributed to a higher concentration of pyrites in the conglomerates of the CLR, as well as stack of alternating layers of scattered and moderately packed quartz, dark chert pebbles. The other samples for CLR from other boreholes were not measured for velocities because they did not have the proper size to perfectly fit into the transducers. The average mean values for the seismic velocities and bulk densities, calculated for all the samples, were 5229 m/s and 2.86 g/cm^3, respectively, while the average mean value for the porosity of the samples was 1.5%. These results indicate that the observed minor velocity differences on our samples may be mainly due to the mineral differences and the presence of macro-fracturing and micro-fracturing.

The P-wave velocity and density measurements obtained from BH-A were used to estimate the seismic impedances and RC of the H/W quartzites and F/W quartzites. The RC of 0.02 obtained for these units is unlikely sufficient to produce a de-tectable CLR reflection on surface seismic data, particularly from a target at depths between 2 km and 4 km. This im-plies that, at least in terms of their acoustic properties, these quartzite units would not produce strong reflections at their interface that coincides with the CLR. However, it may be possible to detect the top of the Green Bar due to a significant density contrast between the Green Bar and quartzite units above.

Velocity versus pressure results

The seismic wave velocities tend to depend on the stress ap-plied to the sample. In some cases, this stress effect is quite strong. The reason for this dependence is well known (Walsh and Brace 1966; Zimmer *et al.* 2002; Kuusisto *et al.* 2006; Mayr and Burkhadt 2006; Kern *et al*. 2009) and due to the ubiquitous mechanical micro-defects (microcracks and grain contacts) that tend to close under the effect of differential stress, thereby increasing the rigidity of the material. To test the dependence of seismic velocities to applied stress, we

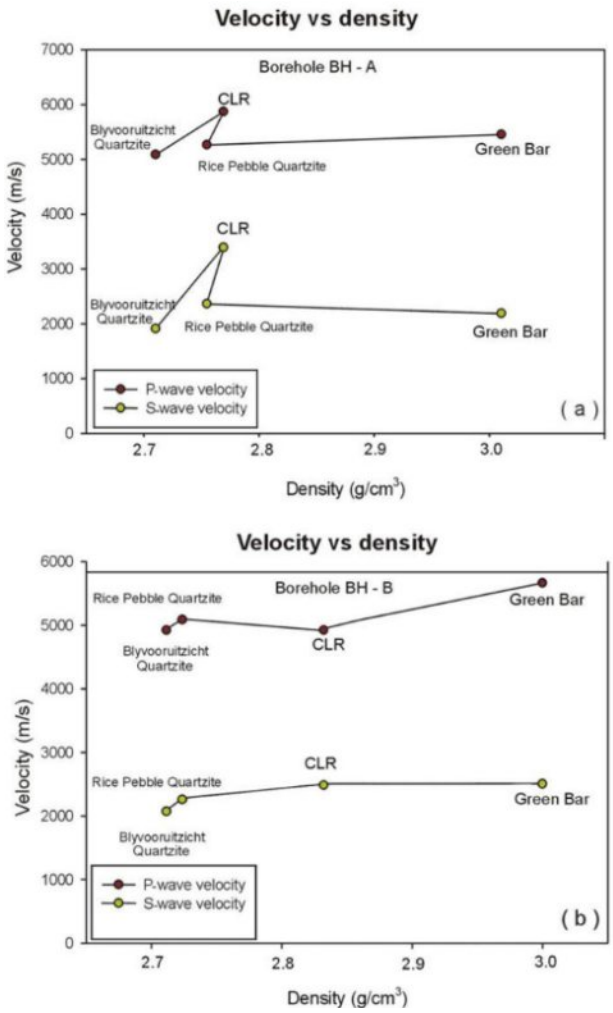


Figure 6 The results of P-wave velocities versus density. (a) P-wave velocities versus density on BH-A. (b) P-wave velocities versus density on BH-A. Note a large density value for the Green Bar Shale compared to quartzites.

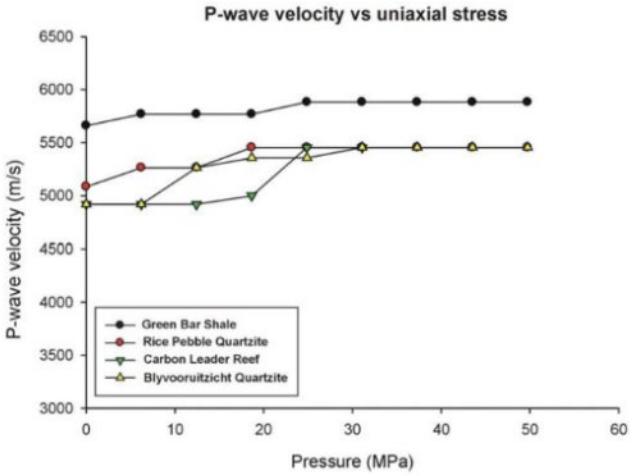


Figure 7 Effect of uniaxial stress on the P-wave velocities. The seismic velocities increase as the uniaxial stress increases and become constant above 20 MPa.

measured the velocities of core samples at elevated stresses up to 65 MPa (corresponding to a lithostratigraphic depth of about 3 km–4 km), at incremental steps of 5 MPa. In order to avoid creating new cracks in the sample during uniaxial loading, samples were loaded only up to 65 MPa.

For all the samples in BH-A from the Rice Pebble Quartzite and Blyvooruitzicht Quartzite units, the P-wave velocity functions of uniaxial stress (Fig. 7) are constant above 25 MPa, indicating a possible closure of macrocracks and microcracks at the stress corresponding to 1.0 km–1.5 km. Note that the seismic velocity in the Green Bar (shale) is generally constant (5550 m/s) at elevated stress (Fig. 7). In the quartzite units, on the other hand, the velocity variations have the same reason: the majority of macrocracks between grain contacts are virtually closed under a differential stress of 20 MPa. The reason may be quite simple: in shales, mechanical micro-defects are much less frequent than in quartzites since they have preferential alignment of open grain-contact microcracks compared to quartzites. This velocity–stress dependence behaviour varies considerably, depending on the rock type. For example, the microcracks for the CLR are closed at a differential stress of 25 MPa (Fig. 7). For other rock types, particularly igneous crystalline rocks, and depend-ing on the shape of the cracks, this may be on the order of 200 MPa (Salisbury *et al.* 2000).

Generally, we observe that the velocity as a function of differential stress shows a nonlinear-type behaviour, at least over a limited stress interval (Walsh and Brace 1966; Zimmer *et al.* 2002; Malehmir *et al.* 2013). It is shown in Fig. 7 that at lower stresses (e.g., 10–25 MPa), the increase in velocity with increasing pressure is steep and nonlinear. In the higher stress zone (e.g., 25 MPa–65 MPa), our samples exhibit the seismic velocity response that is independent of the applied stress as most macrocracks and microcracks are closed (Fig. 7). These results further suggest that metamorphosed sedimentary rocks have little porosity and are therefore less sensitive to the high elevated stresses. These observations are interesting given the megahertz frequency source used to measure the seismic velocities. Future investigations will aim at measuring the seismic velocities using low-frequency apparatus to check scale and frequency dependence of the velocities (e.g., Mikhaltsevitch, Lebedev, and Gurevich 2012; Malehmir *et al.* 2013).

3D SEISMIC DATA

Seismic resolution

The 1995 Mponeng 3D seismic survey was conducted over an area of approximately 300 km^2 (see Figs. 1 and 2; Gibson 1997; Gibson *et al.* 2000). The seismic data were initially interpreted by Gibson (1997) and Gibson *et al.* (2000) to evaluate the VCR for mine planning and production purposes, and for providing better constraints on the tectonic history of the Wits West Line goldfields. In this study, we reinterpret the seismic data by picking not only the VCR but also all the horizons above and below the CLR to derive the CLR ore-body model. The new seismic and structural interpretation is also constrained using the newest boreholes. The pre-stack time migration volume extends to approximately 11 km depth with an east–west extent of 20 km and north–south extent of 15 km, and serves as the basis for the derivation of the geological model of the CLR ore bodies. The data acquisition parameters were suited for optimum imaging of the deeper (3.5 km–4.5 km) gold-bearing reefs, in comparison to the previous 3D seismic surveys in the Witwatersrand Basin (Pretorius *et al.* 2003).

The seismic data had a nominal fold of coverage of 36; this, although not very high, represents a significant increase in fold compared with all previous deep Witwatersrand Basin 3D seismic surveys, which had folds of 16–20 (Pretorius *et al.* 1989, 1994; Gibson *et al.* 2000). The dominant frequency of the reflected signal at the VCR ore zone is about 65 Hz. If we assume the mean velocity of 6000 m/s–6500 m/s as observed during processing (Gibson *et al.* 2000), the dominant seismic wavelength is on the order of 100 m, and the tuning thickness ($\lambda/4$) is approximately 25 m, which is the minimum thickness required to resolve the top and bottom of the auriferous conglomerate reef (Gibson 1997; Jolly *et al.* 2007). The CLR has a thickness less than a tuning thickness and thus could not be directly imaged by the seismic method. However, such thinner reefs can still be detected up to $\lambda/32$ using seismic attributes (Manzi *et al.* 2012a; Manzi *et al.* 2013).

A general assessment of the survey results reveals that the data are of high quality, due mainly to the good fold coverage resulting in high SNR. The strong seismic reflection associated with the VCR is a prominent and reliable indicator of the reef's topography throughout the seismic volume (see Figs. 4 and 8). As predicted by the seismic velocity and density measurements, there is unlikely any major seismic reflection associated with the CLR unit because it is too thin and occurs at the interface where the RC is too low. This horizon, al-though partially detected by seismic amplitude in the seismic

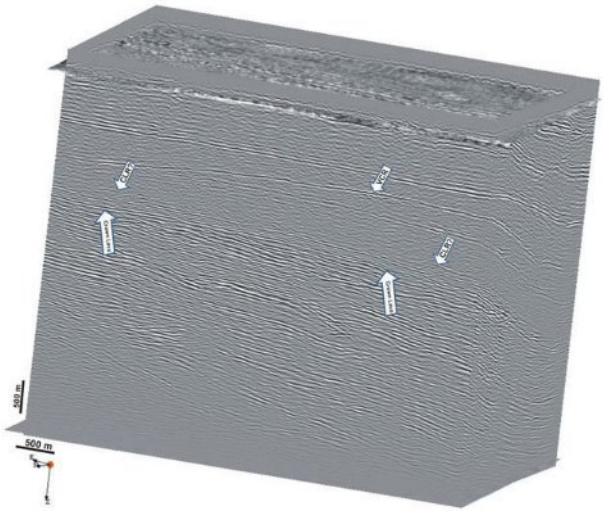


Figure 8 Seismic cube showing poor imaging of the CLR and good imaging of the VCR and Crown Lava (see Figs 1 and 2 for the location of the survey).

volume, is less prominent than the VCR and Crown Lava reflector (Fig. 8). To further enhance the detection of the CLR, we derive a new seismic instantaneous attribute from conventional instantaneous attributes, particularly the instantaneous phase and frequency, to sharpen the frequency peaks that make up the seismic data.

Instantaneous seismic attributes

Since their introduction in 1970s, more than 50 different seismic trace attributes have been developed (Taner *et al.* 1979; Sheriff 1991; White 1991; Brown 1996; Rock Solid Images 2003). Instantaneous attributes describe the characteristics of the seismic trace at each signal point (Taner *et al.* 1979; White 1991; Barnes 1993; Fomel 2007). They can be computed from seismic data, such as the instantaneous amplitude $A(t)$, phase $\theta(t)$, and frequency $v(t)$. For a seismic time series $s(t)$, these are defined as follows (Taner *et al*. 1979):

$$A(t) = \sqrt{s(t)^2 + H(s(t))^2}, \quad (1)$$

$$\theta(t) = \tan^{-1}\left(\frac{H(s(t))}{s(t)}\right), \quad (2)$$

$$v(t) = \frac{\partial \theta(t)}{\partial t}, \quad (3)$$

where $H(s(t))$ is the Hilbert transform of $s(t)$. These are three popular attributes and have played an important role in enhancing seismic interpretations (Chopra, Castagna, and

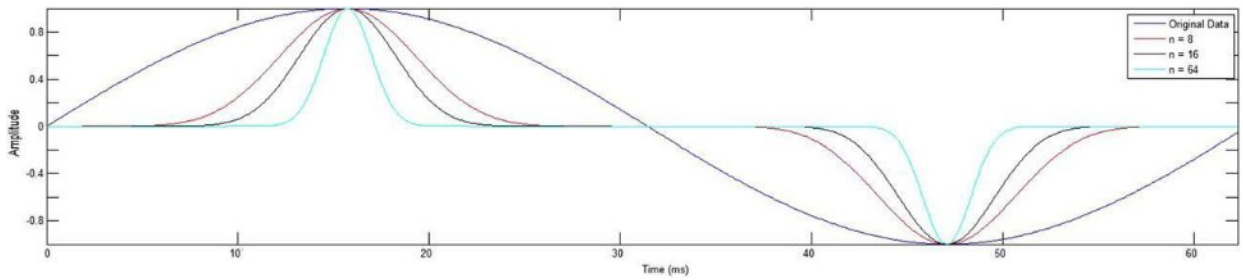


Figure 9 The seismic trace is sharpened by raising the cosine function to the *n*th power. Note the sharpened peaks as '*n*' value increases. The original data is shown in blue and the results of equation 7 with $n = 8$, 16, and 64 are overlain.

Portniaguine 2006; Chopra and Marfurt 2007). The amplitude attribute, for example, helps to identify lithological changes between geological boundaries, whereas the instantaneous phase helps to provide valuable information about the lateral continuity of structures (or reflectors). The instantaneous frequency is useful at highlighting bed thickness changes. However, these attributes also have disadvantages. A disadvantage of the amplitude attribute is that it cannot detect minor lithological changes within a thin bed below the tuning thickness (one-quarter of the dominant seismic wavelength). For example, as shown in the seismic volume in Fig. 8, the amplitude display shows poor detection of the CLR due to minor variations in lithology between the Rice Pebble Quartzite and the Blyvooruitzicht Quartzite. However, such subtle changes can be detectable by seismic attributes that are sensitive to waveform.

Alternative seismic attributes

The aforementioned attributes have been applied to the seismic data without sharpening the shape of the signal (i.e., compressing the peaks and troughs of the data). This motivates us also to consider attributes that will be sensitive to subtle lithological and hence waveform changes. First, we construct a trace from the instantaneous attributes using (Stark 2009)

$$s(t) = A(t)\cos(\theta(t)). \quad (4)$$

Second, we sharpen the trace by raising the cosine function to the *n*th power using

$$s(t) = A(t)\,\mathrm{sign}(\cos(\theta(t)))\,|\cos(\theta(t))|^n, \quad (5)$$

where sign () is the sign function. When $n = 1$, $s(t)$ is unchanged, but using larger values, it progressively sharpens the peaks and troughs that make up the seismic data. To better understand the effect of the n values on the seismic trace, we generated the synthetic trace shown in Fig. 9 and sharpened it by increasing the values of n. Figure 10(a) shows the seismic section as derived from equation (4), showing poor detection of the CLR package.

Third, we removed the amplitude from the reconstructed trace (Fig. 10a), such that the attribute measures the lateral changes in the wave character rather than lithology changes. The results yield a sharpened instantaneous phase, i.e.,

$$\phi(t) = \mathrm{sign}(\cos(\theta(t)))\,|\cos(\theta(t))|^n. \quad (6)$$

The sharpened seismic trace (equation (5)) highlights the lateral continuity of the CLR horizon and weaker events in its F/W (Fig. 10b). In addition, the instantaneous phase at-tribute (Fig. 11a) enhances the shape character and continuity of the CLR horizon that was not resolved clearly on the conventional and sharpened amplitude displays. This modified attribute is independent of the trace reflection amplitude and is thus one of the best detectors for lateral continuities of the thin strata. Finally, the sharpened instantaneous phase (equation (6)) is differentiated to produce a sharpened instantaneous frequency (Fig. 11b). The instantaneous frequency was able to identify and distinguish low amplitude events, such as thin layers, much better than the sharpened instantaneous phase. The increase in instantaneous frequency values may indicate reef thinning, interference, or low SNR areas in the data (Fig. 11b).

The instantaneous frequency is the first derivative of the phase; therefore, it is sensitive to noise associated with low seismic amplitudes. As a result, although the sharpened instantaneous frequency shows much better results than the sharpened instantaneous phase, it does not provide a high degree of confidence; what is observed on the seismic section is the result of lithological changes rather than noise (Fig. 11b). Moreover, although the modified seismic attributes have improved the detection of the CLR, it is still difficult to track the event consistently through the seismic volume due to highly variable reflection character. The results obtained by applying these

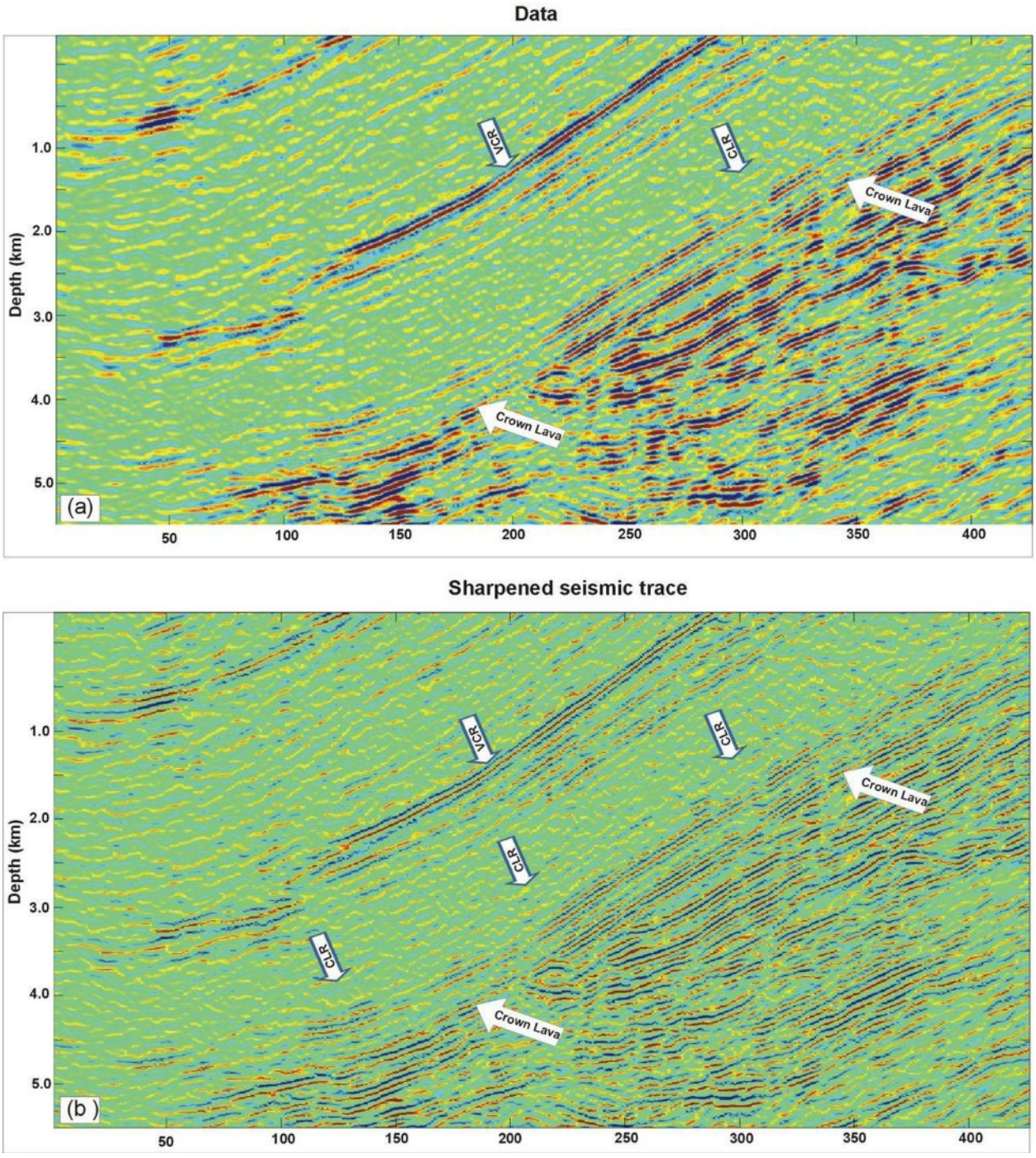


Figure 10 The comparison between an original seismic trace and sharpened trace. (a) Original seismic trace showing poor detection of the CLR. (b) The detection of Carbon Leader Reef is enhanced on the sharpened seismic trace.

attributes increase our confidence in using them as tools for detecting thin beds interbedded between rock types with similar physical properties. On the other side, they warn us that, although such attributes can enhance seismic interpretation, their implementation should be constrained by boreholes.

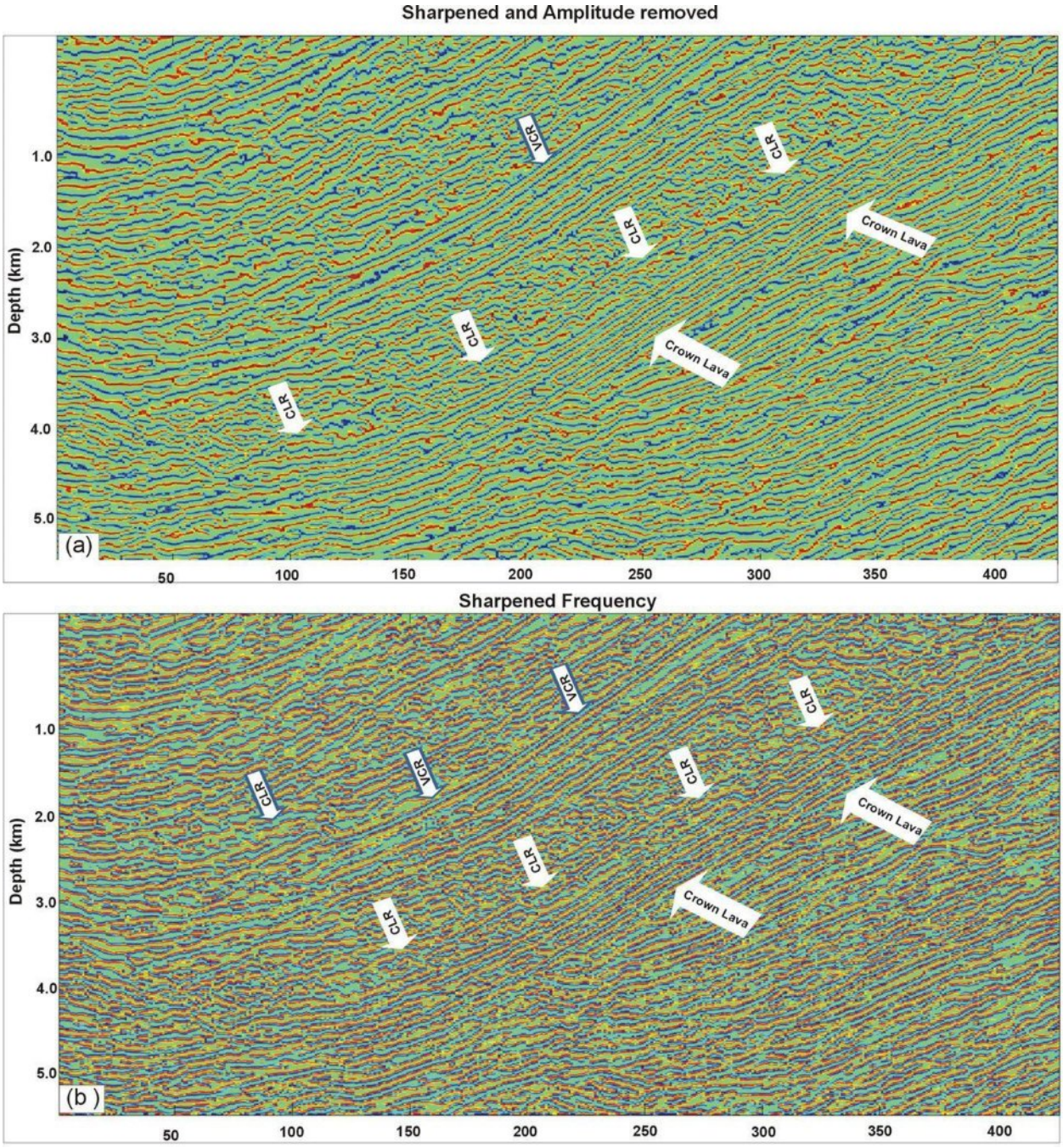


Figure 11 (a) Sharpened Instantaneous phase attribute shows a much improved enhancement of the CLR detection and its lateral continuity. (b) Identification of low amplitude events through the sharpened instantaneous frequency.

SEISMIC INTERPRETATION

Three-dimensional structural model of the Carbon Leader Reef

The derivation of the CLR model was achieved in the following steps: first, the two distinct seismic markers (VCR and Crown Lava) above and below the CLR were interpreted (Fig. 12a). The VCR reflector has a consistently high amplitude throughout the 3D seismic volume due to the strong contrast in seismic velocities and densities between overlying Ventersdorp metabasalts and the underlying Central Rand Group quartzite units. The VCR was therefore easily tracked

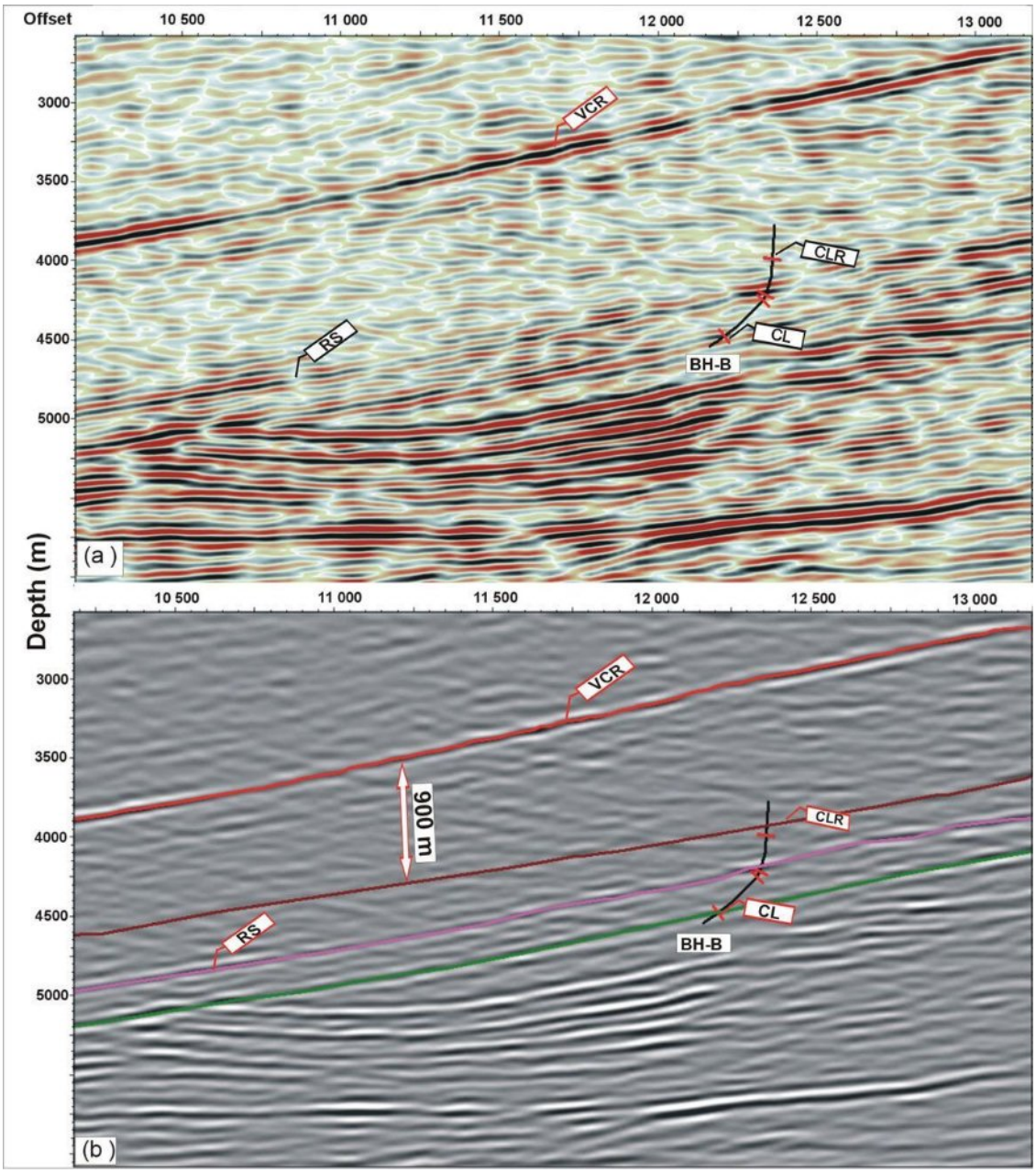


Figure 12 (a) Un-interpreted seismic section showing a good tie between seismic reflectors and the borehole. (b) Interpreted seismic section showing the derived CLR. RS: Roodepoort Shale, CL: Crown Lava.

throughout the seismic volume and interpreted as a peak (positive amplitude), assuming zero phase data. The Crown Lava, on the other hand, was interpreted as a trough because of an increase in impedance from the overlying quartzite units (base of the Central Rand Group) to underlying basaltic lavas (about 600 m below the top of the West Rand Group) in the West Wits Line (McCarthy 2006).

The 3D CLR model was derived by computing the difference between the Crown Lava marker and the VCR marker within the seismic volume. This resulted in a seismic horizon, positioned at approximately 700 m below the VCR, which was bulk-shifted up by 100 m to correlate with the depth position of the CLR as confirmed by seismic attributes and boreholes (Fig. 12b). The information (such as depth position,

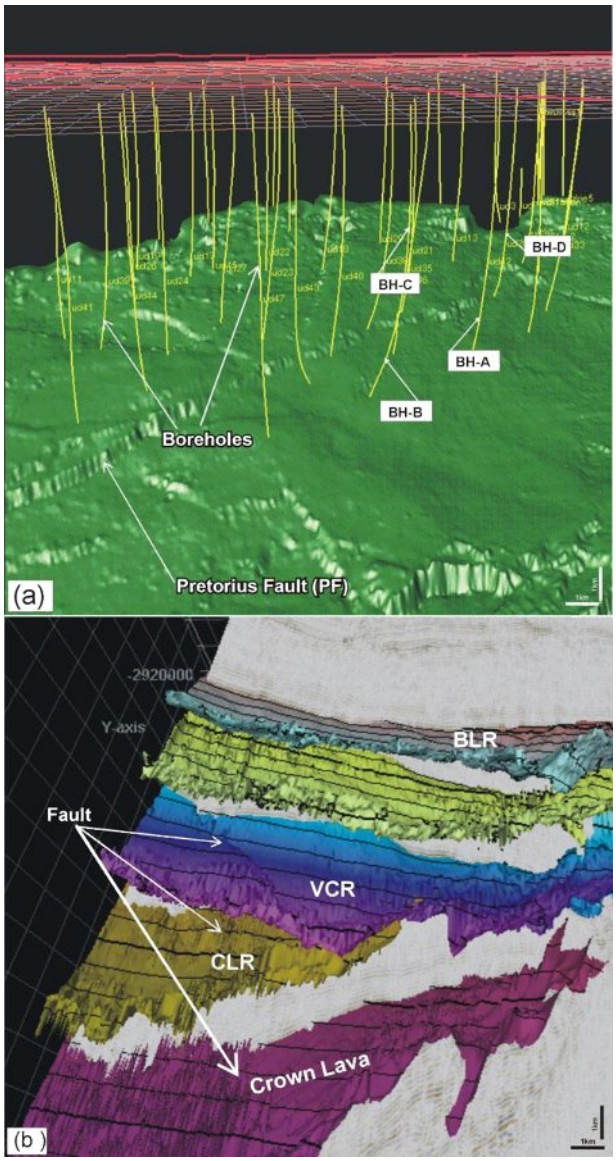


Figure 13 (a) CLR ore body integrated with exploration boreholes that intercept the CLR and the VCR. (b) 3D visualization of the interpreted seismic horizons used to derive the CLR horizon.

shape, and dip of the CLR) from modified seismic attributes and borehole control was used to constrain the CLR interpretation (Fig. 12b). On average, boreholes have a good tie (0–20 m) with the derived CLR reflector, although at some depths, the CLR is slightly (5 m) deeper than the actual depths of the borehole formation tops (Fig. 12b). Some depth mis-ties of several metres (5–10 m) occurred where boreholes were drilled in complex faulted areas. Figure 13(a) shows bore-holes that intersect both the CLR and VCR, as well as the optimum imaging of its related structures through manual interpretation. The majority of boreholes used to constrain seismic interpretation were drilled in a tight grid (<1 km); this provided high confidence in our CLR model.

Finally, the fault surfaces at the VCR and Crown Lava depth levels were projected between the two reflectors as to better define the fault surfaces that cross-cut the CLR (Fig. 13b). The resulting final CLR model across the Mponeng Gold mine has an average dip of 25° to the west. The mine, as seen on the CLR depth elevation map in Figs. 14(a,b), is characterized by a number of north–northeast and north– northwest-trending complex normal faults (500 m maxi-mum throw) particularly on its southwestern flank. In general, the majority of these faults are large enough to be visible on seismic sections and mappable using the seismic depth-structure map (Fig. 14a). Furthermore, 3D seismics has detected and delineated one major north–northeast-trending fault zone, referred to as PFZ. The Pretorius Fault divides Mponeng Gold mine between a structurally complex area to the south and a comparatively less structurally complex area to the north (Fig. 14a). Figure 14(b) displays a north–south depth seismic section through the PFZ. The seismic section shows that the PFZ crosscuts and offsets the VCR, CLR, and Crown lava. Importantly, the geometric nature of this fault suggests that PFZ was active during the deposition of the CLR (Gibson 1997; Dankert and Hein 2010). The identification of this structure is critical for the mine as it may represent losses of mineable ground and potential safety hazards (see Pretorius *et al.* 1994). The depth position and dip of the PFZ has been confirmed in the previous seismic interpretation by Gibson *et al.* (2000) and by underground mapping and drilling (Dankert and Hein 2010).

Edge detection attributes (Dalley *et al.* 1989; Manzi *et al.* 2012a) were generated to confirm the structural information and to delineate subtle faults that fall below the seismic resolution limit (25 m). Prior to application of edge detection techniques, the CLR depth map was smoothed through low-pass filtering using the combination of mean and median filters to remove noise introduced during manual picking. Figure 15(a) shows a smoothed CLR depth structure map. The image shows better detection of individual faults (see red arrows in Fig. 15a) around a complex PFZ. The edge detection map, on the other hand, exhibits a more detail structural architecture (shown by black arrows in Fig. 15b) that was not readily seen on the CLR depth structure map (Fig. 15a). This attribute shows more subtle complex architectural character such as cross-cutting relationship, continuity, connectivity, and bifurcations (shown by black arrows in Fig. 15b). Most importantly, these attributes have imaged the clustering

of minor faults (and possible fractures) around the major PFZ (Fig. 15b). Understanding this distribution is important for a number of reasons including: (i) wall rock stability around fault zones, in terms of fall of ground and micro-seismicity and (ii) transmission of fluids such as water and methane.

Overall, the seismic structural mapping and sampling density is estimated to be 500 times greater than the surface borehole coverage. Thus, the risk of spatially aliasing of the structures, particularly subtle ones, is hugely minimized. This information may greatly increase the confidence towards cost estimation for the extracting of the ore resources, particularly with regard to quantifying geological loss factors (e.g., in the dyke zone and along the fault-crosscutting zones). Horizons and faults were compared with regional control to quantify possible depth discrepancies. The seismically defined VCR, CLR, Crown Lava, and their intersecting faults were modelled to create a robust geologically constrained structural frame-work, which was then imported into mine and exploration plans (Figs. 16 and 17). The model also shows that the major-ity of the structures delineated at the VCR and Crown Lava reflectors were also present at the CLR reflector (Fig. 17). However, the ability to directly correlate the faults at all three depth reflector levels was restricted given the large range in dips of the faults and the large vertical separation of the three reflectors.

DISCUSSION

Petrophysical analysis

To better understand the nature of the seismically transparent gold-bearing conglomerate reef, the CLR, samples of the reef, and its H/W and F/W rocks were collected from the boreholes for seismic wave and bulk density measurements. The density data of the samples for the CLR, H/W quartzites (Rice Pebble Quartzite), and F/W quartzites (Blyvooruitzicht Quartzite) indicate minor variations. The average density values are 2.80 g/cm^3, 2.79 g/cm^3, and 2.75 g/cm^3 for the CLR, Rice Pebble Quartzite, and Blyvooruitzicht Quartzite, respectively. The similarities in mineral composition between these units may be the reason for similar density data. The average density (3.05 g/cm^3) for the Green Bar, in contrast, is relatively higher value than its F/W rocks. This may be attributed to the amount of iron and magnesium found in these metamorphosed chloritoid shale units (Krapež 1985).

Most of the samples were measured at atmospheric pressure; only four samples were measured at elevated stresses up to 65 MPa. As evidenced from the P-wave velocity measurements at atmospheric pressure, the Rice Pebble Quartzite samples show velocities in the range of 5080 m/s–5360 m/s (Table 1), whereas Blyvooruitzicht Quartzite samples show velocities ranging from 4920 m/s to 5170 m/s. Thus, the acoustic impedances of these rocks are very similar. These results are in agreement with the published velocity results for quartzites from the Witwatersrand Basin (Pretorius *et al.* 2003). The Green Bar has P-wave velocities between 5350 m/s–5570 m/s (Table 1), whereas the CLR has P-wave velocities of 4920 m/s and 5870 m/s. It is generally observed that the velocity as a function of density (Fig. 6) shows no particular trend, implying that our results may not be in agreement with Birch's law and that other factors, such as internal structures of the samples, should be considered. However, the average P-wave velocities tend to slightly increase with the increase in bulk density. The acoustic impedance contrast is required between two geological units for reflections to be generated. Our physical property measurements explain the poor reflectivity nature of the CLR in the 3D seismic data.

As evidenced from the P-wave velocity measurements at elevated stresses, the seismic velocities for CLR, Green Bar, and quartzite units (Rice Pebble Quartzite and Blyvooruitzicht Quartzite) slowly increase with increasing stresses (Fig. 7). On average, the rate of increase is high at low stresses (0 MPa– 25 MPa) and levels off at higher stresses (25 MPa–65 MPa). The Green Bar shows, however, a slower (5500 m/s–5600 m/s) velocity increase in the low (0 MPa–20 MPa) stress zone than the CLR, which shows a higher velocity increase (4920 m/s–5500 m/s, see Fig. 7). This is due to mineralogical differences and sample conditions or due to the presence of microcracks. Despite the low porosity (< 2%) in the samples, the results suggest that the velocities are sensitive to macro-fracturing and micro-fracturing. Generally, the response of rock to stress depends on its microstructure and constituent minerals, which is manifested in stress dependence of seismic wave velocities. The macrocracks and microcracks in Mponeng Gold mine drill cores could be attributed to drilling and stress relaxation during the extraction of the core. While our measured S-wave velocities were not interpretable with confidence because of the difficulties in picking the S-wave arrival times, the P-wave velocity measurements were satisfactory with error estimates of about 2% for all the P-wave values.

It is important that the seismic velocities are measured at low frequencies, i.e., frequencies that are representative of seismic surveys. However, this is not possible at this stage, particularly when pressurizing the samples at the same time. We were not able to conduct our measurements at

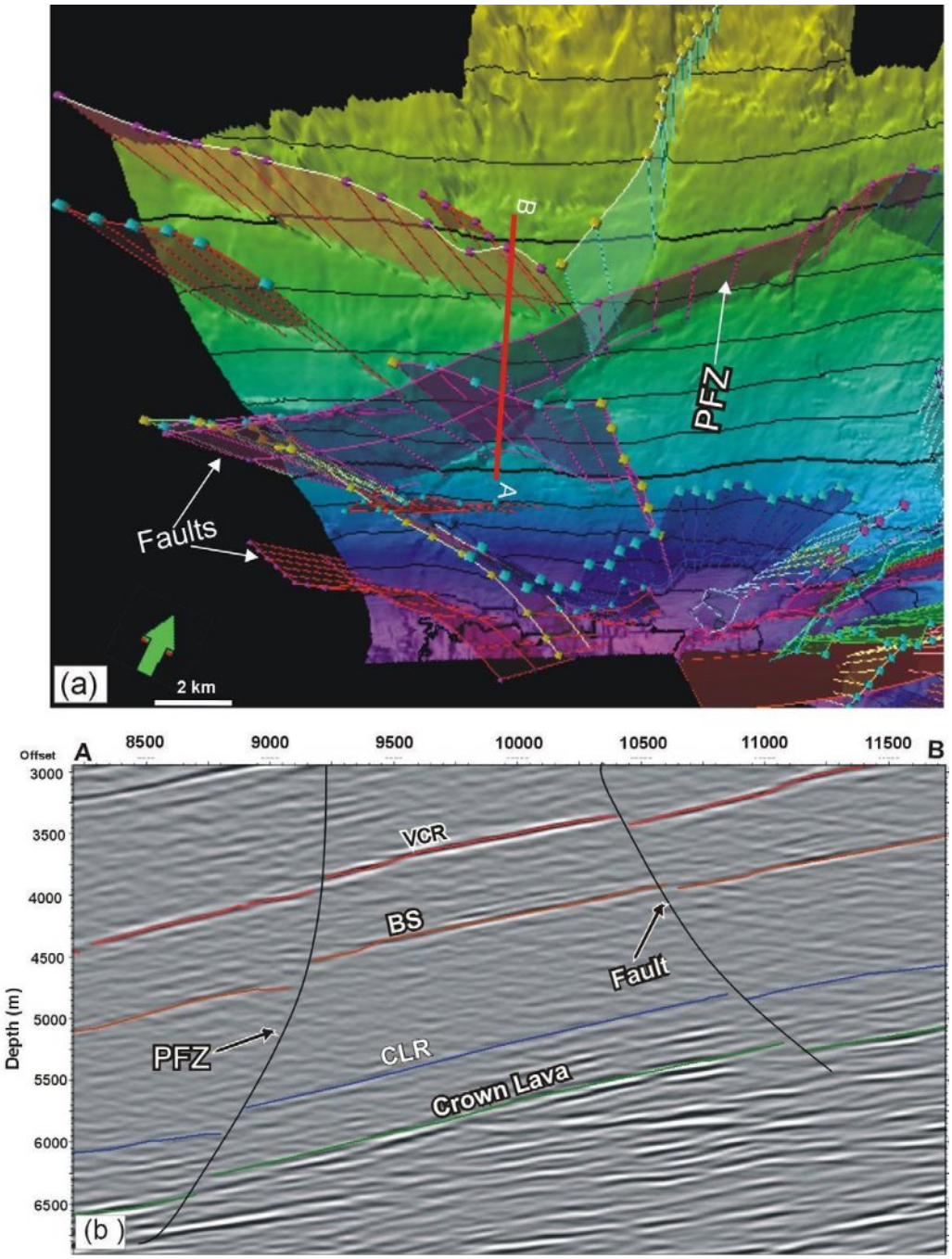


Figure 14 (a) CLR horizon-fault framework defined from the depth structure map. The model shows the stable faulted blocks, bifurcation of faults from a single plane into two branches and cross-cutting relationship between faults. (b) Seismic imaging of the major Pretorius Fault Zone (PFZ). BS: Booysens Shale.

confining stresses, which would have been a better way of estimating velocities at elevated stresses. While we aim to carry out these measurements in the near future, the current measurements provide first-hand information about the potential velocity contrast that may exist between different rock units. The fact that, even at ultra-high frequencies, no significant velocity contrast is observed between the H/W and F/W quartzites of the CLR ore body suggests that the low

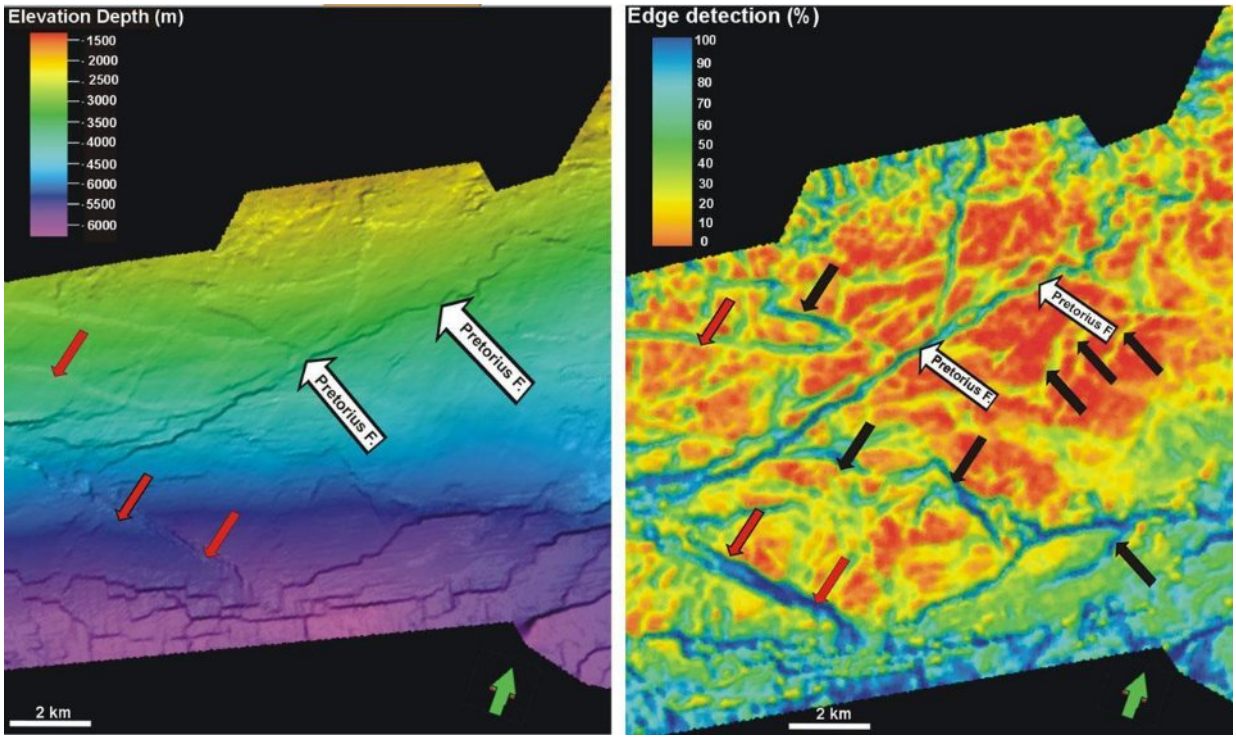


Figure 15 (a) Seismically imaged faults by smoothed conventional interpretation (picking). (b) High-resolution imaging of subtle features (faults and dykes, see black arrows) by an edge detection technique.

frequency measurements will likely provide the same result. This is however left to be confirmed.

Seismic interpretation

We have reinterpreted the high-resolution 3D seismic data, acquired by AngloGold Ashanti in 1995 over the Mponeng Gold mine, to construct a 3D structural model of the world's deepest (4.2–4.5 km) known gold resource, the CLR. The 3D seismic data have been integrated with borehole information to constrain our seismic interpretation and CLR ore-body model.

The 3D seismic data show that the VCR (located 900 m above the CLR) and the Crown Lava marker (located 700 m below the CLR) are good strong seismic reflectors. The reason for strong reflection is that the VCR is an unconformity that occurs at an interface between the overlying high-velocity (6400 m/s), dense (2.90 g/cm^3) basaltic lavas of the Ventersdorp Supergroup and the underlying low-velocity (5750 m/s), less dense (2.67 g/cm^3) quartzite units of the Central Rand Group (Pretorius *et al.* 2003). On the other hand, the Crown Lava is an extensive unconformity that occurs at the interface between the overlying quartzite units at the base of the Central Rand Group and underlying basaltic lavas at the top of the West Rand Group. The 3D seismic data also confirm that the CLR is poorly delineated by the seismic method. These results are confirmed by physical property measurements that the CLR cannot be seismically imaged because it occurs at the low impedance contrast within the overlying Rice Pebble Quartzite units (2.75 g/cm^3 and 5260 m/s) and underlying Blyvooruitzicht Quartzite units (2.71 g/cm^3 and 5080 m/s) of the Central Rand Group. Moreover, the CLR has a maxi-mum thickness (1 m) far less than the tuning thickness and thus cannot be directly detected by the seismic data with a 100-m dominant wavelength.

Conventional instantaneous attributes based on wavelet amplitude fail to delineate thin beds below the tuning thick-ness because the amplitude decreases as the thickness of the thin bed decreases. Furthermore, they are also incapable of detecting thin beds that are embedded between layers having mi-nor variations in velocity and density due to their sensitivity to lithological changes. To enhance the detection of the CLR, we have introduced an alternative amplitude-independent seismic attribute that sharpens the seismic trace and measures the wavelet character rather than lithological changes. Seismic attributes are sensitive to noise; however, the quality of

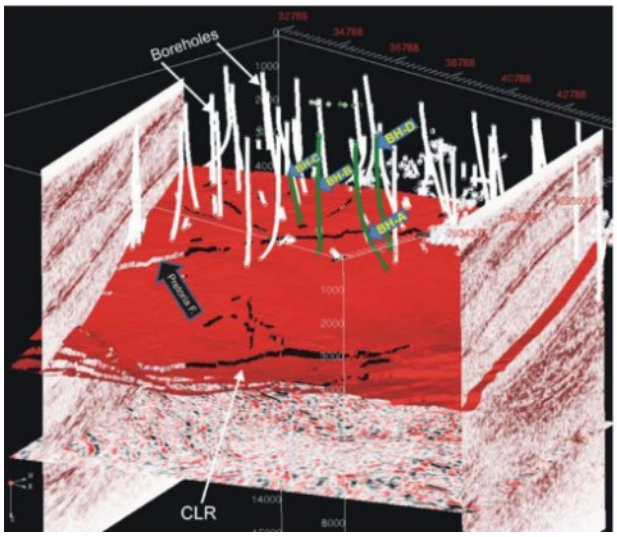


Figure 16 3D visualization of the 3D seismic data integrated with boreholes. The boreholes in green were used for physical property measurements.

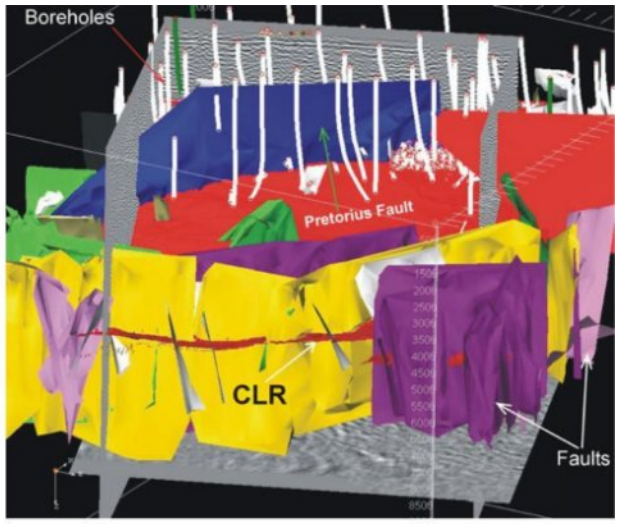


Figure 17 3D structural model of the Carbon Leader Reef model incorporating boreholes and faults.

the 3D seismic data is adequate for the derivation of seismic attributes. We have demonstrated that by removing amplitude on conventional instantaneous attributes and raising their co-sine function to n^{th} power yield the attribute that enhances the detection of the seismically transparent CLR (Figs 10b). The sharpened attributes (Figs 10b and 11a) exhibit greater detail, in terms of highlighting the lateral continuity and detection of shape character of the CLR, than normal amplitude display. Although the sharpened instantaneous frequency was extremely powerful in enhancing the detection of the CLR, it suffers from noise since it is a derivative attribute. Moreover, it is important to note that these attributes are only completely reliable when correlated with borehole data.

The CLR seismic model, derived from interpretation of the VCR and Crown Lava, shows substantial variations in strike and dip throughout the seismic survey area. Based on the seismically derived CLR horizon, the interpretation of the data has revealed complex normal faulting in the vicinity of the mine. An additional benefit of the reinterpretation of the data has been the identification of the major PFZ, which has previously been mapped through underground mapping (see Fig. 5). The PFZ (Fig. 14b) cuts and offsets the overlying VCR through the CLR into the Crown Lava marker. This suggests that the fault is a complex structure that had multiple movement histories. The timing of this fault activity can have a number of impacts on mining. First, if the fault was active during the deposition of the CLR ore body, it may control the palaeotopography and hence affect the facies distribution. Second, if the fault was active prior to the deposition of the CLR and reactivated, it may have controlled the erosion and hence subcrop positions. Third, if the fault was active after the deposition of the CLR and has direct contact with water, i.e., the dolomitic aquifers of the Transvaal Supergroup above the VCR, it may bring water into the mining level or cause mine seismicity. As evidenced from seismic sections, the PFZ has been measured to have a maximum throw of 500 m, and its throw is variable along the length of the fault zone. This amount of vertical displacement has substantial implications in the mine; it can eliminate the entire CLR mining level and affect the siting of exploration boreholes. The model in Fig. 14(a) further reveals a series of faults with throws greater than 25 m clearly offsetting the CLR and VCR ore bodies.

The application of edge detection attributes (Fig. 15b) to a CLR horizon has revealed some degree of structural complexity that would not have been identified using conventional attributes. These are predominantly north–northeast and north–northwest trending faults with throws less than 25 m but greater than 2 m. Pre-conditioning of the horizon data through low-pass filtering prior to application of edge detection attributes helps to remove noise introduced during manual interpretation and enhances the application of edge detection attributes. The detection of the lateral continuity of the CLR reflector and its depth position has been greatly improved by integrating the modified instantaneous attributes with borehole control (Figs. 16 and 17). We observe a relatively good tie between the CLR and borehole intersections. The few depth mis-ties observed are attributed to complex

faulting in the area where these boreholes were drilled, and errors in the velocity field used for depth conversion and/or borehole deviations at depths. These depth errors were considered in the final structural model. The variations in dip angle of the CLR model, the constraints on fault orientations across the mining areas, and the presence of the detected numerous faults are significant and must be factored into mine planning and development. The confidence in the CLR ore-body model and mine plan has been significantly improved, and the new shafts to exploit the deeper ore body can be optimally sited in relatively structurally complex areas.

CONCLUSIONS

The 3D seismic data acquired over the Mponeng Gold mine for future deep mine planning have been reinterpreted for the purposes of building a 3D structural ore-body model of the CLR. We have combined 3D seismic data with petrophysical measurements, borehole information, and underground map-ping data to produce a high-quality 3D CLR ore-body model. The analysis of bulk density and seismic velocity data con-firm that the nature of poor seismic reflectivity seen on the seismic data is the result of small thickness of the CLR and poor impedance contrasts between the H/W and F/W quartzite units of the CLR. The laboratory measurements further indicate that seismic velocities are significantly affected by the presence of macrocracks and microcracks in the rock samples, which may be the main cause for the observed velocity increase at elevated stresses. We have shown the importance of conducting laboratory experiments at stresses relevant for deep targets. This information is essential for future seismic survey design in the Witwatersrand Basin that aims to directly image the CLR ore body.

Our new alternative seismic attributes were successful in achieving the primary objectives of enhancing the detection of the seismically transparent CLR and constraining its depth position at 4.2 km–4.5 km by the borehole data. In this study, we have, for the first time, shown that raising the cosine function of the instantaneous attributes to the n^{th} power and removing the seismic amplitude can sharpen the seismic trace, thereby enhancing the seismic interpretation of layers below the tuning thickness. However, obtaining more convincing results with this new attribute is highly dependent on SNR.

The 3D seismic data provided valuable information in terms of imaging of the complex strato-structural architecture. For example, the PFZ, one of the most important structural elements in the study area, is now precisely mapped, and its subordinate cluster of minor faults is also delineated by edge detection attributes. As such, the CLR model derived from the seismic data, combined with boreholes and underground mapping, allows unprecedented details of both mineable and unmineable areas. The model forms a dynamic and integral part of Mponeng Gold mine's ongoing mine design and planning processes.

ACKNOWLEDGEMENTS

This research was sponsored by CIMERA (Centre of Excellence for Integrated Mineral and Energy Resource Analysis), Thuthuka National Research Funding, National Research Foundation (Pretoria), AngloGold Ashanti Ltd., and Gold Fields Mining Ltd. We would like to thank Oleg Brovko, Rob Burnet, John Bell, and Natasha Coertze for their major scientific contribution towards this project. Uppsala University researchers are also acknowledged for carrying out some of the seismic wave velocity and density measurements and their collaboration with us in this project. A Swedish International Development Cooperation (SIDA) planning grant helped to initiate this collaboration for which we are grateful. We ac-knowledge critical and useful comments provided by S. Mayr, an anonymous reviewer, and the associate editor that greatly improved the quality of the paper.

REFERENCES

Barnes A.E. 1993. Instantaneous spectral bandwidth and dominant frequency with applications to seismic reflection data. *Geophysics* **58**, 419–428.

Beach A. and Smith R. 2007. Structural geometry and development of the Witwatersrand Basin, South Africa. In: *Deformation of the Continental Crust: The Legacy of Mike Coward* (eds A.C. Ries, W.H.R. Butler and R.H. Graham), pp. 533–542. Geological Society of London Special Publication.

Bellefleur G., Malehmir A. and Muller¨ C. 2012. Elastic finite-difference modeling of volcanic-hosted massive sulfide deposits: A case study from Half Mile Lake, New Brunswick, Canada. *Geo-physics* **77**, WC25–WC36.

Brown A.R. 1996. Seismic attributes and their classification. *The Leading Edge* **10**, 1090.

Campbell G. and Crotty J.H. 1990. 3-D seismic mapping for mine planning purposes at the South Deep Prospect. In: *Proceedings International Deep Mining Conference: SAIMM Symposium Series S10 Vol. 2* (eds D.A.J. Ross-Watt and P.D.K. Robinson), pp. 569– 597.

Chopra S., Castagna J. and Portniaguine O. 2006. Seismic resolution and thin-bed reflectivity inversion. *Canadian Society of Exploration Geophysicists Recorder* **1**, 19–25.

Chopra S. and Marfurt K.J. 2007. Curvature attribute applications to 3D surface seismic data. *The Leading Edge* **26**, 404–414.

Coward M.P., Spencer R.M. and Spencer C.E. 1995. Development of the Witwatersrand Basin, South Africa. *Geological Society of London, Special Publication* **95**(1), 243–269.

Dalley R.M.E., Gevers C.A., Stampfli G.M., Davies D.J., Gastaldi C.N., Ruijtenberg P.A. 1989. Dip and azimuth displays for 3D seismic interpretation. *First Break* **7**, 86–95.

Dankert B.T. and Hein K.A.A. 2010. Evaluating the structural char-acter and tectonic history of the Witwatersrand Basin. *Precambrian Research* **177**, 1–22.

Dehghannejad M., Juhlin C., Malehmir A., Skytta¨ P. and Weihed P. 2010. Reflection seismic imaging of the upper crust in the Kristineberg mining area, northern Sweden. *Journal of Applied Geophysics* **71**, 125–136.

Dehghannejad M., Malehmir A., Juhlin C. and Skytta¨ P. 2012. 3D constraints and finite-difference modeling of massive sulfide de-posits: The Kristineberg seismic lines revisited, northern Sweden. *Geophysics* **77**, WC69–WC79.

Erismann F. 2007. The South Deep Au-U ore deposit Witwatersrand Basin, Republic of South Africa, Fluid inclusions and hydrother-mal processes. MSc thesis, Eidgenossische¨ Technische Hochschule Zurich¨ and final report to joint venture partners of South Deep Mine.

Fomel S. 2007. Local seismic attributes. *Geophysics* **72**, 29–33. Frimmel H.E., Groves D.I., Kirk J., Ruitz J., Chesley J. and Minter W.E.L. 2005. The formation and preservation of the Witwatersrand goldfields, the world's largest gold province. *Economic Geology (100th Anniversary Volume)*, pp. 769–797

Gibson M.A.S. 1997. The structural interpretation and seismic char-acterization of a 3-D seismic survey, Western Deep Levels Gold Mine, South Africa. M.Sc. Thesis, University of Leeds, U.K.

Gibson M.A.S., Jolley S.J. and Barnicoat A.C. 2000. Interpretation of the Western Ultra Deep Levels 3D seismic survey. *The Leading Edge* **19**, 730–735.

Jolley S.J., Freeman S.R., Barnicoat A.C., Phillips G.M., Knipe R.J., Pather A. 2004. Structural controls on Witwatersrand Gold miner-alization. *Journal of Structural Geology* **26**, 1026–1086.

Jolley S.J., Stuart G.W., Freeman S.R., Knipe R.J., Kershaw D., McAllister E. 2007. Progressive deformation of a late orogenic thrust system, from duplex development to extensional reactiva-tion and disruption: Witwatersrand basin, South Africa. *Geological Society of London Special Publication* **272**, 543–569.

Juhojuntti N., Wood G., Juhlin C., O'Dowd C., Dueck P. and Cosma C. 2012. 3D seismic survey at the Millennium uranium deposit, Saskatchewan, Canada: Mapping depth to basement and map-ping post-Athabasca structure near the orebody. *Geophysics* **77**, WC245–WC258.

Kern H., Mengel K., Strauss K.W., Ivankina T.I., Nikitin A.N. and Kukkonen I.T. 2009. Elastic wave velocities, chemistry and modal mineralogy of crustal rocks sampled by the Outokumpu scientific drill hole: Evidence from lab measurements and modelling. *Physics of the Earth and Planetary* **175**, 151–166.

Koivisto E., Malehmir A., Heikkinen P., Heinonen S. and Kukkonen I. 2012. 2D reflection seismic investigations in the Kevitsa Ni-Cu-PGE deposit, northern Finland. *Geophysics* **77**, WC149–WC162.

Krapez˘ B. 1985. The Ventersdorp Contact placer: a gold-pyrite placer of stream and debris-flow origins from the Archaean Witwater-srand Basin of South Africa. *Sedimentology* **32**, 223–234.

Kukkonen I.T., Heinonen S., Heikkinen P. and Sorjonen-Ward P. 2012. Delineating ophiolite-derived host rocks of massive sulfide Cu-Co-Zn deposits with 2D high-resolution seismic reflection data in Outokumpu, Finland. *Geophysics* **77**, WC213–WC222.

Kuusisto M., Kukkonen I.T., Heikkinen P. and Pesonen L.J. 2006. Lithological interpretation of crustal composition in the Fennoscan-dian Shield with seismic velocity data. *Tectonophysics* **420**, 283– 299.

Malehmir A. and Bellefleur G. 2009. 3D seismic reflection imaging of volcanic-hosted massive sulfide deposits: Insights from reprocess-ing Halfmile Lake data, New Brunswick, Canada. *Geophysics* **74**, B209–B219.

Malehmir A., Dahlin P., Lundberg E., Juhlin C., Sjostr¨om¨ H. and Hogdahl¨ K. 2011. Reflection seismic investigations in the Dan-nemora area, central Sweden: insights into the geometry of poly-phase deformation zones and magnetite-skarn deposits. *Journal of Geophysical Research* **116**, B11307.

Malehmir A., Durrheim R., Bellefleur G., Urosevic M., Juhlin C., White D. 2012a. Seismic methods in mineral exploration and mine planning: a general overview of past and present case histories and a look into the future. *Geophysics* **77**, WC173–WC190.

Malehmir A., Andersson M., Lebedev M., Urosevic M. and Mikhaltsevitch V. 2013. Experimental estimation of velocities and anisotropy of a series of Swedish crystalline rocks and ores. *Geo-physical Prospecting* **61**, 153–167.

Malehmir A., Koivisto E., Manzi M., Cheraghi S., Durrheim R., Bellefleur R. 2014. A review of reflection seismic investigations in three major metallogenic regions: The Kevitsa Ni-Cu-PGE district (Finland), Witwatersrand goldfields (South Africa), and the Bathurst Mining Camp (Canada). *Ore Geology Reviews* **56**, 423–441.

Malehmir A., Juhlin C., Wijns C., Urosevic M., Valasti P. and Koivisto E. 2012b. 3D reflection seismic investigation for open-pit mine planning and exploration in the Kevitsa Ni-Cu-PGE deposit, North-ern Finland. *Geophysics* **77**, WC95–WC108.

Malehmir A., Tryggvason A., Juhlin C., Rodriguez-Tablante J. and Weihed P. 2006. Seismic imaging and potential field modeling to delineate structures hosting VHMS deposits in the Skellefte Ore District, northern Sweden. *Tectonophysics* **426**, 319–339.

Malehmir A., Tryggvason A., Lickorish H. and Weihed P. 2007. Re-gional structural profiles in the western part of the Palaeoprotero-zoic Skellefte ore district, northern Sweden. *Precambrian Research* **159**, 1–18.

Malinowski M., Schetselaar E. and White D.J. 2012. 3D seismic imaging of volcanogenic massive sulphide deposits in the Flin Flon mining camp, Canada: Part 2-Forward modelling. *Geophysics* **77**, WC81–WC93.

Manzi M.S.D., Durrheim R.J., Hein K.A.A. and King N. 2012a. 3D edge detection seismic attributes used to map potential conduits for water and methane in deep gold mines in the Witwatersrand basin, South Africa. *Geophysics* **77**, WC133–WC147.

Manzi M.S.D., Gibson M.A.S., Hein K.A.A., King N. and Durrheim R.J. 2012b. Application of 3D seismic techniques to evaluate ore resources in the West Wits line goldfield and portions of the West Rand goldfield, South Africa. *Geophysics* **77**, WC163–WC171.

Manzi M.S.D., Hein K.A.A., Durrheim R.J. and King N. 2014. The Ventersdorp Contact Reef model in the Kloof Gold Mine

as derived from 3D seismics, geological mapping and exploration borehole datasets. *International Journal of Rock Mechanics and Mining Sciences* **66**, 97–113.

Manzi M.S.D., Hein K.A.A., King N. and Durrheim R.J. 2013. Neoarchaean tectonic history of the Witwatersrand Basin and Venters-dorp Supergroup: New Constraints from high resolution 3D seismic reflection data.*Tectonophysics* **590**, 94–105.

Mayr S.I. and Burkhardt H. 2006. Ultrasonic properties of sed-imentary rocks: effect of pressure, saturation, frequency and microcracks. *International Journal of Geophysics* **164**, 246– 258.

McCarthy T.S. 2006. The Witwatersrand Supergroup. In: *The Ge-ology of South Africa* (eds M.R. Johnson, C.R. Anhaeusser and R.J. Thomas), pp. 155–186. Geological Society of South Africa, Johannesburg/Council for Geosciences, Pretoria.

Mikhaltsevitch V., Lebedev M. and Gurevich B. 2012. Low-frequency measurements of the mechanical parameters of sandstone with low permeability. *ASEG Extended Abstracts*, pp. 1–4.

Pretorius C.C., Jamison A. and Irons C. 1989. Seismic exploration in the Witwatersrand Basin, Republic of South Africa. In: *Proceedings of Exploration 87*, pp. 241–253. Ontario Geological Survey.

Pretorius C.C., Muller M.R., Larroque M. and Wilkins C. 2003. A review of 16 years of hardrock seismic of the Kaapvaal Craton. In: *Hardrock Seismic Exploration, Geophysical Developments Vol. 10* (eds D.W. Eaton, B. Milkereit and M.H. Salisbury), pp. 247–268. Society of Exploration Geophysicists.

Pretorius C.C., Steenkamp W.H. and Smith R.G. 1994. Developments in data acquisition, processing, and interpretation over ten years of south vibroseismic surveying in South Africa. In: *Proceedings of the 15th CMMI Congress, South African Institute of Mining and Metallurgy Vol. 3*, pp. 249–258.

Rock Solid Images 2003. Seismic trace attributes and their projected use in prediction of rock properties and seismic facies, Houston, Texas, pp. 1–4.

Salisbury M.H., Milkereit B., Ascough G., Adair R., Matthews L., Schmitt D.R. 2000. Physical properties and seismic imaging of massive sulfides. *Geophysics* **65**, 1882–1889.

Sheriff R.E. 1991. *Encyclopedic Dictionary of Exploration Geophysics*. SEG, Tulsa.

Stark T.J. 2009. Frequency enhancement via an integer multiplier or just another GeWizardry attribute? International Exposition and Annual Meeting, SEG, Expanded Abstract, 1092–1096.

Taner M.T., Koehler F. and Sheriff R.E. 1979. Complex seismic trace analysis. *Geophysics* **44**, 1041–1063.

Trickett J.C., Duweke W.A. and Kock S. 2004. Three-dimensional reflection seismic: worth its weight in platinum. *Journal of the South African Institute of Mining and Metallurgy* **105**, 252–263.

Urosevic M.U., Bhat G. and Grochau M.H. 2012. Targeting nickel sulfide deposits from 3D seismic reflection data at Kambalda, Australia. *Geophysics* **77**, WC123–WC132.

Van der Westhuizen W.A., De Bruiyn H. and Meintjes P.G. 1991. The Ventersdorp Supergroup: An overview. *Journal of African Earth Sciences* **3**, 83–105.

Vermaakt D.T. and Chunnet I.E. 1994. Tectono-sedimentary pro-cesses which controlled the deposition of the Ventersdorp Con-tact Reef within the West Wits Line. In: *Proceedings of the 15th Congress of the Council for Mining and Metallurgical Institutions Vol. 3* (ed Anhaeusser C.R.), pp. 117–130. South African Institute of Mining and Metallurgy.

Walsh J.B. and Brace W.F. 1966. Elasticity of rock: A review of recent theoretical studies. *Rock Mechanics Engineering Geology* **4**, 283– 297.

White D.J. and Kjarsgaard B.A. 2012. Seismic delineation of the Orion South Kimberlite, Fort a la Corne, Canada. *Geophysics* **77**, WC191–WC201.

White R.E. 1991. Properties of instantaneous seismic attributes. *The Leading Edge* **10**, 26–32.

Wood G., O'Dowd C., Cosma C. and Enescu N. 2012. An interpre-tation of surface and borehole seismic surveys for mine planning at the uranium deposit, northern Saskatchewan, Canada. *Geophysics* **77**, WC203–WC212.

Zimmer M., Prasad M. and Mavko G. 2002. Pressure and porosity influences on Vp – Vs ratio in unconsolidated sands. *The Leading Edge* **21**, 178–183.

10 Discussion

In this study, the geophysical and geological properties of the Carbon Leader Reef (CLR) were characterized from 8 borehole intersections covering a depth range of 3 km to 4.5 km within a high-resolution 3D seismic cube from the West Wits Line (WWL) goldfields. Geophysical investigations involved laboratory measurements of the physical properties (seismic velocities and bulk densities) on the borehole core samples (~ 50 samples) and interpretation of the 3D reflection seismic data. The geological investigations involved core logging, thin section and polished block microscopy and chemical analysis of each rock unit.

The samples obtained from the rock units mainly consisted of full-core samples (diameter=32 mm), however, only half-core samples (radius=16 mm) could be obtained for the CLR. The main lithological units intersected by the boreholes were the Main Quartzite, Green Bar shale and Rice Pebble Quartzite, which form the hangingwall to the CLR and the Blyvooruitzicht Quartzite, which forms the footwall. The lithological units could be correlated with confidence across the boreholes. An additional borehole that intersects the Maraisburg Quartzite, Roodepoort shale (RS) and Lower Roodepoort Quartzite at depths of ~5 km was also obtained. Detailed core-logging was conducted to constrain the depth location of each unit and to identify mineralogical and textural changes. Physical property measurements were mainly conducted on the drill-core samples from the hangingwall and footwall units of the CLR to study the poor seismic reflective nature of the CLR. P- and S-wave velocity measurement were conducted at both atmospheric and uniaxial elevated stresses up to 65 MPa (equivalent to 2 km - 3 km depth), using 0.5 MHz P- and S-wave transducers. Petrography data were used to study effects of mineralogy, porosity and density on seismic wave velocities.

Seismic velocity

The ultrasonic measurements of P-wave (Vp) and S-wave (Vs) velocities were conducted on all the samples collected from the CLR and RS intersections. These samples largely consisted of quartzites and to a lesser extent shales and conglomerates (from the CLR). The P- and S-wave velocities were simultaneously determined from the measurement of the travel time of high frequency acoustic pulses through the rock samples. The ultrasonic equipment is located in a rock mechanics laboratory that contains various machinery that produce vibrations (noise), such as rock cutters, rock polishing equipment, rock strength testing equipment etc. Due to the sensitivity of the ultrasonic transducers, the accuracy in measuring the P- and S-wave travel times was dependent on the vibration levels in the laboratory. Therefore, calibration in a less ‘noisy’ environment was required before the measurements could be carried out in the laboratory. It was particularly difficult to pick the S-wave travel time as the wave form was sometimes not clearly defined. This could possibly be the result of (1) recurring reflections at the boundary of conversion from body waves to surface wave or (2) the

coupling of the transducers as the particle motion in S-waves is perpendicular to the wave propagation. In addition, P- and S-wave velocity measurements and their dependence on bulk density (ρ), mineralogy, chemical composition and applied stress were investigated.

The results show that the samples dominated by quartz and chert, which are represented by quartzites and conglomerates, are associated with low seismic velocities compared to samples that are deficient in quartz and chert, e.g., shales. The high quartz content in the samples is also confirmed by the high silica (>86 wt. % SiO_2) detected from the XRF chemical analysis. According to Kern *et al.* (2009) and Schön (1996) rocks dominated by quartz and chert will have low seismic velocities because these minerals are less dense and, thus slow down seismic wave propagation. The low velocities of the quartzite and conglomerate samples might also be caused by the presence of macro- and- micro cracks, which are also known to slow down seismic wave propagation (Kern *et al.* 2009; Siegesmund *et al.* 1991). Seismic velocity values obtained for the quartzite units range between 4918 m/s and 5363 m/s which is in agreement with values obtained by (*Weder 1994*).

Seismic wave velocities are sensitive to changes in mineralogy, grain size and presence of fractures, thus measurements were conducted on homogeneous samples to ensure accurate measurement of velocities. The CLR conglomerate samples consisted of quartz and chert pebbles and the Rice Pebble Quartzite samples were characterized by quartz and chert grit, which provided uncertainties in the measured seismic wave velocities. Therefore, samples were measured 3 to 5 times to ensure accurate measurement of the velocities. Contrary to the low seismic velocities of the quartzite units, the shale units exhibit high velocity values possibly due to their fine grain size and high iron content. Schön (1996) mentions that fine-grained rocks are not likely to have macro-and-micro fractures (which slow down seismic waves) due to the increased grain-to-grain contact of the minerals. Studies by Kern *et al.* (2009) confirm that rocks with high iron content have high seismic velocities. High seismic velocities associated with high iron content in rocks were also investigated by Krapež (1985). The seismic velocity values obtained for the shale units in this study range from 5124 m/s to 5636 m/s, which are in agreement with studies conducted by Holt (2003). Seismic velocities also show a strong dependency on the pyrite content in the rock samples. For example, rock samples with high pyrite presence exhibit higher velocities compared to samples with low pyrite content. This is observed in the quartzite samples where the highly mineralized CLR has slightly higher velocities compared to the hangingwall and footwall quartzites. The relationship observed between seismic velocities and pyrite in this study is in agreement with studies conducted by Milkereit *et al.* (1996) and Salisbury and Snyder (2007) who investigated seismic wave velocities in sulphide ores, pyrite in particular. The seismic velocities obtained for the quartzite samples, including the Carbon Leader Reef, show only slight variations as a result of similar mineral composition of the rocks.

Seismic velocity-density

The bulk densities of all the rock samples were measured using Archimedes' Principle and utilizing a digital analytical balance. The rock units sampled from each borehole (quartzites, shale and conglomerate) vary in mineral composition and therefore bulk density and have known density values of 2.6 - 2.8 g/cm3 for quartzites, 2.4 - 2.8 g/cm3 for shales (unmetamorphosed) (Schön 1996). There is no standard bulk density for conglomerate rocks because they are formed from the consolidation and lithification of gravel. This gravel can originate from various sources e.g., sandstones or calcareous rocks. Therefore the density of a given conglomerate will depend on the matrix material as well as the pebble type. The bulk density results (~2.66 g/cm^3 to 2.87 g/cm^3) for all the quartzite units were in agreement with previously measured density values. The CLR is composed of quartz and chert pebbles cemented by a quartzite matrix, which led to the grouping of the conglomerate with the quartzite samples. The density values obtained for the CLR range from 2.74 g/cm^3 to 2.83 g/cm^3 which is similar to the densities obtained for the quartzite units. The density results of the shale units (2.80 g/cm^3 - 3.15 g/cm^3) are not in agreement with known shale values from Pretorius *et al.* (1994). The obtained density values for the shale units range between 2.80 g/cm^3 and 3.15 g/cm^3 which is higher than the known shale values Holt (2003). This may be the result of metamorphism of the rock units which increased the rock density in response to an increase in pressure. The low-grade metamorphism of the rocks yielded mineral assemblages that range from pyrophylite-chloritoid, which is observed in thin-sections. These mineral assemblages are confirmed by Phillips and Powell (2012).

In general, the seismic velocities of the samples tend to increase with increasing bulk density following Birch's Law or the Nafe-Drake trend (Birch 1961; Nafe and Drake 1963) for silicate rocks. This does not hold for the low density Rice Pebble Quartzite sample in BH-C (see Chapter 7, Appendix G) that has a higher velocity than the CLR sample. This could mean that the velocity dependence upon bulk density alone, which is usually assumed for the correlation of seismic velocity and gravity for lithological layers, does not hold entirely true for these rocks. The higher velocity in the Rice Pebble Quartzite may be due to higher pyrite content, which seems to cause an increase in seismic velocities.

The high velocity and density of the Roodepoort shale unit compared to the surrounding quartzites is possibly due to its fine grain size and its deficiency in quartz. An interesting feature in the footwall is the high density of the quartzite sample. Physical observation of the footwall from core-logging showed that this unit is similar in appearance to the RS unit i.e., it is fine-grained from first observations and it contains intercalations of shale. Therefore, the high density of the footwall may be the result of its 'shale like' properties.

Seismic velocity-applied stress

To investigate the dependence of seismic velocities to applied stresses, ultrasonic wave velocities were measured at elevated stresses, of up to 65 MPa. Initially, the stresses were measured at 5 MPa intervals and thereafter at 10 MPa. This was done in order to understand the initial velocity change, which is said to occur at low stress regimes between 0 and 25 MPa for most rocks (Christensen 1965; Kern *et al* 1982; Best 1997; Carlson and Miller 2004; Chang *et al.* 2006). A stress of 65 MPa is said to be equivalent to depths of about 3 km - 4 km, which are equivalent to the depth locations of these samples. The relationship between seismic velocities and applied stress was investigated in an unconfined compressive system on full-core samples. The measurement of applied stress in an unconfined compressive system was favoured over the confined compressive system because it is one of the most efficient and affordable methods used to measure stress. In the unconfined compressive system, only the axial stress is applied and the confining stress is zero. Half core samples from the CLR and other lithological units could not be measured because they lacked the correct size and geometry required for equal stress distribution.

The measurements were conducted at room temperature conditions due to difficulties in the sample heating method. It was envisioned that samples would be heated in a microwave oven and then transferred to the uniaxial compressive system where a load would be applied and the response of the seismic waves would be measured. However this method presented difficulties such as (1) the uncertainty of the temperature that the rock would be heated to (2) the decrease in temperature as the sample is transferred to the uniaxial compressive system and (3) immature fracturing that might be induced in the rock during heating.

Generally, the results show that seismic velocities increase with an applied load for all the samples, at least over a limited stress interval. At lower stress regimes (0 - 20 MPa) higher stress effects on seismic velocities are observed for coarse-grained rocks (quartzites and conglomerates) and lower effects for fine-grained rocks (shales). This concurs with studies conducted by Schon (1996), Elbra *et al.* 2011. At higher stress regimes (~20 - 65 MPa) the velocity increase is smaller than in the lower stress regimes (0 - 20 MPa). The larger velocity increase in the low stress regimes is associated with the initial closure of micro-cracks, which results in the increase of seismic velocities. The smaller velocity increase in the higher stress regimes may be due to the closure of these micro-cracks during loading. These observations concur with the extensive work conducted by Birch (1960), Walsh and Brace (1965) and Christensen (1965). There was no evidence of distinct anisotropies observed in our samples (e.g., foliation), therefore we consider that the variations in seismic velocity in our data are mainly caused by mineral compositions and macro-and-micro factures.

Reflection coefficient

To test the reflectivity of the CLR interface, reflection coefficients (RC) at various lithological boundaries along the length of the borehole were calculated using the seismic velocities and bulk density values of the units. The reflection coefficients calculated at the CLR/Rice Pebble Quartzite and the CLR/Blyvooruitzicht Quartzite interfaces were ~0.02 and 0.05, respectively. These are below the minimum value of 0.06 required to produce a strong reflection, as suggested by Salisbury et al. (2000). The low RC value may suggest that the CLR cannot be directly imaged using seismic reflection methods. However, the Green Bar shale/Main Quartzite and the Green Bar shale/Rice Pebble Quartzite interfaces attain RC values of 0.06 - 0.14 and 0.06 - 0.11, respectively. This may suggest that the Green Bar shale (located 3 m above the CLR) can be imaged using seismic reflection methods provided it has the correct geometry. Furthermore, the calculated reflection coefficient values at the RS/Maraisburg Quartzite (RC ~0.07) and RS/Lower Roodepoort Quartzite (RC ~0.06) confirm the observed seismic reflection in the 3D seismic cube.

Seismic interpretation

In this study, volumetric and horizon-based seismic attributes were applied to 3D reflection seismic data, covering the West Wits Line goldfields to better image seismic horizons and geological structures with throws below the suggested seismic resolution limit (one quarter of the dominant wavelength). This was done through the interpretation of the RS horizon, the uppermost reflective unit of the West Rand Group. This shale unit was interpreted because it is the closest (located ~350 m below the CLR) strong seismic marker to the commercial but non-seismic reflective CLR conglomerate. General observation of the survey area reveals that the data are of good quality, with the exception of the survey boundaries and the south-western part of the survey area, due to low fold coverage, poor migration and structural complexities. In addition, it was particularly difficult to interpret the data in the northern parts of the surveyed area due to the outcropping dolomites of the Transvaal Supergroup. The deterioration of the seismic data quality over dolomites has not only been documented in South Africa (Manzi et al. 2012a), but elsewhere in the world (Wright et al. 2000; Šumanovac and Weisser 2001). The deterioration of the seismic data is due to the scattering of seismic energy due to karst weathering (Manzi et al. 2012a). The scattering of the seismic energy results in poor imaging of the subsurface, making it impossible to interpret.

The interpretation of the RS horizon was done on the Kingdom Suite and Petrel seismic interpretation packages. The Kingdom Suite software was used in the initial interpretation of the RS horizon, which was achieved through conventional picking of the horizon on seismic sections followed by picking of faults (and dykes) where discontinuities occurred. Conventional picking (manual picking) was favoured over autotracking (automatic picking) because the data contained regions of complex faulting and low signal-to-noise, which could have been misinterpreted by the autotracking method.

The use of manual picking enabled full user interpretation control, which enabled consistent picking of the horizon and faults. The integration of the seismic data with the borehole data was crucial in constraining the depth location of the RS horizon and understanding many of the reflections that occur above and below the RS seismic reflector. The interpretation of conventional seismic section provides the initial step to the analysis of the first- and second-scale structures that crosscut the West Wits Line goldfields. One of the major limitations of conventional interpretation of seismic data is its inability to image thin dykes, nearly-vertical faults and faults with throws of less than 25 m. The presence of these sub-seismic structures at mining depths poses a danger to mining activities and provides inaccuracies in geological and mining models.

The RS depth structure map is dominated by numerous steeply dipping (~65° - 80°) faults of varying geometries and orientations. The western region of the depth structure map is dominated by north-east trending faults with throws ranging from 60 m to 25 m (seismic resolution limit of the data). The most identifiable structure in the western to central regions of the depth structure map is the second-order-scale Pretorius Fault (PF). The PF is one of the major structures that cuts through the Mponeng and Tau-Tona gold mines and displays a variable throw across the survey area. The fault attains a maximum throw of ~500 m and a minimum of 40 m in the north-eastern and south-western areas, respectively. Importantly, the PF is part of a ~750 m wide Pretorius Fault Zone (PFZ), which has subordinate normal faults that displace the RS hangingwall by throws as small as 25 m. The eastern regions of the RS depth structure map are characterized by steeply dipping (65° - 80°) faults with throws that range from 40 m to 500 m. The most dominant structure in this part of the map is Fault 4 (F4), which is a north-west trending reverse fault with an apparent dip that slightly increases from ~55° to 65° in the west and east, respectively. On its far eastern margin, at depths of 4.8 km to 5 km below the surface, the RS horizon is displaced by the first-order scale Bank Fault. Although the conventional interpretation of the seismic data delineated a number of faults (mainly first- and second-order scale) dominating the WWL goldfields the method lacked the resolution to fully map other geological features.

The application of seismic attributes to the data and the picked RS horizon has improved the mapping of structures as well as the structural architecture of the horizon, which had not been adequately mapped by the conventional method. For example, the extraction of the antrack volume has revealed the continuity of some of the small-scale and large-scale faults, including the PF, from the RS levels to shallower depth levels (Ventersdorp Contact Reef levels). The seismic activity of this fault has been confirmed by a number of seismic events that have occurred along the fault zones (Durrheim *et al.* 2005; Linzer *et al.* 2007; Heesakkers *et al.* 2011; Riemer and Durrheim 2012). The identification of the dual nature of the Pretorius Fault concur with studies by van der Westhuizen *et al.* (1991), Beach and Smith (2007) and Dankert and Hein (2010) and that the Witwatersrand Basin underwent inversion tectonics during and after the deposition of the Central Rand0 Group (extension to compression) and

the Ventersdorp Supergroup (compression to extension). In addition to mapping the full vertical extent of the PF, the ant-tracking method has also successfully mapped the subordinate faults associated with the PF that had throws less than 25 m. The identification of these small-scale faults is important because they are likely to induce weak ground conditions during mining. Furthermore, it is also observed from the antrack volume that these faults crosscut the RS at the top of the West Rand Group, the Central Rand Group and the VCR at the base of the Ventersdorp Supergroup. However, they do not breach the Black Reef (BLR) at the base of the Transvaal Supergroup. This implies that these faults were active prior to the deposition of the BLR and may represent faults that were reactivated during the post-BLR deformation event described by Coward *et al.* (1995), Gibson *et al.* (2000) and Dankert and Hein (2010).

In addition to faults, high amplitude areas that do not correlate with any underground geological features have been identified (Chapter 8, Fig. 8). These features have been interpreted to be caused by stopes or shaft infrastructures, resulting from the high acoustic impedance contrast between the rocks and the air. Furthermore, low amplitude vertical features distinctive of dykes have been identified on seismic sections across the survey area. The majority of these dykes strike north to north-northeast with thicknesses that vary from 1 m to 90 m. However, the ones that can be mapped by our 3D seismic data have a minimum thickness of 25 m, which is the vertical resolution limit of our data. Studies by Litthauer (2009) and Manzi *et al.* (2012b) have confirmed the existence of these structures in the Witwatersrand Basin. The reason for the attenuation of the seismic amplitude, instead of strong reflections known to be associated with dykes and sills, may have been caused by the interaction of dykes with known methane gas within the basin, which is known to highly attenuate the seismic amplitude (Priest *et al.* 2005). The interaction of methane and water in underground workings is known to cause explosions that can cause serious harm or in some cases lead to the death of mine workers. Authors such as Cook (1998), Manzi *et al.* (2012b), Wanger *et al.* (2012) have suggested dykes and faults could be possible conduits for methane gas from various sources (e.g., shale units, coal seams and the mantle) to mining levels in the Witwatersrand goldfields. The proposed general idea is that: methane migrates from the source to mine workings through faults and fractures, either as a gas or dissolved in saline ground water. However, the sources of these methane gases still remain unclear. Nevertheless, considering that the faults that have been identified in this study crosscut both the RS and the economic horizons, the RS could be the most probable candidate for the source of methane. The identification of these structures could assist in mitigating risks faced by miners, which are caused by methane explosions.

The application of horizon-based seismic attributes, including dip, dip-azimuth and edge detection to the data have successfully imaged a number of faults that were not visible on the seismic sections and depth structure map. Comparison of the dip and azimuth attribute displays show that the azimuth attribute display provides better delineation of faults relative to the dip attribute display. The edge

detection attribute, in particular, has several advantages over the dip and dip-azimuth maps, including mapping faults with variable orientation and throws and variable colour tables that maximize the usefulness of this attribute. The utilization of these techniques to old 3D seismic data can reduce structural risks in strategic mine planning. For example, several structures interpreted through traditional picking by previous workers in the mining areas were found not to exist, whereas many new structures were identified. Finally, these attributes enhanced the accuracy in positioning and projecting traditionally picked surfaces to the 3D RS topographic map. Although we have made an attempt to constrain our structural interpretation with borehole data, there is still some ambiguity in the dip and spatial positioning of the interpreted fault surfaces. Our final structural model can be used for the CLR exploration projects and should be constantly updated as new information becomes available, particularly as the mining operation continues deeper.

11 Conclusions

The merged 3D seismic data acquired in the 1990's covering the West Wits Line goldfield have been reinterpreted for the purpose of deriving a 3D strato-structural model from the Roodepoort shale for future mine planning purposes and designs. The 3D seismic data have been integrated with physical property measurements (bulk density and seismic wave velocities) and mineralogy of rocks, borehole logs and underground mapping information to constrain the seismic and structural interpretation. The data have also been modelled using state-of-the-art modelling techniques that have better imaged the continuity of key seismic horizons that occur above and below the Roodepoort shale.

The analysis of the physical property data of the rocks shows a dependence of seismic velocities on the mineralogy and chemical composition. Minerals such as quartz and chert slow down seismic velocities. The presence of pyrite in the samples corresponds to an increase in seismic velocities. It is unsurprising that the silica saturated rocks, in this case the CLR and the quartzite units, have lower velocities compared to the iron-rich shale units (the Roodepoort shale and Green Bar shale). Results show that coarse-grained samples are more sensitive to the increase in applied stress compared to fine-grained samples. This is evident by the sharp velocity increase in the quartzite samples and gentle velocity increase in the shale samples, at low stress regimes (0 - 25 MPa). The seismic velocities of the rocks tend to increase with increasing density, thus supporting Birch's Law. Further analysis of the bulk density and seismic velocity of the data confirm that the poor imaging of the CLR is due to its small thickness and low impedance contrast between the reef and adjacent units. While the bulk density and seismic velocities of the Roodepoort shale and its adjacent units confirm that the strong seismic reflection is the result of its thickness and the strong impedance contrast between its top and the overlying quartzite unit. This allows the Roodepoort shale to be interpreted with confidence throughout the seismic volume.

The interpretation of the seismic stratigraphy across the West Wits Line goldfield using careful analysis of the volumetric (e.g., edge enhancement and ant-tracking) and horizon-based seismic attributes (e.g., dip, dip-azimuth and edge detection) have enhanced the imaging of complex structural patterns throughout the seismic volume and interpreted horizons. The ant-tracking attribute has improved the imaging of the key seismic reflectors as well as faults in structurally intricate regions. This enabled the confident tracking of faults to shallower stratigraphic levels, thus allowing the activity of these structures to be constrained. The horizon-based attributes successfully imaged first- and second-order scale faults, but more importantly the subtle faults with vertical displacements of less than 25 m. In particular, the edge detection technique has unravelled intricate fault geometries (e.g., fault continuity, fault connectivity and cross-cutting relationships) that are difficult to identify on the amplitude seismic sections.

11.1 Recommendations

To address the limitations of the analyses conducted and the seismic data interpreted in this study the follow recommendations are proposed:

- To ensure that noise does not factor into the measurement of P- and S-wave velocities, measurement should be conducted during the less 'noisy' periods.
- Obtain full core samples for the measurement of seismic velocities during the loading.
- The use of a confining pressure system and the heating of samples to prevailing temperatures may yield more accurate results.
- Use the handheld XRF equipment to determine the chemical composition of strategic rock units that cannot be crushed and milled due to scarcity of samples.
- Find better ways to remove the high silica content of the quartzite rocks to ensure the successful analysis of the XRD method.
- Conduct more image analysis (using, for example, scanning electron microscope (SEM) to enhance the interpretation. Use neutron tomography to analyse the 3D internal structure of the samples, since this technique will provide the information about the pore-connectivity and the presence of macro-fractures.
- A new velocity field during reprocessing of the 3D seismic data and prestack depth migration could improve the quality of the structural mapping resolution.
- Always integrate the seismic interpretations with geological information such as borehole logs and surface and underground mapping to ensure the accurate interpretations of seismic horizons and structures where the seismic method falls short.

12 References

Armstrong, R., Compston, W., Retief, E., Williams, I. and Welke, H. (1991). Zircon ion microprobe studies bearing on the age and evolution of the Witwatersrand triad. *Precambrian Research,* **53**, 243-266.

Badley, M. E. (1985). Practical seismic interpretation. IHRDC, Boston, Reidel, vi, 266 s. P.

Bacon, M., Simmonds, R. and Redshaw, T. (2003). 3-D seismic interpretation, first ed. Cambridge University Press, 84, 102-117, 146.

Basir, H. M., Javaherian, A. and Yaraki, M. T. (2013). Multi-attribute ant-tracking and neural network for fault detection: a case study of an Iranian oilfield. *Journal of Geophysics and Engineering*, **10**.

Beach, A. and Smith, R. (2007). Structural geometry and development of the Witwatersrand Basin, South Africa: In: Ries A. C., Butler R. W. H. and Graham R., (Eds). Deformation of the continental crust: The Legacy of Mike Coward, Geological Society, *Special Publication,* **272**, 533-542.

Bellefleur, G., Malehmir, A. and Muller, C. (2012). Elastic finite- difference modeling of volcanic-hosted massive sulfide deposits: A case study from Half Mile Lake, New Brunswick, Canada. *Geophysics* **77**, WC25–WC36.

Berryhill, J. R. (1977). Diffraction response for nonzero separation of source and receiver. *Geophysics,* **42**, 1137-1145.

Best, A.I. (1997). The effect of pressure on ultrasonic velocity and attenuation in near-surface sedimentary rocks. *Geophysical Prospecting*, **45**(2), 345-364.

Birch, F. (1961). The velocity of compressional wave in rocks to 10 kilobars, Part 1. *Journal of Geophysical Research*, **65** (4), 1083-1102.

Blake, W. D. and Gilbert, R. B. (1997). Investigation of possible relationship between undrained shear strength and shear wave velocity for normally consolidated clays. Proceedings offshore technology conference, 411-420.

Braun, R. (1987). Ore Estimation Western Deep Levels. *Proceedings of the Twentieth International Symposium on the Application of Computers and Mathematics in the Mineral Industries*, **3**, 233-243.

Brown, A. R. (1996). Seismic attributes and their classification. *The Leading Edge*, **10**, 1090.

Brown, A. R. (2001). Understanding seismic attributes. *Geophysics*, **66**, 47-48.

Buck, S. G. and Minter, W. E. L. (1985). Placer formation by fluvial degradation of an alluvial fan sequence: the Proterozoic Carbon Leader placer, Witwatersrand Supergroup, South Africa. *Journal of the Geological Society,* **142**, 757-764.

Carlson, R. and Miller, J. (2004). Influence of pressure and mineralogy on seismic velocities in oceanic gabbros: Implications for the composition and state of the lower crust. *Journal of Geophysical Research,* **109**, B09205.

Chang, C., Zoback, M. and Khaksar, A. (2006). Empirical relations between rock strength and physical properties in sedimentary rocks. *Journal of Petroleum Science and Engineering*, **51**, 223-237.

Chopra, S., Castagna, J. and Portniaguine, O. (2006). Seismic resolution and thin-bed reflectivity inversion, *CSEG Recorder,* 19-25.

Chopra, S., Castagna, J. and Xu, Y. (2009). Thin-bed reflectivity inversion and some applications. *First Break*, **27**, 17-24.

Christensen, N. (1965). Compressional wave velocities in metamorphic rocks at pressures to 10 kilobars. *Journal of Geophysical Research*, **70**, 6147-6162.

Christensen N. I. and Salisbury M. H. (1975). Structure and constitution of the lower oceanic crust. *Review of Geophysics,* **13**, 57-86.

Cook, A. P. (1998). The occurrence, emission, and ignition of combustible strata gases in Witwatersrand gold mines and Bushveld platinum mines, and means of ameliorating related ignition and explosion hazards: Final project report, project GAP 504, Safety in Mines Research Advisory Committee, 89.

Cox, T. and Seitz, K. (2007). Ant tracking seismic volumes for automated fault interpretation. AAPG Search and Discovery Article, GeoConvention 2007, Calgary, Alberta, Canada.

Dalley R. M., Gevers E. C. A., Stampfli G. M., Davies D. J., Gastaldi C. N., Ruijtenberg P. A. and Vermeer G. J. O. (1989). Dip and azimuth displays for 3D seismic interpretation. *First Break*, **7**, 86-95.

Dankert, B. T. and Hein, K. A. (2010). Evaluating the structural character and tectonic history of the Witwatersrand Basin . *Precambrian Research,* **177**, 1-22.

Davis, G. H. and Reynolds, S. J. (1996). *Structural Geology of Rocks and Regions* (2nd ed.), John Wiley and Sons, 372-424.

Dehghannejad, M., Juhlin, C., Malehmir, A., Skyttä, P., Weihed, P. (2010). Reflection seismic imaging of the upper crust in the Kristineberg mining area, northern Sweden. *Journal of Applied Geophysics* **71**, 125-136.

Dehghannejad, M., Bauer, T., Malehmir, A., Juhlin, C. and Weihed, P. (2012). Crustal geometry of the central Skellefte district, northern Sweden-constraints from reflection seismic investigations. *Tectonophysics* 524-525, 87-99.

De Kock, W. P. (1964). The geology and economic significance of the West Wits Line. In: Haughton S. H., (Eds), The geology of some ore deposits in southern Africa. *Geological Society of South Africa,* **1**, 323-386.

De Wit, M. J., Roering, C., Hart, R. J., Armstrong, R. A., De Ronde, C. E. J., Green, R. W. E., Tredoux, M., Peberdy, E. and Hart, R. A. (1992). Formation of an Archaean Continent, *Nature,* **357**, 553-562.

Durrheim, R. J., Spottiswoode, S. M., Roberts, M. K. C. and van Z. Brink, A. (2005). Comparative seismology of the Witwatersrand Basin and Bushveld Complex and emerging technologies to manage the risk of rockbursting. *The Journal of the South African Institute of Mining and Metallurgy*, **105**, 409-416.

Elbra, T., Karlqvist, R., Lassila, I., Hæggström, E. and Pesonen, L., (2011). Laboratory measurements of the seismic velocities and other petrophysical properties of the Outokumpa deep drill core samples, eastern Finland. *International Journal of Geophysics,* **184**, 405-415.

Els, B. G., van den Berg, W. A. and Mayer, J. J. (1994). The Black Reef Quartzite Formation in the western Transvaal: sedimentological and economic aspects, and significance for basin evolution. *Mineralium deposita,* **30**, 112-123.

Engelbrecht, C. J., Baumbach, G. W., Matthysen, J. and Fletcher, P. (1989). The West Wits Line. In: Anhaeusser C. A. and Maske S., (Eds). Mineral deposits of southern Africa, **1**, 599-648.

Eriksson, P. G. and Reczko, B. F. F. (1995). The sedimentary and tectonic setting of the Transvaal Supergroup floor rocks to the Bushveld Complex. *Journal of African Earth Sciences,* **21**, 487-504.

Eriksson, P. G., Altermann, W., Hartzer, F. J. (2007). The Transvaal Supergroup and its precursors. In: Johnson, M.R., Anhaeusser, C.R., Thomas, R.J. (Eds.), The Geology of South Africa. Geological Society of South Africa, Johannesburg/Council for Geoscience, Pretoria, 237-260.

Fletcher, P. (2009). Carbon Leader Reef West Wits Line internal report.

Frimmel, H. E. and Minter, W. E. L. (2002). Recent developments concerning the geological history and genesis of the Witwatersrand gold deposits, South Africa. *Society of Economic Geologists, Special Publication,* **9**, 17-45.

Frimmel, H. E., Groves, D. I., Kirk, J., Ruiz, J., Chesley, J. and Minter, W. E. (2005). The formation and preservation of the Witwatersrand goldfields, the world's largest gold province. *Economic Geology 100th Anniversary Volume*, 769-717.

Gadallah, M. R. and Fisher, R. (2009). Exploration Geophysics: An introduction, Springer-Verlag Berlin, Heidelberg, Germany, 262.

Gibson, M. A. S. (1997). The structural interpretation and seismic characterization of a 3-D seismic survey, Western Deep Levels Gold Mine, South Africa. M.Sc. Thesis, University of Leeds, U.K.

Gibson, M. A. S., Jolley, S. J. and Barnicoat, A. C. (2000). Interpretation of the Western Ultra Deep Levels 3D seismic survey, *The Leading Edge,* **19**, 730-735.

Gibson, M. A. S. (2004). Goldfields KEA 3D Seismic Project: Final Report. Unpublished report to Gold Fields Mining, 52.

Gibson, M. A. S. (2005). Interpretation of the 2003 South Deep 3D Seismic Survey. Unpublished report to Gold Fields Mining, 62.

Grové, D. and Harris, C. (2010). O - and H - isotope study of the Carbon Leader Reef at the Tau Tona and Savuka mines (Western Deep Levels), South Africa: Implications for the origin and evolution of Witwatersrand Basin fluids. *South African Journal of Geology*, **113** (1), 1-14.

Han, D., Nur, A. and Morgan, D. (1986). Effect of porosity and clay content on wave velocity in sandstones. *Geophysics* **51**, 2093-2107.

Hart, R. J., Hargraves, R. B., Andreoli, M. A. G., Tredoux, M. and Doucouré, M. (2011). Magnetic anomaly near the centre of the Vredefort structure: Implications for impact-related magnetic signatures. *Geology,* **23**, 277-280.

Heesakkers, V., Murphy, S. and Reches, Z. (2011). Earthquake rupture at focal depth, part 1: Structure and rupture of the Pretorius Fault, Tau-Tona mine, South Africa. *Pure and Applied Geophysics*, **168**, 2395-2425.

James, D. E., Niu, F. and Rokosky, J. (2003). Crustal structure of the Kaapvaal craton and its significance for early crustal evolution, *Lithos,* **71**, 413-429.

Johnston, D. H and Coper, M. R. (2010). Methods and Applications in Reservoir Geophysics. *Investigations in Geophysics*, **15**. Society of Exploration Geophysics.

Jolley, S.J., Freeman, S.R., Barnicoat, A.C., Phillips, G.M., Knipe, R.J. and Pather, A. (2004). Structural controls on Witwatersrand Gold mineralization. *Journal of Structural Geology,* **26**, 1026-1086.

Kearey, P. and Brooks, M. (1991). An introduction to Geophysical exploration, 2nd edition. Oxford, Blackwell Scientific Publications, 254.

Kearey, P., Brooks, M. and Hill, I. (2002). An introduction to geophysical exploration, 3rd edition. Oxford, Blackwell Science, 272.

Kern, H., (1982). P- and S-wave velocities in crustal and mantle rocks under the simultaneous action of high confining pressure and high temperature and the effect of the rock microstructure. In: Schreyer W. (Eds.), High pressure researchers in geosciences. Schweizerbart, Stuttgart, 15-45.

Kern, H., Mengel, K., Strauss, K. W., Ivankina, T. I., Nikitin, A. N. and Kukkonen, I. T. (2009). Elastic wave velocities, chemistry and modal mineralogy of crustal rocks sampled by the Outokumpu scientific drill hole: Evidence from lab measurements and modelling. *Physics of the Earth and Planetary Interiors,* **175**, 151-166.

Kern, H. and Mengel, K. (2011). P- and S-wave velocities and velocity anisotropy of core samples from the Outokumpu 2500 m crustal section: implications for the nature of seismic reflections. *Geological Survey of Finland, Special Paper*, **51**, 83-94.

Kositcin, N. and Krapež, B. (2004). SHRIMP U-Pb detrital zircon geochronology of the late Archean Witwatersrand Basin, relation between zircon provenance age spectra and basin evolution, *Precambrian Research,* **129**, 141-168.

Krapež, B. (1985). The Ventersdorp Contact placer: a gold-pyrite placer of stream and debris flow origins from the Archaean Witwatersrand Basin of South Africa. *Sedimentology*, **32,** 223-234.

Kukkonen, I. T., Heinonen, S., Heikkinen, P. and Sorjonen-Ward, P. (2012). Delineating ophiolite-derived host rocks of massive sulphide Cu-Co-Zn deposits with 2D high-resolution seismic reflection data in Outokumpu, Finland. *Geophysics* **77**, WC213-WC222.

Litthauer, A. (2009). Geochemistry of the Dykes in the Carletonville Goldfield. MSc thesis, University of the Free State, South Africa.

Linzer, L. M., Bejaichund, M., Cichiwicz, A., Durrheim, R. J., Goldbach, O. D., Kataka, M. O., Kijko, A., Milev, A. M., Saunders, I., Spottiswoode, S. M and Webb, S. J. (2007). Recent research in seismology in South Africa. *South African Journal of Science*, **103**, 419-426.

Lowrie, W. (1997). Fundamentals of Geophysics. Cambridge University Press, 354.

Malehmir, A. and Bellefleur, G. (2009). 3D seismic reflection imaging of volcanic-hosted massive sulfide deposits: Insights from reprocessing Halfmile Lake data, New Brunswick, Canada. *Geophysics* **74**, B209–B219.

Malehmir, A., Durrheim, R., Bellefleur, G., Urosevic, M., Juhlin, C. and White, D. (2012). Seismic methods in mineral exploration and mine planning: A general overview of past and present case histories and a look into the future. *Geophysics*, **77** (5), WC173-WC190.

Malehmir, A., Andersson, M., Lebedev, M., Urosevic, M. and Mikhaltsevitch, V. (2013). Experimental estimation of velocities and anisotropy of a series of Swedish crystalline rocks and ores. *Geophysical Prospecting* **61**, 153–167.

Malehmir, A., Koivisto, E., Manzi, M., Cheraghi, S., Durrheim, R.J., Bellefleur G., Wijns C., Hein, K. A. A. and King, N. (2014). A review of reflection seismic investigations in three major metallogenic regions: The Kevitsa Ni–Cu–PGE district (Finland), Witwatersrand goldfields (South Africa), and the Bathurst Mining Camp (Canada). *Ore Geology reviews,* **56**, 423-441.

Mambane, P. W., Hein, K. A. A., Twemlow, S. G. and Manzi, M. S. D. (2011). Pseudotachylite in the south boundary fault at the Cooke Shaft, Witwatersrand Basin, South Africa: South African Journal of Geology, **114**, 109-120.

Manzi, M.S.D., Gibson, M.A.S., Hein, K.A.A., King, N. & Durrheim, R.J. (2012a). Application of 3D seismic techniques to evaluate ore resources in the West Wits line Goldfield and portions of the West Rand Goldfield, South Africa, *Geophysics,* **77,** WC163-WC171.

Manzi S. D., Durrheim R. J., Hein A. A. and King N. (2012b). 3D edge detection seismic attributes used to map potential conduits for water and methane in deep gold mines in the Witwatersrand Basin, South Africa, *Geophysics*, **77** (5), WC133-WC147.

Manzi, M. S. D., Hein, K. A. A., King N. and Durrheim R. J. (2013). Neoarchaean tectonic history of the Witwatersrand Basin and Ventersdorp Supergroup: New Constraints from high resolution 3D seismic reflection data. *Tectonophysics* **590**, 94–105.

Manzi, M.S.D., Hein, K.A.A., Durrheim, R.J. and King, N. (2014). The Ventersdorp Contact Reef model in the Kloof Gold Mine as derived from 3D seismics, geological mapping and exploration borehole datasets, *Int. J. Rock Mech. Min. Sci.,* **66,** 97–113.

McCarthy, T. S. (2006). The Witwatersrand Supergroup. In: Johnson M. R., Anhaeusser C. R., and Thomas, R. J., (Eds). The geology of South Africa. *Geological Society of South Africa*, Johannesburg/Council for Geoscience, Pretoria, 155-186.

McQuillin, R. M., Bacon, M., and Barclay, W. (1979). An introduction to seismic interpretation. Graham and Trotman, London.

Milkereit, B., Eaton, D., Wu, J., Perron, G., Salisbury, M., Berrer, E. K. and Morrison, G. (1996). Seismic imaging of massive sulphide deposits: Part II. Reflection seismic profiling, *Economic Geology*, **91**, 829-834.

Moon, C. J. and Whateley, M. K. (1989). Witwatersrand conglomerate gold: West Rand. In: *Introduction to mineral exploration*, **91**, pp. 258-291, eds. Evans, A. M., Blackwell science.

Mussett, A. E. and Khan, M. A. (2000). Looking into the earth: an introduction to geological geophysics. Cambridge: Cambridge University Press, 492.

Myers, R. E., McCarthy, T. S., Bunyard, M., Cawthorn, R. G., Falatsa, T. M., Hewitt, T., Linton, P., Myers, J. M., Palmer, K. J., Spencer, R. (1990a). Geochemical stratigraphy of the Klipriviersberg Group volcanic rocks. *South African Journal of Geology*, **93**, 224-238.

Myers, R. E., McCarthy, T. S. and Stanistreet, I. G. (1990b). A tectono-sedimentary reconstruction of the development and evolution of the Witwatersrand Basin, with particular emphasis on the Central Rand Group. *South African Journal of Geology*,**93**, 180-201.

Nafe, J. E., and C. L. Drake (1963), Physical properties of marine sediments, In: Hill, M. N. (Eds), The Sea, **3**, 794-815, Interscience, New York.

Ngeri, A. P., Tamunobereton-ari, I. and Amakiri, A. R. C. (2015) Ant-tracker attributes: an effective approach to enhancing fault identification and interpretation. *Journal of VLSI and Signal Processing*, **5** (6), 67-73.

Pater, I. and Lissauer, J. J. (2001). Planetary sciences. Cambridge: Cambridge University Press, 528.

Park, R. G. (2004). Foundation of structural geology (3rd edition). Routledge, 11.

Pedersen, S. I., Randen, T., Sonneland, L., and Steen, O. (2002). Automatic 3D Fault Interpretation by Artificial Ants: 64th Meeting, EAEG Expanded Abstracts, G037.

Peng, S. and Zhang, J. (2007). Engineering geology for underground rocks. Springer.

Phillips, N. G. and Powell, R. (2012). Origin of Witwatersrand gold: a metamorphic devolatilisation-hydrothermal replacement model. *Applied Earth Science*, **120** (3), 112-129.

Pretorius, C. C., Steenkamp, W. H. and Smith, R. G. (1994), Developments in data acquisition, processing, and interpretation over ten years of south vibroseismic surveying in South Africa: Proceedings of the XVth CMMI Congress. *South African Institute of Mining and Metallurgy*, **3**, 249-258.

Pretorius, C. C., Muller M. R., Larroque M., and Wilkins C. (2003). A review of 16 years of hardrock seismic of the Kaapvaal Craton. In Eaton D. W., Milkereit B. and Salisbury M. H., (Eds). Hardrock seismic exploration, geophysical developments: SEG, 10, 247-268.

Punturo, R. Kern, H. Cirrincoine, R. Mazzoleni, P. and Pezzino, A. (2005). P- and S-wave velocities and densities in silicate and calcite rocks from the Peloritani Mountains, Sicily (Italy): The effect of pressure, temperature and direction of wave propagation. *Tectonophysics,* **409**, 55-72.

Randen, T. and Sønneland, L. (2002). Mathematical methods and modelling in hydrocarbon exploration and production, **7**, 23-46.

Riemer, K. L. and Durrheim, R. J. (2012). Mining seismicity in the Witwatersrand Basin: monitoring, mechanisms and mitigation strategies in perspective. *Journal of Rock Mechanics and Geotechnical Engineering,* **4** (3), 228-249.

Rijks, E. J. H. and Jauffred, J. C. E. M. (1991). Attribute extraction: An important application in any detailed 3D interpretation study. *The Leading Edge*, **10**, 11-19.

Robb, L. J. and Meyer, M. F. (1995). The Witwatersrand Basin, South Africa: Geological framework and mineralization processes. *Ore Geology Reviews*, **10**, 67-94.

Robb, L. J., Charlesworth, E. G., Drennan, G. R., Gibson, R. L and Tongu, E. L. (1997). Tectonometamorphic setting and paragenetic sequence of Au-U mineralisation in the Archaean Witwatersrand Basin, South Africa, Australian Journal of Earth Sciences: An International Geoscience *Journal of the Geological Society of Australia*, **44** (3), 353-371.

Robb, L. J., Brandl, G., Anhaeusser, C. R. and Poujol, M. (2006). Arachaean granitoid intrusions. In: Johnson M. R., Anhaeusser C. R. and Thomas R. J. (Eds.), *The Geology of South Africa*. Geological Society of South Africa, Johannesburg/Council for Geoscience, Pretoria 57-94.

Salisbury, M. H., Milkereit, B., Ascough, G., Adair, R., Matthews, L. and Schmitt, D. R. (2000). Physical properties and seismic imaging of massive sulphides. *Geophysics,* **65**, 1882-1889.

Salisbury, M. H., Harvey, G. W. and Mathews, L. (2003). The acoustic properties of ores and host rocks in hardrock terranes. In: Eaton D. W., Milkereit B., Salisbury M. H., (Eds.), Hardrock Seismic Exploration. Geophysical Development Series, **10**, *Society of Exploration Geophysics*, 9-19.

Salisbury, M. and Snyder, D. (2007). Application of seismic methods to mineral exploration. In: Goodwell, W. D. (Eds.), Mineral deposits of Canada: a synthesis of major deposit types district metallogeny, the evolution of geological provinces and exploration methods. *Geological Association of Canada Mineral Deposits Division Special Publication*, **5**, 971-982.

Schön, J. H. (2004). Physical properties of rocks: fundaments and principles of petrophysics, Handbook of geophysical exploration seismic exploration, 18, 59-76, 133-233.

Shearer, P. M. (1996).Transition zone velocity gradients and the 520-km discontinuity. *Journal of Geophysical Research,* **101**, 3053-3066.

Sheriff R. E. (1991). Encyclopedic Dictionary of Exploration Geophysics. SEG, Tulsa.

Siegesmund, S., Kern, H. and Vollbrecht, A. (1991). The effect of oriented microcracks on seismic velocities in an ultramylonite. *Tectonophysics*, **186**, 241-251.

Spudich, P and Orcutt, P. (1980). A new look at the seismic velocity structure of the oceanic crust. *Reviews of Geophysics*, **18**, 627-645.

Subrahmanyam, D. and Rao, P. H. (2008). Seismic attributes-A review. *7th International conference and Exposition on Petroleum Geophysics*, 398.

Stanistreet, I. G. and McCarthy, T. S. (1991). Changing tectono-sedimentary scenarios relevant to the development of the Late Archaean Witwatersrand Basin. *Journal of African Earth Sciences*, **13**, 65-81.

Šumanovac, F. and Weisser, M. (2001), Evaluation of resistivity and seismic methods for hydrogeological mapping karst terrains: Journal of Applied Geophysics, **47**, 13-28.

Taner, M. T., Koehler, F. and Sheriff, R. E. (1979). Complex seismic trace analysis. *Geophysics*, **44**, 1041-1063.

Tankard, A. J., Jackson, M. P. A., Eriksson, K. A., Hobday, D. K., Hunter, D. R., Minter, W. E. L. (1982). Crustal Evolution of Southern Africa: 3.8 Billion Years of Earth History. Springer-Verlag, New York, 523.

Trickett, J. C., Duweke, W. A. and Kock, S. (2004). Three-dimensional reflection seismics: worth its weight in platinum. *The Journal of the South African Institute of Mining Metallurgy,* **105**, 357-363.

Urosevic, M.U., Bhat, G. and Grochau, M. H. (2012). Targeting nickel sulfide deposits from 3D seismic reflection data at Kambalda, Australia. *Geophysics* **77**, WC123-WC132.

van der Westhuizen, W. A., De Bruiyn, H. and Meintjes, P. G. (1991). The Ventersdorp Supergroup: an overview. *Journal of African Earth Sciences,* **3**, 83-105.

Veeken, P. C. H. (2007). Seismic stratigraphy, basin analysis and reservoir characterisation. The Boulevard, Langford Lane, Kidlington, United Kingdom, Elsevier, **37**, 509.

Viljoen, M. (2009). The life, death and revival of the Central Rand goldfield. *Special Publication for the World Gold Conference*, 131-138.

Vos, R. G. (1975). An alluvial plain and lacustrine model for the Precambrian Witwatersrand deposits of South Africa. *Journal of Sedimentary Petrology,* **45**, 480-493.

Walsh, J. B. and Brace, W. (1964). A fracture criterion for brittle anisotropic rock. *Journal of Geophysical Research,* **69** (16), 3449-3456.

Wanger, G., Moser, D., Hay, M., Mynent, S., Onstott, T. C and Southam, G. (2012). Mobile hydrocarbon microspheres from > 2-billion-year-old carbon-bearing seams in the South African deep subsurface. *Geobiology***, 10**, 1472-4669.

Warner, M. (1990). Absolute reflection coefficients from deep seismic reflections. In: Leven J. H., Finlayson D. M. Wright C., Dooley J. C. and Bennett B. L. N., (Eds). Seismic Probing of Continents and their Margins. *Tectonophysics,* **173,** 15-23.

Weder, E. E. W. (1994). Structure of the area south of the central rand gold mines as derived from a gravity and vibroseis surveys: Proceedings of the XVth CMMI Congress. *South African Institute of Mining and Metallurgy*, 271-281.

White, D. J. and Kjarsgaard, B. A. (2012). Seismic delineation of the Orion South Kimberlite, Fort a la Corne, Canada. *Geophysics* **77**, WC191-WC201.

Widess, M. B. (1973). How thin is thin bed? *Geophysics*, **38**, 1176-1180.

Wood, G., O'Dowd, C., Cosma, C. and Enescu, N. (2012). An interpretation of surface and borehole seismic surveys for mine planning at the uranium deposit, northern Saskatchewan, Canada. *Geophysics* **77**, WC203-WC212.

Wyllie, M. R. J., Gregory, A. R. and Gardner, G. H. F. (1956). An experimental investigation of factors affecting elastic wave velocities in porous media. *Geophysics*, **23** (3), 459-493.

Wright, C., Walls, E. J. and de J. Carneiro, D. (2000). The seismic velocity in the vicinity of a mine tunnel at Thabazimbi, South Africa: Journal of Applied Geophysics, **44**, 369-382.

Wronkiewicz, D. and Condie, K. C. (1987). Geochemistry of Archaean shales from the Witwatersrand Supergroup, South Africa: source-area weathering and provenance. Department of Geosciences, New Mexico. *Institue of Mining and Technology. Geochimica et Cosmochimica Acta*, **51**, 2401-2416.

Yilmaz, Ö. (2001), Seismic data analysis-Processing, inversion, and interpretation of seismic data. Society of Exploration Geophysicists, Tulsa, Oklahoma, 2027.

Zhao, B., Robb, L. J., Harris, C. and Jordaan, L. J. (2006). Origin of hydrothermal fluids and gold mineralization associated with the Ventersdorp Contact Reef, Witwatersrand Basin, South Africa: Constraints from S, O, and H isotopes. In: Reimold W.U and Gibson R.L., Process on the Early Earth: Geological Society of America, *Special Paper,* **405**, 333-352.

Appendix A

Core-logging

BH-A

BH-B

BH-C

BH-D

BH-E

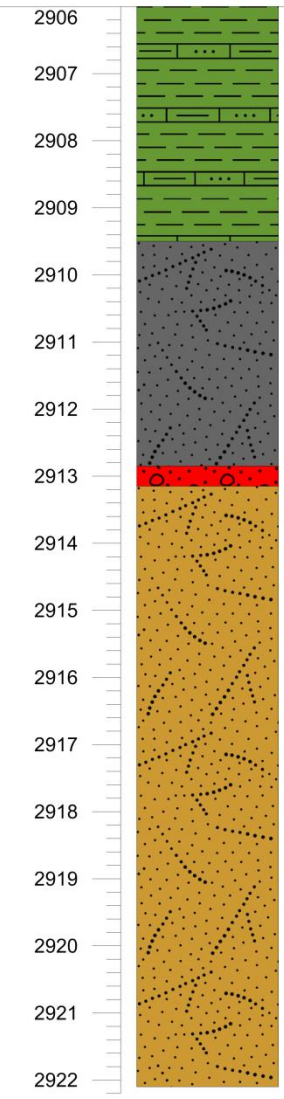
BH-F

BH-G

BH-H

BH-I

Core Log: BH-A

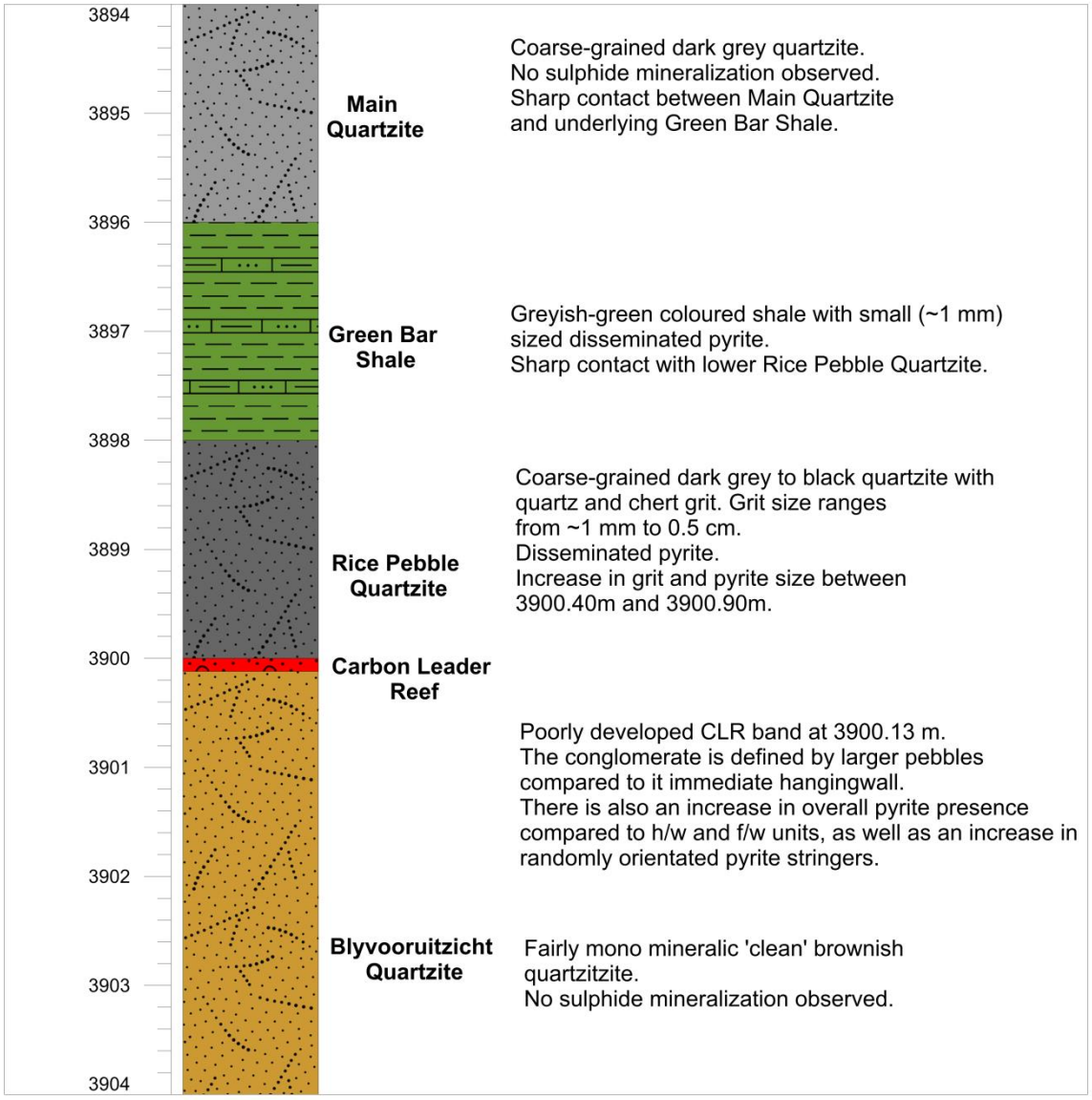


Rock unit	Description
Green Bar Shale	Khakhi green shale unit with small (~1 mm) euhedral disseminated pyrite grains. The rock contains planar laminations of black material (possicly chlorite). Sharp contact between this unit and the lower Rice Pebble Quartzite.
Rice Pebble Quartzite	Dark grey medium- to coarse grained quartzite with quartz and chert grit (~2 mm to 4 mm). Towards the base the unit grades into a light grey less altered quartize with quartz and chert grit. Disseminated to slightly massive pyrite occurs throughout the unit.
Carbon Leader Reef	The reef is defined by a matric supported conglomerate (~ 3 cm). The unit is made up of quartz and chert pebbles (~3 mm to 0.5 cm) set in a quartzite matrix. Massive pyrite occurs between pebbles.
Blyvooruitzicht Quartzite	Brownish coarse-grained fairly mono mineralic quartzite unit. Very little disseminated pyrite mineralization. The rock unit is characterized by sporadic conglomerate bands at its base.

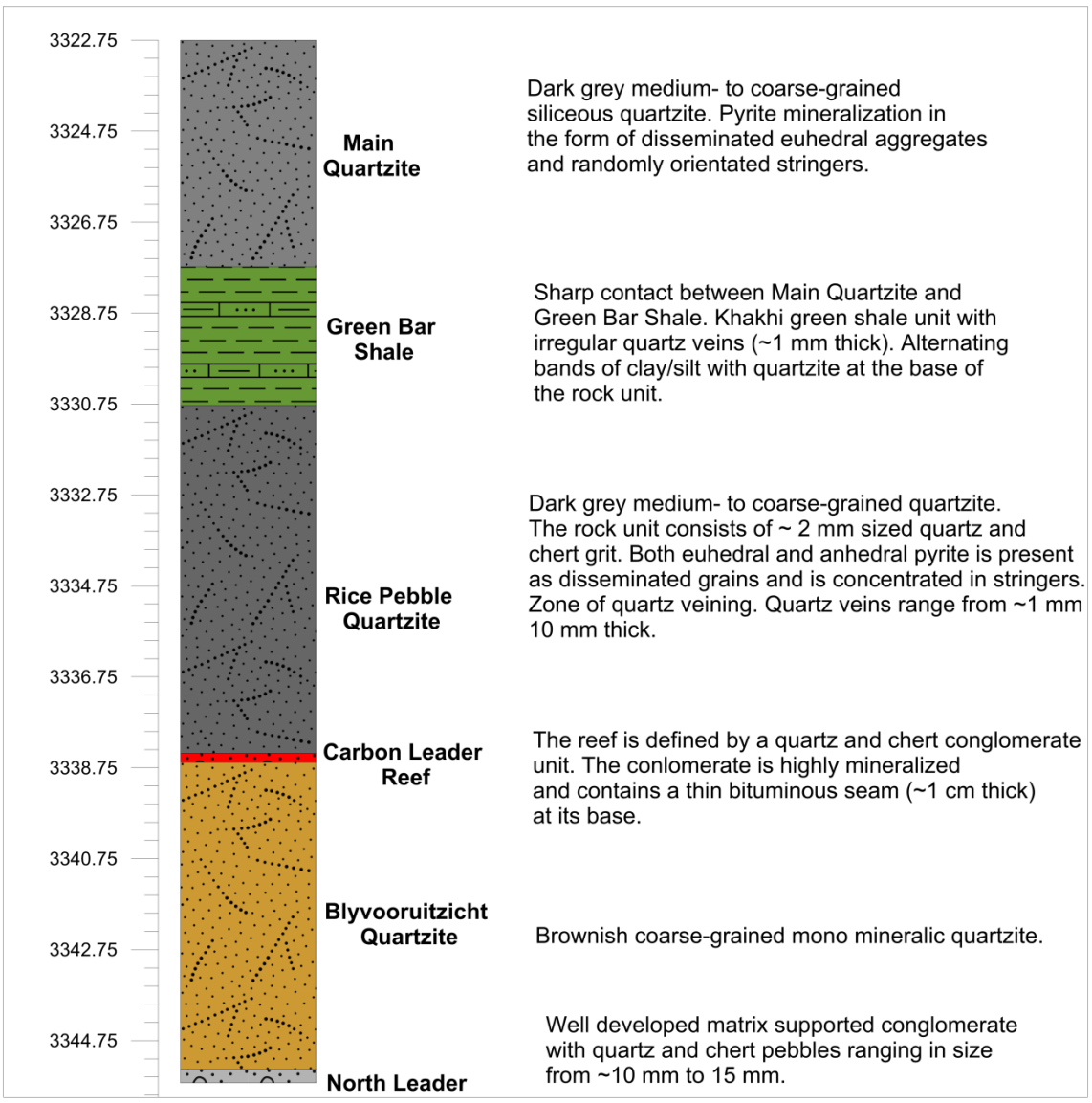
Legend

- Green Bar Shale
- Rice Pebble Quartzite
- Carbon Leader Reef
- Blyvooruitzicht Quartzite

Core Log: BH-B


Depth
Lithology
Rock unit
Description
3894
3895
3896
3897
3898
3899
3900
3901
3902
3903
3904
Main Quartzite
Coarse-grained dark grey quartzite.
No sulphide mineralization observed.
Sharp contact between Main Quartzite and underlying Green Bar Shale.
Green Bar Shale
Greyish-green coloured shale with small (~1 mm) sized disseminated pyrite.
Sharp contact with lower Rice Pebble Quartzite.
Rice Pebble Quartzite
Coarse-grained dark grey to black quartzite with quartz and chert grit. Grit size ranges from ~1 mm to 0.5 cm.
Disseminated pyrite.
Increase in grit and pyrite size between 3900.40m and 3900.90m.
Carbon Leader Reef
Poorly developed CLR band at 3900.13 m.
The conglomerate is defined by larger pebbles compared to it immediate hangingwall.
There is also an increase in overall pyrite presence compared to h/w and f/w units, as well as an increase in randomly orientated pyrite stringers.
Blyvooruitzicht Quartzite
Fairly mono mineralic 'clean' brownish quartzitzite.
No sulphide mineralization observed.
Legend
Main Quartzite
Green Bar Shale
Rice Pebble Quartzite
Carbon Leader Reef
Blyvooruitzicht Quartzite

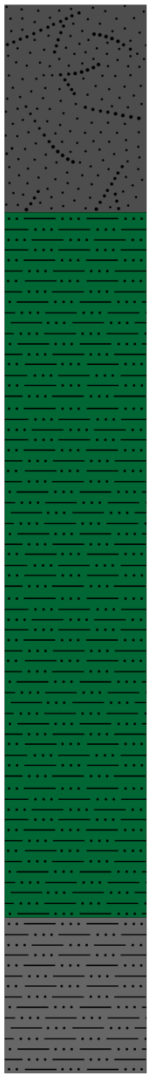
Core log: BH-C



Legend

- Main Quartzite
- Green Bar Shale
- Rice Pebble Quartzite
- Carbon Leader Reef
- Blyvooruitzicht Quartzite
- North Leader

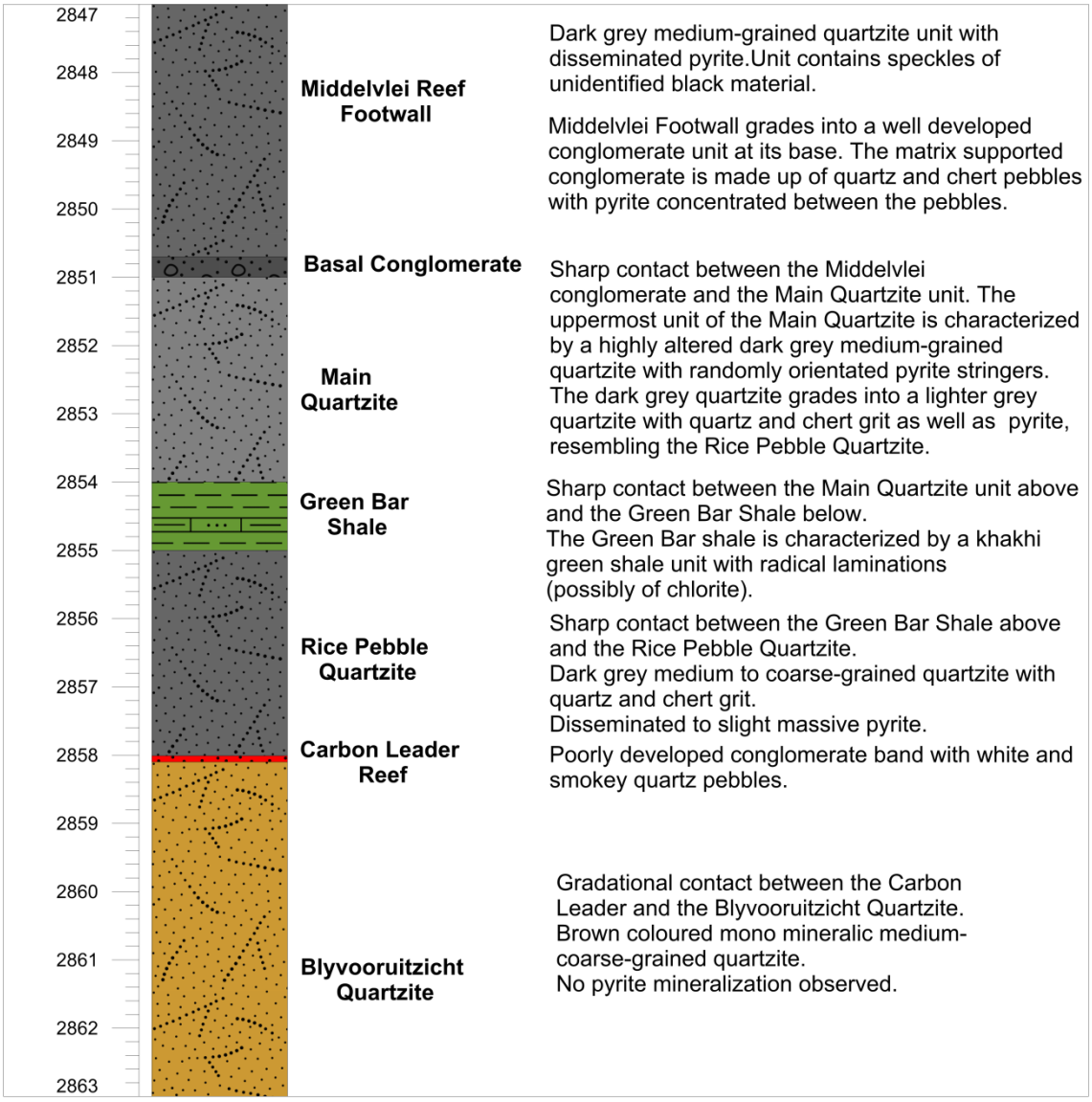
Core Log: BH-D

Depth (m)	Lithology	Rock unit	Description
2584 – 2684		**Maraisburg Quartzite**	Dark grey fine to medium-grained argillaceous quartzite with intercalated silt. Radical quartzite and chlorite veins dominate. This unit becomes increasingly shaly towards the base. No pyrite mineralization observed. Minerals: quartz, silt, chlorite.
		Roodepoort Shale	Dark green fine-grained shaly unit with angular white quartz fragments dominated by black chlorite veins. Minerals: silt, chlorite, quartz.
		Lower Roodepoort Quartzite	Dark greenish grey fine-grained shaly quartzite with angular quartz fragments. Thin radical chlorite veins encompass quartz fragments. Slight slaty foliation. Minerals: quartz, silt, chlorite.

Legend

- Maraisburg Quartzite
- Roodepoort Shale
- Lower Roodepoort Quartzite

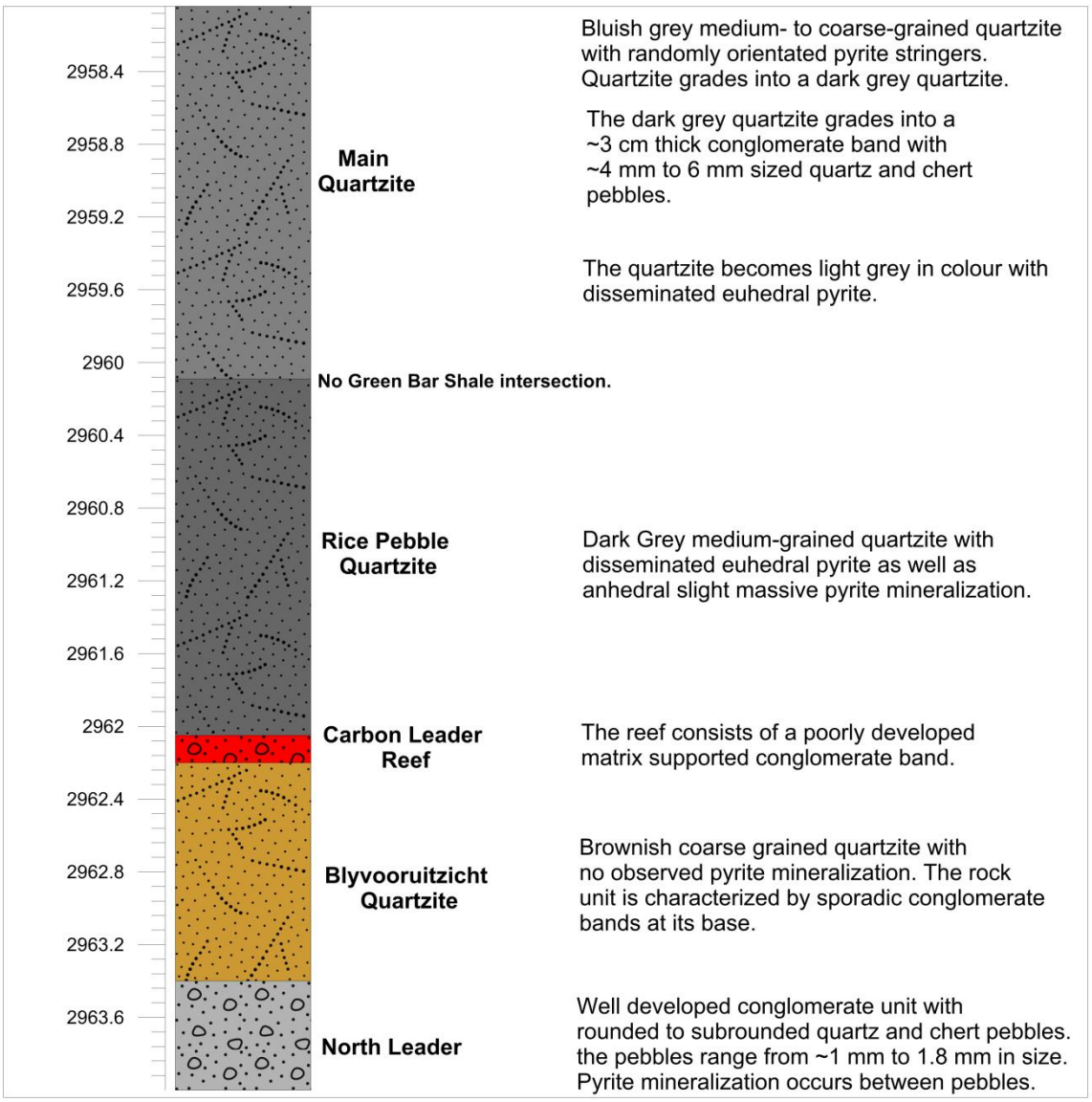
Core Log: BH-E



Legend

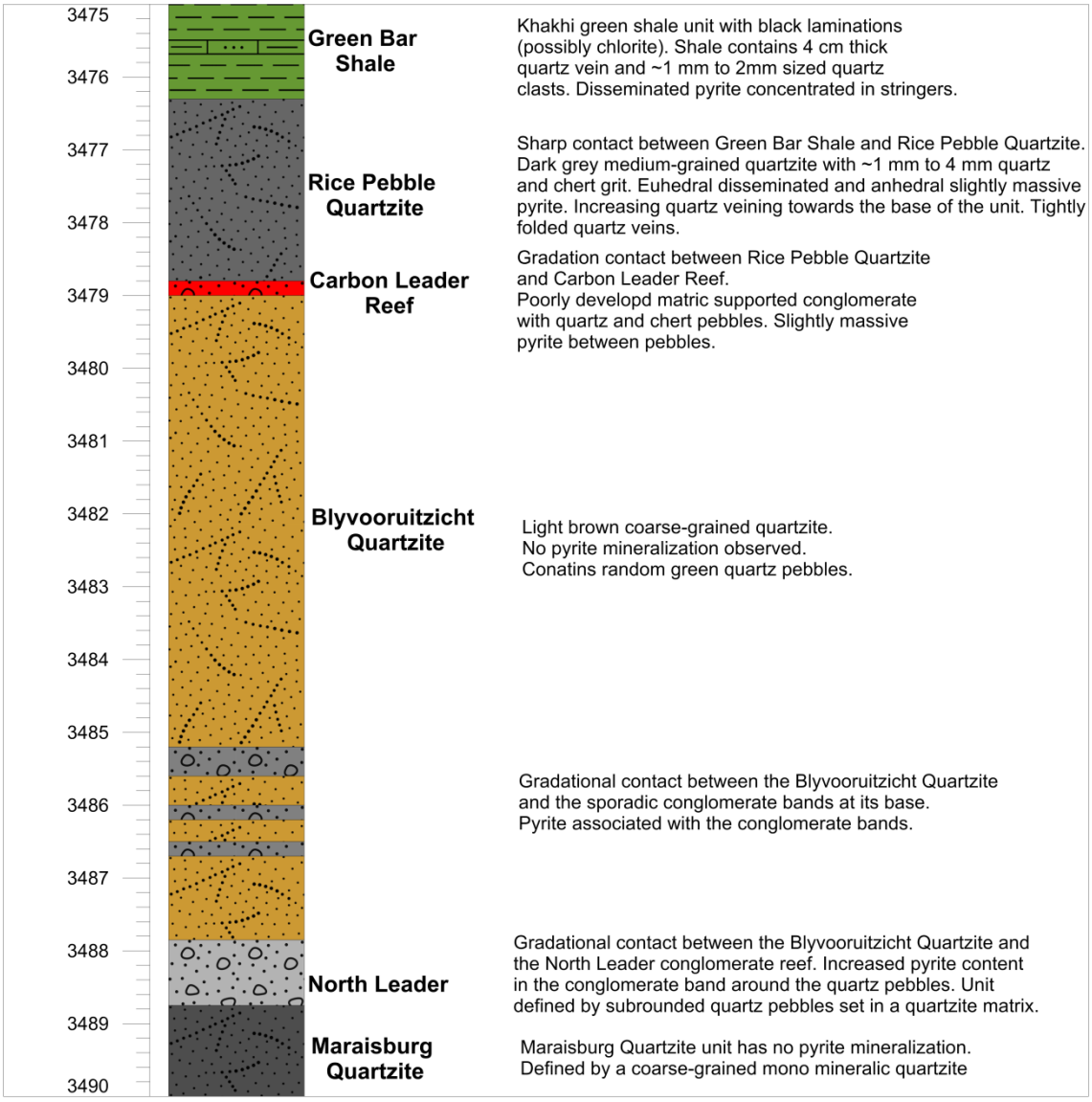
- Middelvlei Reef Footwall
- Middelvlei Reef Footwall conglomerate
- Main Quartzite
- Green Bar Shale
- Rice Pebble Quartzite
- Carbon Leader Reef
- Blyvooruitzicht Quartzite

Core Log: BH-F

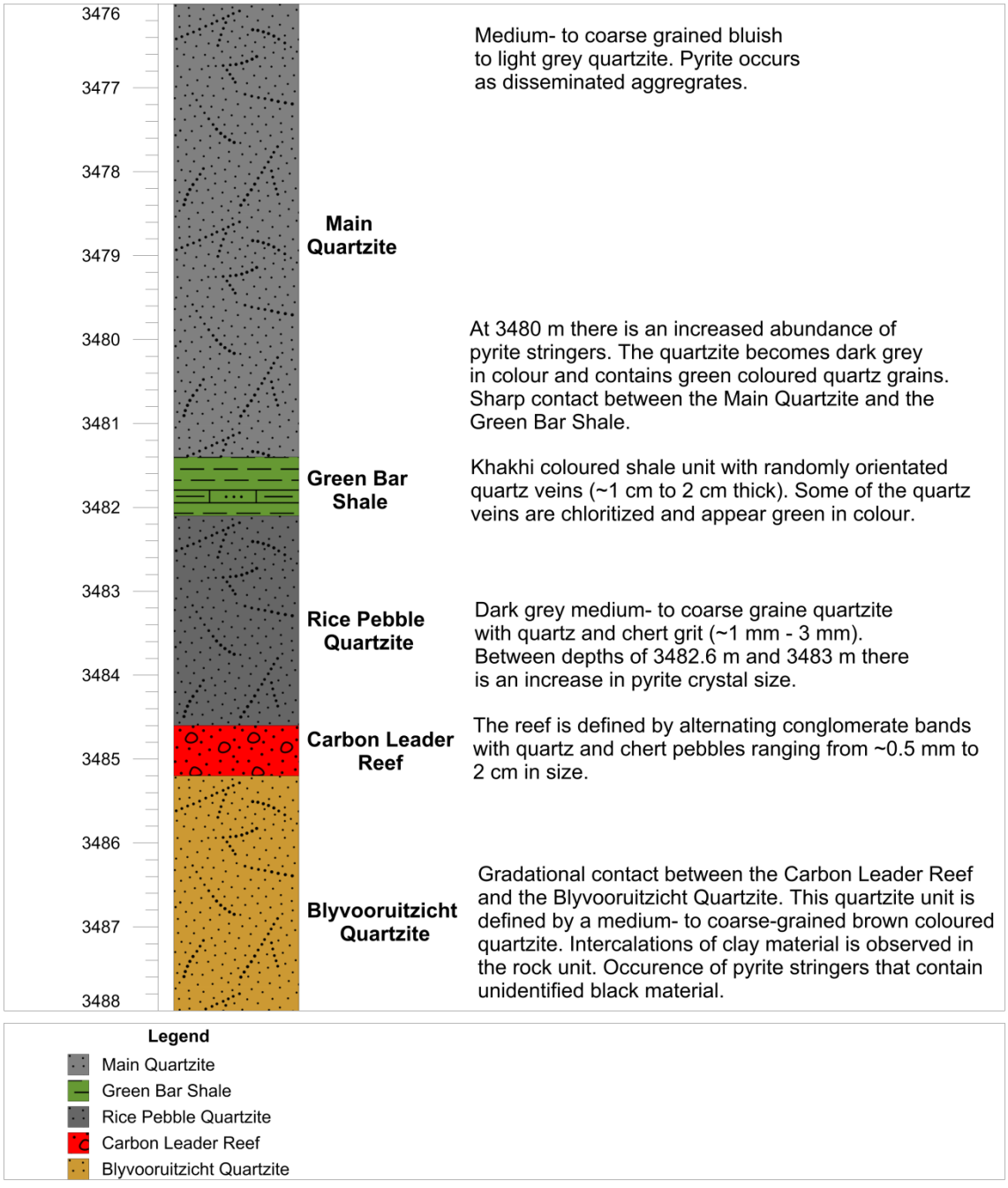

Depth (m)
Lithology
Rock unit
Description
2958.4
2958.8
2959.2
2959.6
2960
2960.4
2960.8
2961.2
2961.6
2962
2962.4
2962.8
2963.2
2963.6
Main Quartzite
Bluish grey medium- to coarse-grained quartzite with randomly orientated pyrite stringers. Quartzite grades into a dark grey quartzite.
The dark grey quartzite grades into a ~3 cm thick conglomerate band with ~4 mm to 6 mm sized quartz and chert pebbles.
The quartzite becomes light grey in colour with disseminated euhedral pyrite.
No Green Bar Shale intersection.
Rice Pebble Quartzite
Dark Grey medium-grained quartzite with disseminated euhedral pyrite as well as anhedral slight massive pyrite mineralization.
Carbon Leader Reef
The reef consists of a poorly developed matrix supported conglomerate band.
Blyvooruitzicht Quartzite
Brownish coarse grained quartzite with no observed pyrite mineralization. The rock unit is characterized by sporadic conglomerate bands at its base.
North Leader
Well developed conglomerate unit with rounded to subrounded quartz and chert pebbles. the pebbles range from ~1 mm to 1.8 mm in size. Pyrite mineralization occurs between pebbles.


Legend
Main Quartzite
Rice Pebble Quartzite
Carbon Leader Reef
Blyvooruitzicht Quartzite
North Leader

Core Log: BH-G


Depth (m)
Lithology
Rock unit
Description
3475
3476
3477
3478
3479
3480
3481
3482
3483
3484
3485
3486
3487
3488
3489
3490
Green Bar Shale
Khakhi green shale unit with black laminations (possibly chlorite). Shale contains 4 cm thick quartz vein and ~1 mm to 2mm sized quartz clasts. Disseminated pyrite concentrated in stringers.
Rice Pebble Quartzite
Sharp contact between Green Bar Shale and Rice Pebble Quartzite. Dark grey medium-grained quartzite with ~1 mm to 4 mm quartz and chert grit. Euhedral disseminated and anhedral slightly massive pyrite. Increasing quartz veining towards the base of the unit. Tightly folded quartz veins.
Carbon Leader Reef
Gradation contact between Rice Pebble Quartzite and Carbon Leader Reef.
Poorly developd matric supported conglomerate with quartz and chert pebbles. Slightly massive pyrite between pebbles.
Blyvooruitzicht Quartzite
Light brown coarse-grained quartzite.
No pyrite mineralization observed.
Conatins random green quartz pebbles.
Gradational contact between the Blyvooruitzicht Quartzite and the sporadic conglomerate bands at its base.
Pyrite associated with the conglomerate bands.
North Leader
Gradational contact between the Blyvooruitzicht Quartzite and the North Leader conglomerate reef. Increased pyrite content in the conglomerate band around the quartz pebbles. Unit defined by subrounded quartz pebbles set in a quartzite matrix.
Maraisburg Quartzite
Maraisburg Quartzite unit has no pyrite mineralization.
Defined by a coarse-grained mono mineralic quartzite
Legend
Green Bar Shale
Rice Pebble Quartzite
Carbon Leader Reef
Blyvooruitzicht Quartzite
Conglomerate
North Leader
Maraisburg Quartzite

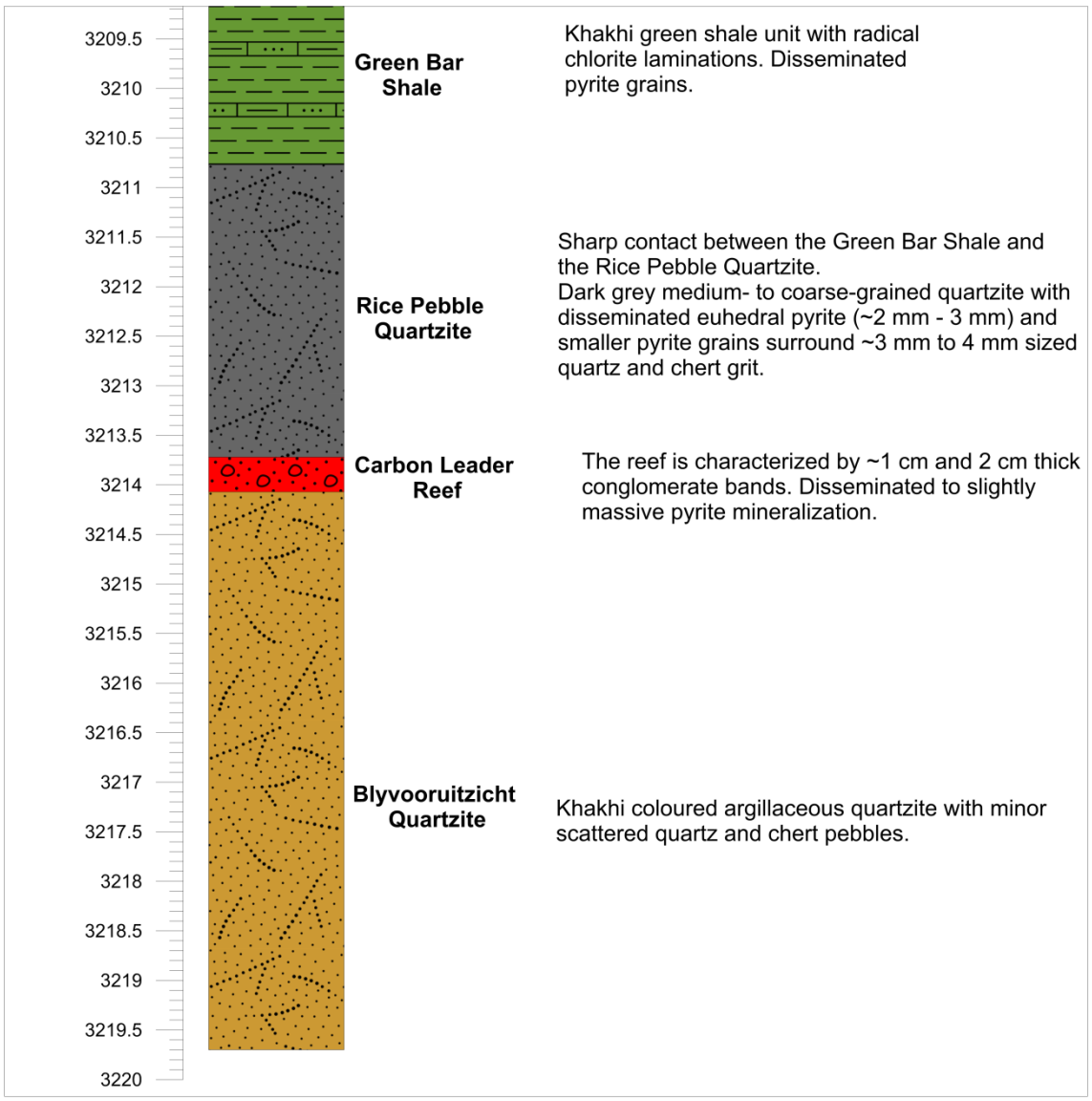
Core Log: BH-H



Legend

- Main Quartzite
- Green Bar Shale
- Rice Pebble Quartzite
- Carbon Leader Reef
- Blyvooruitzicht Quartzite

Core Log: BH-I



Legend

- Green Bar Shale
- Rice Pebble Quartzite
- Carbon Leader Reef
- Blyvooruitzicht Quartzite

Appendix B

Geochemical Data: X-ray Fluorescence

Major Element Data

Minor and Trace Element Data

Appendix B

Table 1 Major element geochemical data for entire borehole suite. The rock type of the sample is also listed. Elemental compositions are measured in wt. % which is the mean composition weight. n.d. =not determined.

BH order	BH ID	Rock Type	SiO2	Al2O3	Fe2O3	FeO	FeTotal	MnO	MgO	CaO	Na2O	K2O	TiO2	P2O5	Cr2O3	NiO	TOTAL
BH A	GBH 6005	Green Bar shale	62.11	23.93	1.06	8.58	9.53	0.07	1.12	0.04	0.68	1.54	0.82	0.05	0.07	0.02	100.09
	GBH 6005	Rice Pebble Quartzite	90.28	3.53	0.39	3.15	3.50	0.01	1.04	0.03	0.08	0.16	0.09	0.02	0.01	0.01	98.80
	GBH 6005	Blyvooruitzicht Quartzite	90.42	6.12	0.15	1.23	1.36	0.01	0.11	0.03	0.19	0.37	0.11	0.03	0.00	0.00	98.78
BH B	E1G	n.d	n.d	n.d	n.d	n.d	n.d	n.d	n.d	n.d	n.d	n.d	n.d	n.d	n.d	n.d	n.d
BH C	GBH 6023	Green Bar shale	61.52	24.22	1.06	8.56	9.51	0.06	1.22	0.04	0.26	1.79	0.83	0.05	0.08	0.06	99.74
	GBH 6023	Rice Pebble Quartzite	86.67	4.58	0.67	5.43	6.03	0.01	1.57	0.06	0.05	0.03	0.08	0.04	0.01	0.01	99.07
	GBH 6023	Blyvooruitzicht Quartzite	91.87	4.48	0.18	1.17	1.33	0.01	0.18	0.03	0.00	0.18	0.17	0.01	0.03	0.01	99.65
BH D	E1U	n.d	n.d	n.d	n.d	n.d	n.d	n.d	n.d	n.d	n.d	n.d	n.d	n.d	n.d	n.d	n.d
BH E	GBH 6003A	Main Quartzite	90.21	5.93	0.23	1.97	2.18	0.02	0.38	0.03	0.02	0.16	0.17	0.03	0.01	0.00	99.34
	GBH 6003A	Green Bar shale	62.31	23.29	1.23	8.25	9.36	0.06	1.21	0.04	0.52	1.52	0.80	0.06	0.06	0.02	100.73
	GBH 6003A	Rice Pebble Quartzite	89.56	5.91	0.36	2.96	3.28	0.02	0.36	0.03	0.00	0.17	0.18	0.02	0.02	0.01	99.60
	GBH 6003A	Blyvooruitzicht Quartzite	90.78	5.56	0.23	1.84	2.05	0.01	0.19	0.03	0.02	0.17	0.12	0.03	0.01	0.00	98.99

BH F	GBH 6027	Main Quartzite	89.65	5.89	0.48	4.36	4.79	0.01	1.32	0.03	0.03	0.08	0.10	0.03	0.01	0.00	99.78
	GBH 6027	Rice Pebble Quartzite	90.65	3.17	0.39	3.20	3.55	0.01	1.28	0.03	0.06	0.03	0.08	0.02	0.00	0.01	98.76
	GBH 6027	Blyvooruitzicht Quartzite	91.02	6.86	0.08	0.67	0.74	0.00	0.08	0.04	0.04	0.15	0.16	0.03	0.01	0.00	99.14
BH G	GBH 2742	Green Bar shale	42.39	36.95	1.45	11.71	13.01	0.09	2.81	0.05	0.78	3.62	1.14	0.06	0.14	0.03	101.21
	GBH 2742	Rice Pebble Quartzite	90.22	7.39	0.09	0.71	0.79	0.01	0.11	0.04	0.20	1.00	0.15	0.02	0.01	0.00	99.94
	GBH 2742	Blyvooruitzicht Quartzite	90.24	3.07	0.48	3.86	4.29	0.01	1.10	0.03	0.05	0.03	0.10	0.03	0.03	0.01	98.88
BH H	E1T	n.d	n.d	n.d	n.d	n.d	n.d	n.d	n.d	n.d	n.d	n.d	n.d	n.d	n.d	n.d	n.d

Table 2 Minor and Trace element geochemical data for entire borehole suite. Elemental compositions are measure in parts per million (ppm). n.d. =not determined. d.l. =detection low.

BH order	BH ID	Sample Type	Sc	V	Cr	Co	Ni	Cu	Zn	Ga	Rb	Sr	Y	Zr	Nb	Mo	Ba	Pb	Th	U
			(ppm)	(ppm)	(ppm)	(ppm)	(ppm)	(ppm)	(ppm)	(ppm)	(ppm)	(ppm)	(ppm)	(ppm)	(ppm)	(ppm)	(ppm)	(ppm)	(ppm)	(ppm)
BH A	GBH 6005	Green Bar shale	22.34	184.41	439.77	22.09	116.73	7.76	15.52	28.88	53.17	102.47	32.61	176.2	12.11	1.5	389.42	6.63	7.62	d.l.
	GBH 6005	Rice Pebble Quartzite	0.88	14.56	80.98	16.47	56.53	3.46	8.57	3.7	7.19	25.4	4.93	93.3	2.31	1.02	55.53	6.16	2.16	d.l.
	GBH 6005	Blyvooruitzicht Quartzite	2.86	22.71	49.74	4.93	15.25	5.49	6.25	6.63	13.1	38.47	4.03	58.13	2.12	1.26	71.85	5.39	1.79	0.41
BH B	E1G	n.d.	n.d.	n.d.	n.d.	n.d.	n.d.	n.d.	n.d.	n.d.	n.d.	n.d.	n.d.	n.d.	n.d.	n.d.	n.d.	n.d.	n.d.	d.l.
BH C	GBH 6023	Green Bar shale	24.79	194.24	472.51	54.7	326.34	1.74	25.84	28.24	62.23	63.32	36.74	167.69	11.29	1.36	373.44	8.07	10.99	d.l.
	GBH 6023	Rice Pebble Quartzite	3.97	23.14	88.71	7.16	85.23	35.18	19.19	7.83	0.66	5.17	5.81	77.95	0.53	0.62	4.79	5.33	3.1	d.l.
BH D	E1U	n.d.	n.d.	n.d.	n.d.	n.d.	n.d.	n.d.	n.d.	n.d.	n.d.	n.d.	n.d.	n.d.	n.d.	n.d.	n.d.	n.d.	n.d.	d.l.
BH E	GBH 6003A	Rice Pebble Quartzite	3.95	25.69	99.98	18.29	70.59	2.81	9.89	6.48	7.43	12.88	5.8	106.64	1.6	0.34	33.02	5.16	2.69	d.l.
	GBH 6003A	Blyvooruitzicht Quartzite	4.16	20.61	71.57	7.09	49.43	8.24	4.88	6.29	8.14	11.9	5.42	105.75	0.5	0.42	39.93	4.13	1.31	d.l.

Table 2 Continued.... Minor and Trace element geochemical data for entire borehole suite.

BH order	BH ID	Sample Type	Sc	V	Cr	Co	Ni	Cu	Zn	Ga	Rb	Sr	Y	Zr	Nb	Mo	Ba	Pb	Th	U
			(ppm)	(ppm)	(ppm)	(ppm)	(ppm)	(ppm)	(ppm)	(ppm)	(ppm)	(ppm)	(ppm)	(ppm)	(ppm)	(ppm)	(ppm)	(ppm)	(ppm)	(ppm)
BH F	GBH 6027	Rice Pebble Quartzite	2.16	4.57	29.02	3.75	53.39	51.14	15.53	4.2	0.84	5.59	4.04	47.24	0.65	0.36	-1.17	5.49	1.01	d.l.
	GBH 6027	Blyvooruitzicht Quartzite	2.83	26.15	77.84	13.91	20.62	3.57	2.52	7.01	6.72	17.35	6.96	74.26	1.61	1.96	29.96	4.07	3.75	d.l.
BH G	GBH 2742	Green Bar shale	3.08	27.82	67.5	9.4	17.43	1.92	11.34	6.65	32.78	37.65	6.03	62.48	1.37	0.85	141.42	5.5	1.58	d.l.
	GBH 2742	Rice Pebble Quartzite	d.l	7.54	170.41	13.32	53.23	53.15	23.36	4.75	1.65	12.02	9.27	150.84	1.45	1.31	-3.74	5.02	8.05	d.l.
	GBH 2742	Blyvooruitzicht Quartzite	31.36	230.4	753.32	52.16	212.13	2.17	85.1	40.93	117.23	157.37	16.44	187.44	15.18	3.2	607.08	11.53	13.25	d.l.
BH H	E1T	n.d.	n.d.	n.d.	n.d.	n.d.	n.d.	n.d.	n.d.	n.d.	n.d.	n.d.	n.d.	n.d.	n.d.	n.d.	n.d.	n.d.	n.d.	d.l.
BH I	GBH 6012	Green Bar shale	24.45	191.07	469.43	18.74	158.58	4.22	31.91	29.54	45.59	49.45	34.95	170.94	11.04	1.84	297.84	9.28	8.64	d.l.
	GBH 6012	Rice Pebble Quartzite	1.83	15.36	78.67	4.4	116.33	202.29	19.22	7.34	0.11	9.56	8.46	72.55	1.22	0.7	1.46	5.61	0.51	d.l.
	GBH 6012	Blyvooruitzicht Quartzite	1.02	16.03	42.15	4.52	9.34	4.53	4.82	5.71	4.83	11.86	4.05	66.04	2.15	0.13	31.31	5.59	1.98	d.l.

Appendix C

Geochemical Data: X-ray Diffraction

SPT Mineral Separation

XRD Data

Appendix C

X-ray Diffraction (XRD)

The diffraction patterns collected on samples from borehole GBH 2742, i.e., 164.23 H Green Bar shale, 164.67 H Rice Pebble Quartzite (RPQ), 164.67 Q and 167.59 H Blyvooruitzicht Quartzite (BLYV) are shown below in Figure 1. H: Heavy minerals; Q: Quartz.

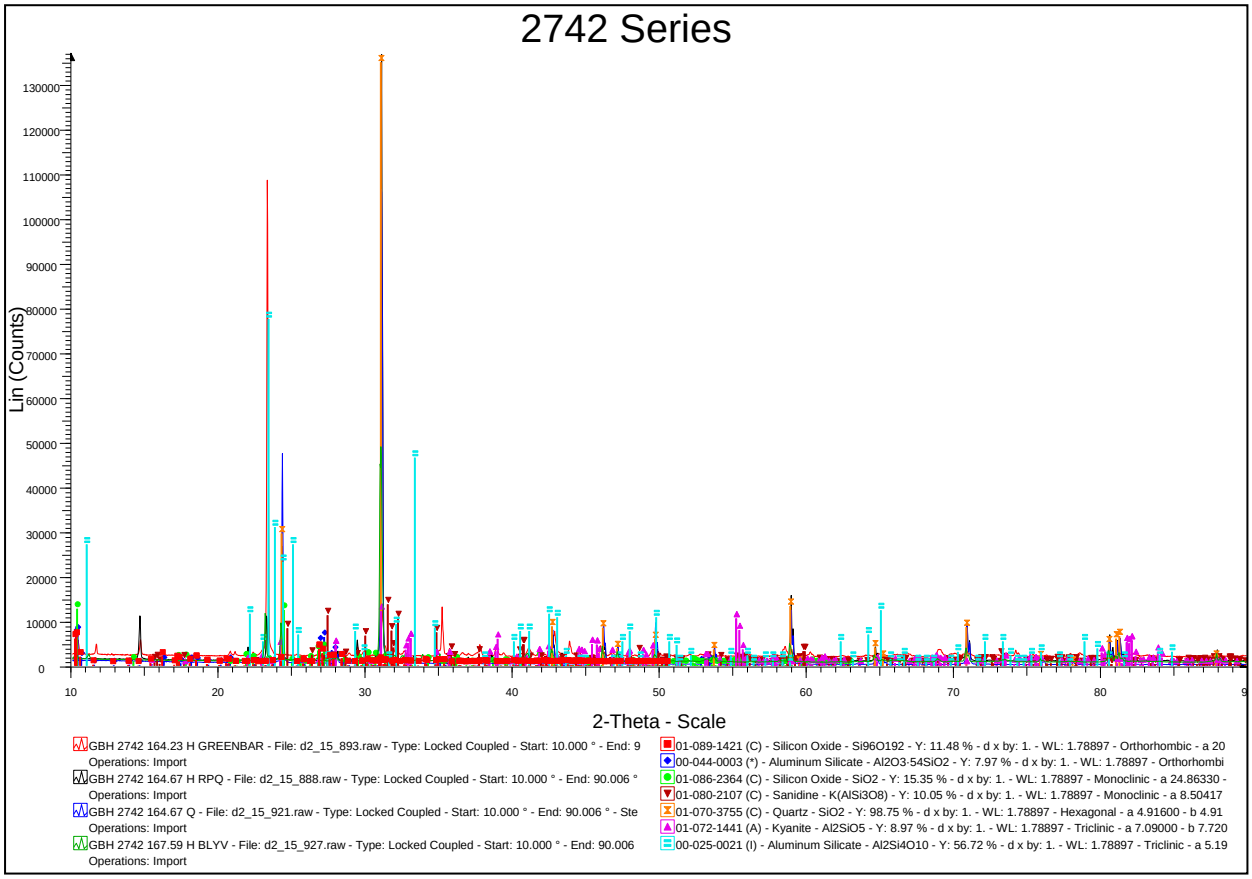


Figure 1: A stacked plot of the phase identification for the borehole GBH 2742 samples: 164.23 H GREENBAR, 164.67 H RPQ, 164.67 Q and 167.59 H BLYV. Phases are included at the bottom of the diagram. H: Heavy minerals; Q: Quartz.

Comments

- Quartz (SiO_2) constitutes the main component of all of the diffraction patterns shown in Figure 1, with the exception of sample 164.23 H GREENBAR.
- SiO_2 is the only phase for which all of the necessary reflections are observed. For all other phases the assignments can at best be considered tentative. This is due to the absence of several necessary reflections for all other phases. Since these samples have a geological origin it is not uncommon that the minerals present are unique solid solutions that have previously not been described, or for which no crystallographic data exists. These minerals should therefore be identified by other means or isolated and characterized separately. The

modifications to the crystal structure may also have occurred as a result of synthetic sample treatments.

- The reflections observed from 10 - 20 °2θ are indicative of large lattice spacings, which are common to clays. However, no clay could be identified.

The diffraction patterns collected for samples from borehole GBH 6003A, i.e., 70.58 Q RPQ and 70.58 H RPQ are shown below in Figure 2.

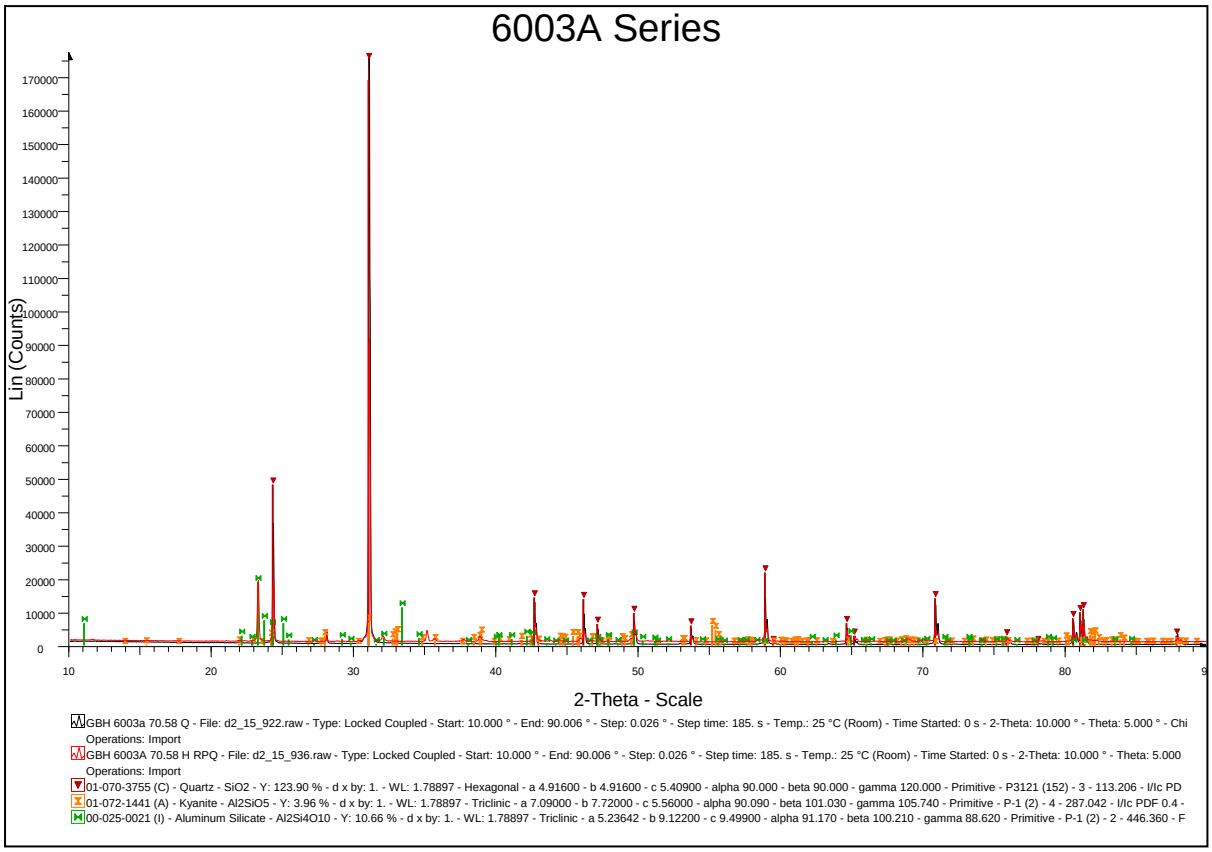


Figure 2: A stacked plot of the phase identification of the borehole GBH 6003A samples: 70.58 Q and 70.58 H RPQ. Phases are included at the bottom of the diagram. H: Heavy minerals; Q: Quartz.

Comments

- Quartz (SiO_2) constitutes the main component of both samples shown in Figure 2. As expected the intensity differences between the most intense reflection of quartz in both samples suggests enrichment in sample 70.58 Q RPQ.

- As with the data shown in **Figure 1**, SiO_2 is the only phase for which all of the necessary reflections are observed. For all other phases the assignments can at best be considered tentative.

The diffraction patterns collected on samples GBH 6005, i.e., 127.71 H GREENBAR, 117.57 H BLYV, 123.19 H RPQ, and 117.57 Q are shown below in Figure 3.

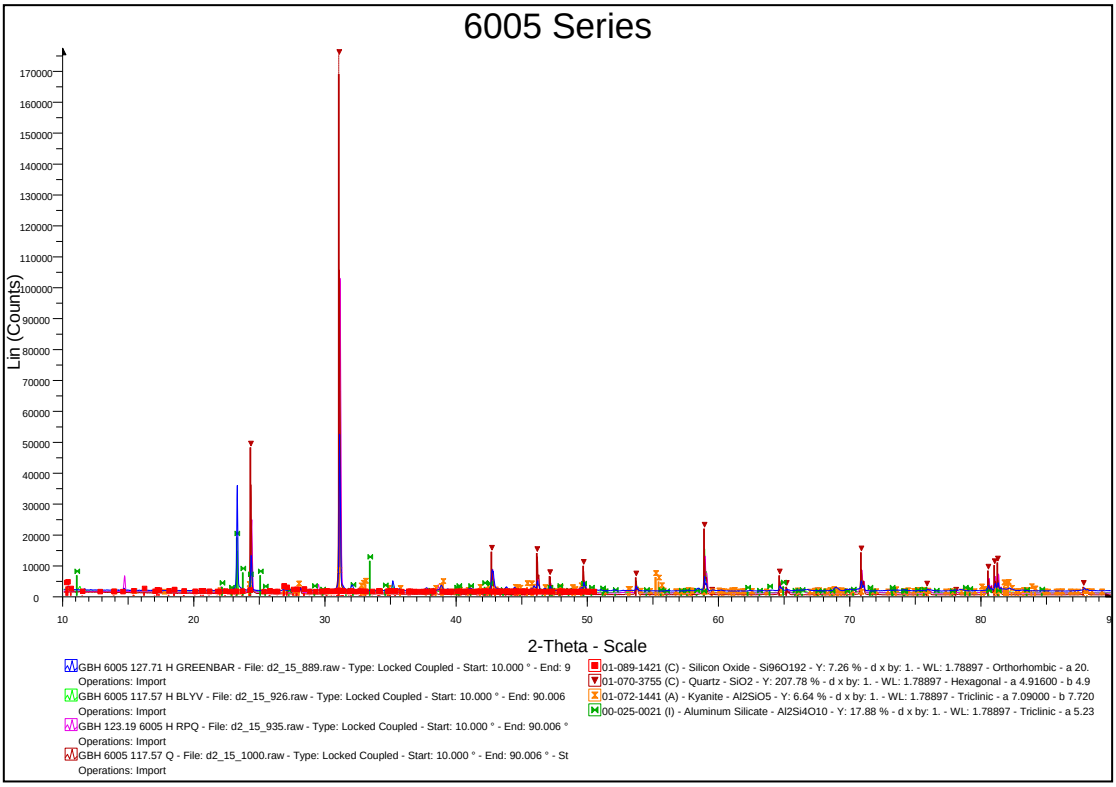


Figure 3: A stacked plot of the phase identification of the GBH 6005 samples: 127.71 H GREENBAR, 117.57 H BLYV, 123.19 H RPQ, and 117.57 Q. Phases are included at the bottom of the diagram. H: Heavy minerals; Q: Quartz.

Comments

- Quartz (SiO_2) constitutes the main component of all samples shown in Figure 3.
- As with the data shown in Figure 1 and Figure 2, SiO_2 is the only phase for which all of the necessary reflections are observed. For all other phases the assignments can at best be considered tentative.

The diffraction patterns collected for samples from borehole GBH 6012, i.e., 57.20 H GREENBAR, 52.58 H BLYV and 56.14 H RPQ are shown below in Figure 4.

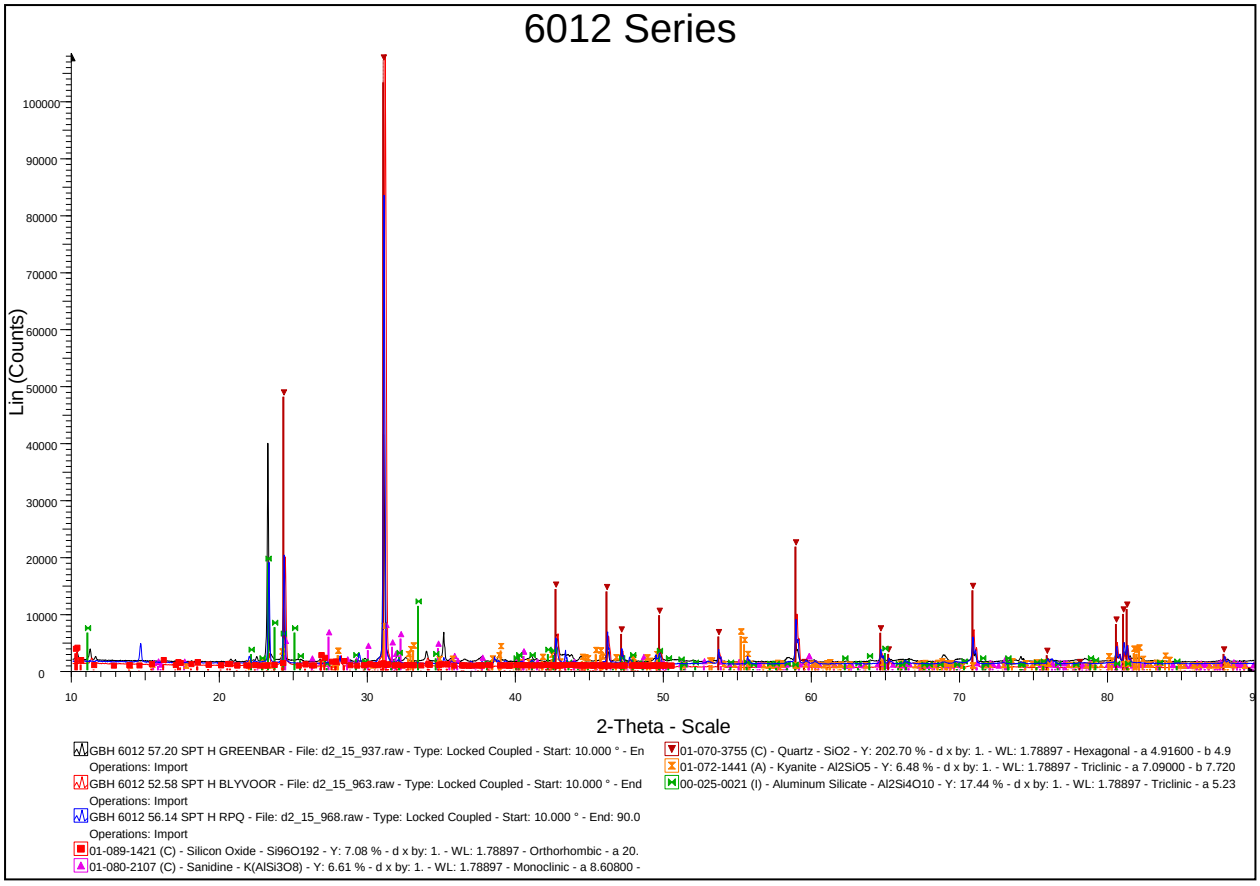


Figure 4: A stacked plot of the phase identification of the 6012 samples: 57.20 H GREENBAR, 52.58 SPT H BLYV and 56.14 H RPQ. Phases are included at the bottom of the diagram. H: Heavy minerals; Q: Quartz.

Comments

- Quartz (SiO_2) constitutes the main component of all samples shown in Figure 4.
- As with the data shown in Figure 1 - 3, SiO_2 is only phase for which all of the necessary reflections are observed. For all other phases the assignments can at best be considered tentative.
- The reflections observed from 10 - 20 °2θ are indicative of large lattice spacings which are common to clays. However, no clay could be identified.

The diffraction patterns collected for samples from GBH 6023, i.e., 160.5 H GREENBAR, 157.8 H RPQ and 152.8 H BLYV are shown below in Figure 5.

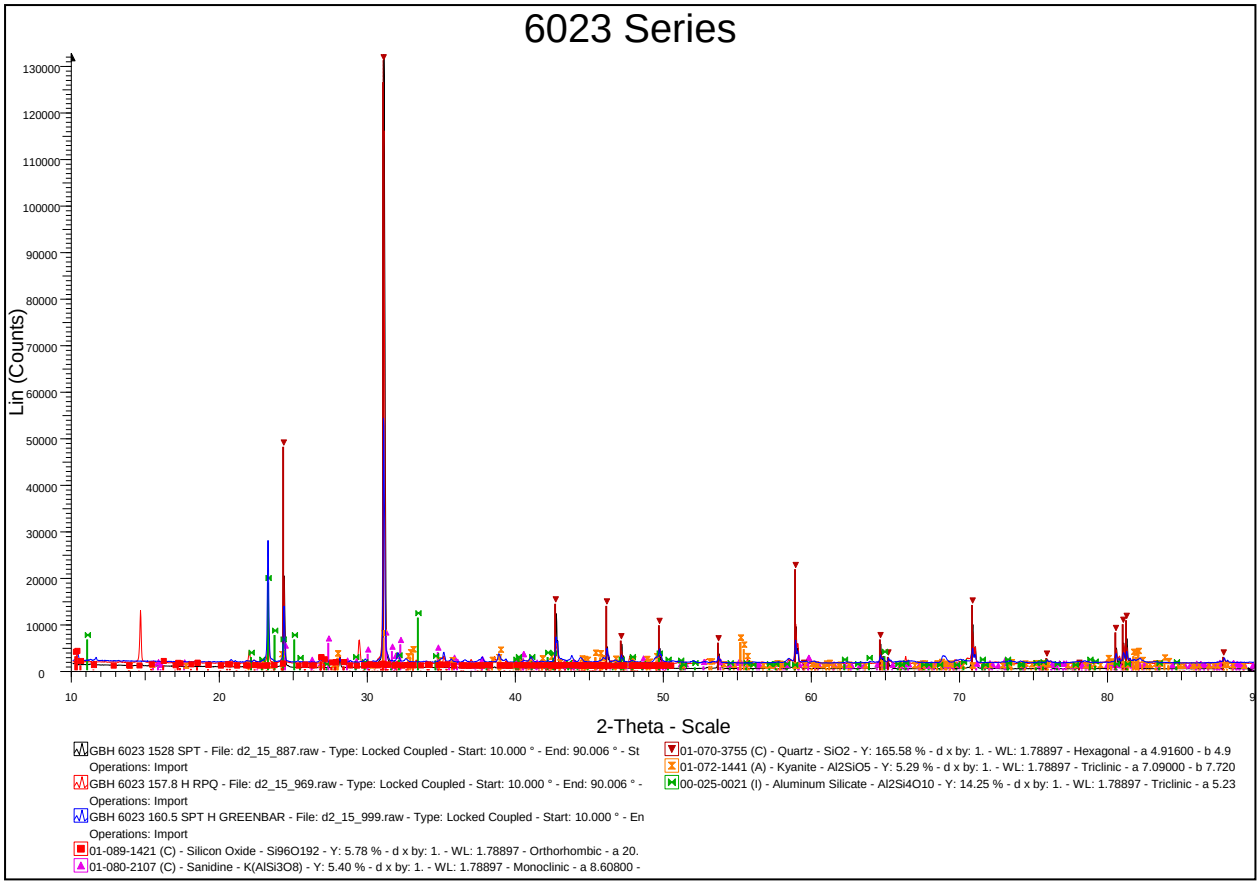


Figure 5: A stacked plot of the phase identification of the 6023 samples: samples 160.5 H GREENBAR, 157.8 H RPQ and 152.8 H BLYV. Phases are included at the bottom of the diagram. H: Heavy minerals; Q: Quartz.

Comments

- Quartz (SiO_2) constitutes the main component of all samples shown in Figure 5.
- As with the data shown in Figure 1 - 4, SiO_2 is only phase for which all of the necessary reflections are observed. For all other phases the assignments can at best be considered tentative.
- The reflections observed from 10 - 20 °2θ are indicative of large lattice spacings which are common to clays. However, no clay could be identified.

The diffraction patterns collected for samples from borehole GBH 6027, i.e., 88.61 H BLY and 94.32 H RPQ are shown below in Figure 6.

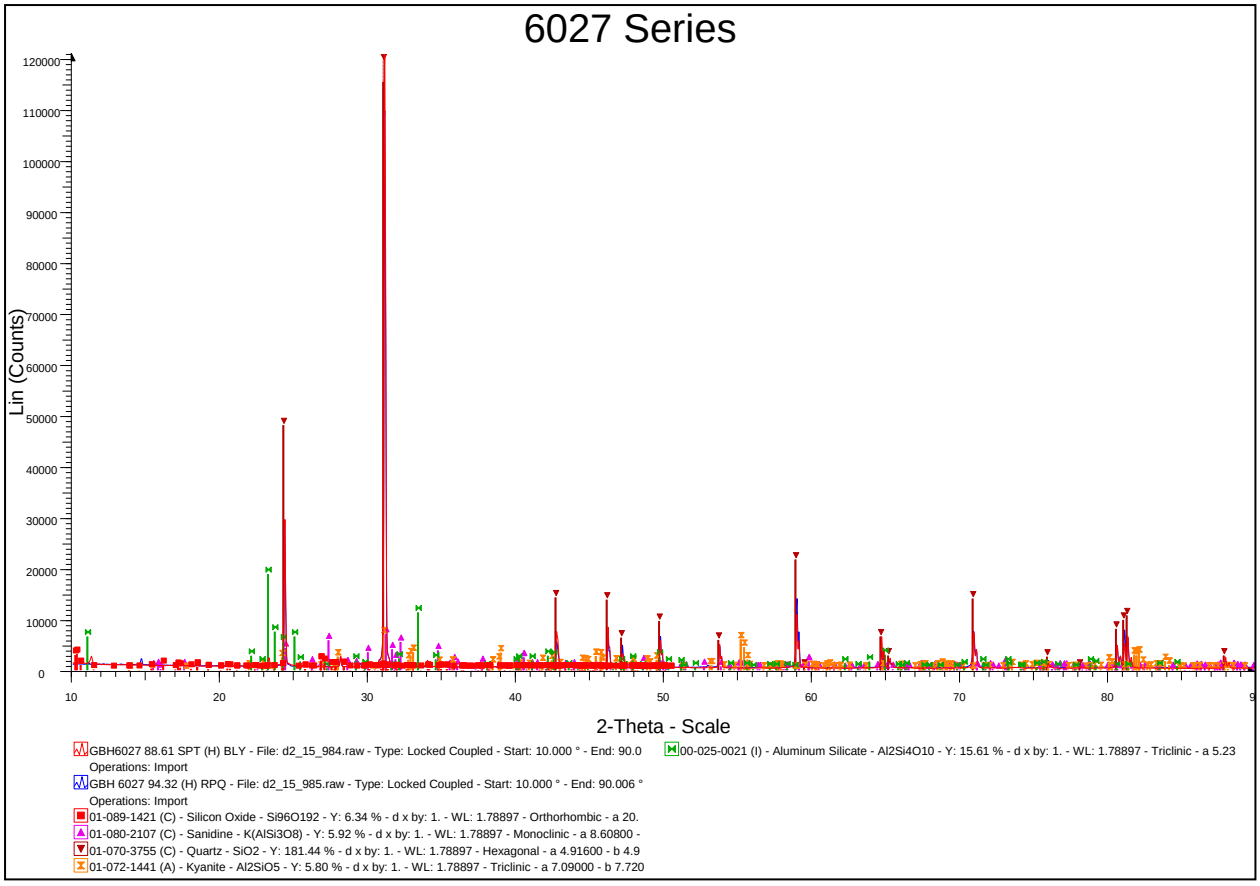


Figure 6: A stacked plot of the phase identification of the **6023** samples: **88.61 H BLY** and **94.32 H RPQ.** Phases are included at the bottom of the diagram. H: Heavy minerals; Q: Quartz.

Comments

- Quartz (SiO_2) constitutes the main component of all samples shown in Figure 6.
- As with the data shown in Figure 1 - 5, SiO_2 is only phase for which all of the necessary reflections are observed. For all other phases the assignments can at best be considered tentative.

The diffraction pattern collected from borehole GBH 6003A for sample 74.53 H BLY is shown below in Figure 7.

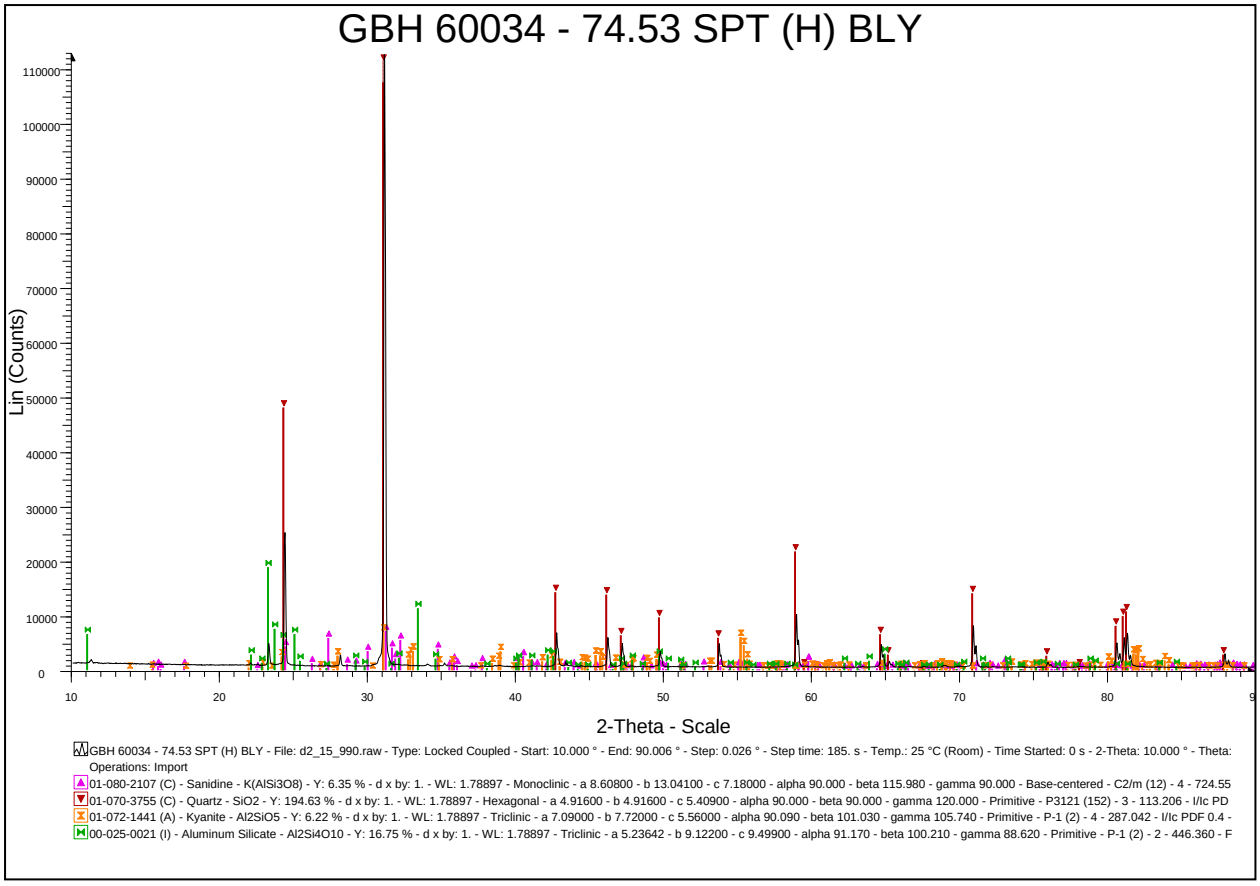


Figure 7: A plot of the phase identification sample **74.53 H BLY.** Phases are included at the bottom of the diagram. H: Heavy minerals; Q: Quartz.

Comments

- Quartz (SiO_2) constitutes the main component of sample GBH 6034- 74.53 SPT (H) BLY shown in Figure 7.
- As with the data shown in Figure 1 - 6, SiO_2 is only phase for which all of the necessary reflections are observed. For all other phases the assignments can at best be considered tentative.
- The reflections observed from 10 - 20 °2θ are indicative of large lattice spacings which are common to clays. However, no clay could be identified.

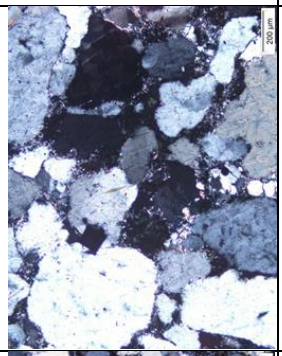
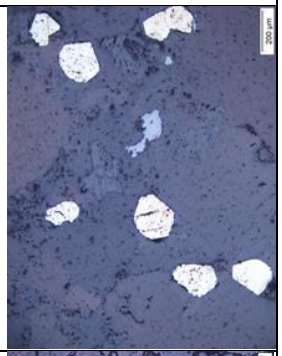
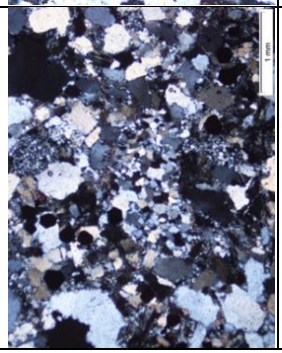
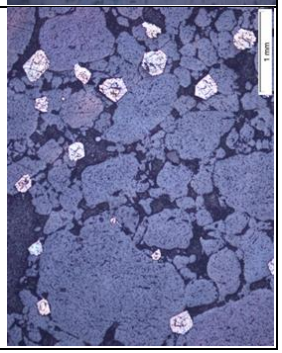
Appendix D

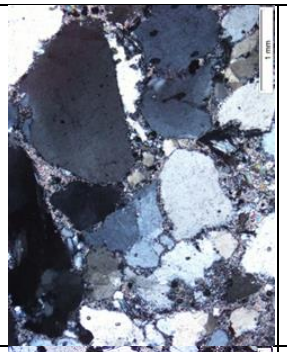
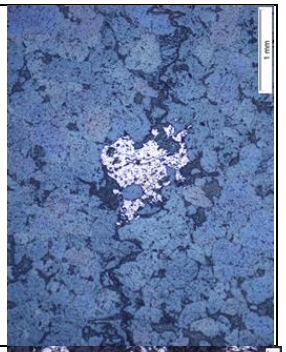
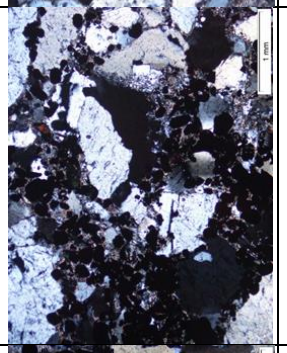
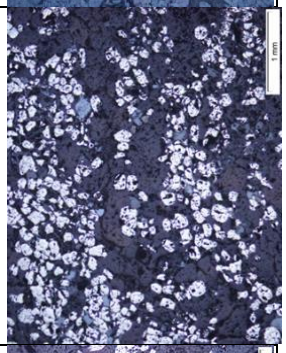
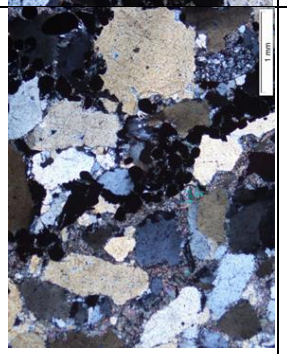
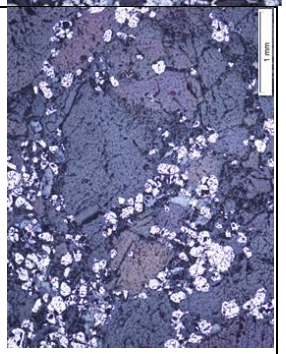
Petrography

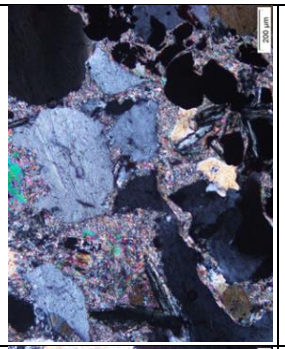
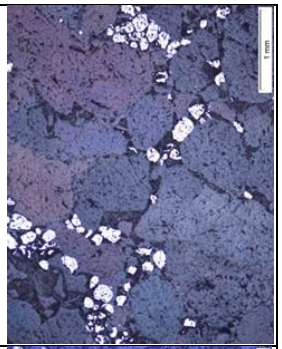
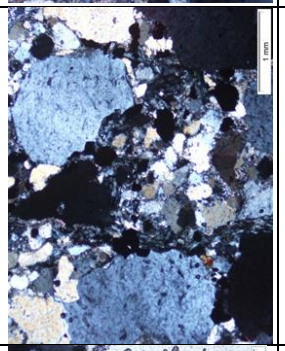
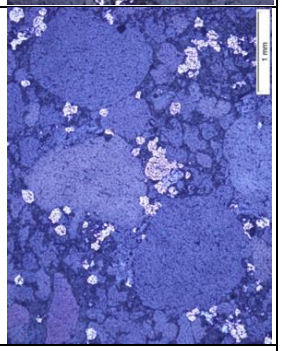
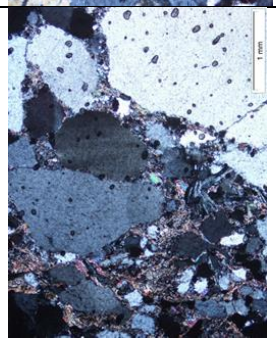
Thin section microscopy

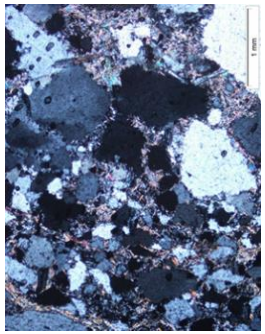
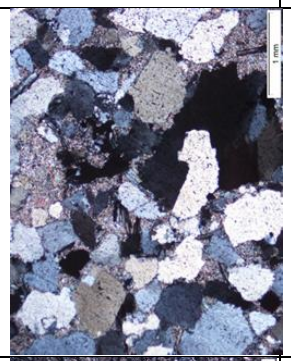
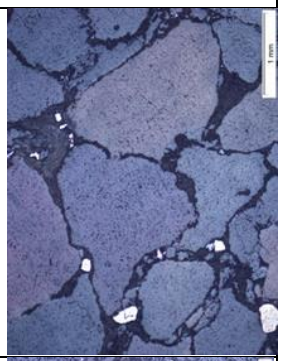
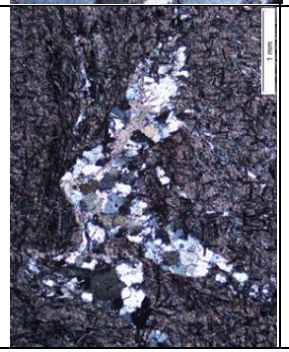
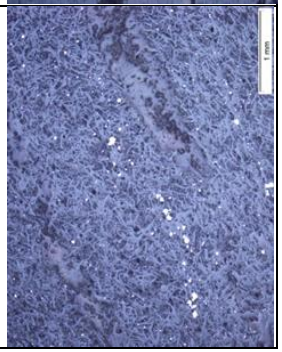
Appendix D

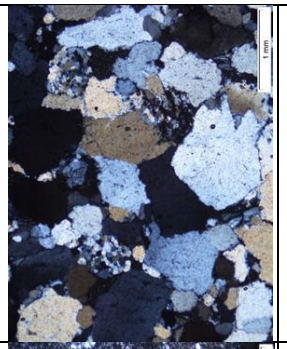
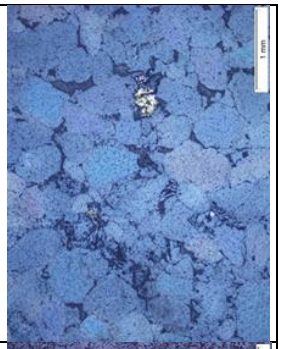
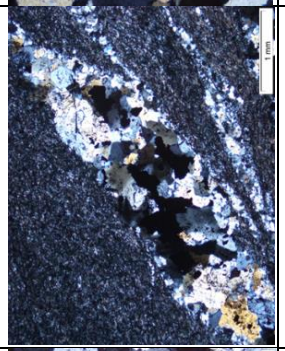
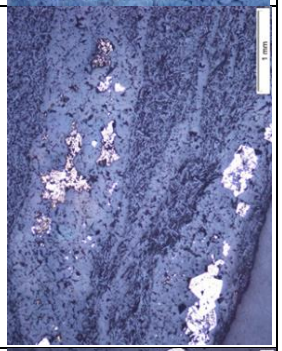
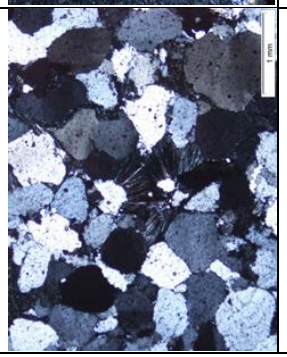
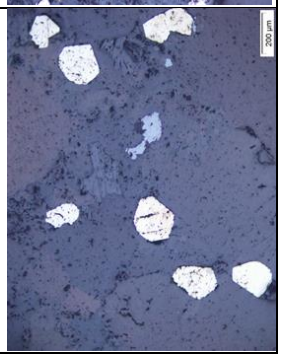
Table 1 Polished thin section descriptions for borehole samples observed in cross polarized and reflected light. Borehole identification (BH ID) and the depth of the sample are shown in column 1.

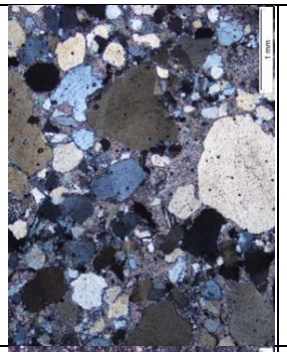
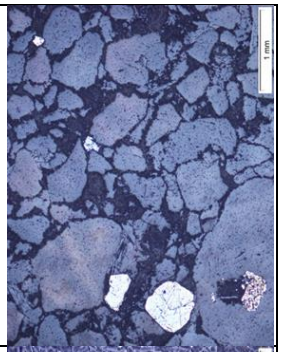
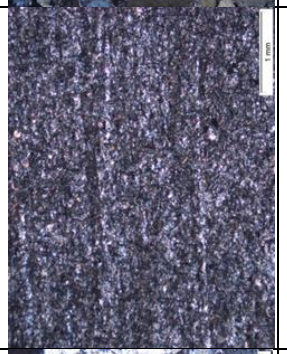
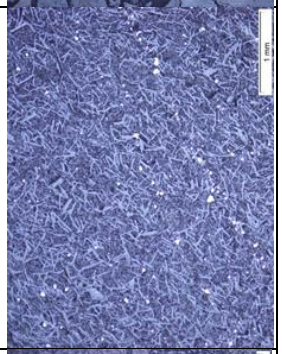
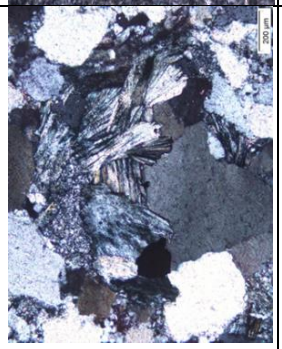
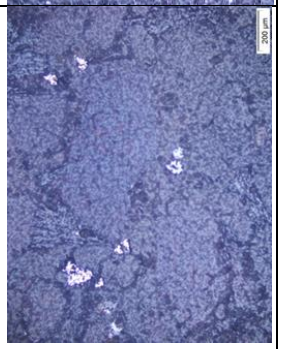
BH ID	Major Minerals	Minor Minerals	Textures	Alteration	Reflected light observations	Modal abundance (%) and rock name	Polished thin section (Cross polarized light)	Polished thin section (Reflected light)
GBH6005-123.38 m	Quartz	Chloritoid	Angular to sub-rounded quartz crystals set in a sericite matrix. Matrix has a distinctive black colour. Cluster of smaller quartz crystals, probably quartz sub-grains that formed as a result of grain boundary rotation during deformation.		Pyrite crystals have a cubic shape with straight and well defined edges. The pyrite crystals occur as disseminated aggregates.	97 % Quartz 3 % Chloritoid **Rice Pebble Quartzite**		
GBH6005-125.25 m	Quartz	Chloritoid, sericite	Polycrystalline quartz grains occur. The smaller quartz grains/sub-grains occurs between the larger quartz grains. Chloritoid occurs as clusters and form a “radiating” pattern. Minor sericite is found mostly in the groundmass.	Sericitization	Euhedral pyrite crystals.	90 % quartz 7 % chloritoid 3 % sericite **Rice Pebble Quartzite**		

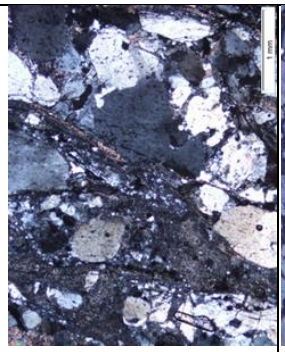
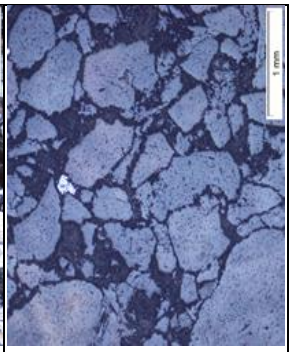
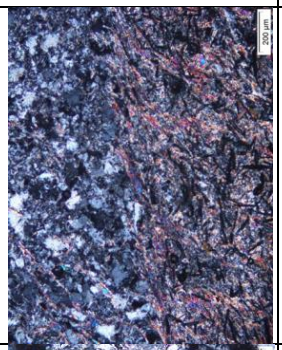
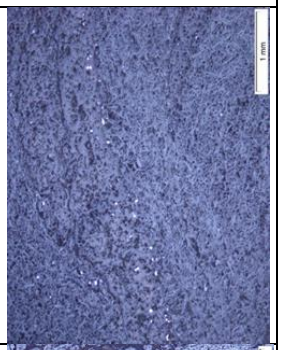
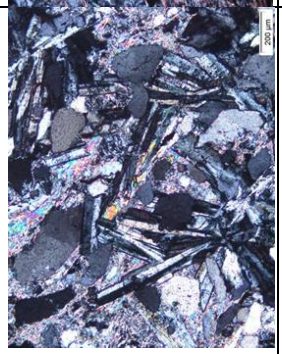
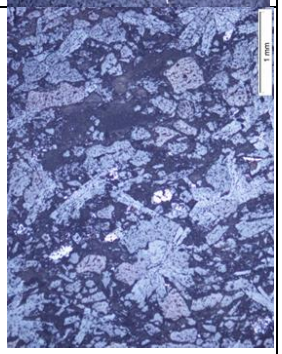
GBH6005-117.89 m	Quartz, sericite	Chloritoid, muscovite	Polycrystalline quartz crystals. The larger crystals range from 8-12 µm and the smaller crystals range from 0.3-0.6 µm. Sericite occurs in the groundmass along with muscovite. Chloritoid crystals occur as clusters.	Sericitization, chloritization.	Minor anhedral and subhedral pyrite crystals are observed between grain boundaries.	77% Quartz 33% Muscovite 15% Sericite 5% Chloritoid **Blyvooruitzicht Quartzite**		
GBH6005-118.29 m	Quartz	Sericite	Quartz displays a strained texture and undulating extinction. Sample shows no presence of chloritoid. Sericite constitutes the groundmass.	Sericitization	Massive pyrite mineralization. Recrystallized pyrite occurs within cracks/fractures and between grain boundaries. Minor magnetite occurs in the cracks with the pyrite.	85 % Quartz 15 % Sericite **CLR conglomerate**		
GBH6005-118.29 m	Quartz	Sericite, chloritoid	Quartz grains of 2.5-4.0 µm. Chloritoid crystals occur as clusters and can either be grey/blue or green with carlsband twinning. Sericite constitutes the groundmass.	Sericitization, chloritization.	Massive pyrite mineralization. Pyrite crystals show evidence of both primary and secondary mineralization. They are euhedral with straight well defined edges on one side and curvy and jagged on the other side.	80 % quartz 15 %sericite 5%chloritoid **CLR conglomerate**		

GBH6023-151.0 m	Quartz	Sericite	Sub-rounded to angular quartz crystals. Sericite occurs in the groundmass between the quartz grains.	High degree of sericitization.	Massive pyrite grains between and around quartz grains. Euhedral and recrystallized pyrite grains. Some of the pyrite grains have straight edges (euhedral) and rugged edges.	90% quartz 10% sericite **CLR conglomerate**		
GBH6023-165.65 m	Quartz	Chloritoid, sericite.	Polycrystalline quartz grains with rugged edges. Chloritoid crystals are 6.5 µm. Quartz crystals have a size range of 0.3 µm.	Moderate chloritoid occurrence. Sericitization occurs in the groundmass.	Disseminated euhedral and anhedral (circular) pyrite crystals. Euhedral pyrite has a size range of 1.0-1.5 µm, anhedral (circular) pyrite has a size range of 0.3-0.5 µm.	80% quartz 10% sericite 3%muscovite 7% chloritoid **Rice Pebble Quartzite**		
	Quartz,	Muscovite, chlorite	Quartz grains-colourless in PPL. XPL: anhedral, interlocking crystals, crystal size ranges from 1 mm-5 mm, crystals have undulating extinction. Quartz is recrystallized with irregular grain boundaries. Muscovite crystals have a slight greenish colour in PPL. XPL. Muscovite occurs in between the quartz crystals and makes up the groundmass. Chlorite crystals are: elongated crystals with		No mineralization evident	Quartz: 89% Muscovite: 8% Chloritoid: 2% Chlorite: 1%		

			good cleavage, undulating extinction, crystal colour changes when the stage is rotated from dark green to dark grey.					
GBH6023-168.73 m	Quartz	Sericite	Quartz crystals are significantly fractured. High presence of smaller quartz grains, evidence of sub-grain rotation and recrystallization. The size of the sub-grains ranges from 0.3-0.5µm. Randomly orientated chloritoid crystals.	Sericitization.	No pyrite mineralization.	80% Quartz 20% Sericite **Blyvooruitzicht Quartzite**		
GBH6012-57.34 m	Chloritoid, sericite	Quartz, muscovite	Fine grained sample. Chloritoid crystals are randomly orientated in the sericite matrix as grey, blue or black crystals. Sample has significant radical laminations. The laminations are made up of quartz lenses. Muscovite occurs only with the quartz crystals.	Chloritization, sericitization.	Sample contains tiny euhedral pyrite crystals scattered throughout the sample. Pyrite crystal have a size rang 0.3-0.5 µm.	Difficult to determine. **Green Bar shale**		

GBH6012-56.07 m	Quartz	Chloritoid	Sample almost entirely consists of quartz interlocking quartz crystals with minor randomly orientated chloritoid crystals.	Chloritization	Anhedral pyrite and minor disseminated chalcopyrite crystals.	95% Quartz 5% Chloritoid **Rice Pebble Quartzite**		
GBH2742-163.54 m	Chloritoid, quartz	Muscovite, sericite	Sample is very fine grained with laminations. The laminations are planar filled with quartz and opaque minerals.	Sericitization occurs in the groundmass.	Euhedral and anhedral pyrite crystals occur in the laminations. Pyrite crystals have straight and irregular edges.	Difficult to determine. **Green Bar**		
GBH6027-94.67 m	Quartz		Irregularly shaped quartz grains with rugged edges. Randomly orientated chloritoid crystals	Chloritization	Single fractured pyrite crystal	95% Quartz 5% Chloritoid **Rice Pebble Quartzite**		

GBH6027-86.93 m	Quartz, sericite	Chloritoid, muscovite	Anhedral and strained quartz crystals with undulating extinction. Randomly orientated chloritoid crystals. Minor muscovite crystals.	Sericitization, chloritization.	Anhedral pyrite crystals occur between mineral boundaries and fractures.	77% Quartz 33% Muscovite 15% Sericite 5% Chloritoid **Blyvooruitzicht Quartzite**		
GBH6023-161.07 m	Chloritoid	Quartz, muscovite	Sample appears fine grained. Randomly orientated chloritoid crystals ranging in size from 0.5-1 µm. Quartz crystals ranging in size from 0.2-0.4 µm occur as clusters. Minor muscovite occurs with the quartz crystals.	Sericitization occurs in the groundmass.	Tiny pyrite crystals occur randomly throughout the sample.	Difficult to determine. **Green Bar shale**		
GBH6003A-70.58 m	Quartz	Chloritoid, sericite, muscovite, magnetite.	The quartz crystal in this sample appears to be strained, probably during deformation. This has resulted in quartz that has deformed into domains with slightly different extinction angles. Sericite forms the groundmass and with increased magnification one can clearly see platy mineral (white micas). Chloritoid crystals occur in clusters and have a grey/blue colour.	Sericitization, chloritization	Anhedral disseminated pyrite grains with size ranging from 1.0-1.4 µm. About 2 magnetite crystals found in the sample.	91 % QUARTZ 7 % Chloritoid 2 % sericite **Rice Pebble Quartzite**		

GBH6003A -74.53 m	Quartz, sericite	Chloritoid	Strained quartz grains with undulating extinction. Quartz grains are interlocking and there is a higher degree of fracturing. Higher degree of sericitization in the matrix.	Sericitization chloritization.	Anhedral pyrite grains occurring between the grain boundaries.	75% Quartz 20% Sericite 5% Chloritoid **Blyvooruitzicht Quartzite**		
GBH6003A -69.09 m	Chloritoid	Quartz, sericite	Tiny tabular (needle shaped) and randomly orientated crystals of chloritoid. The chloritoid crystals have distinct carlsband twinning and have a grey/blue colour in ppl and high relief with slight greenish pleochroism in ppl.	Sericitization, chloritization.	Tiny and disseminated pyrite crystals.	Difficult to determine. **GB**		
GBH2742-173.50 m	Quartz	Chloritoid	Polycrystalline quartz. Higher degree of fracturing of the quartz crystals. Smaller quartz crystal form clusters. Smaller quartz crystals are probably a result of grain boundary rotation during deformation. Tabular shaped chloritoid crystals are randomly orientated and are larger in size.	Chloritization	Minor pyrite mineralization. Anhedral pyrite grains are concentrated in one continuous fracture.	80% Quartz 20% Chloritoid **Blyvooruitzicht Quartzite**		

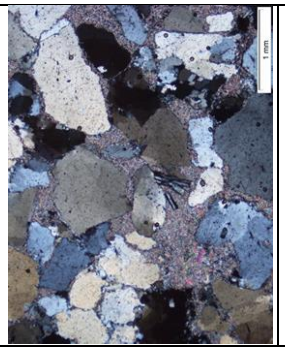
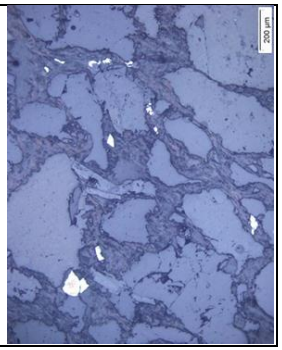
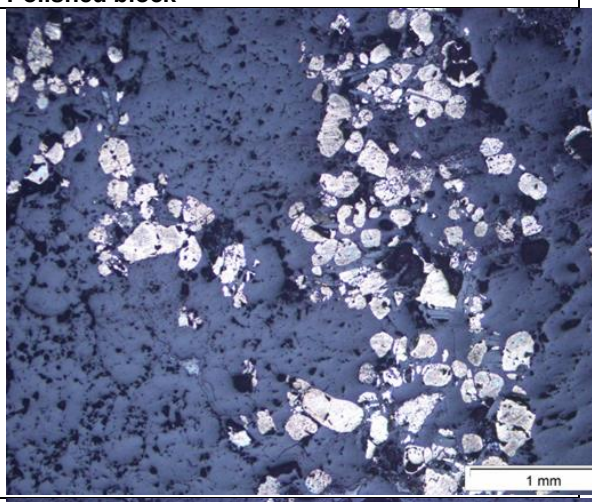
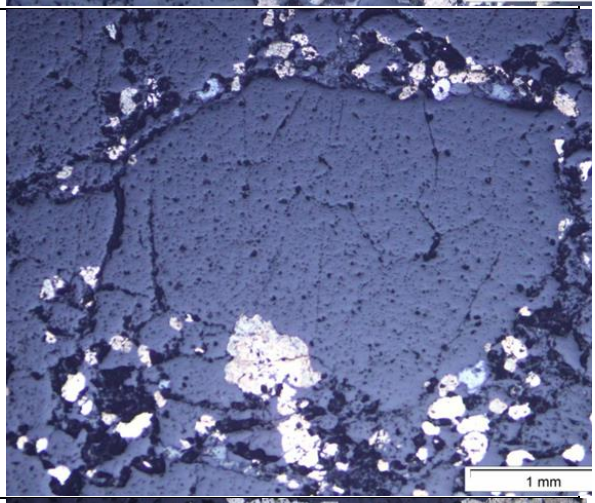
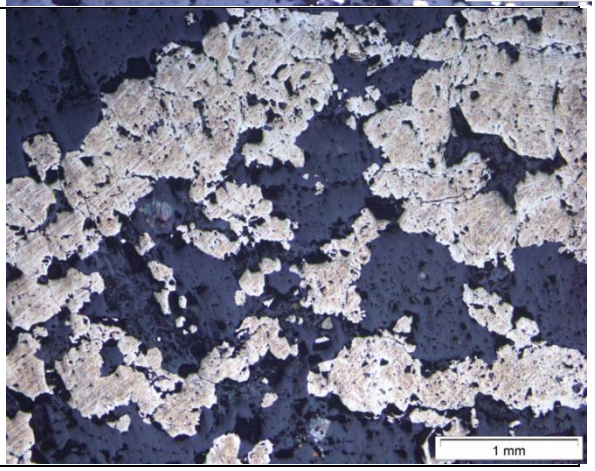
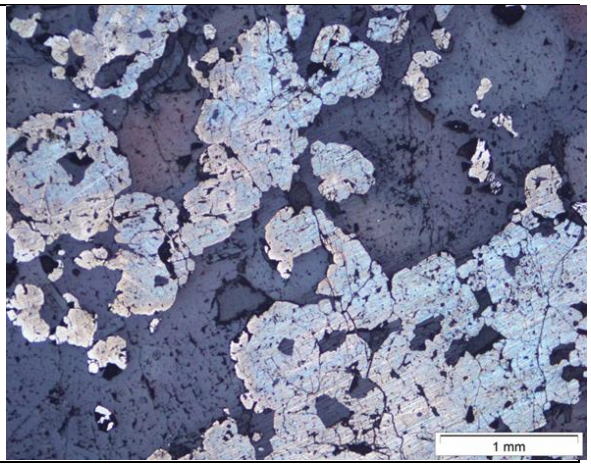
GBH6012-53.13 m	Quartz	Muscovite, chloritoid	Irregularly orientated chloritoid and muscovite crystals. Fractured quartz crystals with patchy extinction. Sericite forms the groundmass.		Euhedral fractured pyrite crystals. Pyrite crystals occur in quartz fractures and grain boundaries.	82 % Quartz 12 %Chloritoid 6 % Muscovite **Blyvooruitzicht**		

Table 2 Polished block descriptions for borehole samples.

BH ID	Mineralization	Description	Polished block
GBH6023-151.0 m	Pyrite	Anhedral pyrite grains occur around the quartz crystals. The pyrite crystals are recrystallized and have sizes ranging from 1.0-2.0 µm. Although still disseminated to some degree there is a high concentration of pyrite in this sample. Larger pyrite crystals of 5.0 µm have inclusions of chloritoid crystals.	
GBH6005-118.29 m	Pyrite	Anhedral pyrite crystals occur in fractures and between grain boundaries. Larger pyrite crystals with sizes of 3.0 µm have inclusions of silicate minerals. Smaller pyrite crystals have sizes of 0.4-1.0 µm.	
GBH2742-164.51 m	Pyrite Chalcopyrite	Euhedral, partly euhedral and anhedral disseminated pyrite crystals. Minor chalcopyrite crystals of 0.7-1.3 µm in size are observed in fractures and grain boundaries. The chalcopyrite is a moderately bright yellow colour.	

GBH2742-164.51 m	Pyrite Chalcopyrite	Massive pyrite mineralization. The pyrite occurs as one continuous horizon. Some pyrite crystals contain chalcopyrite inclusions. Euhedral, partly euhedral and anhedral crystals are observed in this sample.	

Appendix E

Physical Properties

Density

Appendix E

Table 1 Density measurements conducted on borehole samples, with the lithologies listed. The weight in air and water (g) are listed as well as the calculated density (g/cm^3) using Archimede's principal.

BH ID	Sample Type	Weight air (g)	Weight water (g)	Density, (g/cm^3)
GBH 6005	Green Bar shale	139.83	93.22	3.00
	Rice Pebble Quartzite	133.06	84.21	2.72
	CLR conglomerate	60.78	39.32	2.83
	Blyvooruitzicht Quartzite	132.68	83.75	2.71
E1G	Main Quartzite 1	86.27	54.05	2.68
	Main Quartzite 2	81.83	51.47	2.70
	Green Bar shale 1	111.66	72.77	2.87
	Green Bar shale 2	117.56	77.22	2.91
	Rice Pebble Quartzite 1	108.40	68.05	2.69
	Rice Pebble Quartzite 2	101.43	63.60	2.68
	CLR conglomerate	96.66	61.35	2.74
	Blyvooruitzicht Quartzite 1	92.48	57.66	2.66
	Blyvooruitzicht Quartzite 2	103.59	64.69	2.66
	Blyvooruitzicht Quartzite 3	86.83	54.18	2.66
	Blyvooruitzicht Quartzite 4	83.13	51.94	2.67
GBH 6023	Green Bar shale	144.90	96.77	3.01
	Rice Pebble Quartzite	134.22	85.50	2.75
	CLR conglomerate	133.62	85.37	2.77
	Blyvooruitzicht Quartzite	130.45	82.32	2.71
E1U	Maraisburg Quartzite 1	524.02	334.01	2.76
	Maraisburg Quartzite 2	525.44	335.32	2.76
	Maraisburg Quartzite 3	288.09	183.06	2.74
	Roodepoort shale 1	372.78	239.54	2.80
	Roodepoort shale 2	529.01	341.76	2.83
	Roodepoort shale 3	543.46	356.54	2.91
	Lower Roodepoort Quartzite 1	366.41	235.37	2.80
	Lower Roodepoort Quartzite 2	531.80	344.10	2.83
GBH 6003A	Main Quartzite	364.79	230.00	2.71
	Green Bar shale	271.71	180.98	2.99
	Rice Pebble Quartzite	306.82	194.62	2.73
	Blyvooruitzicht Quartzite	219.83	138.45	2.70

Table 1 Continued…. Density measurements.

BH ID	Sample Type	Weight air (g)	Weight water (g)	Density, (g/cm^3)
GBH 6027	Main Quartzite	231.33	146.52	2.73
	Rice Pebble Quartzite	134.31	84.88	2.72
	Blyvooruitzicht Quartzite	132.76	83.83	2.71
GBH 2742	Green Bar shale	80.47	54.90	3.15
	Rice Pebble Quartzite	137.31	89.43	2.87
	Blyvooruitzicht Quartzite	127.34	82.02	2.81
E1T	Main Quartzite 1	515.26	324.06	2.69
	Main Quartzite 2	412.60	260.71	2.72
	Main Quartzite 3	513.97	322.51	2.68
	Main Quartzite 4	444.95	279.74	2.69
	Green Bar shale	263.67	176.87	3.04
	Rice Pebble Quartzite 1	240.66	151.80	2.71
	Rice Pebble Quartzite 2	224.27	143.24	2.77
	Rice Pebble Quartzite 3	247.51	155.31	2.68
	Blyvooruitzicht Quartzite	510.33	319.67	2.68
GBH 6012	Green Bar shale	142.08	96.62	3.13
	Rice Pebble Quartzite	132.94	84.66	2.75
	Blyvooruitzicht Quartzite	132.05	84.36	2.77

Appendix F

Physical Properties

Velocity Data

Appendix F

Table 1 P- and S-wave velocity measurements conducted on borehole samples at ambient pressure, with lithologies listed. The sample length (mm), P-wave arrival time (µs), S-wave arrival time (µs) as well as the P-wave (m/s) and S-wave (m/s) velocities are listed in the table.

BH ID	ROCK TYPE	Sample length (mm)	P-wave (µs)	S-wave (µs)	Vp (m/s)	Vs (m/s)
GBH 6005	Green Bar shale	60	10.60	30.00	5636	2214
	Rice Pebble Quartzite	60	11.90	27.00	5028	2479
	CLR conglomerate	60	11.80	24.20	5070	2562
	Blyvooruitzicht Quartzite	60	12.20	28.00	4918	2071
E1G	Main Quartzite	57	10.55	17.94	5403	3178
	Main Quartzite	80	14.70	24.99	5442	3201
	Green Bar shale	80	14.30	24.31	5594	3291
	Green Bar shale	80	14.60	24.82	5479	3223
	Rice Pebble Quartzite	80	15.10	25.67	5298	3116
	Rice Pebble Quartzite	80	15.05	25.59	5316	3127
	CLR conglomerate	80	15.10	25.67	5298	3116
	Blyvooruitzicht Quartzite	80	15.10	25.67	5298	3116
	Blyvooruitzicht Quartzite	80	14.80	25.16	5405	3180
	Blyvooruitzicht Quartzite	62	12.90	21.93	4806	2827
	Blyvooruitzicht Quartzite	65	13.20	22.44	4924	2897
GBH 6023	Main Quartzite	60	11.10	22.30	5882	2685
	Green Bar shale	60	10.20	17.34	5263	3460
	Rice Pebble Quartzite	60	11.40	19.38	5088	3096
	CLR conglomerate	135	24.70	41.99	5085	3027
	Blyvooruitzicht Quartzite	60	11.80	20.06	5333	2919
E1U	Maraisburg Quartzite	80	15.00	25.50	5369	3137
	Maraisburg Quartzite	80	14.90	25.33	4592	3158
	Maraisburg Quartzite	45	9.80	16.66	5085	2701
	Roodepoort shale	60	11.80	20.06	5479	2991
	Roodepoort shale	80	14.60	24.82	5556	3223
	Roodepoort shale	80	14.40	24.48	4955	3268
	Lower Roodepoort Quartzite 1	55	11.10	18.87	5000	2915
	Lower Roodepoort Quartzite 2	80	16.00	27.20	4970	2941
GBH 6003A	Main Quartzite	164	33.00	65.00	5914	2523
	Green Bar shale	110	18.60	49.00	5458	2245
	Rice Pebble Quartzite	137	25.10	56.00	5211	2446
	Blyvooruitzicht Quartzite	99	19.00	42.00	5636	2357

Table 1 Continued…. P- and S-wave velocity measurements at ambient pressure.

BH ID	ROCK TYPE	Sample length (mm)	P-wave (µs)	S-wave (µs)	Vp (m/s)	Vs (m/s)
GBH6027	Main Quartzite	112	21.50	36.55	5209	3064
	Rice Pebble Quartzite	60	11.60	26.00	5172	2308
	Blyvooruitzicht Quartzite	60	11.90	27.00	5042	2222
GBH 2742	Green Bar shale	31	6.05	15.00	5124	2067
	Rice Pebble Quartzite	60	11.50	28.00	5195	2143
	Blyvooruitzicht Quartzite	60	12.10	19.00	4959	3158
E1T	Main Quartzite	80	16.80	28.56	4762	2801
	Main Quartzite	80	16.00	27.20	5000	2941
	Main Quartzite	80	15.00	25.50	5333	3137
	Main Quartzite	80	14.80	25.16	5405	3180
	Main Quartzite	80	17.00	28.90	4706	2768
	Green Bar shale	80	14.30	24.31	5594	3290
	Rice Pebble Quartzite	80	14.65	24.91	5461	3212
	Rice Pebble Quartzite	80	14.60	24.82	5479	3223
	Rice Pebble Quartzite	80	14.55	24.74	5498	3234
	Blyvooruitzicht Quartzite	80	16.50	28.05	4706	2852
	Blyvooruitzicht Quartzite	80	17.00	28.90	5769	2768
GBH 6012	Green Bar shale	60	10.40	25.00	5263	2400
	Rice Pebble Quartzite	60	11.40	26.00	5150	2308
	Blyvooruitzicht Quartzite	60	11.60	27.00	5209	2222

Appendix G

Physical Properties

Acoustic Impedance

and

Reflection coefficient

Appendix G

Table 1 Summary of bulk density (ρ), P-wave velocity (Vp), acoustic impedance (Z) and reflection coefficient (Rc) measured at ambient stress for 9 boreholes. The Z is calculated from the product of the velocity and density and the Rc = $(\rho_2 Vp_2 - \rho_1 Vp_1) / (\rho_2 Vp_2 + \rho_1 Vp_1)$. Quartzite (Qtzt.); Carbon Leader Reef (CLR).

BH Name	Sample Type	Sample thickness (mm)	Velocity (Vp, m/s)	Density (ρ, g/cm^3)	Z (*10^5, g/cm^{2}s)	[Rc]
BH-A	Green Bar shale	60	5636	3.00	16.91	0.10
	Rice Pebble Qtzt.	60	5028	2.72	13.70	0.02
	CLR	60	5070	2.83	14.36	0.04
	Blyvooruitzicht Qtzt.	60	4916	2.71	13.32	
BH-B	Main Qtzt.	80	5423	2.69	14.59	0.05
	Green Bar shale	80	5537	2.89	16.00	0.06
	Rice Pebble Qtzt.	80	5307	2.68	14.22	0.02
	CLR	80	5468	2.74	14.97	0.05
	Blyvooruitzicht Qtzt.	80	5108	2.66	13.59	
BH-C	Green Bar shale	60	5882	3.01	17.71	0.10
	Rice Pebble Qtzt.	60	5263	2.76	14.53	0.02
	CLR	60	5088	2.77	14.03	0.01
	Blyvooruitzicht Qtzt.	60	5085	2.71	13.78	
BH-D	Maraisburg Qtzt.	80	4980	2.76	13.75	0.07
	Roodepoort shale	80	5518	2.87	15.84	0.06
	Lower Roodepoort Qtzt.	80	4977	2.81	13.99	

BH-E	Main Qtzt.	60	4970	2.71	13.47	0.14
	Green Bar shale	60	5914	3.00	17.74	0.09
	Rice Pebble Qtzt.	60	5458	2.73	14.90	
	Blyvooruitzicht Qtzt.	60	5211	2.70	14.07	-
BH-F	Main Qtzt.	60	5209	2.73	14.22	-
	Rice Pebble Qtzt.	60	5172	2.72	14.07	-
	Blyvooruitzicht Qtzt.	60	5042	2.71	13.66	-
BH-G	Green Bar shale	31	5124	3.15	16.14	0.04
	Rice Pebble Qtzt.	60	5195	2.87	14.91	
	Blyvooruitzicht Qtzt.	60	4959	2.72	13.49	-
BH-H	Main Qtzt.	80	5041	2.69	13.56	0.11
	Green Bar shale	80	5594	3.04	17.01	0.07
	Rice Pebble Qtzt.	80	5480	2.72	14.90	
	Blyvooruitzicht Qtzt.	80	4777	2.68	12.80	
BH-I	Green Bar shale	60	5769	3.13	18.06	0.11
	Rice Pebble Qtzt.	60	5263	2.75	14.47	
	Blyvooruitzicht Qtzt.	60	5150	2.77	14.27	

Appendix H

Physical Properties

Velocity-Pressure Data

Appendix H

Table 1 P-wave velocity (m/s) as a function of increasing Stress (MPa) for borehole samples. The velocities of the half-core samples could not be measured at elevated stresses. These are denoted with n.d. =not determined.

BH ID	Sample Type	Stress										
		0 MPa	5 MPa	10 MPa	15 MPa	20 MPa	25 MPa	30 MPa	40 MPa	50 MPa	60 MPa	65 MPa
GBH 6005	Green Bar shale	5636	5769	5769	5769	5882	5882	5882	5882	5882	5882	5882
	Rice Pebble Quartzite	5028	5263	5263	5455	5455	5455	5455	5455	5455	5455	5455
	CLR conglomerate	5070	5070	5070	5152	5455	5455	5455	5455	5455	5455	5455
	Blyvooruitzicht Quartzite	4918	5120	5120	5263	5357	5455	5455	5455	5455	5455	5455
E1G	Main Quartzite	5403	n.d.	n.d.	n.d.	n.d.	n.d.	n.d.	n.d.	n.d.	n.d.	n.d.
	Main Quartzite	5442	n.d.	n.d.	n.d.	n.d.	n.d.	n.d.	n.d.	n.d.	n.d.	n.d.
	Green Bar shale	5594	n.d.	n.d.	n.d.	n.d.	n.d.	n.d.	n.d.	n.d.	n.d.	n.d.
	Green Bar shale	5479	n.d.	n.d.	n.d.	n.d.	n.d.	n.d.	n.d.	n.d.	n.d.	n.d.
	Rice Pebble Quartzite	5298	n.d.	n.d.	n.d.	n.d.	n.d.	n.d.	n.d.	n.d.	n.d.	n.d.
	Rice Pebble Quartzite	5316	n.d.	n.d.	n.d.	n.d.	n.d.	n.d.	n.d.	n.d.	n.d.	n.d.
	CLR conglomerate	5298	n.d.	n.d.	n.d.	n.d.	n.d.	n.d.	n.d.	n.d.	n.d.	n.d.
	Blyvooruitzicht Quartzite	5298	n.d.	n.d.	n.d.	n.d.	n.d.	n.d.	n.d.	n.d.	n.d.	n.d.
	Blyvooruitzicht Quartzite	5405	n.d.	n.d.	n.d.	n.d.	n.d.	n.d.	n.d.	n.d.	n.d.	n.d.

Table 1 Continued…. P-wave velocity an increasing Pressure relationship.

BH ID	Sample Type	Pressure										
		0 MPa	5 MPa	10 MPa	15 MPa	20 MPa	25 MPa	30 MPa	40 MPa	50 MPa	60 MPa	65 MPa
	Blyvooruitzicht Quartzite	4806	n.d.	n.d.	n.d.	n.d.	n.d.	n.d.	n.d.	n.d.	n.d.	n.d.
	Blyvooruitzicht Quartzite	4924	n.d.	n.d.	n.d.	n.d.	n.d.	n.d.	n.d.	n.d.	n.d.	n.d.
GBH 6023	Green Bar shale	5882	n.d.	n.d.	n.d.	n.d.	n.d.	n.d.	n.d.	n.d.	n.d.	n.d.
	Rice Pebble Quartzite	5263	n.d.	n.d.	n.d.	n.d.	n.d.	n.d.	n.d.	n.d.	n.d.	n.d.
	CLR conglomerate	5088	n.d.	n.d.	n.d.	n.d.	n.d.	n.d.	n.d.	n.d.	n.d.	n.d.
	Blyvooruitzicht Quartzite	5085	n.d.	n.d.	n.d.	n.d.	n.d.	n.d.	n.d.	n.d.	n.d.	n.d.
E1U	Maraisburg Quartzite	5333	5063	5096	5096	5128	5128	5128	5128	5128	5128	5128
	Maraisburg Quartzite	5369	5031	5031	5063	5096	5096	5096	5096	5096	5096	5096
	Maraisburg Quartzite	4592	4688	4688	4787	5000	5000	5000	5000	5000	5000	5000
	Roodepoort shale	5085	5172	5263	5263	5455	5455	5455	5455	5455	5455	5455
	Roodepoort shale	5479	5479	5556	5556	5714	5714	5714	5714	5714	5714	5714
	Roodepoort shale	5556	5556	5634	5654	5714	5714	5714	5714	5714	5714	5714
	Lower Roodepoort Quartzite	4955	5000	5189	5288	5392	5392	5392	5392	5392	5392	5392

Table 1 Continued…. P-wave velocity an increasing Pressure relationship.

BH ID	Sample Type	Pressure										
		0 MPa	**5 MPa**	**10 MPa**	**15 MPa**	**20 MPa**	**25 MPa**	**30 MPa**	**40 MPa**	**50 MPa**	**60 MPa**	**65 MPa**
	Lower Roodepoort Quartzite	5000	5161	5333	5333	5479	5479	5556	5556	5556	5556	5556
GBH 6003A	Main Quartzite	4970	5125	5206	5248	5248	5248	5248	5248	5248	5248	5248
	Green Bar shale	5914	5914	5914	5914	5946	5946	5946	5946	5946	5946	5946
	Rice Pebble Quartzite	5458	5524	5524	5661	5661	5708	5708	5708	5708	5708	5708
	Blyvooruitzicht Quartzite	5211	5266	5323	5323	5380	5380	5380	5380	5380	5380	5380
GBH 6027	Main Quartzite	5209	5234	5283	5283	5333	5333	5333	5333	5333	5333	5333
	Rice Pebble Quartzite	5172	5263	5263	5263	5357	5455	5455	5455	5455	5455	5455
	Blyvooruitzicht Quartzite	5042	5085	5172	5172	5357	5357	5357	5357	5357	5357	5357
GBH 2742	Green Bar shale	5124	5345	5439	5439	5536	5536	5536	5536	5536	5536	5536
	Rice Pebble Quartzite	5195	5217	5217	5263	5357	5405	5405	5405	5405	5405	5405
	Blyvooruitzicht Quartzite	4959	5085	5263	5263	5357	5357	5357	5357	5357	5357	5357
E1T	Main Quartzite	4762	5128	5128	5195	5195	5333	5333	5333	5333	5333	5333
	Main Quartzite	5000	5161	5161	5263	5263	5405	5405	5405	5405	5405	5405

Table 1 Continued…. P-wave velocity an increasing Pressure relationship.

BH ID	Sample Type	Pressure										
		0 MPa	**5 MPa**	**10 MPa**	**15 MPa**	**20 MPa**	**25 MPa**	**30 MPa**	**40 MPa**	**50 MPa**	**60 MPa**	**65 MPa**
	Main Quartzite	5333	5333	5479	5479	5479	5517	5517	5517	5517	5517	5517
	Main Quartzite	5405	5479	5556	5634	5634	5714	5714	5714	5714	5714	5714
	Main Quartzite	4706	5000	5031	5229	5229	5263	5263	5263	5263	5263	5263
	Green Bar shale	5594	n.d.	n.d.	n.d.	n.d.	n.d.	n.d.	n.d.	n.d.	n.d.	n.d.
	Rice Pebble Quartzite	5461	n.d.	n.d.	n.d.	n.d.	n.d.	n.d.	n.d.	n.d.	n.d.	n.d.
	Rice Pebble Quartzite	5479	n.d.	n.d.	n.d.	n.d.	n.d.	n.d.	n.d.	n.d.	n.d.	n.d.
	Rice Pebble Quartzite	5498	n.d.	n.d.	n.d.	n.d.	n.d.	n.d.	n.d.	n.d.	n.d.	n.d.
	Blyvooruitzicht Quartzite	4706	5000	5000	5229	5229	5263	5263	5263	5263	5263	5263
GBH 6012	Green Bar shale	5769	5882	5941	5970	6000	6000	6000	6000	6000	6000	6000
	Rice Pebble Quartzite	5263	5357	5357	5357	5556	5556	5556	5556	5556	5556	5556
	Blyvooruitzicht Quartzite	5150	5217	5263	5263	5357	5357	5357	5357	5357	5357	5357